A thesis on

THE ELECTROCHEMICAL AND ELECTROCATALYTIC BEHAVIOUR OF GOLD NANOPARTICLES

Submitted in partial fulfilment of the requirements

for the Degree of Doctor of Philosophy in

Chemical & Process Engineering at the University of Canterbury

By Jared Steven

University of Canterbury

2017

"The life to which I belong uses me, and will pass beyond me, and I am content"

H. G. Wells

Acknowledgements

The support of the following people has been greatly appreciated in helping me achieve my research goals and this thesis. I would like to thank the following people;

- First and foremost, my senior supervisor: Dr Aaron Marshall. Aaron has believed in my ability from my beginnings in undergraduate projects and summer research work right through to the conclusions of this thesis. Aaron's constant availability, advice and enthusiasm have provided me with the support and encouragement needed to guarantee my success. Aaron's work has been perfectly complemented by my co-supervisor, Dr Vladimir Golovko, whose additional ideas, viewpoints and resources have given my research further scope.
- The University of Canterbury staff who have supported me through their advice and technical skills, these include; Stephen Beuzenberg, Graham Furniss, Tony Allen, Stephen Hood, Leigh Richardson, Michael Sandridge, Glenn Wilson and Tim Moore.
- Mike Flaws in Mechanical Engineering for helping with SEM/TEM imaging, Alistair Duff in Chemistry with his help with AAS and amino-silane/gold adsorption, Dr Colin Doyle from the University of Auckland for his help with XPS and Dr Bernt Johansson from the Australian Synchrotron for the use of and help with the XAS beamline.
- Dr Peter Gostomski and the CAPE department for providing a welcoming and nourishing research environment.
- The MacDiarmid Institute and Royal Society of New Zealand Marsden Fund for their financial aid.
- My research peers Calvin Lim, Tobias Baldhoff, Asadollah Kariman and Diandre Padayachee for their office discussions and problem-solving sessions. I also thank my colleague in Chemistry, Rohul Adnan who helped synthesise the Au_{101} and Au_9 catalysts.
- My extended family and friends for support through the times where my passion was diminished and their excitement when my enthusiasm was strong.
- Finally, my children, Hollie and Jack, and my wife, Tash have my unending gratitude. The years of my study have put us under such strain that I would never wish on anyone, yet they have stuck by me. Without their support, I could never have climbed to the heights I have reached and I now look forward to repaying their forbearance by accompanying them in a life of which they could only dream.

Abstract

Despite the commonly held belief that gold is unreactive, in 1986, gold was shown to be active toward the electrocatalytic oxidation of CO and hydrochlorination of ethyne. Since then, research into additional reactions catalysed by gold has been conducted on bulk gold, gold nanoparticle and gold-alloyed catalysts. In this thesis, a study of the electrochemical behaviour of gold nanoparticles and their electrocatalytic promotion of the glycerol oxidation and CO_2 reduction reactions has been undertaken.

Gold nanoparticles between 0.8 nm and 23.9 nm were produced and the size and surface area of each batch of nanoparticles was characterised. Models based on a number-weighted particle size distribution with a mean particle size of 10.0 nm showed that if the same distribution was weighted according to the particle volume, surface area or specific surface area, the mean particle size would be 10.8, 10.4 and 9.0 nm, respectively. Electrochemical surface area characterization was performed by cyclic voltammetry and measuring the charge associated with the gold oxide reduction peak. Quantitatively measuring this charge for an electrode containing 3.2 nm gold particles showed a gradient of 2.52 $mC \cdot V^{-1}$ for bulk gold electrodes and 1.62 $mC \cdot V^{-1}$. These gradients were only applicable for the electrodes that were being tested as a change in the electrode surface area will lead to a different amount of gold oxide reduction and hence a different charge capacity of the electrode.

As gold dissolution occurs across the same potential range as gold oxide formation, the inherent stability of the electrode is linked to the time spent in this region of a CV scan. It was found that 50 CV scans in 0.5 M H_2SO_4 will artificially age 3.2 nm nanoparticles. This is seen by an electrode that had an initial gold oxide reduction charge of 969 $\mu C \cdot cm_{Au}^{-2}$ for CV scans with a maximum potential of 1.85 V vs. RHE, whereas by the end of the 50^{th} CV scan, the gold oxide charge was recorded as 29 $\mu C \cdot cm_{Au}^{-2}$, a reduction of 97%. CV scans with a maximum potential of 1.55 V vs. RHE reached a maximum gold oxide reduction charge of 115 $\mu C \cdot cm_{Au}^{-2}$, however, this value decayed to 89 $\mu C \cdot cm_{Au}^{-2}$ by the end of the 50^{th} CV scan, a reduction of 23%. The maximum useable depth of the catalytic layer was determined to be 26.6 μm, after which the full availability of the layer is uncertain. The Nafion content of the layer was found to prevent all gold oxide formation at 10 wt% due to insufficient ionic transfer through the layer, and caused rapid ageing of the sample at 47 wt%. Intermediate loadings of 20 wt% and 33 wt% measured a smaller maximum gold oxide reduction charge than the 47 wt% electrode, however, they exhibited comparatively slow ageing, suggesting between 20 wt% and 33 wt% are the preferred targets for the Nafion content of a catalytic layer.

Gold nanoparticles, ranging in size from 0.8 nm clusters up to 4.5 nm nanoparticles were synthesised by a variety of different methods and supported on carbon black. An accelerated ageing process was applied to a catalytic layer containing these nanoparticles by performing 100 CV scans to establish the long-term stability of the nanoparticles in an electrochemical cell. Particle growth was observed via TEM imaging such that the average

number-weighted particle size after CV scanning ranged from 4.5 nm to 8.2 nm. The gold content of the electrolyte indicated 3% – 6% of the gold in the electrode was lost to the electrolyte during the ageing process. The results of this accelerated ageing investigation were published in Electrochimica Acta [1].

The gold surface plasmon resonance feature was investigated by performing CV scanning of 23.9 nm gold particles while simultaneously recording the UV-Vis spectrum. Analysis of the SPR absorption intensity showed how an absorption-based spectroscopic CV scan could be produced for electrodes in 0.5 M H_2SO_4 while a similar analysis on the SPR peak wavelength produced a wavelength-based spectroscopic CV scan for electrodes in 1.0 M KOH. These analysis techniques were then applied to an electrode performing glycerol oxidation in a 1.0 M KOH + 0.1 M glycerol solution. The wavelength-based spectroscopic CV scan was able to show a promotion of the reduction of gold oxide by a shift in the gold oxide reduction feature by +0.09 ± 0.01 V, relative to the corresponding spectroscopic CV scan in 1.0 M KOH. A small, but the similar promotion of gold oxide formation was seen via a shift in the gold oxide formation feature by -0.02 ± 0.01 V. The spectroscopic observations of electrochemical processes are a new technique that allows for the monitoring of the underlying gold behaviour during catalytic reactions, typically unable to be observed in electrochemical measurements.

The electrocatalytic reduction of CO_2 was performed on 3.2 nm gold nanoparticles supported by carbon black in a CO_2 saturated solution of 0.2 M $KHCO_3$. GC and HPLC measurements confirmed that CO and H_2 were the major products of all reactions on both bulk gold and nanoparticle-based electrodes. It was found that a bulk gold electrode, while the rate of CO production began at 2.45 $\mu mol \cdot min^{-1}$, by the end of a four-hour galvanostatic charging experiment, this rate had dropped to 0.59 $\mu mol \cdot min^{-1}$. Comparatively, the gold nanoparticles had less than 30% of the electrochemical surface area of the bulk gold, yet retained a constant CO production rate of 1.10 $\mu mol \cdot min^{-1}$ throughout the four-hour experiment. Catalytic gold loading experiments showed that ~1.5 wt% gold electrodes (98.5% carbon) produced CO at similar rates to 7.5 wt% and 15.1 wt% gold electrodes. Layer thickness experiments showed that as the layer thickness decreased, both the normalised and the overall CO production rates increased. This effect has been attributed to the carbon support playing an active role in the hydrogen evolution reaction and with the removal of carbon from the electrodes, the gold was able to reduce more CO_2.

Deputy Vice-Chancellor's Office
Postgraduate Office

UNIVERSITY OF CANTERBURY
Te Whare Wānanga o Waitaha
CHRISTCHURCH NEW ZEALAND

Co-Authorship Form

This form is to accompany the submission of any thesis that contains research reported in co-authored work that has been published, accepted for publication, or submitted for publication. A copy of this form should be included for each co-authored work that is included in the thesis. Completed forms should be included at the front (after the thesis abstract) of each copy of the thesis submitted for examination and library deposit.

Please indicate the chapter/section/pages of this thesis that are extracted from co-authored work and provide details of the publication or submission from the extract comes:
Chapter 4 is a reproduction of the publication:
Steven, J. T., V. B. Golovko, B. Johannessen and A. T. Marshall (2016). "Electrochemical stability of carbon-supported gold nanoparticles in acidic electrolyte during cyclic voltammetry." Electrochimica Acta ***187****: 593-604*

Please detail the nature and extent (%) of contribution by the candidate:
I synthesised the 4.5 nm Au and 2.9 nm Au. The 0.8 nm Au and 3.1 nm Au were prepared by other students in our group
Performed EXAFS with Dr Aaron Marshall, Calvin Lim & Dr Bernt Johannessen
Alistair Duff – AAS
Colin Doyle – XPS
I performed EXAFS modelling, XPS fitting, TEM imaging, electrochemistry, sample preparation, and all other analysis
Written by myself (80%) & Dr Aaron Marshall (20%)

Certification by Co-authors:

If there is more than one co-author then a single co-author can sign on behalf of all

The undersigned certifys that:

- The above statement correctly reflects the nature and extent of the PhD candidate's contribution to this co-authored work
- In cases where the candidate was the lead author of the co-authored work he or she wrote the text

Name: *Aaron Marshall* Signature:  Date: *30/01/2017*

CONTENTS

LIST OF TABLES

List of Figures

NOMENCLATURE

Nomenclature

- Ag/AgCl Silver-silver chloride reference electrode
- CV Cyclic voltammetry / Cyclic voltammogram
- CCS Carbon capture and sequestration
- DFT Density functional theory
- EASA Electrochemically active surface area
- E-QCN Electrochemical quartz crystal nanobalance
- EXAFS Extended X-ray absorption fine structure
- ITO Indium-doped tin oxide
- IR Infrared
- FCC Face-centred cubic
- FTO Fluorine doped tin oxide
- GC Gas chromatograph
- HER Hydrogen evolution reaction
- Hg/HgO Mercury-mercury oxide reference electrode
- HOMO Highest occupied molecular orbital
- HPLC High-pressure liquid chromatograph
- LUMO Lowest unoccupied molecular orbital
- OCP Open circuit potential
- P-EIS Potentiostatic electrochemical impedance spectroscopy
- PCC Pierson product-moment correlation coefficient
- PEM Proton exchange membrane
- PSD Particle size distribution
- RHE Reversible hydrogen electrode
- SCE Standard calomel electrode
- SEM/TEM Scanning/transmission electron microscope
- SPR Surface plasmon resonance
- STM Scanning tunnelling microscope
- UHV Ultra-high vacuum
- UPD Underpotential deposition
- UV-Vis Ultraviolet-visible (spectroscopy)

- XANES X-ray absorption near edge spectroscopy
- XAS X-ray absorption spectroscopy
- XPS X-ray photoelectron spectroscopy
- XRD X-ray diffraction

Variables and Constants

• a	Lattice parameter	Å
• A	SPR peak area	Absorbance · nm
• D	Diameter	nm
• $E_{Ag/AgCl}$	Potential of the Ag/AgCl reference electrode	V
• $E_{L3,gold}$	Gold L_3 absorption step energy	eV
• E_{max}	Maximum anodic potential of the CV	V
• E_{RHE}	Potential of the RHE	V
• $E-E_0$	Edge energy shift (EXAFS)	eV
• F(k)	Effective scattering amplitude (EXAFS)	-
• F	Faraday's constant	$C \cdot mol^{-1}$
• N	Number of particles	-
• n	number of electrons	-
• N_i	Path degeneracy (EXAFS)	-
• N_A	Avogadro's number	$molecules \cdot mol^{-1}$
• P	Pressure	Pa
• PD	Packing density	$atoms \cdot Å^{-1}$
• r	CO selectivity	-
• R_0	Theoretical path length (EXAFS)	Å
• ΔR	Change in path length (EXAFS)	Å
• S_0^2	Amplitude reduction factor (EXAFS)	-
• SCD	Specific charge density	$\mu C \cdot cm^{-2}$
• SSA	Specific surface area	$m^2 \cdot g^{-1}$
• TOF	Turnover frequency	s^{-1}
• w	SPR peak width (Lorentz)	nm
• γ	Specific surface stress	$J \cdot nm^{-2}$
• κ	Compressibility	$nm^3 \cdot N^{-1}$
• λ	Wavelength	nm
• λ(k)	Mean free path (EXAFS)	Å
• μ(D)	Chemical potential of a particle at a diameter, D.	$J \cdot mol^{-1}$
• μ(∞)	Chemical potential of the bulk metal	$J \cdot mol^{-1}$
• σ_i^2	Debye-Waller factor (EXAFS)	-
• χ(k)	Electron scattering path (EXAFS)	-
• φ(k)	Effective scattering phase shift (EXAFS)	Å
• Ω	Bulk metal atomic volume	$nm^3 \cdot mol^{-1}$

Chemicals

The following is a list of chemicals used in this thesis, along with the concentration at purchase and supplier;

Common Name	Full Name	Concentration	Supplier
Amino-silane	(3-aminopropyl)triethoxysilane	99%	Sigma-Aldrich
Argon	Argon	99.999%	BOC gases
Carbon	Vulcan XC-72R, carbon black	>99%	Cabot
Celite	Silicon Dioxide (filter aid)	ACS	Sigma-Aldrich
Chloroform	Chloroform	99.0-99.4%	Merck
CO_2	Carbon dioxide	99.995%	BOC gases
DCM	Dichloromethane	ACS	Merck
DI water	Deionized water	18.2 MΩ · cm	Sartorius Arium 611UV
Glycerol	Glycerol	99.95%	BDH Chemicals Ltd.
H_2SO_4	Sulfuric Acid	99.7% ACS	Ajax Finechem
$HAuCl_4 \cdot 3H_2O$	Chloroauric acid	99.90%	Sigma-Aldrich
HCl	Hydrochloric acid	34-37%	Fisher Sci.
Hexane	Hexane	99+%	Sigma-Aldrich
HNO_3	Nitric acid	ACS	Merck
IPA	Isopropanol	99%	Allied Petroleum
$KHCO_3$	Potassium bicarbonate	ACS	Sigma-Aldrich
KOH	Potassium hydroxide	>85.0%	Ajax Finechem
Methanol	Methanol	HPLC grade	Fisher Sci.
$Na_3C_6H_5O_7 \cdot 2H_2O$	Sodium citrate	99.0%	Sigma-Aldrich
NaBH4	Sodium borohydride	95%	BDH
NaCl	Sodium chloride	ACS	Merck
Nafion	LIQUion EW1100		Ion Power, Inc.
NaOH	Sodium hydroxide	AnalaR	BDH
Pentane	N-pentane	>98.0%	Fisher Sci.
PPh_3	Triphenylphosphine	>99.0%	Merck
THPC	Tetrakis(hydroxymethyl) -phosphonium chloride	80%	Sigma-Aldrich
TOAB	Tetraoctylammonium bromide	>98.0%	Merck
Toluene	Toluene	>99.5%	BDH Chemicals Ltd.

Chapter 1 LITERATURE REVIEW

1.1 Thesis Outline

Each chapter within the main 'body' of this thesis (Chapters 2-5) is written in the style of a research paper including an individual and detailed literature review. The following chapter is an overview of the entire thesis and includes a broad outline of the topics, methods and theories used within. As such, some information is repeated or expanded upon throughout the thesis as required

1.2 Brief History

Since Hutchings [2] published a paper in 1985 and Haruta [3] wrote his independent letter two years later, the number of papers written about gold catalysis has gone through a rapid growth phase. These two publications showed gold to be a leading catalyst for both the hydrochlorination of ethyne [2] and the low-temperature oxidation of CO [3]. The following 18 years saw an increase in papers about gold catalysis from around 40 in 1987 to over 800 in 2005 [4].

During the late 1990's Teles et al. [5] published research regarding heterogeneous gold catalysis adding alcohol groups to alkynes while Hashmi et al. [6] performed cycloisomerization of allenyl ketones using a homogenous gold solution as a catalyst. By showing the feasibility of a gold-based catalyst, these experiments initiated the massive growth in gold catalysis research that was experienced throughout the 2000's, right up to the present day.

This growth is showing no signs of slowing, in fact, Rudolph and Hashmi, authors of a broad 2008 review entitled "*Gold catalysis in total synthesis*" [7], published an update to this work just four years later as they considered it to be overdue [8]. From this point, Hashmi has gone on to publish almost annual reviews [9-12] with the latest including inspiring statements such as "*…gold catalysis is considered a thriving field with numerous novel and unexpected discoveries every year"* and *"the application of gold catalysed reactions in total synthesis is still increasing with many beautiful examples"* [11]. While these reviews are published by Hashmi's group, they are not in isolation – other reviews are continuously being published by additional authors [13-21].

1.3 Properties of Gold Nanoparticles

Gold ([Xe], $6s^1$, $4f^{14}$, $5d^{10}$) is the 79th element of the periodic table, preceded by platinum and in close proximity to other precious metal catalysts like ruthenium, rhodium, palladium and silver. It is commonly agreed that the significant factor that makes group VIII and Ib elements effective catalysts is their partially empty d-band orbitals [22, 23]. While gold does not have a vacancy in the 5d orbital, the vacancy in the 6s orbital has a similar effect on its catalytic properties [24]. Taylor [25] found that the interactions between the 5d, 6s and 4f orbitals gives rise to an interesting phenomenon where, as the number of atoms in clusters rises from 2 through to 58 atoms, the electron affinity of single metal clusters goes through a zig-zag pattern as the half full 6s orbitals are precisely complementary for clusters with an even number of atoms bind electrons tighter than clusters with an odd number of atoms which have a single electron left unpaired.

1.3.1 Differences between Bulk and Nanoparticle

It is well known that as gold particles transition from bulk gold particles to nanoparticles their behaviour undergoes changes such as separation of the HOMO-LUMO gap, contraction of Au-Au bond length, and discretization of gold atoms. These effects impact many characteristics of the gold including its reactivity, surface plasmon resonance (SPR) feature, metallic behaviour, surface bond stresses etc. [26, 27]. Aside from these electronic-based nano-effects, the total number of surface atoms per unit mass of gold increases, which means there is more gold surface available for catalysis. As a rough guide, a 5 nm gold nanoparticle has approximately 8000 atoms, 20% of which are surface atoms while a 2 nm gold nanoparticle has approximately 50% of its 500 atoms as surface atoms.

1.3.2 Lattice Constant

In bulk gold (Figure 1-1), the FCC lattice constant is 4.08 Å and the covalent radius is 1.44 Å [28] however, these values have been shown to decrease once the cluster diameter drops below 4.5 nm [1, 29-31]. Miller [30] also correlates the Au-Au coordination number and bond length and finds that as the coordination number decreases, the bond length also decreases. This can be considered as analogous to small liquid spheres where the pressure inside the sphere is calculated via the Laplace equation;

$$\Delta P = \frac{4\gamma}{D} \qquad 1\text{-}1$$

where the internal pressure (ΔP) is directly proportional to the specific surface stress (γ) and inversely proportional to the sphere diameter (D). This has been shown in EXAFS measurements by Apai et al. [32] and confirmed as described by Crescenzi et al. [33] with the equation;

$$\frac{\Delta a}{a} = -\frac{4\kappa\gamma}{3D} \qquad 1\text{-}2$$

where the changes in the lattice parameter (a) is directly proportional to the compressibility (κ) and the specific surface stress (γ) and is inversely proportional to the diameter of the particle (D).

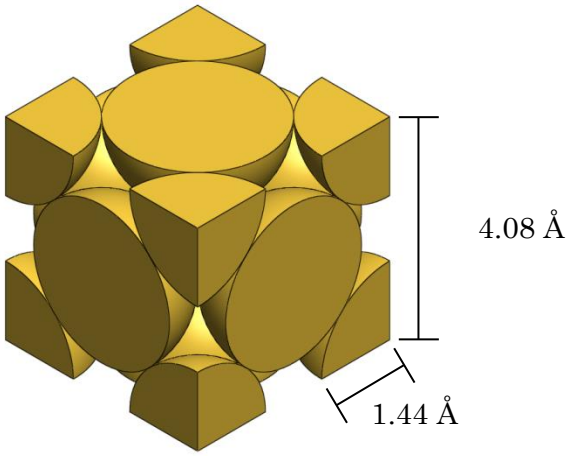

Figure 1-1. Unit cell of gold.

1.3.3 Theoretical Shape of Nanoparticles

Another consideration to make with respect to atomic clusters is what shape they will be. Generally, larger nanoparticles can be considered to be spheres, however, when the nanoparticles become smaller, they lose sphericity and their true shape must be considered. Cleveland et al. [34], through energy minimization calculations, determined that 1.4 nm – 3.0 nm nanoparticles (100 atoms – 1000 atoms) have three energetically favourable shapes; decahedron, truncated octahedron, and twinned truncated octahedron. Their study concludes, via XRD patterns and comparison with other work, that 1.7 nm, 1.9 nm and 2.5 nm gold nanoparticles transition from a decahedral nanoparticle below 1.8 nm (~180 atoms) to a mono-crystal or twinned crystal FCC structure above 1.8 nm. The exact behaviour of these clusters is dependent on the local environment of the clusters, with a particular emphasis on the stabilising ligand, or capping atoms [35]. Uppenbrink and Wales [35], through molecular dynamics simulations, state that "*the presence or absence of particular capping or surface atoms can be crucial in determining structural stability*" and as such, any assumption of comparability between gold clusters with different stabilising ligands must be carefully considered.

1.3.4 Magic Numbers

It is typical when studying small, theoretical nanoclusters to consider complete shell approximations due to the ease of calculation, i.e. if a single atom is missing from a complete shell – which position in the shell is the atom missing from? The number of atoms within a complete shell model is called the 'magic number'. For example, an icosahedron with a single, central atom surrounded a by single icosahedral layer (defined as 'one shells') requires 13 atoms while a second complete shell will produce a particle with 55 atoms and a third shell will produce a particle with 147 atoms.

An additional benefit to these magic numbers is that they are the same for complete shells for cuboctahedral, dodecahedral and icosahedral arrangements (Figure 1-2). The overlay on the three complete shell particles outline the (111) facets and the (100) facets; it is clear to see that each arrangement of atoms has its own specific ratio of (111) to (100) facets. Due to the fact that each facet may have different catalytic properties and surface energies, a catalyst can be tailored to have more or less of a particular facet by manipulating the nanoparticle configuration. The facet ratios of these shapes is discussed further in Chapter 2.

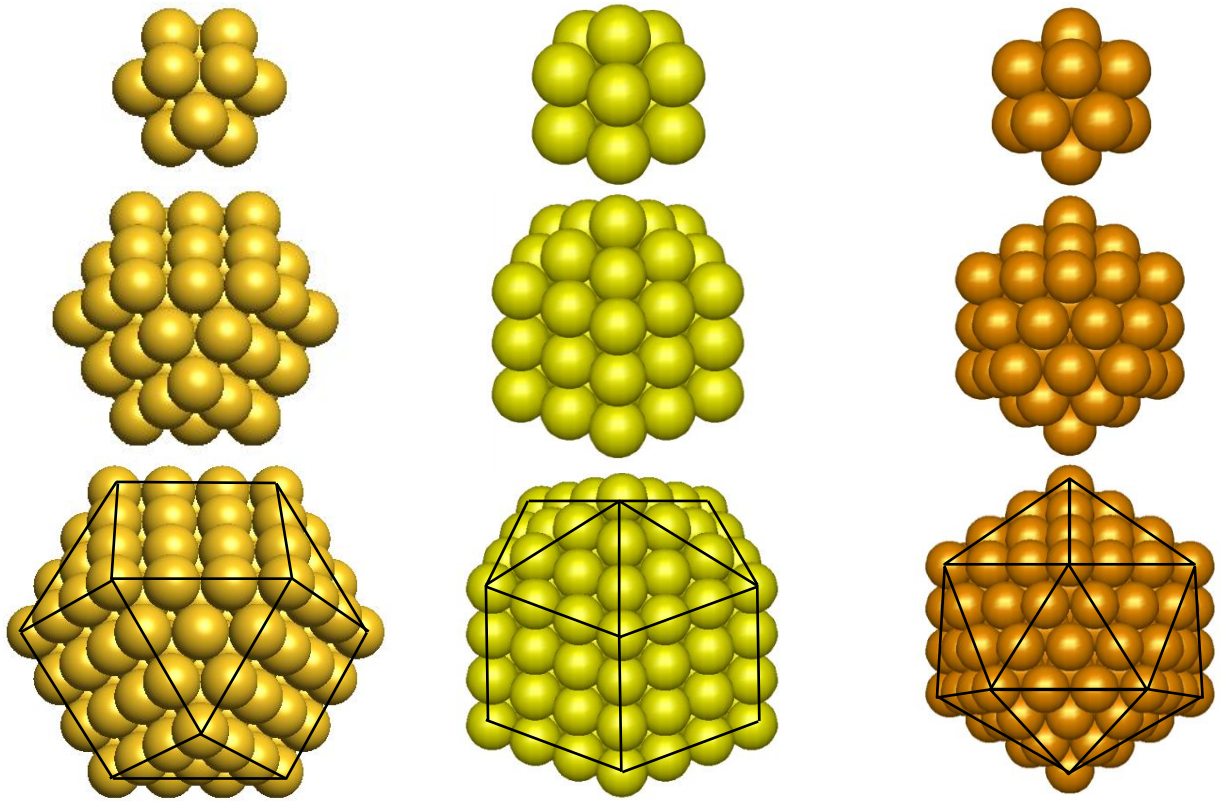

Figure 1-2. Representations of cuboctahedral (pale orange), decahedral (yellow) and icosahedral (orange) arrangements of Au-13, Au-55 and Au-147, the first three 'magic number' clusters. Edge lines have been indicated in the largest representations with Au(111) faces shown in the triangles and Au(100) faces shown in the squares.

1.4 Reactivity

The reactivity of gold per unit mass is clearly dependent on particle size. As the apparent particle diameter decreases, the surface area increases by a factor of the square of the ratio of the decrease in diameter [36]. This leads to a similar increase in available surface sites and thus an increase in reactivity. Despite this assumption, it is found that there is a limit to this effect. Valden et al. [37] found that below 3.0 nm, the surface area normalised activity of gold starts decreasing again. Janz et al. [38] found that 1 nm gold particles could adsorb twice as much alkanethiol on a per unit surface area compared to

bulk gold surfaces. Janz et al. [38] also made the assumption that hemispherical particles are analogous to spherical particles while others have reported experimental results that show hemispherical particles have a higher turnover frequency (TOF) than spherical particles with similar diameters [22].

Different crystal faces have also been shown to have different affinities to different chemicals [23, 39, 40], a fact that can be used to target reactions using facet promotion techniques [39, 41-44]. For example, Rodriguez and Koper [45] show the facet-specific activity towards oxidation of ethanol and ethylene glycol to be Au(111) > Au(100) > Au(poly oriented) > Au(110). This order of facet-specific activity is attributed to the relative difficulty of gold oxide formation on each facet, with gold oxide formation starting on Au(111) facets at higher potentials. Since the alcohol oxidation occurs only while a partial monolayer of gold oxide is present, and the Au(111) electrode has a higher potential during this time compared to the Au(110); a greater oxidative driving force is applied to any adsorbed alcohol, and thus, more alcohol oxidation occurs on these facets.

1.4.1 Gold versus Platinum

When considering the activity of catalysts towards electrochemical organic oxidation, gold and platinum are considered the foremost metals of choice [46]. With these two metals being neighbouring atoms on the periodic table, their physical properties are very similar (Table 1-1), however, platinum is more active toward organic oxidation in acidic conditions while gold is more active in alkaline conditions [47]. In addition to this, platinum is known to be affected by poisoning of the surface, often by intermediate species, leading to a decrease in activity [46]. Gold does not experience this inhibition effect due to comparatively weak adsorption characteristics. In alkaline solutions, adsorbed hydroxyl ions enhance the dehydrogenation of organic molecules, leading to the improved activity in relative to platinum [46].

Table 1-1. Properties of platinum and gold.

	Platinum	Gold
Element Number	78	79
Electronic Structure	[Xe], $6s^1$, $4f^{14}$, $5d^9$	[Xe], $6s^1$, $4f^{14}$, $5d^{10}$
Crystal Lattice Type	FCC	FCC
Crystal Lattice Constant / nm	0.392	0.408
Metallic Diameter / nm	0.277	0.288
Atomic Mass / $g \cdot mol^{-1}$	195.08	196.97
Molecular Density / $g \cdot cm^{-3}$	21.4	19.3
Melting Temperature / °C	1769	1064
Average Market Price Nov. 2016 / $\$US \cdot kg^{-1}$ [48]	$30,638.95	$39,736.76

1.4.2 Stability

While large gold particles are stable under catalysis conditions, nanoparticles often lose their stabilising ligands and sinter together during the course of the reaction [49, 50]. This leads to a loss of surface area and thus a loss of reactivity. Above a potential of 1.3 V vs. RHE in 0.5 M H_2SO_4, gold oxide will begin to form on a gold electrode. At the same potential, gold will also begin to dissolve off the surface of the electrode, causing changes in the electrode topology [51]. This dissolution process can be used to either roughen or smooth an electrode surface using techniques known as 'electrochemical etching' and 'electrochemical polishing'.

1.4.3 Reactions on Gold

Gold has, until recently, been considered to have "*the reputation of being one of the least catalytically useful*" metals [52]. However recent work showing a particular affinity for CO oxidation [3] has provoked further research into organic catalysis on gold surfaces. Gold is the most electronegative metal and has a very high $Au^+/Au°$ redox potential of +1.691 V. Gold will also form alloys with many metals including copper, aluminium, tin, titanium, platinum, palladium and even mercury. Alongside this, gold is commonly able to exist in a +1 and +3 oxidation state and its high electronegativity provides it with an ability to exist in a -1 oxidation state [52]. This is the major reason why gold is typically unreactive with oxygen and will only dissolve by combining a strong oxidizer with a chloride ion, e.g. aqua regia (conc. HNO_3 + conc. HCl). For these reasons, under appropriate conditions, gold can be a very effective catalyst.

1.4.3.1 Catalysis on Gold Electrodes

In 1987, Haruta et al. [3] published work showing the oxidation of CO on a range of gold-metal oxide alloyed catalysts. They found that Au-α-Fe_2O_3 and Au-Co_3O_4 catalysts with 5 at% gold, and Au-NiO catalysts with 10 at% gold achieved the greatest CO oxidation activity. It was also found that these catalysts could perform complete oxidation of the reaction gas at temperatures as low as -70 °C, much lower than the 300 °C required for bulk gold catalysis of CO. In 2006, Lahr and Ceyer [53] published results showing a Au/Ni(111) alloy achieving CO oxidation at temperatures of -203 °C.

These experiments are beneficial on an industrial scale as the reverse water-gas shift reaction requires the oxidation of CO (Equation 1-3). Using an efficient gold catalyst in a fuel cell whereby the conversion of CO to CO_2 is achieved will lower the activation energy required for the reaction to occur and hence, improve the energy efficiency of the fuel cell. For example, Andreeva et al. [54] reported that Au-α-Fe_2O_3 catalyst alloys with less than 5 at% gold showed finely divided gold particles that were approximately 3.5 nm in size. These catalysts were able to achieve high CO conversion rates compared to pure α-Fe_2O_3 catalysts and industrially available, CuO-ZnO-Al_2O_3 catalysts.

$$CO_2 + H_2 \rightleftharpoons CO + H_2O \qquad 1\text{-}3$$

In addition to CO oxidation in fuel cells, the oxidation of alcohols has also been studied. For example, Kwon et al. [55] found that the oxidation of alcohols, requiring two protons to be removed from the molecule, required an alkaline solution to catalyse the first deprotonation as well as the presence of a metal to catalyse the second deprotonation. It was found that the low amount of poisoning of the gold surface meant it was able to achieve glycerol oxidation activity at "*much higher current densities*" compared to similar platinum catalysts.

Padayachee, Golovko and Marshall [56] performed CV scans on a range of carbon-supported gold nanoparticles between 2.1 nm and 120 nm in a solution of 1.0 M KOH and 0.5 M glycerol. By measuring the maximum current during the glycerol oxidation, it was found that 2.1 nm to 4.7 nm nanoparticles achieved a mass activity of ~26-33 $A \cdot mg_{Au}^{-1}$ while 43 nm to 120 nm nanoparticles achieved a mass activity of ~9-15 $A \cdot mg_{Au}^{-1}$. However, the specific activity of the nanoparticles, normalised on a surface area-basis rather than a mass-basis, it was found that the 120 nm nanoparticles were ~5 times more active than the 2.1 nm – 4.7 nm nanoparticles.

In a similar study by the same group [57], the effect of the loading of gold nanoparticles on the carbon support was investigated. Here it was found that catalytic layers with higher loadings of gold were able to pass more current (on a mass normalized-basis) through the catalyst than the corresponding layers with low loadings of gold. It was suggested that an increase of gold in the layer produced a build-up of glycerol oxidation products, thus inhibiting full gold oxide formation, and therefore enabling further glycerol oxidation. However, the specific activity (on a surface area normalized-basis) showed the highest activity of ~200 $mA \cdot cm^{-2}$ was achieved with a catalyst loading of 5 wt% which decreased to ~100 $mA \cdot cm^{-2}$ with catalyst loadings of 20 wt%.

Other work revolves around the oxidation of other alcohols, a topic for which it has been acknowledged that the accepted platinum and palladium nanoparticles catalysts, while they are effective catalysts, achieve poor selectivity when larger organic molecules are involved. However, Prati and Rossi [58] found that their gold-based catalyst could convert 94% of the ethane-1,2-diol in the reactor with a selectivity of 90%. This was reported to be comparable from the best available, an iridium/carbon catalyst which could achieve 98% conversion but only 87% selectivity. Similarly, Carrettin et al. [59] were able to show that a 1 wt% Au/C catalyst was able to convert 32% of a propan-1,2-diol reactant to its 'monoacid' product with 100% efficiency as long as NaOH was present in the reactor.

While gold has been shown to be inferior to platinum and palladium catalysts for the complete oxidation of unsaturated hydrocarbons, Haruta and Masatake compared the metal-based catalytic oxidation of short-chained saturated carbons, e.g. CH_4 and C_3H_8, shows the gold catalyst to be as active and in some cases more active than other metal counterparts [60]. Comparatively, the partial oxidation of propylene to propenal on a gold

catalyst will increase the propenal yield whereas using a platinum or palladium catalyst will drive the reaction through to the fully oxidised, carbon dioxide product.

1.4.4 Particle Size versus Activity

Experiments investigating the effect of particle size on the activity of CO oxidation show an 'ideal' particle size of 2.5-3.0 nm (Figure 1-3) [37, 61]. The peak activity has been attributed to the CO oxidation mechanism requiring the participation of oxygen species adsorbed at the gold-support interface [62]. Smaller particles have larger interface perimeters; however, they also have a lower ratio of perimeter:surface area, thus reducing the availability of adsorbed CO molecules (on a perimeter length basis). Density functional theory (DFT) studies have also shown that low coordination atoms, i.e. edge atoms, corner atoms or dislocated atoms, are more reactive towards CO oxidation due to the unreactive 'bulk-like' behaviour of facet atoms [62].

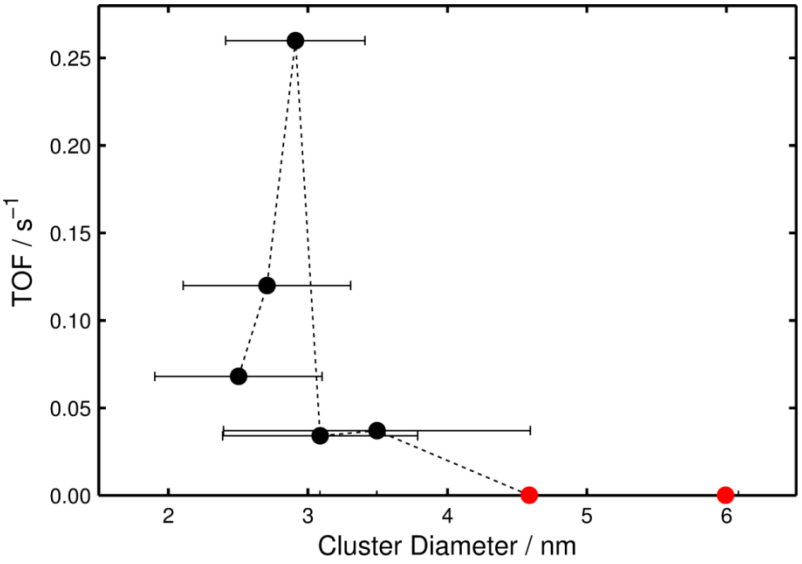

Figure 1-3. CO oxidation TOF at 300 K as a function of nanoparticle size. Samples were prepared by deposition-precipitation (black circles) and photochemical deposition onto TiO_2 (red circles). Figure created from data within Table 1 of ref [61].

1.4.4.1 Oxygen Reduction

Low overpotentials for oxygen reduction are a necessary feature for an efficient fuel cell. While platinum catalysts have been extensively studied as possible cathodes, the relative scarcity of the metal has driven researchers to investigate non-platinum catalysts [63]. The oxygen reduction reaction has been investigated on gold nanocluster of 0.8 nm – 1.7 nm and was found to exhibit a much larger oxygen reduction current density than both bulk gold and single crystal gold surfaces, as well as larger gold nanoparticles. The study also found the performance of the gold nanoclusters to be comparable to commercial platinum catalysts [63].

1.4.4.2 Carbon Monoxide Oxidation

One of the original publications that initiated the current interest in gold catalysis was written by Haruta et al. [3] in which it was shown how 5 nm gold crystals were active for CO oxidation at temperatures below 0 °C. Comparatively, 20 nm gold nanoparticles required a temperature of at least 100 °C before CO oxidation occurred and bulk gold powder catalysts required a minimum temperature of 280 °C. Potential uses of carbon monoxide oxidation include propylene oxidation, nitrous oxide reduction (by carbon monoxide) and the water gas shift reaction [60].

1.4.4.3 Organic Oxidation

Gold is also active for the oxidation of alcohols such as glycerol, a highly functionalized triol that is very promising both as a reactant in fuel cells and as a precursor to many other hydrocarbons (Figure 1-4). Annual glycerol availability as a by-product of biodiesel production is expected to reach over 15 billion litres in 2016 [64] which, with a 99.9% pure, refined glycerol cost of 0.85 USD $\cdot$ L^{-1} [65], makes it a cheap and abundant resource. The size of a gold nanoparticle catalyst can influence the selectivity of glycerol oxidation, for example, a glyceric acid selectivity of 75% was achieved on 3.7 nm gold nanoparticles whereas 2.7 nm gold nanoparticles only achieved 40% glyceric acid yield, yet achieved an increase in glycolic acid selectivity from 15% up to 36% [66].

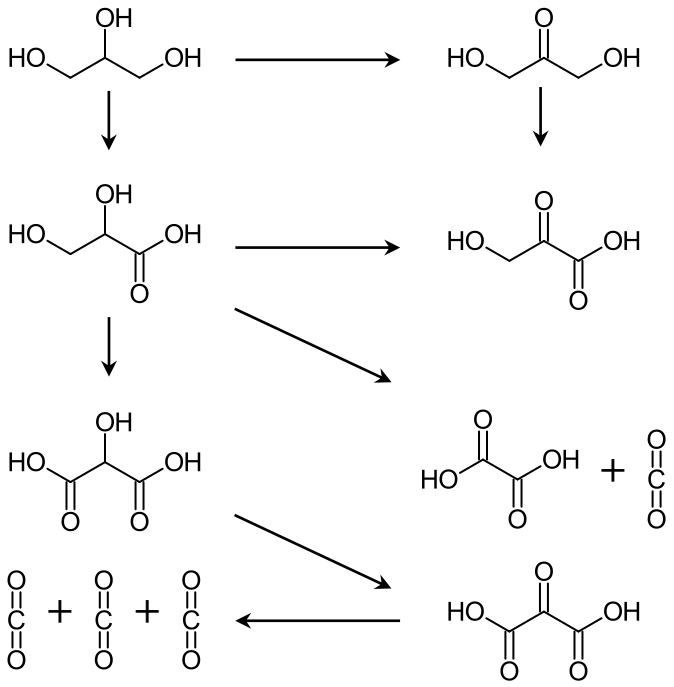

Figure 1-4. A range of the different oxidation products of glycerol.

1.4.4.4 Carbon Dioxide Reduction

In the last 60 years, an increase of approximately 70 ppm carbon dioxide in the Earth's atmosphere has been recorded [67]. This is an increase of almost 22% from the carbon dioxide concentration in the 1950's and is the most recent part of a climb that started in the industrial era. Carbon dioxide has been produced by humans at an ever increasing rate ever since and has had a pronounced effect on local and global climate as well as acidification of seawater. Jones and Schmitz [68] have reviewed 240 independent studies on large scale environment recovery from human impact and calculated that even in the best case scenario, the Earth would take at least 40 years before it could be considered to have 'recovered'.

While oxidising carbon monoxide via a fuel cell arrangement will produce electrical energy, through the input of energy in an electrolysis cell the reverse can occur. This reduction of carbon dioxide is a potentially viable way to reduce the atmospheric carbon dioxide. Currently, the typical overpotential for this conversion is approximately 200 mV, however, Chen et al. [50] have recently reached a lower overpotential of 140 mV. Although this value is a long way from a perfect conversion of energy, by using renewable energy sources that would have otherwise been wasted (e.g. surplus wind energy during a low demand period), the amount of stored energy will still have increased.

The products from the electrochemical reduction of carbon dioxide vary from carbon monoxide to simple carbohydrates like formaldehyde to longer chained molecules like hexane [69, 70]. These larger products are viable fuels – they can be gases or liquids and are able to be burned in engines or industrial furnaces. The exact product distribution is a topic of ongoing research and is dependent on a large variety of factors including catalyst particle size, exposed catalyst facets, reaction time, reaction potential, carbon dioxide concentration, solution pH, exposed surface area, reaction temperature, etc. [23].

1.5 Particle Characterisation

1.5.1 Theoretical Modelling

Many people have looked at the theoretical behaviour of both gold particles and CO_2 adsorption using DFT [62, 70-77]. This method of modelling was first published in 1964 by Hohenberg and Kohn [78] and has since been used extensively in the theoretical particle modelling world. It correlates quantum mechanical atomic values such as bond energy, electron affinity, lattice structures, and electronic structure to produce probability functions of particle shape and behaviour. For example, Burgess and Keast [79] used DFT to calculate the optical absorption spectra of gold clusters with up to 171 atoms, confirming absorption features of clusters that had been predicted by the Mie theory and observing a transition from molecule-like clusters to spherical or rod-like particles.

1.5.2 Physical Modelling

Physical particle modelling can come from direct observation of the particles using a scanning electron microscope (SEM) or a transmission electron microscope (TEM), or from indirect measurements such as X-ray diffraction (XRD) or extended X-ray absorption fine structure spectroscopy (EXAFS). Nanoparticles will typically be imaged via SEM or TEM to analyse the size distribution and as such, these images can be used to find the specific surface area of the nanoparticle sample.

In conjunction with a direct image, the physical aspects of particles can be measured using XAS/EXAFS via algorithms in an IFEFFIT programme [80, 81]. Using this technique, features such as the interatomic bond distances, average coordination number and particle size can be extracted. In a similar fashion, using XRD can provide information on the size and crystal structure of the particles.

1.5.3 Electrochemical Characterisation

Many features of electrochemical measurements can be used to identify characteristics of a surface. For example, the hydrogen adsorption peaks on platinum surfaces are often used as a quick and easy way to measure the number of surface atoms in the sample. In a similar way, copper UPD is used to measure the electrochemically active number of surface atoms in a gold electrode. Plowman & Compton [82] measured the potential of both the underpotential deposition of copper and the bulk deposition region of copper on a gold electrode. The measured potential difference between the two regions was sufficient to allow them to isolate the UPD region, and thus, allowed them to measure the surface area of the gold disc. They also made measurements on citrate-capped 123 nm, 60 nm, 12 nm and 1.8 nm gold nanoparticles and found a decreasing amount of copper was adsorbed to the gold surface as the nanoparticle diameter decreased (Figure 1-5). The reduction of 95.8% monolayer coverage of copper on the bulk gold disc to 62.4% coverage on the largest nanoparticle down to less than 5% copper coverage on the smallest nanoparticle clearly shows that capping effects of the citrate on the nanoparticles causes sufficient discrepancy to render this method impractical for surface analysis of capped gold nanoparticles.

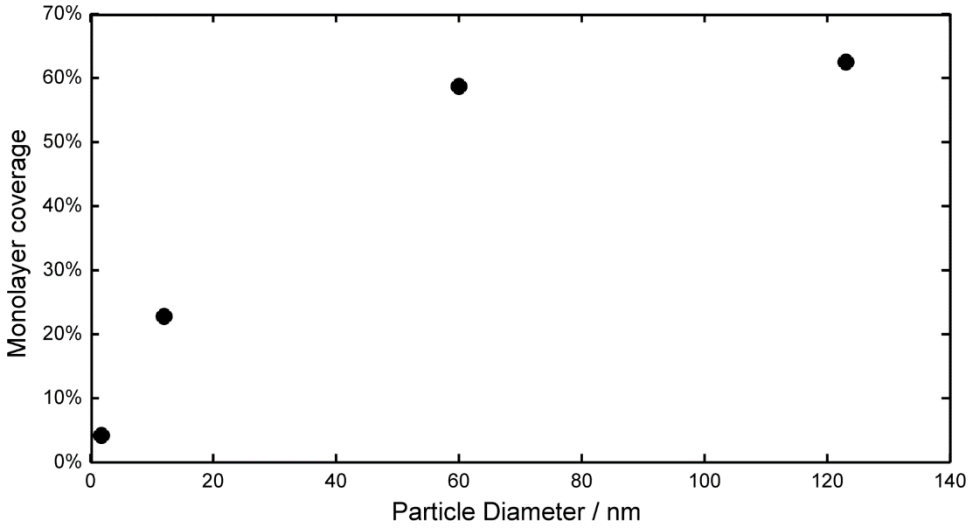

Figure 1-5. Fractional monolayer coverage of copper UPD as a function of particle diameter for a range of citrate-capped gold nanoparticles. Figure recreated from data within Figure 3 of ref [82].

Another way to measure the electrochemical surface area of gold nanoparticles is to measure the charge associated with gold oxide reduction. One of the most frequently used electrochemical surface area measurements for gold is to perform gold oxidation then reduction, typically via cyclic voltammetry. By measuring the area of the gold oxide reduction peak and, taking into account the scan rate, the charge – and hence, the number of electrons – can be measured. This method has its own difficulties such as;

- There are two forms of gold oxide. The first is $Au(OH)_x$, a compact layer that is only 2-3 monolayers thick. The second is a hydrated form of $Au_2O_3.xH_2O$, which can form many layers, however, formation begins at higher potentials than the first, compact layer.
- The potential at which a single monolayer is formed has been described as *"the minimum directly following the first oxidation peak"* [83]. Despite this, many different upper potential limits are chosen, or roughness factors applied, and single monolayer formation is implicitly or explicitly assumed.
- The longer the electrode is above the gold oxide formation potential, the more gold oxide is formed. This implies that the sweep rate can be just as influential on the gold oxide reduction charge as the upper potential of the CV scan.
- The gold electrode may not have been fully reduced prior to oxidation. This can arise if the electrode has not been scanned to a sufficiently low potential to fully reduce both the hydrous and anhydrous forms of gold oxide and thus, will lead to an artificially high measured surface area.

These difficulties are discussed further in Chapter 3. It is important to note that while the specific surface area of a nanoparticle can be known at a certain time, by performing reactions on the nanoparticle sample– whether they are oxide formation/reduction or a catalytic reaction – the nanoparticle can degrade. The mechanism of this degradation can be due to gold dissolution/redepositing, surface rearrangement, particle sintering, or even particle loss from the surface of the support [1, 84]. As such, the electrochemically active surface area of nanoparticles often changes during use and this instability should be considered when reporting results.

1.5.4 Surface Plasmon Resonance

Surface plasmon resonance (SPR) is a phenomenon where the free electrons of a metal will, depending on the metal properties, absorb distinct wavelengths of incident light [85]. SPR requires coherent oscillations of the electrons on the gold surface and is not visible for macro-sized gold metal due to the underlying bulk electronic stability, nor is it visible on very small nanoparticles due to the inability of the electrons to achieve a coherent resonance. This feature gives rise to the characteristic ruby red colour often attributed to gold nanoparticles, and why nanoparticles were often used in ornamental vases and stained glass many centuries ago. The Lycergus cup (Figure 1-6) has been found to have incorporated nanoparticles with its glass structure with an amalgam ratio of 3:7 (Au:Ag). It has been suggested that the gold component of these nanoparticles give rise to the red, transmitted colouring while the silver component are responsible for the green, reflected colouring [86].

Figure 1-6. Images of the Lycurgus Cup showing the reflected light (left) and transmitted light (right) [87].

The SPR feature of gold is very adaptable and can be used for the sensing of metal ions, small organic compounds, heavy metals, as well as a multitude of biological compounds including cancer biomarkers [88]. This flexibility is available by attaching a wide range of receptors to the gold nanoparticle/thin sheet, and these receptors, when bound to their target molecule, will alter the SPR wavelength position or the SPR absorbance intensity.

1.6 Particle Synthesis and Electrochemistry

1.6.1 Particle Synthesis

Gold nanoparticles have been used for many hundreds of years to colour glass with one of the most famous examples being the Lycurgus Cup (Figure 1-6). Despite this, it was not until 1857 when Faraday [89] produced gold nanoparticles by reducing a gold chloride solution with phosphorus in ether and forming a ruby coloured colloid. These experiments formed the foundation of the modern era of gold nanoparticles.

Table 1-2. A small selection of methods to produce gold nanoparticles via chemical reduction of a gold solution.

Particle size / nm	Reducing Agent	Stabilising Ligand (solute)	Year of publication	Reference	
0.8	$NaBH_4$	Phosphine	1972	Cariati et al.	[90]
1.4	TOAB	Phosphine	2000	Weare et al.	[91]
1.5	THPC	THPC	1993	Duff et al.	[49]
1.9 – 7.0[1]	Phosphorus	Phosphorus (diethyl ether)	1857	Faraday	[89]
1 – 3	$NaBH_4$	BH_4^- (aq), DDT (toluene)	1994	Brust et al.	[92]
1 – 4	$NaBH_4$	BH_4^- (aq), DDT (n-hexane)	2005	Hussain et al.	[93]
3.2 – 5.2	$NaBH_4$	BH_4^- (aq), DDT (hexane)	2010	Martin et al.	[94]
10 – 50	Citric acid		1951	Turkevich	[95]
20	Sodium citrate	Sodium citrate (aq)	1951	Turkevich	[95]
20	Acetone		1929	Davies	[96]
20 – 40	Formaldehyde		1976	Granqvist et al.[2]	[97]

Nanoparticles may be produced through an electrochemical breakdown of a gold wire as described by Bredig & Haber [98], however, this method produces nanoparticle with a wide particle size distribution. Alternatively, they are able to be chemically produced by the reaction of a thin gold film laid on a solution of chlorine [89], with the solution turning the characteristic dark red colour. Despite these methods, gold nanoparticles are generally

[1] Faraday solutions were prepared by Turkevich et al. [95] in an attempt to ascertain the approximate size distribution that was originally attained.

[2] Method originally publishing by R. Zsigmondy, Physikalische Zeitschrift 56, p.65 (1906); 56, 77 (1906).

produced via reduction of a gold chloride solution (Table 1-2). Stabilising ligands, or capping agents, are added during the synthesis to provide stability of the nanoparticles, preventing further growth or coagulation. Many different methods are available to produce nanoparticles, with some being able to be produced in a matter of minutes [94] while other take several days to complete all purifications or crystallisations [91].

1.6.2 The Support

Inert materials such as carbon, titania or silica are used to enhance the functionality of nanoparticles. Powdered supports are useful due to their high surface area, for example, carbon black has a surface area of 50 $m^2 \cdot g^{-1}$, activated carbon has a surface area of at least 1100 $m^2 \cdot g^{-1}$ while titania typically has a surface area of 50 – 100 $m^2 \cdot g^{-1}$. Nanoparticles are deposited to these powders either by direct addition of the powder to a colloidal solution, or the addition of the powder along with an additional chemical to initiate adsorption. By using these powders, the gold particles, which may be inherently unstable, will be physically separated by the support. This makes any sintering or aggregation of the particles less likely to occur. Additional benefits include an increase in catalyst volume for ease of handling and a decrease in gold density of the catalyst, which may improve mass transfer limitations of any reactions.

In contrast, flat supports like silica, fluorine-doped tin oxide (FTO), and glassy carbon are used when only a thin layer of the catalyst is required. This could be several monolayers of a powder-supported catalyst, or simply a partial monolayer of 'naked' gold nanoparticles. Flat supports are helpful when a powdered support adds a high amount of additional data, such as capacitance current, to a data set and thus, overwhelming useful information. Optically transparent supports like an FTO-coated glass slide are useful for performing a light-based experiment where a black, carbon support would absorb all incident light.

1.6.3 Catalytic Layers

The basic requirement for a catalytic layer is that the catalyst itself must be available for the reactants. That is, the layer must prevent or minimise mass transfer limitations. As has already been stated, powdered supports provide separation of the nanoparticles which can provide channels for electrolyte penetration (Figure 1-7). This porosity can have a detrimental effect on the mechanical structure of the electrode so a third chemical, e.g. Nafion, is often introduced during the electrode production. This Nafion provides a cohesion effect as well as improved ionic conductivity through the layer.

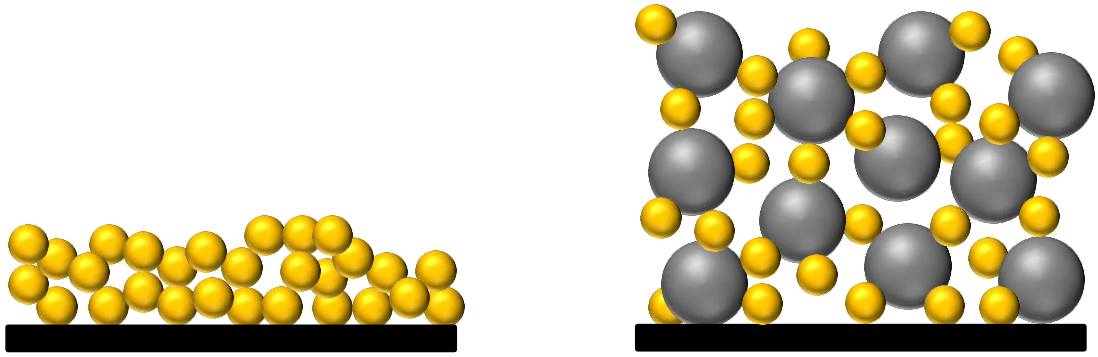

Figure 1-7. The difference of a catalytic layer without a powder support (left) and with a powdered support (right). As the porosity of the layer increases, the availability of the catalyst deeper within the layer increases.

Complete or partial monolayers of naked gold atoms can be produced by adsorption to a glass, an FTO-coated or an ITO-coated glass slide. This is achieved by attaching an amino-silane to the slide then exposing the slide to a colloidal solution of gold nanoparticles [99]. The adsorption of the nanoparticles to the slide may take several hours and a colloid-slide contact time of 24 hours is not uncommon [100]. Due to their conductive nature, FTO and ITO are used if electrochemical processing is to occur to the nanoparticles after adsorption. Coating a slide in this fashion produces a partial monolayer of 20% to 30% for short silanization times, or complete monolayers for longer silanization times [99].

1.6.4 The Cyclic Voltammogram

Cyclic voltammetry (CV) is a technique widely used throughout the electrochemical discipline [101]. Its uses vary from cleaning electrode surfaces [102], to measuring surface area [103], to molecule-surface adsorption properties [104], to electrode catalytic promotion and inhibition properties [105]. Like a lot of electrochemical methods, a CV scan is carried out in a 3-electrode cell (Figure 1-8) made up of a working electrode, where the catalyst/reaction of interest is located, a counter electrode to complete the electrical circuit, and a reference electrode to provide a reference potential. To run a CV scan, the three electrodes are placed into an electrolyte solution (H_2SO_4, $HClO_4$, KOH, NaOH etc.) and the potential of the working electrode is scanned between two defined potentials. This process is very useful in that it allows for ions to be adsorbed/desorbed, oxides to be formed/reduced and reactions to take place.

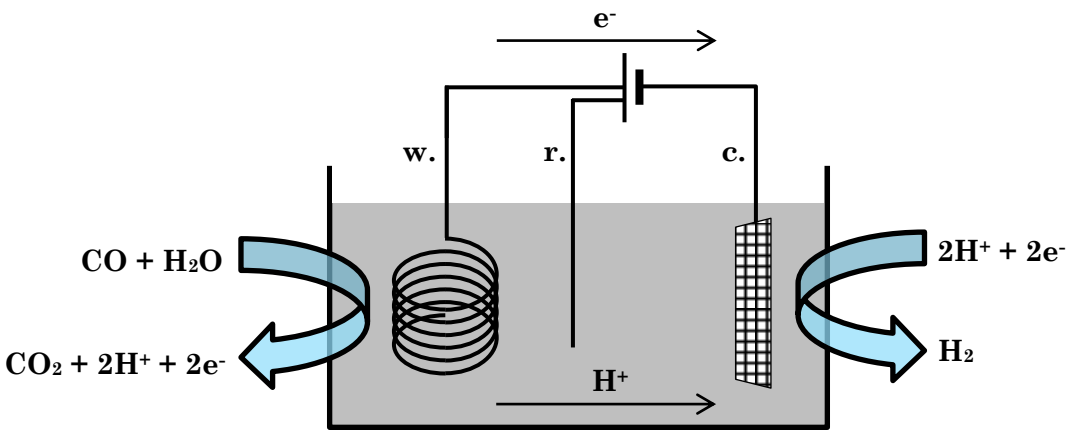

Figure 1-8. An example of a three-electrode cell performing CO oxidation. Electrodes are denoted as working (w.), reference (r.) and counter (c.)

Gold cyclic voltammetry has several, well-defined regions. While I will briefly outline the regions of most significance to this these, Hamelin [106] details the gold CV in both H_2SO_4 and $HClO_4$ in much greater depth. Starting from the most cathodic potential, a region of hydrogen evolution is seen as water electrolysis occurs on the electrode surface. The main reason a CV will be scanned to large cathodic potentials is to clean the gold surface and to remove or reduce contaminants that may interfere with additional experiments. Between the hydrogen evolution region and the gold oxide formation region is a period of capacitance charging. This region has few features; although adsorption of ions can sometimes be seen e.g. sulfate adsorption is sometimes visible when CV scans are produced in sulfuric acid.

As the CV is scanned into the anodic region, gold oxide begins to form (just below 1.4 V vs. RHE in Figure 1-9). The exact nature of this oxide varies as the CV is scanned to higher potentials, with a single monolayer of gold oxide typically assumed to have occurred at the minima immediately after the first oxide formation peak [83]. As the CV is scanned further into the anodic region, a hydrated gold oxide continues to form, while oxygen evolution begins to occur. As with the hydrogen evolution, additional scanning is used as a tool to aid any electrode surface cleaning.

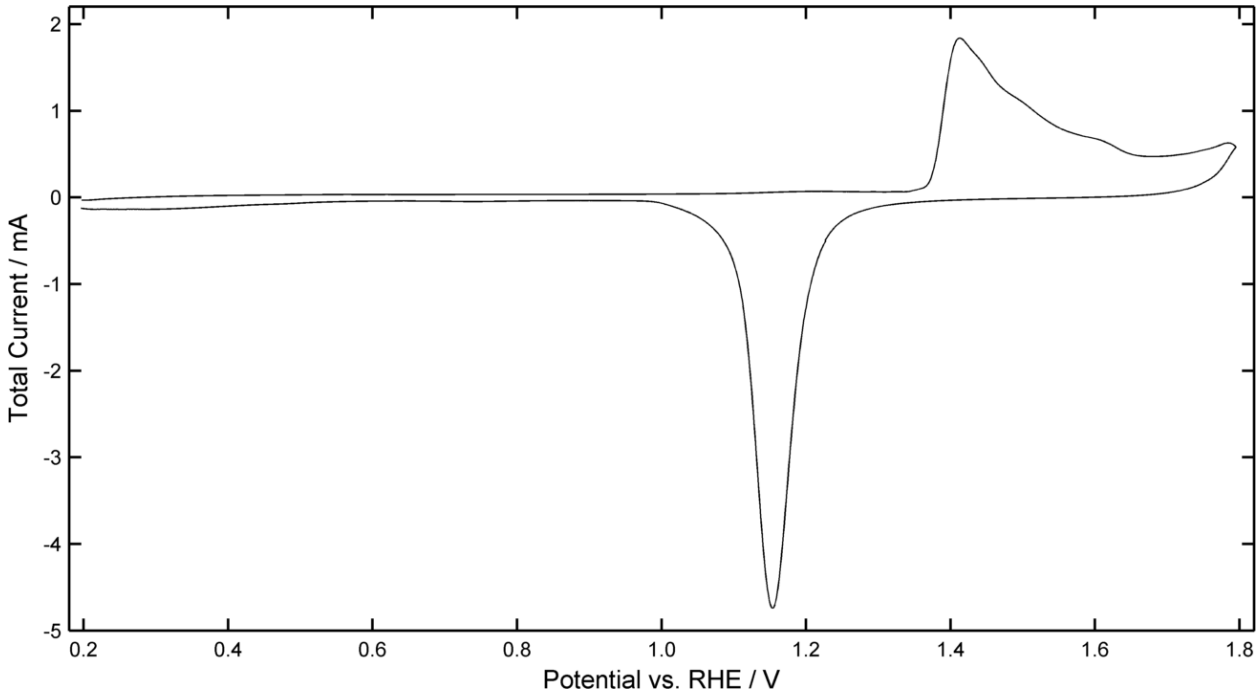

Figure 1-9. CV scan of a gold wire in 0.5 M H_2SO_4 with a sweep rate of 50 mV· s^{-1}.

The gold oxide is reduced to metallic gold during the cathodic sweep, as evidenced by a large cathodic peak starting below the oxide formation potential, around 1.3 V vs. RHE (Figure 1-9). The anodic limit, as well as the duration of time in the oxide region, will alter the magnitude of the oxide reduction peak, however, the area of the peak may be measured and, if the type of gold oxide is known (e.g. Au(OH) vs. Au_2O_3), the quantity of gold atoms reduced is able to be calculated. Finally, as further cathodic scanning occurs, any ion adsorption peaks will have a matching desorption peak until the onset of hydrogen evolution.

1.7 Carbon Dioxide Reduction on Metal Catalysts

With the current situation of increasing CO_2 concentration in the Earth's atmosphere (discussed further in Chapter 5), using a metal-based electrode as an electrocatalyst to convert waste CO_2 into a useable product is the focus of many research efforts [50, 69, 107-110]. When considering which metal catalyst to use for CO_2 reduction, the desired product is the most important consideration as different metals will produce different reactions products.

For example, Kuhl et al. [74] performed CO_2 reduction on copper electrodes in 0.1 M $KHCO_3$ at electrode potentials of -1.18 V vs. RHE to -0.67 V vs. RHE for one hour. These potentials produced current densities between -20 mA· cm^{-2} and -0.4 mA· cm^{-2}. Sixteen different reduction products were identified over the 10 experiments and it was found that an electrode potential of -1.08 V vs. RHE resulted in the least amount of H_2 production while an electrode potential of -1.18 V vs. RHE resulted in the greatest amount

of methane production. These potentials corresponded to current densities of approximately -10 $mA \cdot cm^{-2}$ and -18 $mA \cdot cm^{-2}$. At higher electrode potentials, methane production ceased while CO and formate production increased.

Hori et al. [111] perfomed CO_2 reduction on 16 different transition metals and found gold, silver and zinc out-performed the other 13 catalysts by over 50% faradaic efficiency for CO production. That is, the measured faradaic efficiency for CO production on the gold catalyst was 87.1 %, the silver catalyst was 81.5 %, the zinc catalyst was 79.4 % while the next best catalyst, palladium, had a faradaic efficiency for CO production of 28.3 %. These catalysts were then modified via an adatom of one of five different metals to produce a shift in the product distribution of the electrocatalyst towards formate production (Table 1-3).

Table 1-3. Variations in the CO selectivity (r) of three electrocatalysts modified with adatoms*. Table created from data within Table 2 of ref [111].

	CO Selectivity with Specific Adatom					
Electrocatalyst	None	Cadmium	Tin	Indium	Lead	Thallium
Gold	0.99	0.82	0.54	0.60	0.53	0.95
Silver	0.99	0.92	0.59	0.40	0.39	0.05
Zinc	0.93	0.19	0.08	0.03	0.01	0.01

*CO selectivity defined by $r = \frac{CO}{CO+HCOO^-}$

In systems where the major products are CO and H_2, the system is effectively performing the reverse of the water-gas shift reaction (Equation 1-3). Stone and Waller [112] compared the effectiveness of copper, copper-zinc oxide alloy, and zinc electrodes on the reverse water-gas shift reaction and found that catalysts with a copper:zinc ratio of approximately 3:1 produced the greatest CO_2 conversion rate. The role of the zinc oxide in these experiments is thought to be as a separating agent, preventing the copper in the electrode surface from becoming a homogenized, bulk copper catalyst and possibly preventing the nano-sized copper crystals from sintering due to the increased temperature as a result of the exothermic nature of the reaction.

Hansen et al. [113] used DFT to probe the metal catalyst surface-CO_2 reduction product adsorption energies. In particular, they produced a 'kinetic volcano' plot comparing the optimum metals for CO and COOH evolution. It was found that of the noble metals that were studied, gold is the most active, followed by silver and copper. Palladium, nickel, rhodium and platinum were all substantially rate limited as a result of strong CO binding.

1.8 Carbon Dioxide Reduction on Gold

With the apparent superiority of gold towards the reduction of CO_2 (Section 1.7), and the efficiency of nano-sized catalysts (Section 1.4.4) compared to their corresponding bulk-metal catalysts, the natural progression is to investigate the reduction of CO_2 on gold nanoparticles. Chen, Li and Kanan [50] performed CO_2 reduction on 23 nm oxide-derived

gold nanoparticles in 0.5 M $NaHCO_3$ by applying a constant potential and measuring the corresponding current. It was found that the oxide-derived nanoparticle catalysts required an overpotential that was up to 60 mV lower than similarly tested polycrystalline catalysts. They suggest that this is due to a different reaction mechanism occurring on the nanoparticle surface (Figure 1-10). The reason for the different mechanism is due to the poor stabilization of the CO_2^- radical on polycrystalline gold whereas their kinetic data indicates that HCO_3^- present in the solution will react with this radical when it is bound to the oxide-derived nanoparticle.

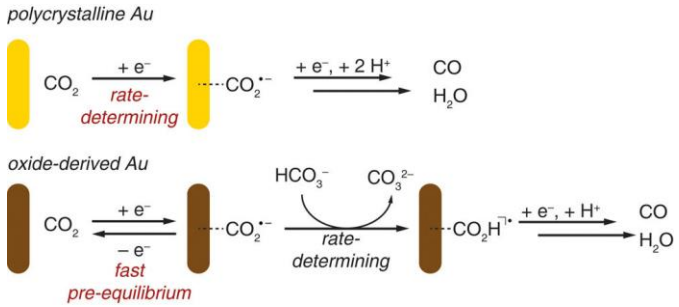

Figure 1-10. Proposed mechanism for CO_2 reduction on polycrystalline and oxide-derived gold catalysts. Figure reprinted with permission from [50].

Zhu et al. [114] similarly discuss the reduction of CO_2 on gold nanowires via an COOH intermediate. The nanowires had a cross-sectional diameter of 2 nm and lengths of 15 – 500 nm, and were deposited on a Ketjen carbon support before being pasted to carbon paper via a PVDF-based ink. When reducing CO_2 in 0.5 M $KHCO_3$ at -0.35 V vs. RHE, only H_2 and CO were produced, with a maximum faradaic efficiency towards CO production of 94%. Long-term measurements showed the stable reduction of CO_2 for 6 hours followed by a slight reduction in the faradaic efficiency to approximately 85% after 12 hours. This reduction was due to the nanowires degrading into nanoparticles.

Kauffman et al. [72] performed CO_2 reduction on Au_{25} gold clusters and found that, at the potential of their highest CO production rate, they out-performed 5 nm gold catalysts and bulk gold catalysts by a factor of up to 700 and 2 nm gold catalysts by a factor of 10-100. These clusters produced CO with a faradaic efficiency of ~7% at -0.193 V vs. RHE up to ~100% at -0.973 V vs. RHE. Mistry et al. [115] investigated the effect of nanoparticle size on the reduction of CO_2 by producing nine different nanoparticle catalysts between 1.1 nm and 7,7 nm in diameter. In this study, it was found that the smallest nanoparticles were over 100 times more active towards CO production; however the faradaic efficiency was typically around 20% for all nanoparticles below 5 nm, except for the smallest, which had a faradaic efficiency of only 10%. These tests were performed at lower potentials of -1.2 V vs. RHE compared to a potential of -0.973 V vs. RHE as performed by Kauffman et al. [72]. However, the CO production rate for the comparably sized particles were 3.6 $mmol \cdot hr^{-1} \cdot cm^{-2}_{Au}$ compared to 1.26 $mmol \cdot hr^{-1} \cdot cm^{-2}_{Au}$ in the Mistry and Kauffman studies, respectively.

The nature of the catalytic layer can also have an effect on the reduction of CO_2. For example, Andrews, Flake and Fang [107] performed CO_2 reduction in a 0.1 M $KHCO_3$ electrolyte on Au_{25} clusters and found that using a Nafion-based ink in their catalytic layer resulting in >90% faradaic efficiency towards CO production while an otherwise identical catalytic layer with a PVDF-based ink resulted in ~55% faradaic efficiency towards CO production. In another paper by Kauffman's group [116], it was shown that 1.0 nm, Au_{25} clusters grew to 1.4 nm upon deposition to a carbon black support and that the CO formation rate is highly dependent on the catalyst loading. For example, at a gold loading of ~8 $\mu g \cdot cm^{-2}_{geo}$ catalyst, the CO formation rate was 0.0030 $mmol \cdot hr^{-1} \cdot cm^{-2}_{Au}$, whereas at low gold loadings of 0.96 $\mu g \cdot cm^{-2}_{geo}$, the CO formation rate was 0.0145 $mmol \cdot hr^{-1} \cdot cm^{-2}_{Au}$.

Table 1-4. CO production rate and faradaic efficiencies of gold nanoparticle catalysts.

Nanoparticle Size / nm	Electrolyte	Electrode Potential / V vs. RHE	CO Production Rate / $mmol \cdot hr^{-1} \cdot cm^{-2}_{Au}$	CO Faradaic Efficiency	Ref.
Au film (500 nm)	0.5 M $KHCO_3$	-0.30	$9.3x10^{-5}$	28%	[117]
Au film (500 nm)	0.5 M $KHCO_3$	-0.50	0.0056	70%	[117]
Au film (500 nm)	0.5 M $KHCO_3$	-0.65	0.0112	62%	[117]
23	0.5 M $NaHCO_3$	-0.25	0.007	65%	[50]
10	0.5 M $NaHCO_3$	-0.65	0.00010	59%	[118]
8	0.5 M $NaHCO_3$	-0.65	0.00014	71%	[118]
6	0.5 M $NaHCO_3$	-0.65	0.00027	90%	[118]
4	0.5 M $NaHCO_3$	-0.65	0.00021	77%	[118]
2x500	0.5 M $KHCO_3$	-0.35	0.15	94%	[114]
2x100	0.5 M $KHCO_3$	-0.35	0.06	45%	[114]
Bulk	0.2 M $KHCO_3$	-1.42	0.0187	23.6%	†
3.2	0.2 M $KHCO_3$	-1.45	0.0573	21.3%	†
Bulk	0.1 M $KHCO_3$	-0.973	0.0018	1.3%	[72]
5	0.1 M $KHCO_3$	-0.973	0.0058	10.6%	[72]
2	0.1 M $KHCO_3$	-0.973	0.19	88.8%	[72]
1.0	0.1 M $KHCO_3$	-0.973	1.26	105%	[72]
1.0	0.1 M $KHCO_3$	-0.193	0.0024	7%	[72]
1.4	0.1 M $KHCO_3$	-0.8	0.0052	*	[116]
1.4	0.1 M $KHCO_3$	-1.2	0.0145	*	[116]
1.4	0.1 M $KHCO_3$	-1.6	0.0109	*	[116]
1.1	0.1 M $KHCO_3$	-1.2	3.6	20%	[115]
1.0	0.1 M $KHCO_3$	-0.79	*	90%	[107]

*not reported †this work

Chapter 2 DETERMINING THE SURFACE AREA OF GOLD NANOPARTICLES

2.1 Introduction

Determining the surface area of gold nanoparticle electrodes is complex. While the calculation of available gold sites is trivial for a known particle shape and size distribution, using the traditional electrochemical approach (often used for bulk gold electrodes) is more difficult. This is because the true nature of the gold oxide layer is not inconsequential even on bulk gold electrodes [83, 119-123], and, in the case of gold nanoparticles, the atomic packing and effects of edge and corner atoms may also be significant. This chapter will review such literature and compare experimental results in order to explain and demonstrate the complexities of how to calculate gold nanoparticle surface area.

2.2 Electrochemically Determined Surface Area

2.2.1 Electrochemical Processes to Determine Surface Area

The electrochemically active surface area (EASA) of electrodes is often measured by calculating the charge required for a known surface reaction, e.g. hydrogen adsorption or oxide reduction. With the comparable CO affinity between gold and platinum, and their proximity on the periodic table, it is natural to assume that the same EASA measurements could be used for both metals. The most widely used method of EASA calculation is used for platinum electrodes, where the surface area is measured via the charge associated with hydrogen adsorption peaks (Equation 2-1 and shaded area, Figure 2-1).

$$Pt + H^+ + e^- = Pt\text{-}H_{ads} \qquad 2\text{-}1$$

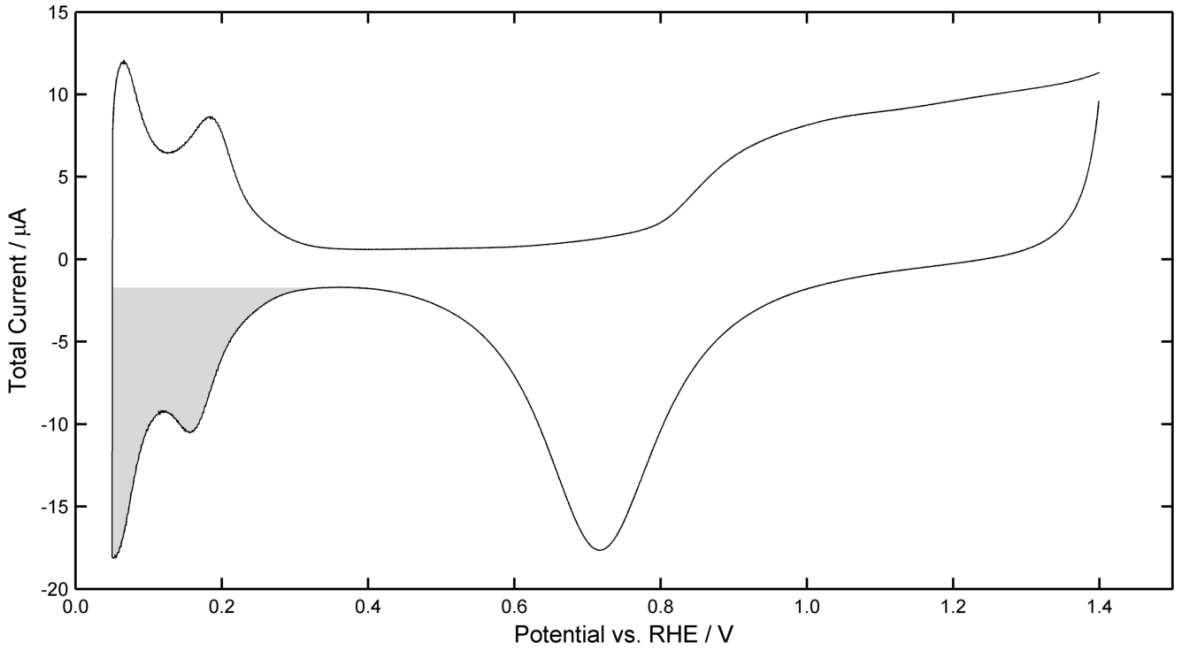

Figure 2-1. Platinum wire CV scan recorded in 0.5 M H_2SO_4 with a sweep rate of 50 mV·s^{-1}. The shaded area represents the charge corresponding to H_2 adsorption on the platinum surface.

For example, peaks seen in a CV scan on a platinum wire in 0.5 M H_2SO_4 at a sweep rate of 50 mV· s^{-1} (Figure 2-1) show the hydrogen adsorption feature corresponding to hydrogen adsorption on specific faces of the platinum surface where the Pt(110) face will bind hydrogen at lower potentials than the Pt(100) face which will bind hydrogen more strongly, at higher potentials [124]. Unfortunately, this form of underpotential deposition (UPD) does not translate to gold electrodes, whose hydrogen affinity is so weak that hydrogen adsorption prior to bulk hydrogen reduction is essentially not observable in a typical CV scan [125].

Another technique for determining the EASA of gold is that of a metal-based UPD. This is achieved in much the same way as hydrogen adsorption by measuring the charge associated with adsorption of an ion such as lead or copper; however the potential is kept above (i.e. more positive than) the equilibrium potential for the bulk reduction of the ion and hence, surface adsorption *and* desorption can be measured without significant changes to the solution or electrode [126, 127]. Plowman & Compton [82] found that copper UPD surface coverage dropped from 95% coverage for a bulk gold electrode to 23% coverage on 12 nm gold particles. Copper UPD on 1.8 nm gold nanoparticles resulted barely observable UPD (Table 2-1).

Table 2-1. Copper UPD coverage recorded by Plowman & Compton [82].

Nanoparticle Size	% Monolayer Coverage
Bulk Gold	95%
123 nm	62%
60 nm	58%
12 nm	23%
1.8 nm	4.2%

2.3 Gold Oxide Reduction Peak

The gold CV scan is often characterised by the gold oxide reduction peak. A CV scan performed on a gold plate in 0.5 M H_2SO_4 at a sweep rate of 50 $mV \cdot s^{-1}$ (Figure 2-2) shows the peak corresponding to the number of electrons required to fully reduce the gold oxide surface to a metallic gold surface (a full description of the required calculations is provided in Section A1.4.2.1). A charge density (e.g. 400 $\mu C \cdot cm^{-2}$) can then be applied to produce an EASA for the electrode. Literature values of the charge density of gold varies greatly with early papers calculating 192 $\mu C \cdot cm^{-2}$ [128] while others use values such as; 386 $\mu C \cdot cm^{-2}$ [56, 129-133], 390 $\mu C \cdot cm^{-2}$ [40, 134-137], 482 $\mu C \cdot cm^{-2}$ [119, 138, 139], and 723 $\mu C \cdot cm^{-2}$ [140-143]. Often, the charge density is quoted with unwavering conviction, despite the apparent variations.

As an example, Yancey et al. [134] mention in their text *"The oxide reduction peak was integrated and converted to a total Au surface area using the* ***widely accepted*** *[emphasis added] conversion factor of 390 μC/cm²"* while Carvalhal et al. [137] state *"…the value of 390 ± 10 μC cm⁻² was* ***a proper measure*** *[emphasis added] of the standard reference charge…"* whereas the text from their cited literature states *"A value of 390±10 μC cm⁻² has* ***been suggested*** *[emphasis added] for polycrystalline Au"* [135]. These types of unequivocal statements, taken from a source that is being deliberately reserved, are dangerous to the researcher as they often have no background or caveat included in the text and as such can be mistaken as an established fact. Reasons for the variations in charge densities are discussed in Section 2.2.1 and Section 2.3.1.

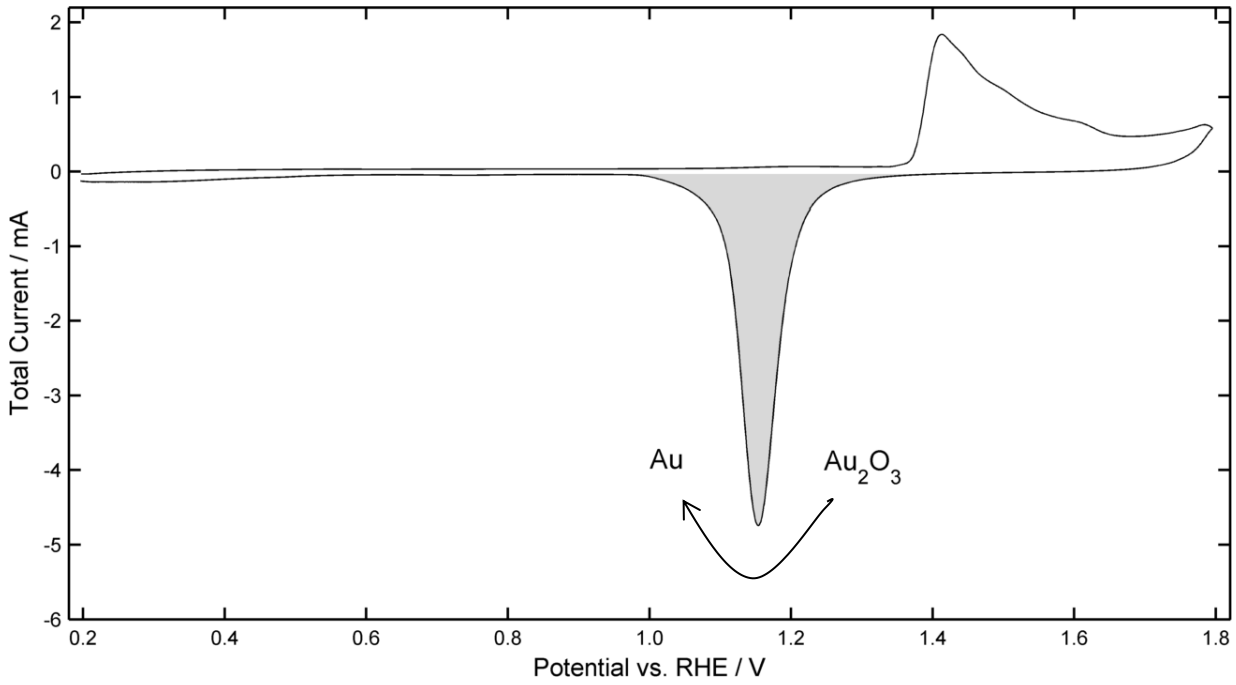

Figure 2-2. Gold plate CV scan recorded in 0.5 M H_2SO_4 with a sweep rate of 100 mV· s^{-1}. The shaded area represents the charge corresponding to gold oxide reduction.

2.3.1 Forms of Gold Oxide

A significant complication researchers find when performing gold oxide reduction/EASA calculations is: at what point during the CV should the experimenter assume that a monolayer of gold oxide has been formed? Then, they must ask what form of gold oxide has been produced? While it is accepted that there are multiple forms of gold oxide (Table 2-2 and Table 2-3), neither the definition of when a single monolayer of oxidised gold has occurred, nor the magnitude of the charge density are agreed upon. For example, Oesch and Janata [119] discuss how a single monolayer of divalent (Au:O ratio = 1) gold oxide has a specific charge density of 482 $\mu C \cdot cm^{-2}$ yet in the next sentence they state that '*complete oxidation of the top layer*' requires bulk Au_2O_3 formation with a specific charge density of 723 $\mu C \cdot cm^{-2}$. Tremiliosi-Filho et al. [144] state the anhydrous gold oxide form consists of AuO or $Au(OH)_2$ and has a specific charge density of 390 $\mu C \cdot cm^{-2}$, however, this value is a theoretical value as the minimum experimental charge density they were able to measure was 600 $\mu C \cdot cm^{-2}$.

Table 2-2. Properties of the anhydrous and hydrous gold oxide layers as extracted from Oesch and Janata [119].

	Anhydrous Gold Oxide	Hydrous Gold Oxide
Chemical formula	Au_2O_3	$Au(OH)_3$
Oxidation onset potential / V vs. RHE	1.55 V	>2.55 V
Reduction onset potential / V vs. RHE	~1.45 V	~1.15 V
Maximum number of monolayers	2-3	100+
Layer Packing	Dense, non-porous	Porous

Table 2-3. Properties of the four states of gold oxide as extracted from Tremiliosi-Filho, Dall'Antonia and Jerkiewicz [144].

	Anhydrous Gold Oxide	Hydrous Gold Oxide
Chemical formula	AuO or $Au(OH)_2$	Au_2O_3 or $Au(OH)_3$
Maximum number of monolayers	3 (acid), 1 (base)	No limit
Specific charge density / $\mu C \cdot cm^{-2}$	1150 (acid), 390 (base)	-

2.3.2 Theoretical Gold Oxide

While the true nature of the hydrous/anhydrous gold oxide layers varies between literature sources, the theoretical specific charge density of crystal planes can be calculated. First, the theoretical gold atomic packing density (PD) of the three low index gold crystal planes, namely, (100), (110), and (111), can be calculated using the following assumptions and Equations 2-2 to 2-5.

1. Each face exhibits perfect FCC crystal structure with two gold atoms per unit cell face.
2. Each gold site is in a Au^+ oxidation state, i.e. one electron is transferred during the oxidation of each surface gold atom.
3. The gold metallic bond diameter (D) is 2.887 Å [128].
4. A complete, monolayer coverage of gold oxide is formed.

$$PD(xyz) = \frac{\#atoms}{Area_{xyx}} \qquad 2\text{-}2$$

$$PD_{(100)} = \frac{2}{2D^2} = 0.1200\ atoms \cdot Å^{-2} \qquad 2\text{-}3$$

$$PD_{(110)} = \frac{2}{2\sqrt{2}D^2} = 0.0848\ atoms \cdot Å^{-2} \qquad 2\text{-}4$$

$$PD_{(111)} = \frac{2}{\sqrt{3}D^2} = 0.1385\ atoms \cdot Å^{-2} \qquad 2\text{-}5$$

Using the calculated packing densities, the face-specific charge density (SCD) can then be calculated by first assuming a single electron reduction reaction and then converting into $\mu C \cdot cm^{-2}$. We find that;

$$SCD = \frac{PD \times n}{N_A \times F} = \frac{PD \times n_{e^-\ per\ Au} \times 10^{16}_{Å^2 \cdot cm^{-2}} \times 10^{6}_{\mu C \cdot C^{-1}}}{6.24 \times 10^{18}_{e^- \cdot C^{-1}}} \qquad 2\text{-}6$$

By performing these calculations for the three low index faces and by applying different oxidation states for the surface atoms, the expected SCD can be shown to range from 135.9 $\mu C \cdot cm^{-2}$ ($SCD_{(100),\ n=1}$) to 887.9 $\mu C \cdot cm^{-2}$ ($SCD_{(111),\ n=4}$). The $SCD_{(100)}$ shows how Angerstein-Kozlowka et al. [128] reached their value of 192 $\mu C \cdot cm^{-2}$, and how Tremiliosi-Filho et al. [144] are able to reach a value of 390 $\mu C \cdot cm^{-2}$ (see values in italics in Table 2-4). While experimental results will not achieve the theoretical SCD due to aspects such as electrode roughness and non-single monolayer coverage, the theoretical SCD can provide a standard point of comparison.

Table 2-4. Calculated specific charge density of the three low index FCC planes.

Oxidation State	+1	+2	+3	+4
Possible gold oxide forms	Au_2O† $Au(OH)$Ŧ	† AuO Ŧ	Au_2O_3 $Au(OH)_3$	AuO_2
$SCD_{(100)}$ / $\mu C \cdot cm^{-2}$	*192.2*	*384.5*	576.7	768.9
$SCD_{(110)}$ / $\mu C \cdot cm^{-2}$	135.9	271.9	407.8	543.7
$SCD_{(111)}$ / $\mu C \cdot cm^{-2}$	222.0	443.9	665.9	887.9
Average / $\mu C \cdot cm^{-2}$	183.4	366.7	550.1	733.5

†Atlas of Electrochemical Equilibria in Aqueous Solutions does not consider Au_2O or any Au^{2+} oxidation states as a viable oxide state of Au.
Ŧ Ref [145, 146]

2.4 Ideal Particle Model

While using an average gold oxide reduction charge density (Section 2.3) can be useful for bulk gold surface area calculations, due to the size dependence of the atomic packing on small nanoparticles, using a gold oxide reduction charge density for these small particles is less appropriate. Furthermore, the edge or corner atoms on small gold nanoparticles may have different affinities for gold oxide formation and reduction. While larger nanoparticles can be modelled as spherical particles, this method is only applicable for particles above 5-10 nm where the impact of corners, and edges within the nanoparticle surface are minimal. For small particles, consideration of non-spherical shapes such as cuboctahedrons, decahedrons and icosahedrons may be more appropriate [147].

Before considering the true surface area of nanoparticles, it is helpful to consider how an ideal particle may behave. Figure 2-3 shows representations of three different shapes of nanoparticles, each containing three complete shells and 147 atoms. The lines delineate the Au(111) and Au(100) facets of each solid, showing how the structure of each particle varies. These considerations are helpful to demonstrate how the different surface energies of atoms in different relative locations can influence the overall structure and reactivity/catalytic activity of the particle. For example, while each of these nanoparticles contains the same number of surface and internal atoms, the differences in the types of facets leads to differences in the particle surface area and hence the SCD (Table 2-5).

When considering small clusters ($n < 200$) the icosahedron exhibits the overall energy minimum in DFT calculations, indicating that this shape is the energetically most favourable. Both icosahedron and decahedron are quasi-crystal structures, i.e. not a face centred cubic (FCC) crystal meaning they are less densely packed, yet, due to their higher proportion of closely packed *surface* atoms they are more stable than the cuboctahedron (Table 2-5). A 5% increase in interlayer distance between consecutive shells is predicted for the icosahedron [35] which leads to a transition of the energetically favourable shape for icosahedron to decahedron at ~1.6 nm and from decahedron to the FCC cuboctahedron at ~2.5 nm [29].

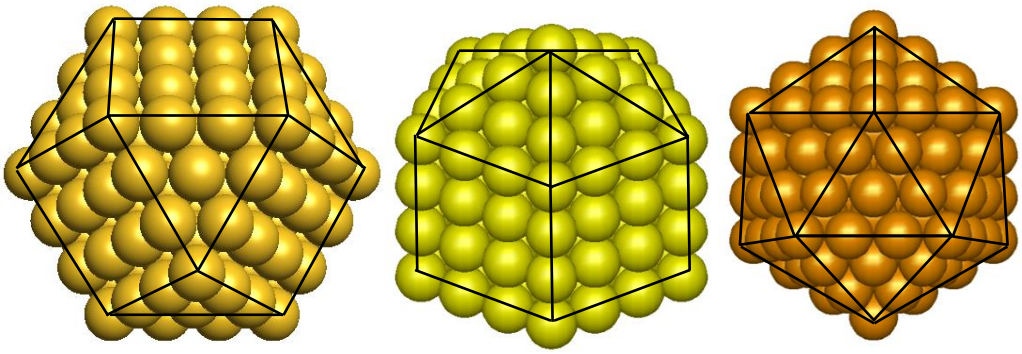

Figure 2-3. Representations of cuboctahedral (pale orange), decahedral (yellow) and icosahedral (orange) arrangements of Au-147 nanoparticles. Plane edge lines have been indicated with Au(111) faces shown in the triangles and Au(100) faces shown in the squares.

Table 2-5. The number of atoms occupying unique positions within cuboctahedral, decahedral and icosahedral solids with four complete shells.

	Cuboctahedron	Decahedron	Icosahedron
(100) face atoms	24	20	0
(111) face atoms	8	10	20
(100) – (100) edge atoms	0	10	0
(100) – (111) edge atoms	48	20	0
(111) – (111) edge atoms	0	20	60
Vertices	12	12	12
Surface atoms	92	92	92
Internal atoms	55	55	55
Total atoms	147	147	147
Particle surface area† / nm^2	12.6	12.4	11.5
Surface charge density₸ / $\mu C \cdot cm^{-2}$	223.4	231.8	277.5†

† The particle surface area has been calculated assuming a covalent radius of 1.4435 Å for all surface particles

₸ The surface charge density for gold oxide reduction is calculated assuming each surface site is in a Au+ oxidation state.

The equations for the chemical potential of liquid droplets are often used as an analogue of the chemical potential for nanoparticles due to their dependence on the inverse of their radius. In this relationship, the chemical potential of the particle, $\mu(D)$, is related to the chemical potential of the bulk metal, $\mu(\infty)$, via Equation 2-7 [148], a function of the specific surface stress, γ, the bulk metal atomic volume per atom, Ω, and the particle diameter, D. This relationship ignores strain effects [149], a factor which must be included for small particles whose atomic positions no longer occupy a FCC crystal lattice. The strain each surface atom experiences is dependent on its relative position on the surface and as such, the chemical potential of individual atoms varies according to the number and proximity of neighbouring atoms. These differences in chemical potential affect how the atoms will bond with reacting molecules, showing how the different ratios of (100) faces to (111) faces (Figure 2-4) can have a marked effect on the overall catalytic activity of a nanoparticle. Indeed, just by knowing that different atomic positions in a nanoparticle will

have different chemical potentials, it is intuitively obvious that some of the atomic positions will be more/less likely to form gold oxide than their neighbours.

$$\mu(D) - \mu(\infty) = \frac{4\gamma\Omega}{\mathrm{D}} \qquad 2\text{-}7$$

Furthermore, metal-metal bond lengths of nanoparticles will contract as the size of the metal decreases below ~3.0 nm. Miller et al. [30] measured a 0.018 nm contraction for very small gold clusters (<1 nm), a 6.3% reduction in the Au-Au bond length (Figure 2-5). By considering a combination of these four processes, namely that the nanoparticle shape is dependent on particle size, an abundance of (111) facets in small nanoparticles can lengthen the Au-Au bond, atomic positions within the nanoparticle will have different chemical potentials, and a reduction in the nanoparticle diameter can cause a contraction of the Au-Au bond, it becomes clear that physical measurement of the particle size cannot be used to directly infer an effective EASA.

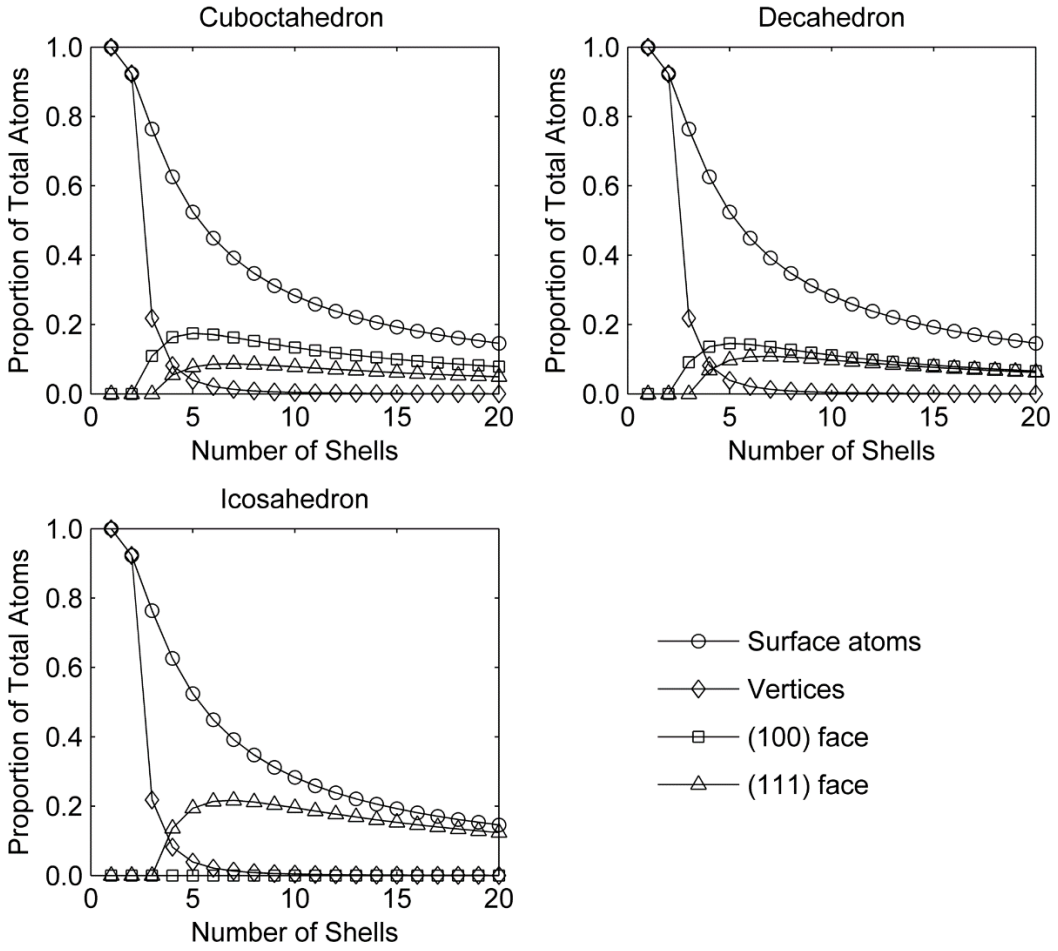

Figure 2-4. A modelled comparison of the proportion of surface atoms, vertices, (100) faces and (111) faces to the total number of atoms within three ideal nanoparticle solids.

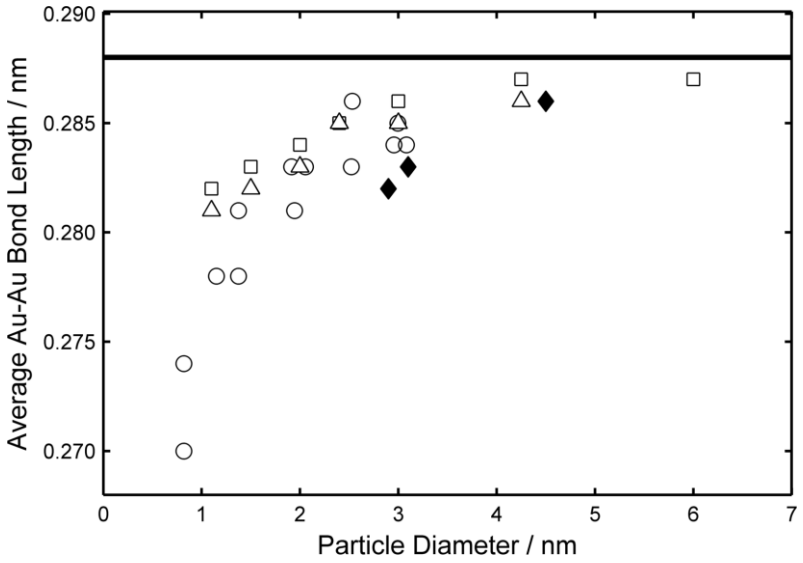

Figure 2-5. EXAFS determined Au-Au bond lengths as a function of particle size. Data extracted from Balerna et al. [150] (□),Balerna et al. [151] (▵),Miller et al. [30] (○), and Steven et al. [1] (♦). The solid line denotes the bulk Au-Au bond length of 0.288 nm

2.5 Electron Microscopy and the Physical Particle

Direct imaging of particles can be the most straightforward way to identify particle size. By using SEM (20X – 30,000X magnification) or TEM (up to 5,000,000X magnification), an image of the particles can be captured from which the individual particle sizes can be measured. Typically, these measurements will be 'binned' into a set of discrete particle sizes and then average particle sizes calculated. These average particle sizes can be reported as a number based diameter ($D_{avg} \propto D^1$), surface area based diameter ($D_{avg} \propto D^2$), volume based diameter ($D_{avg} \propto D^3$) or specific surface area based diameter ($D_{avg} \propto D^{-1}$). These factors inherently weight the data and can introduce an element of ambiguity depending on how the data is analysed. In addition to the complications discussed in this section, the weighting and distribution assumptions are often not stated in literature reports and hence, introduce an additional level of vagueness in the publications.

The first error when analysing small particles is the assumed type of distribution, for example, normal or log-normal distribution. If a particle size is sufficiently small and a normal distribution is assumed, a non-trivial number of particles (i.e. >5% [152]) will be modelled below a single atomic van der Waals diameter (0.332 nm). This will lead to an erroneous particle size distribution. As an example of this, two number-weighted distributions were produced in MatLab with an average particle size of 2.0 nm and a standard deviation of 1.5 nm (Figure 2-6). The number of unfeasible particles below 0.332 nm makes up 13.2% of the total normal distribution data set while 1.8% of the particles in the log-normal distribution are below this threshold. As the particle distribution model shifts to larger particle sizes, the influence of the unfeasible, D<0.332 nm, particles decreases such that a normal distribution can become a viable option.

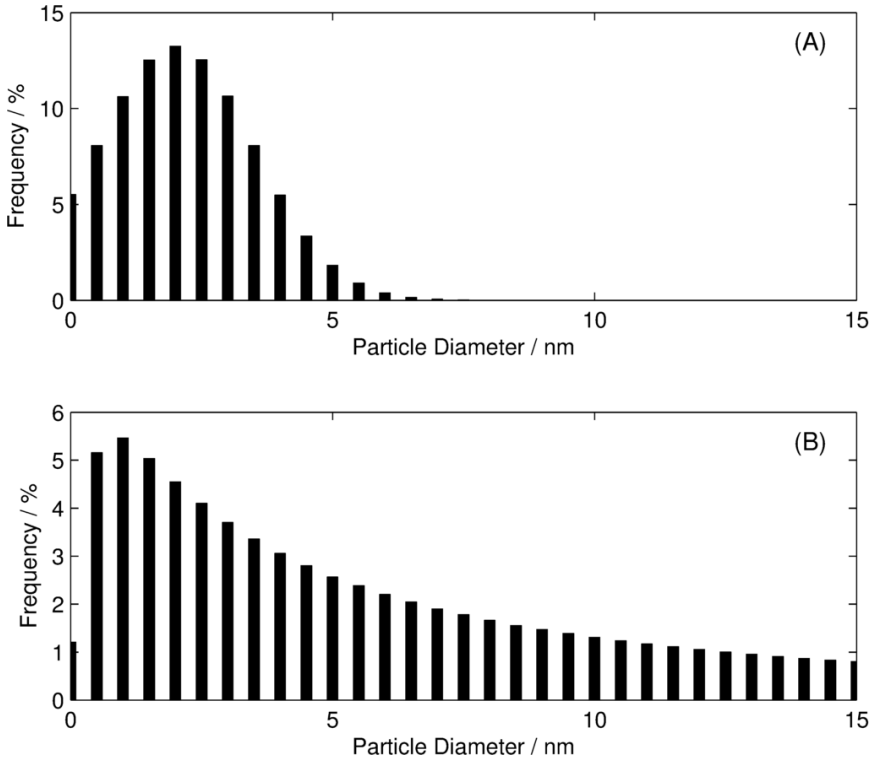

Figure 2-6. Normal distribution (A) and log-normal distribution (B) of a data set with a mean of 2 nm and a standard deviation of 1.5 nm.

In a separate model, two distributions were created using a normal distribution with a number weighted mean of 10.0 nm and a standard deviation of 2.0 nm. The method of calculation of the average particle size will change the number-weighted distribution as shown in Equations 2-8 – 2-11. These weighting factors were applied to the models of an 'ideal' distribution of 10^8 particles and a 'small' data set of 250 particles (Figure 2-7). The resultant average diameter for the weighted distributions of the ideal model varied by 1.73 nm, with the D_{SSA} average being calculated as 9.04 nm and the D_{Vol} average being calculated as 10.77 nm. Comparatively, the average diameter for the small model varied by 2.24 nm, with the D_{SSA} average being calculated as 8.53 nm and the D_{Vol} average being calculated as 10.77 nm – note that despite the D_{Vol} being the same for both models, this is only coincidental and as the bin size is increased, the two comparative values diverge.

$$D_{Num} = \frac{\sum_{i=1}^{n} D_i N_i}{N_t} \quad 2\text{-}8$$

$$D_{Area} = D_{Num} * D_i = \pi \frac{\sum_{i=1}^{n} D_i^2 N_i}{N_t} \quad 2\text{-}9$$

$$D_{Vol} = D_{Num} * D_i^2 = \frac{\sum_{i=1}^{n} D_i^3 N_i}{N_t} \quad 2\text{-}10$$

$$D_{SSA} = D_{Num} * D_i^{-2} = \frac{\sum_{i=1}^{n} D_i^{-1} N_i}{N_t} \quad 2\text{-}11$$

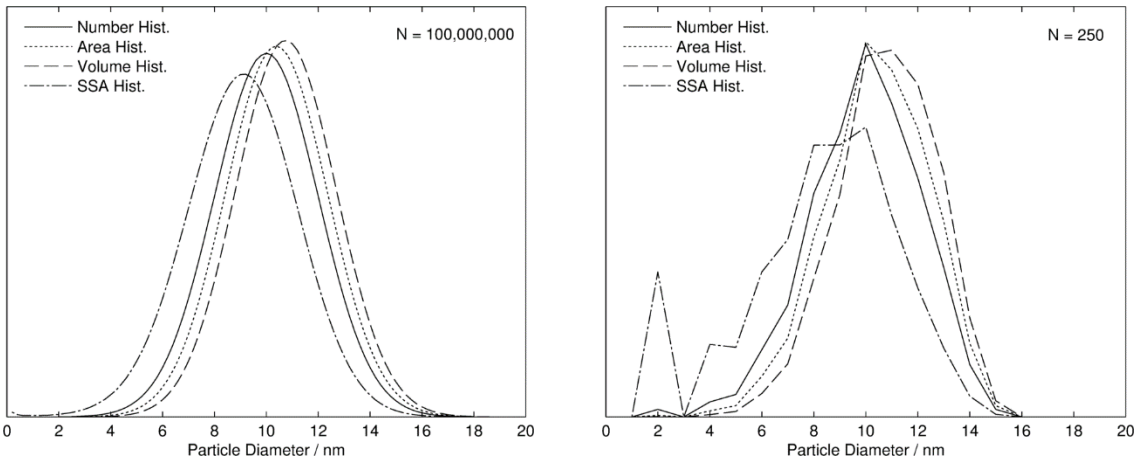

Figure 2-7. Histograms calculated from number weighted PSD models with N=10^8 and N=250 particles.

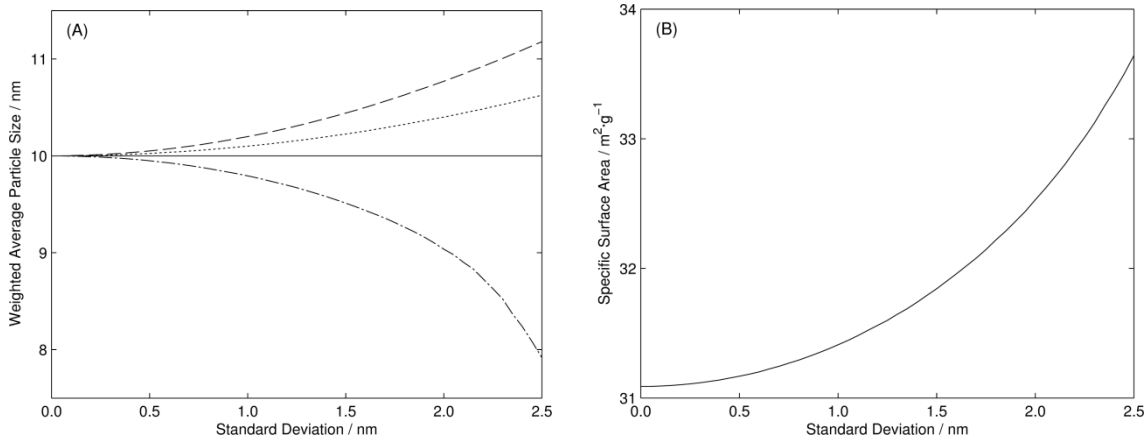

Figure 2-8. The effect of standard deviation on the weighted average particle size (A) and the effect of standard deviation on the specific surface area (B). Weightings are denoted in (A) as number weighting (solid line), area weighting (dotted line), volume weighting (dashed line) and specific surface area weighting (dashed/dotted line).

The generalised case of how the standard deviation affects the average particle size with the four different types of weighting the data was investigated (Figure 2-8A). It was found that for an overall population (i.e. a large enough sample count that the data is truly representative), the average particle size will follow the trend $D_{Vol} > D_{Area} > D_{Num} > D_{SSA}$. In the same way, the SSA can also be represented as a function of the standard deviation of a data set (Figure 2-8B). This is due to smaller particles generating a larger effect on the overall mass-normalized surface area than the larger particles. Hence, as the standard deviation increases, the number of larger and the number of smaller particle increases, however the smaller particles influence the overall SSA parameter to a greater degree.

While it may be ideal for each particle to be measured and quantified individually, there will still be uncertainties associated with the measurement techniques. These may arise from the resolution of the microscope, poor quality images, incorrectly scaled images, or from uncertainties in the measurement and analysis of the particles. The size of each

'bin' must also be considered when measuring a range of particles, with the lower bound of the bin size being controlled by the overall measurement uncertainties.

The effect of bin size was found from the same MatLab simulation as in Figure 2-7. As the number of particles increased, the simulated distribution became closer to ideal, such that a bin size of 0.2 nm produced a coherent histogram whereas a larger bin size of 1.0 nm was required for a similarly coherent histogram for the data set with 250 particles (Figure 2-9). In the case of the small data set, fluctuations in the random data produced an uneven distribution when the bin size was set to 0.2 nm. These simulations also show how an increase in the bin range can produce non-uniform variations in the calculated average size, e.g. the number weighted average particle size for the N=250 data set was 10.39 nm, 10.40 nm, 10.45 nm and 9.94 nm for bin sizes of 0.2 nm, 1.0 nm, 2.0 nm and 5.0 nm respectively. This indicates that 1) the bin size *for a normal distribution* does not have a large impact on these results, 2) an increase in bin size does not *consistently* correspond to an increase/decrease in the calculated average particle size, and 3) average particle sizes can be calculated from a relatively low sample size (provided sampling is random).

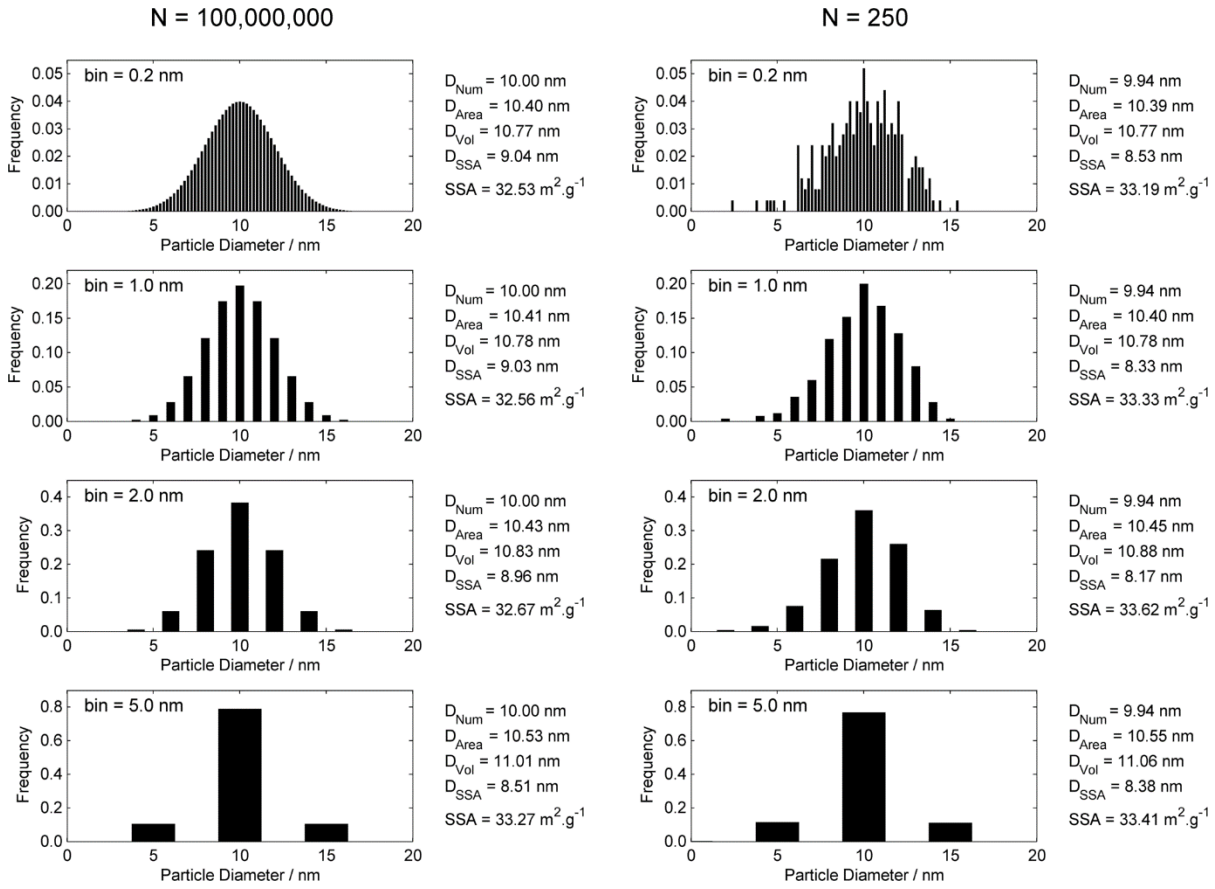

Figure 2-9. Modelled particle distributions with N=10^8 and N=250 particles. The particle diameter was averaged via number-weighted, area-weighted, volume-weighted and specific surface area-weighted calculations at each coarseness, along with the specific surface area as calculated via Equations 2-8 to 2-11.

2.6 Synchrotron Particle Size – EXAFS

Probing the interatomic bond distances is a proven way to investigate the atomic structure of nanoparticles and thus potentially to experimentally determine the surface atomic packing and thus the specific surface area of small gold nanoparticles. Such analysis can be performed by *X-ray absorption spectroscopy* (XAS). This measurement is often separated into one of two regions within the XAS spectrum; the *X-ray absorption near edge structure* (XANES) region which extends only ~50 eV above the primary absorption edge, or the *extended X-ray absorption fine structure* (EXAFS) region which can extend up to 1000 eV above the primary absorption edge. Stated simply, electrons within each atom in a sample will absorb photons at different energies, i.e. each electron has a specific energy requirement to shift it into a higher orbital. By scanning a synchrotron beam across a range of photon energies, the energy requirement to shift an electron from its orbital can be found via a characteristic 'edge' in the XAS data (See Figure 3-11 at ~11.9 keV). This 'edge' is chosen based on the desired atom and can be labelled as the K-edge, the L-edge or the M-edge depending on the shell from which the excited electron is emitted. For example, electrons from the 1s, 2s or 3s orbitals correspond to the K-edge, the L_1 edge and M_1 edge, respectively.

When considering the physical mechanism of EXAFS, it is useful to designate the atom that absorbs the photon and ejects an electron as the 'central atom' while all interacting atoms are the 'neighbouring atoms'. Electrons are ejected if the incident photon energy is at or above the binding energy of the target electron (in the case of the gold L_3 edge, $h\nu$ = 11.919 keV). While this edge energy may be informative, a lot more information can be found by looking at the oscillations in the absorption profile immediately after the edge energy.

As the sample is irradiated with energy-specific photons, a central atom may absorb an incident photon (Figure 2-10A) and, if the energy of the photon is large enough, an electron is emitted as a photoelectron wave (Figure 2-10B). These waves are scattered by neighbouring atoms (Figure 2-10C) and, depending on the photoelectron wavelength, can either cause constructive or destructive interference. This interference will then either increase or decrease the subsequent photon absorption probability of the central atom, giving rise to the oscillations seen in the EXAFS spectrum (Figure 2-11).

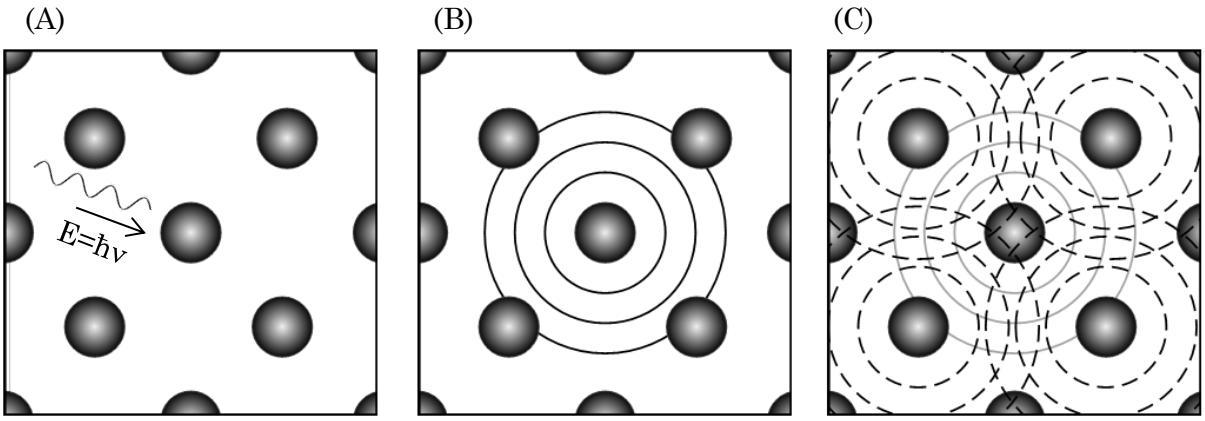

Figure 2-10. Schematic of how (A) synchrotron radiation is absorbed by a central atom (A), the central atom emits a photoelectron wave which then interacts with a neighbouring atom (B), the neighbouring atom scatters the incoming photoelectron wave causing constructive or destructive interference with the central and other neighbouring atoms (C).

The data analysis of the XAS data involve several steps and is often simplified for the end-user via dedicated XAS analysis programmes such as the Demeter [153], FDMNES [154], SixPACK [81] and IFEFFIT [80] software packages. For the work within this thesis, the Demeter package, in particular, the Athena programme was used for data correction and the Artemis programme was used for model fitting. These programmes provide a helpful way to interpret and fit the "EXAFS Equation" (Equation 2-12).

As an example, Figure 2-11 to Figure 2-14 show a typical data set and transformations for a gold foil measured across the gold L_3 edge. The raw data (Figure 2-11) has the pre-edge and post-edge backgrounds estimated to account for downward trend of the data corresponding to the absorption coefficient of the 'central' atom [155]. The energy of the step is well known ($E_{L3,gold}$ = 11.919 keV [156]) and this point is used to calibrate the data, while the pre-edge line is normalised to an absorbance of zero and the post-edge line is normalised to 1 (Figure 2-12). The data is then transformed into the 'k-space' via Equation 2-15 (See Table 2-6 for nomenclature, Figure 2-13 for transformed data). A Fourier transform can then be applied to shift the data into the 'R-space' (Figure 2-14).

$$\chi_i(k) = \frac{(N_i S_0^2) F_i(k)}{kR_i^2} \sin\left(2kR_i + \varphi_i(k)\right) e^{-2\sigma_i^2 k^2} e^{\frac{-2R_i}{\lambda(k)}} \qquad 2\text{-}12$$

$$R_i = R_0 + \Delta R \qquad 2\text{-}13$$

$$k^2 = \frac{2m_e(E-E_0)}{\hbar} \qquad 2\text{-}14$$

$$\chi(k) = \Sigma_i \chi_i(k) \qquad 2\text{-}15$$

Table 2-6. Nomenclature for the "EXAFS Equation" and variables within (Equations 2-12 to 2-15). The subscript '*0*' denotes the reference value and the subscript '*i*' denoted the specific path.

Theoretically Calculated Parameters	
$F_i(k)$	Effective scattering amplitude
$\varphi_i(k)$	Effective scattering phase shift
$\lambda(k)$	Mean free path
R_0	Theoretical path length
Fitted Parameters	
N_i	Path degeneracy – average coordination number for path i
S_0^2	Amplitude reduction factor
$E\text{-}E_0$	Edge energy shift
ΔR	Change in the path length
σ_i^2	Debye-Waller factor – a measure of disorder

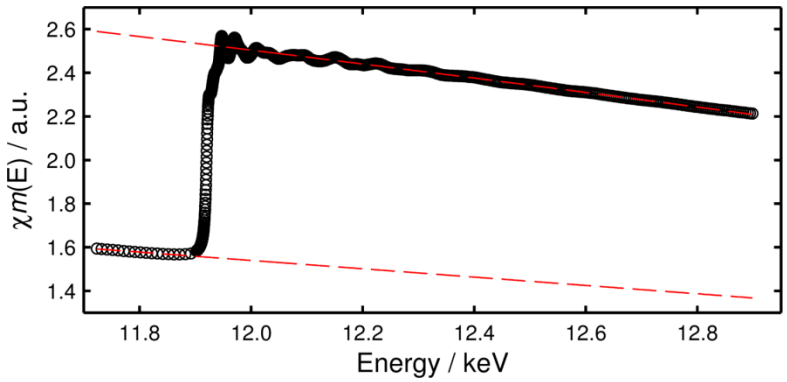

Figure 2-11. Raw EXAFS transmission data for a gold foil. The red lines indicate the pre-edge and post-edge background, while the distance between them is defined as the "edge step".

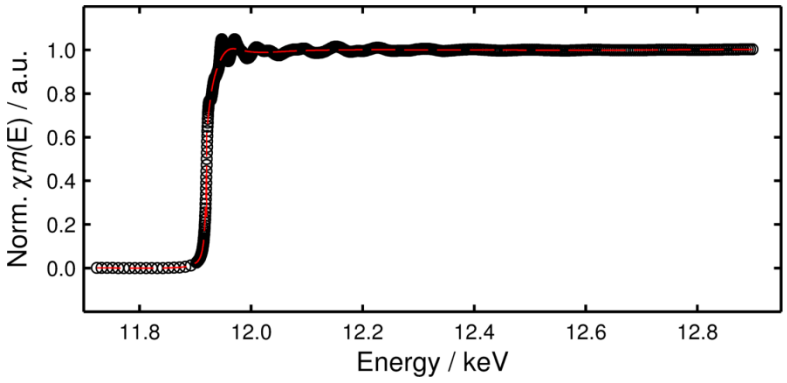

Figure 2-12. Normalised EXAFS transmission data for a gold foil. The red line is the pre-edge and post-edge line fitted as a background. The data is normalised such that the pre-edge line is set to 0, the post-edge line is set to 1 and the edge step is hence, defined as 1.

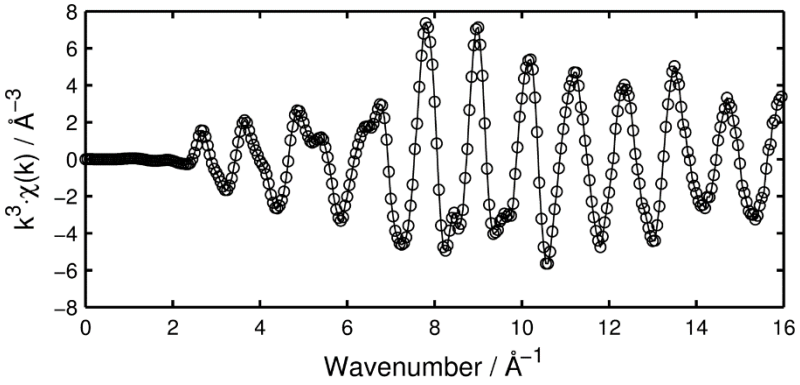

Figure 2-13. k-transform of normalised EXAFS transmission data as per Equation 2-15 with a weighting of k^3.

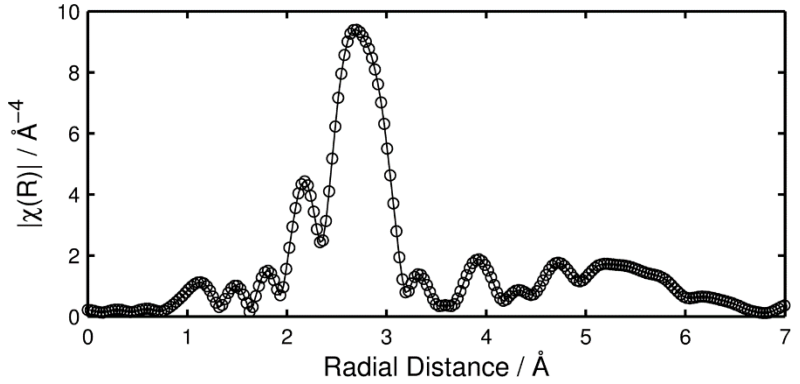

Figure 2-14. Fourier transform of Equation 2-15. The relative height of the major peak indicates the average coordination number while the peak position indicates the average bond distance of the nearest neighbours.

From this set of data, a theoretical fit can be applied using known quantities such as radial distance, and amplitude factor, and estimated quantities such as the Debye-Waller factor, change in path length and the expected coordination number. Typically, anywhere from 1 to 3 pathways are fitted to a pure sample such as gold, although more pathways can be fitted if the sample contains several different atoms in its structure. As an example, using the amplitude factor determined with the bulk gold sample shown in Figure 2-11 to Figure 2-14, the first two, single scattering paths were fitted to EXAFS data of a sample of 4.5 nm gold particles (Figure 2-15). This fit determined a bond length contraction (relative to bulk gold) of 3.4 ± 0.7% and average coordination numbers of 9.6 ± 1.0 and 2.7 ± 2.5 for the first and second shells respectively.

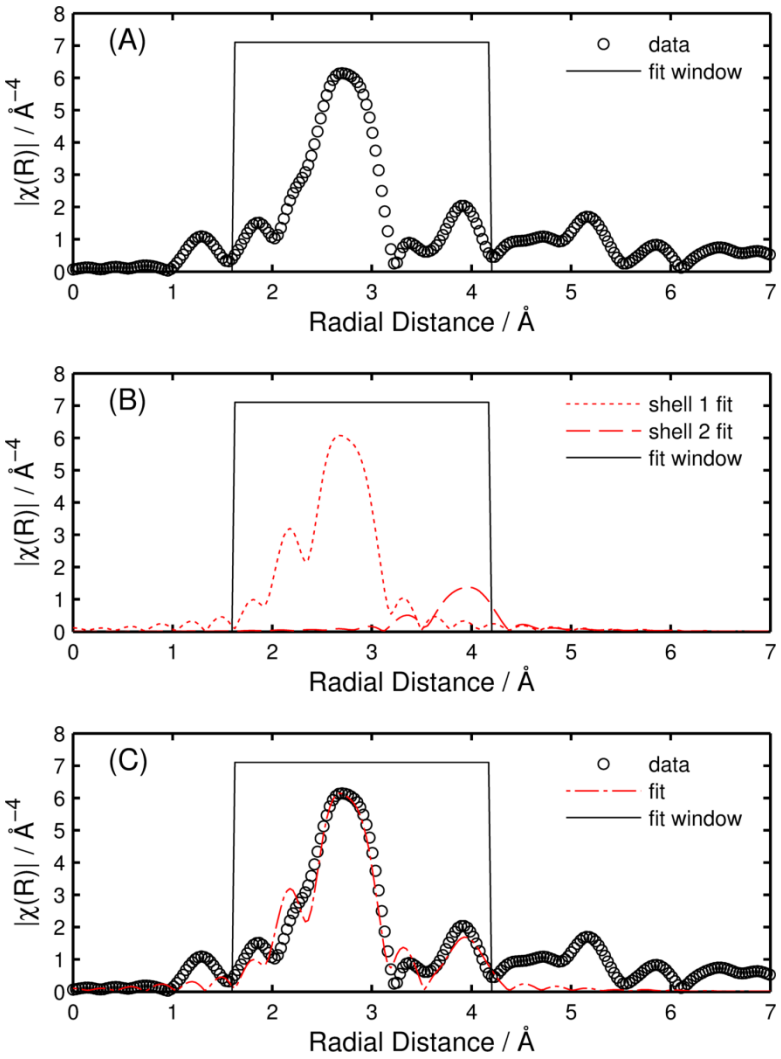

Figure 2-15. An example of the fitting procedure for 4.5 nm gold nanoparticles. Subplots indicate the raw data after it has been transformed into the R^3 space (A), the fits for the first two single scattering paths (B) and an overlay of the raw data and final fit (C).

2.7 Nanoparticle Measurements

In an attempt to understand how the surface area of gold nanoparticles can be estimated by electrochemical methods, a series of measurements were performed on both a bulk gold disc and a 3.2 nm Au nanoparticle catalyst supported on carbon black. The experiments included; variations in the gold oxide reduction peak with respect to the upper potential limit, Au/C electrode preparation and stability, and the effects of the Au/C electrode layer physical properties such as layer thickness and Nafion content.

2.7.1 Experimental

2.7.1.1 Electrochemistry

A traditional 3-electrode electrochemical cell was attached to a Gamry Reference 600 potentiostat for all measurements. The working electrode was either a gold disc electrode

(geometric surface area = 3.14 cm^2) or a gold nanoparticle catalytic layer (geometric surface area = 0.28 cm^2). The counter electrode was either Pt foil for the gold disc or a Pt/Ir wire for the gold nanoparticle electrode. The reference electrode was a Ag/AgCl (sat. KCl). All measurements were conducted in 0.5 M H_2SO_4 and all potential measurements have been converted to, and reported against the RHE scale via Equation 2-16 (See Section A1.4.4 for reference electrode conversion factors).

$$E_{RHE} = E_{Ag/AgCl} + E° + 0.0591pH \qquad 2\text{-}16$$

2.7.1.2 1.5 nm Au synthesis

1.5 nm Au nanoparticles were synthesised according to the Weare method [91]. All chemicals were purchased from established suppliers (Sigma-Aldrich, Merck etc) and were of Analytical Grade purity. Once synthesised, the nanoparticles were stored at -20 °C in their crystal form as $Au_{101}[P(C_6H_5)_3]_{21}Cl_5$ to ensure their long-term stability. Prior to deposition onto a carbon black support, a sample of the Au_{101} crystal was dissolved in dichloromethane (DCM) and measured via NMR to ensure the broad peak associated with Au_{101} was present. The remaining Au_{101} nanoparticles was then dissolved in 10 mL DCM and carbon black was suspended in an additional 10 mL DCM (gold loading of 15.1 wt%). The two solutions were then mixed and additional DCM (~3-5 mL) was used to ensure complete transfer of the carbon black to the mixture. The mixture was then stirred until it was almost dry then resuspended in DI water, filtered and washed with additional DI water. The powder was then dried at 50 °C for 3 hours, ground and stored in a dark environment.

2.7.1.3 Catalytic Layer Preparation

Catalytic layers were produced by ultrasonication of 5-6 mg Au/C in an equivalent quantity (5-6 mL) of 0.5 $mg \cdot mL^{-1}$ Nafion in a 4:1 IPA:DI water solution. This produced an ink containing 1 $mg \cdot mL^{-1}$ Au/C and 0.5 $mg \cdot mL^{-1}$ Nafion. Four small sections of graphite sheet were held in a mask with four 6 mm holes to ensure a consistent electrode diameter. The mask and graphite were then heated on a hotplate to 80 °C for the duration of the electrode preparation. 4.65 mL of the catalyst ink suspension was pipetted into an airbrush and the ink was slowly sprayed onto the graphite at a pressure of ~0.5 bar and a rate of ~0.1 $mL \cdot min^{-1}$. The catalyst/graphite sheets were cooled and attached to a cuvette with a predrilled, 0.8 cm hole, via an epoxy glue.

2.7.1.4 Particle Size Analysis

Particle size analysis was conducted using transmission electron microscopy (TEM) utilising a Philips CM200, operating at 200 kV. Samples were prepared by depositing and drying a 2x10 µL of the Au/C catalyst, suspended in IPA, onto lacey carbon grids. A diameter weighted particle size distribution of 3.2 nm (standard deviation = 1.3 nm) was calculated by measuring 452 particles across 21 representative images in the ImageJ software package (See Section A2.2 for the full analysis method). Using the entire particle size distribution, the specific surface area of the gold nanoparticles was calculated to be 70.75 $m^2 \cdot g^{-1}$.

2.8 Electrochemistry Results

2.8.1 Maximum Potential – Gold Oxide Reduction Charge

The bulk gold electrode disc was first cleaned according to the procedure outlined by Ma et al. [157] by holding the electrode at 2.2 V for 5 seconds and -0.15 V for 10 seconds. The potential was then scanned 20 times between 1.9 V and -0.15 V at a sweep rate of 4000 $mV \cdot s^{-1}$. The CV scans began with the anodic sweep, starting at the estimated OCP of 0.7 V vs. RHE. The electrolyte solution was replaced and four CV scans were performed between 0.2 V and 2.0 V at a sweep rate of 100 $mV \cdot s^{-1}$. This procedure was repeated for upper potential limits of 1.8 V, 1.6 V and 1.4 V (Figure 2-16). The total gold oxide reduction charge increases as a function of the upper potential limit (Figure 2-18), agreeing with measurements shown by Hoare [103], albeit with a slight positive shift of the gold oxide reduction peak due to a pH difference. As the roughness of the gold electrodes is unknown, the current density has been calculated on the geometric area for the bulk gold electrode and on the TEM-based gold surface area for the Au/C electrodes.

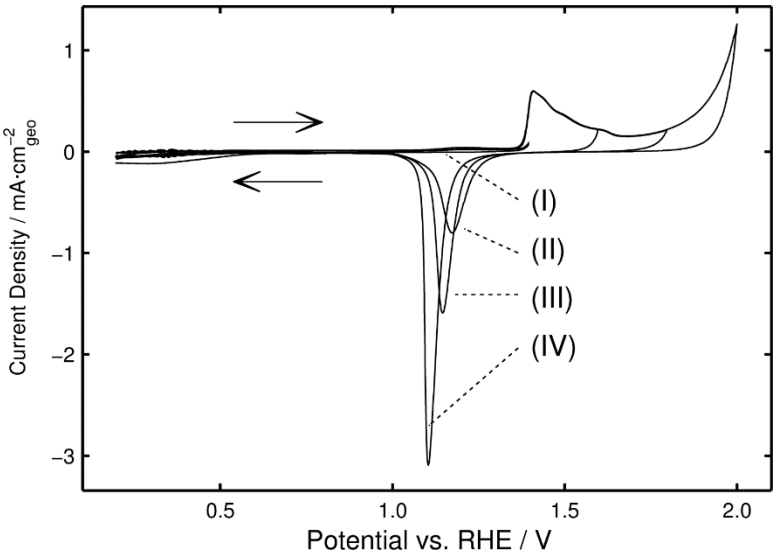

Figure 2-16. CV scans of the bulk gold disc in 0.5 M H_2SO_4. Gold oxide reduction peaks indicated for upper potential limits of 1.40 V (I), 1.60 V (II), 1.80 (III), and 2.00 V (IV).

A similar set of experiments were conducted for the gold nanoparticle catalytic layer. However, Cherevko et al. [158] show that as gold oxide formation begins at approximately 1.3 V vs. RHE, gold begins to dissolve into the electrolyte. Due to this dissolution, the cleaning procedure applied to the bulk gold electrode cannot be carried over to the nanoparticle electrode as any potential above the gold oxide formation potential will cause ageing and hence, an inaccurate and unreproducible result. The dissolution also limits the viability of the upper potential of the CV scan (further discussed in Section 2.8.2) which in turn, limits the maximum potential for nanoparticle tests. As a comparison to the bulk gold data in Figure 2-16, four sets of CV scans were performed on the gold nanoparticle catalyst with upper potential limits of 1.85 V, 1.70 V, 1.55 V and 1.40 V (Figure 2-17). The CV scans began with the anodic sweep, starting at the estimated OCP of 0.7 V vs. RHE.

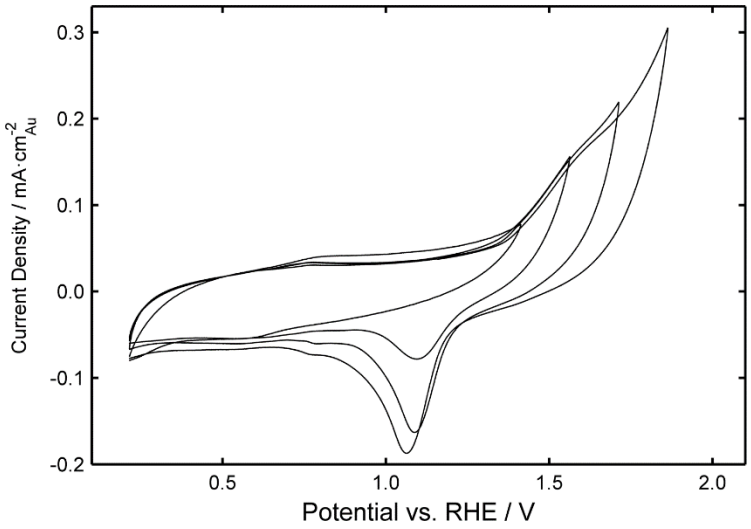

Figure 2-17. CV scans of gold/carbon electrode in 0.5 M H_2SO_4. A new electrode was used for each measurement, while the upper potential limit was reduced from 1.85 V to 1.40 V by 150 mV for each measurement.

These data sets can be used to determine the EASA of the sample by measuring the gold oxide reduction charge (Figure 2-2) and converting it to an area by assuming a specific charge density (a value of 386 $\mu C \cdot cm^{-2}$ is used in this thesis as this is equivalent to a single monolayer of AuO on the Au(100) face). Alternatively, by knowing the disc size/particle size distribution, the geometric surface area of the sample is known and the specific charge of the gold oxide reduction peak can be calculated (Figure 2-18).

Oesch and Janata [119] mention that gold oxide formation is both potential and time dependent. These experiments were performed at a constant sweep rate, minimising any time-related dependencies of the data. This experiment confirms the potential-dependent hypothesis and, by assuming linear interpolation as proven by Oesch and Janata [119], a gradient can be applied to relate the specific charge to the upper potential limit. However, a gradient of 2.52 $mC \cdot V^{-1}$ for the gold disc and 1.62 $mC \cdot V^{-1}$ for the Au/C electrode indicates that the type of gold electrode being oxidised is also an influential factor on the specific charge density of the sample. As such, Figure 2-18 demonstrates how using a specific charge density to measure the EASA can only be related to individual gold samples while using a defined potential limit. For example, to be able to assume a charge density of 450 $\mu C \cdot cm^{-2}$, the bulk gold plate requires an upper potential limit of 1.33 V while the gold nanoparticles require an upper potential limit of 1.72 V.

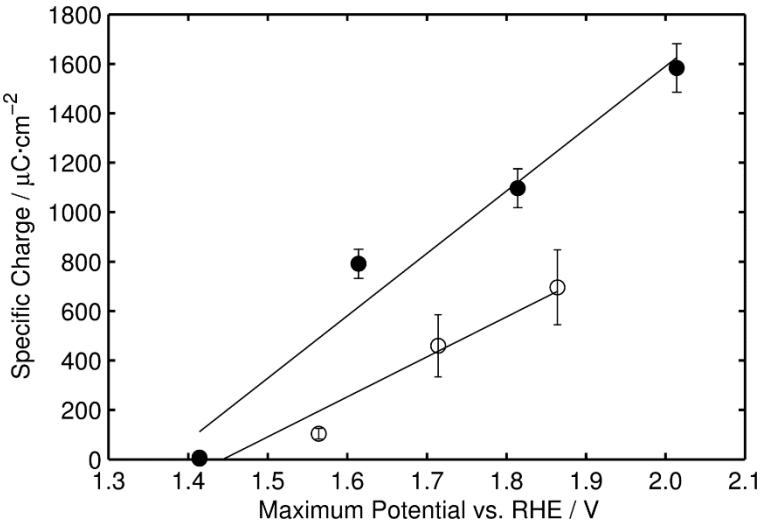

Figure 2-18. Specific peak charge for a gold plate (filled circles) and gold nanoparticles (empty circles). Measurements on the gold disc were taken in 0.5 M H_2SO_4 at a sweep rate of 100 mV· s^{-1} according to the procedure outlined by Ma et al. [157] while measurements on the gold nanoparticle catalyst were performed via the same CV scans without any pre-conditioning of the surface.

2.8.2 Maximum Potential – Stability

When considering the stable cyclic voltammetry of a bulk gold electrode, the gold oxide reduction peak remains unchanged between CV scans. This stability is not seen on nanoparticle CV scans due to the dissolution of atomic gold, or desorption or sintering of the nanoparticles (discussed in depth in Chapter 4). Rand & Woods [159] insist that for any anodic electrochemical process on noble metals, the effects of the dissolution, and its associated current, ought to be recognised.

While desorption and sintering have no directly measurable current, their effect on the gold oxide reduction peak is measurable. Desorption of nanoparticles can either occur evenly across the particle sizes resulting in an unchanged distribution, or it can occur asymmetrically which will produce an altered distribution. As the gold oxide reduction peak potential is a function of the average particle size [160], an increase in the PSD caused by small particles desorbing preferentially will produce an anodic drift of the gold oxide reduction peak while a decrease in the PSD caused by large particle desorbing preferentially will produce a cathodic drift of the gold oxide reduction peak. In both cases, as the particles desorb the total gold surface area will decrease, producing a smaller gold oxide reduction peak charge.

On the other hand, sintering of particles will produce an anodic shift of the gold oxide reduction peak potential and an overall decrease of the gold oxide reduction peak charge. The peak potential shifts to higher potentials due to the larger particles becoming closer to typical bulk gold behaviour which has a higher potential for gold oxide reduction. The decrease in the area of the gold oxide reduction peak is simply due to the reduction in gold surface area on the electrode.

The gold oxide reduction charge was measured over 50 CV scans for each of the maximum potential ranges mentioned in Section 2.8.1 (Figure 2-19). The long-term reproducibility of the CV scans is reduced as the maximum potential increases, where an E_{max} of 1.55 V shows only a small decay in charge and an E_{max} of 1.70 V or 1.85 V shows an increasingly rapid decay in the measured charge. These results align with predicted responses of the inherent instabilities of the gold nanoparticles, i.e. due to gold dissolving at potentials above 1.32 V, a CV with E_{max} of 1.55 V run at 100 $mV \cdot s^{-1}$ would be above the dissolution potential for 4.6 seconds while a CV with an E_{max} of 1.85 V run at 100 $mV \cdot s^{-1}$ would be above the dissolution potential for 10.6 seconds. Over 50 CV scans, this represents 3.8 minutes and 8.8 minutes respectively.

As has already been shown, the gold oxide reduction peak charge is very dependent on the maximum potential (Figure 2-18). As such, the maximum recorded gold oxide reduction charge has been chosen as the 'representative surface' of the electrode, however, the number of CV scans to reach this maximum is not consistent between different E_{max} potentials, i.e. the maximum charge with an E_{max} of 1.55 V occurs during the 24^{th}-26^{th} CV scan while with an E_{max} of 1.85 V the maximum charge occurs at the 8^{th}-9^{th} CV scan. The surface area of the fresh catalyst (before CV scans have started) is likely to be higher than this 'representative surface' and may be able to be back-extrapolated from the curve, however, this approach has not been attempted as the behaviour of the nanoparticles during the early CV scans is unknown. As such, it is recommended that if CV scans are employed as a part of an electrode preparation or cleaning procedure, the effect of the chosen maximum potential limit must be explored prior to implementation.

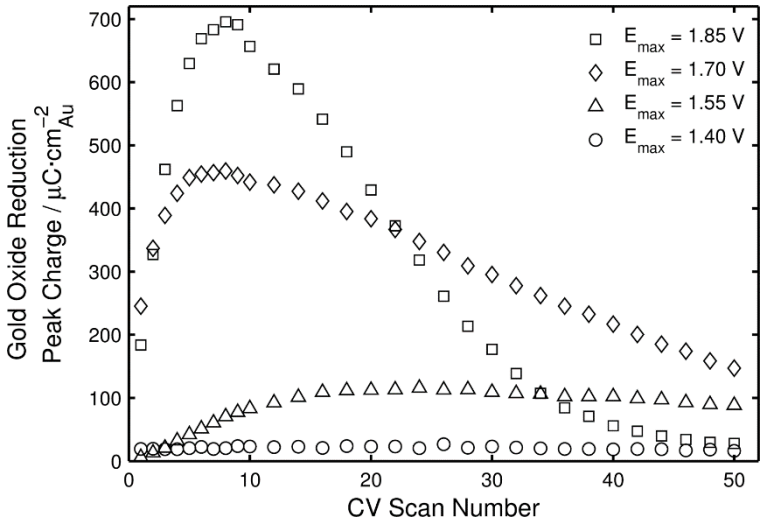

Figure 2-19. Gold oxide reduction charge stability for samples with different maximum potentials. E_{max} is the maximum potential of the CV set with respect to the RHE.

Section 2.8.1 and section 2.8.2 show how a single maximum potential limit cannot be used as an absolute measure of gold electrode surface area and how the decreasing stability of the gold oxide reduction peak with increasing maximum potential must be considered when performing pre-experiment CV scans. These two factors necessitate that either a correlation or caveat is included in any work when the gold oxide reduction charge is used to produce an electrode surface area.

2.8.3 Spray Casting – Loading Repeatability

In addition to the inherent challenges of using gold oxide reduction to determine the electrochemically active surface area of gold nanoparticles, the electrode fabrication (i.e. taking the Au/C powder sample and forming an electrode layer on an inert substrate) will also impact the measured surface area of the sample. Spray cast electrode layers are prone to variations between individual electrodes and between different electrode sprays. These variations can be caused by;

1. The cleanliness of the airbrush.
2. The pressure of the compressed air.
3. The viscosity of the ink.
4. The size of the opening of the ink delivery port.
5. The temperature of the hotplate.
6. The local air convection behaviour.
7. The distribution of particles in the ink.
8. The angle of ink application.
9. The distance between the airbrush and the catalytic layer.

Some of these items, such as #1, #2 and #5 can be controlled through careful preparation and appropriate equipment while other items, such as #3 have little effect with an IPA-based ink near room temperature. However, items such as #6, #8 and #9 are inherently variable and have been found to affect the integrity of the sprayed layer with only minor alterations. As such, electrodes were spray cast in batches of three or four electrodes using an aluminium mask in order to minimise daily variations. Repeatability measurements produced a gold oxide reduction peak charge confidence interval of ~10-15% with the majority of this uncertainty arising from these environmental fluctuations.

2.8.4 Spray Casting – Layer Thickness

Unlike drop-cast electrodes, where the catalyst layer is thin with relatively large aggregation features [161], the thickness of a spray-cast layer can be altered by increasing or decreasing the quantity of Au/C sprayed onto the substrate. This increased thickness, along with a reduction in individual droplet size allows for a more uniform electrode to be prepared via spray casting compared to drop-casting. For gold to be electrochemically active it needs to be both electrically connected to the substrate and to be in contact with the electrolyte. At very low layer thicknesses, the electrochemistry of a spray-cast layer is expected to be very similar to that of a drop cast layer due to the elimination of any self-blocking that may occur on thicker layers. However, as spray coated layers become thicker,

limited electrolyte penetration into the layer will likely reduce the number of gold nanoparticles that are electrochemically active, i.e. the gold nanoparticles closest to the substrate might be inactive. Similarly, poor electrical contact through a thick layer might limit the number of gold nanoparticles in the outer-most part of the layer that are electrochemically active. The outcome of this reduced gold availability, whichever mechanism has caused it, is that as the layer thickness increases, a smaller proportion of the gold nanoparticles in the layer will be electrochemically active. This means that thick electrocatalytic layers can be expected to underestimate the geometric surface area of the sample.

This active catalyst limit can be seen in experiments where a different volume of catalytic ink was sprayed onto electrodes during preparation. In four separate catalyst preparations, different quantities of a 1 $mg_{cat} \cdot mL^{-1}$ ink were sprayed to create four catalytic layers with loadings between 0.55 $mg_{cat} \cdot cm^{-2}_{geo}$ and 3.3 $mg_{cat} \cdot cm^{-2}_{geo}$. With a gold loading of 15.1 wt% and a geometric surface area of 70.75 $m^2 \cdot g^{-1}_{Au}$, this corresponds to 59 $cm^2_{Au} \cdot cm^{-2}_{geo}$ and 351 $cm^2_{Au} \cdot cm^{-2}_{geo}$ respectively. Based on the individual components of the electrodes, density estimates (See Section 6.3.4) showed that this produced layers that were 13.3 µm, 26.6 µm, 39.9 µm and 79.7 µm thick. 50 CV scans were performed on all catalytic layers and the maximum gold oxide reduction peak charge was recorded as both the raw result and as a surface area-normalized result (Figure 2-20). These findings (Figure 2-20B) show that while the unmodified charge consistently increases as the layer thickness increases, below 26.6 µm the normalised charge remains constant around 300 $mC \cdot cm^{-2}_{Au}$ and above this thickness, the normalised charge is seen to decrease significantly to below 150 $mC \cdot cm^{-2}_{Au}$ at a layer thickness of 79.7 µm. These experiments confirm the 'active catalyst depth limit' and suggest that catalytic layers should be limited to a thickness of less than 26.6 µm, to ensure that all of the gold nanoparticles are electrochemically active.

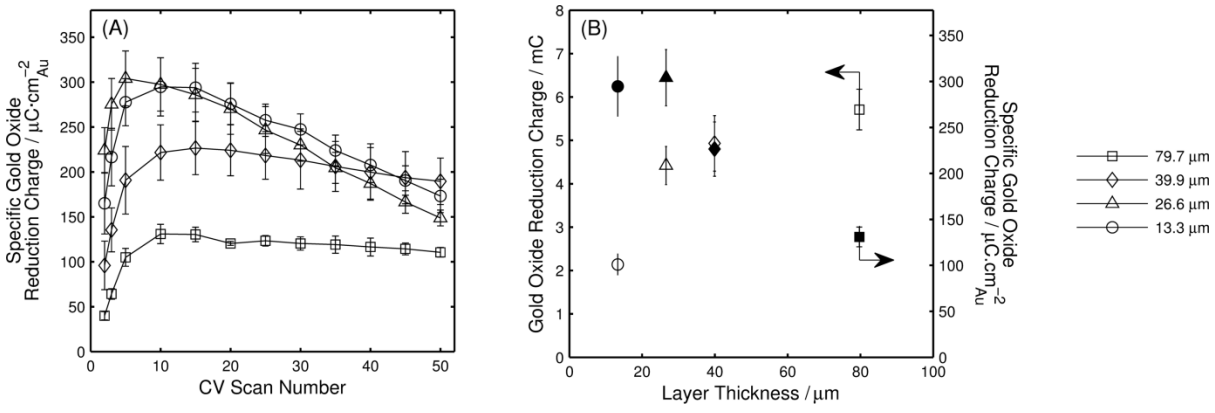

Figure 2-20. (A) Stability of the gold oxide reduction peak charge over 50 CV scans (A). Maximum recorded gold oxide reduction charge for each layer thickness where empty symbols denote the absolute charge and filled symbols denote the area-normalized charge (B).

2.8.5 Spray Casting – Nafion Content

Another factor that introduces variation within the spray cast electrocatalytic layers is the Nafion content. Nafion has two functions within the layer; 1) it acts as a binding agent, and 2) it enhances cation transport, and by extension water transport, within the electrode [162]. By virtue of the Nafion acting as a binding agent, there may be an upper limit where an excess of Nafion will cause blocking of the gold sites, as well as a lower limit where the Nafion content either no longer binds the catalytic layer coherently, or the benefit gained from the cation transport action is no longer significant compared to the reaction rate.

Electrocatalytic layers with the same, 3.2 nm nanoparticles and 15.1 wt% gold-carbon catalyst were produced with four different Nafion ratios: 47 wt%, 33 wt%, 20 wt% and 10 wt%. It was found that as the Nafion content of the layer increased, the largest gold oxide reduction peak was recorded on earlier CV scans (Figure 2-21). This reinforces the conclusions from Figure 2-19 where the maximum recorded gold oxide reduction charge is not representative of the fresh nanoparticle surface area. These results also show that the lower Nafion content limit for spray cast electrodes lies between 20 wt% and 10 wt% Nafion content. This limit is likely to be due to the hydrophobicity of the carbon support preventing ionic transfer which is normally facilitated by the Nafion. Conversely, the highest Nafion content of 47 wt% showed both an earlier gold oxide reduction peak maximum as well as faster degradation of the electrode. This feature is caused by the increased cationic transfer and is used by Wang et al. [163] to perform 'Accelerated Durability Tests' for spray-cast PEM fuel cell electrodes.

While the CV scan number at which the maximum gold oxide reduction peak charge occurs is a feature of the Nafion content of the electrode, this is only an intermediate justification. By pre-soaking a fresh electrode in the electrolyte for 1.5 hours, the measured charge is increased for the first ~10-15 CV scans, after which it falls to within the normal range (Figure 2-22). Pre-wetting the electrode for longer than 1.5 hours does not change the behaviour further, with the initial increase in recorded charge remaining for all experiments. This adds additional weight to the argument that the representative charge for a fresh electrode could not be back-extrapolated.

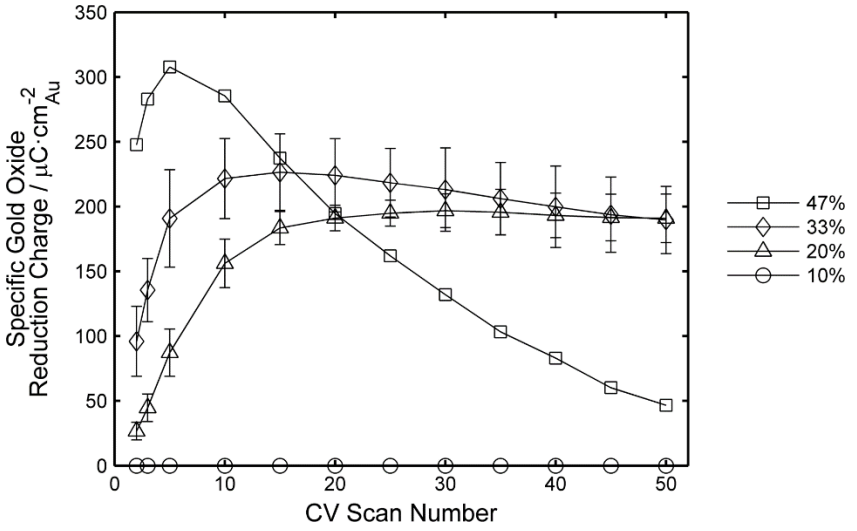

Figure 2-21. Stability of the gold oxide reduction peak charge over 50 CV scans with varying Nafion content within the electrocatalytic layer.

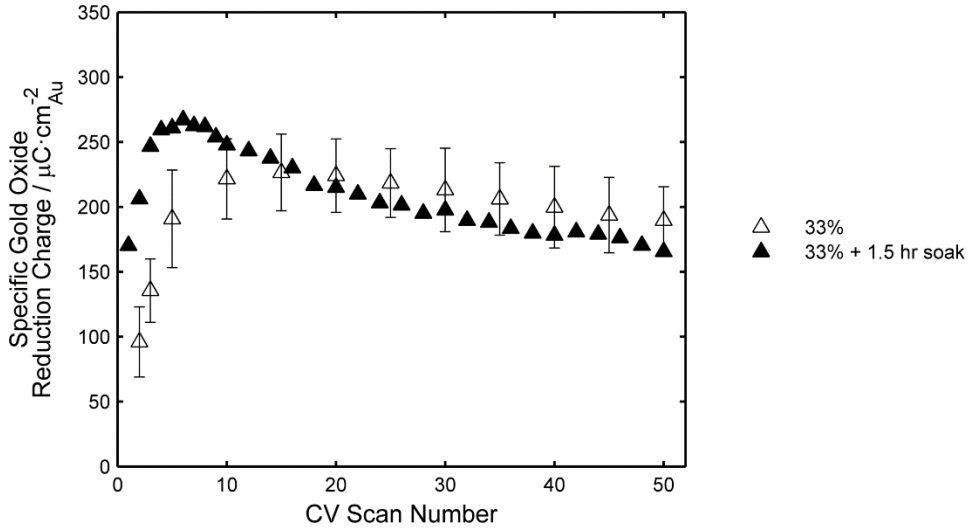

Figure 2-22. Stability of the gold oxide reduction peak over 50 CV scans for Nafion content of 33% and a comparison to a 33% Nafion electrode that had been pre-soaked in 0.5 M H_2SO_4 for 1.5 hours prior to the CV scans.

2.9 Summary

This chapter has discussed the main points on how the surface area of nanoparticles can be calculated. DFT calculations show how small (<2.5 nm) particles have a quasi-crystal structure, enabling them to form low-energy polyhedrons with a higher proportion of close-packed Au(111) faces than a regular FCC crystalline nanoparticle.

The calculation of particle parameters from physical measurements such as TEM provides an accurate description of variables such as the specific surface area and average particle diameter. Similarly, synchrotron techniques such as EXAFS are useful to measure the average coordination number and bond distances for nanoparticles. While these

measurements are useful to quantify a nanoparticle sample, care must be taken as the *electrochemically* active surface area may not be accurately represented by the theoretical or physical models.

The electrochemical surface area of catalysts can be measured through ionic (e.g. H^+) adsorption or underpotential deposition of metals, however, these methods are unavailable to supported gold nanoparticles due to the interference of the support material. Measurement of the gold oxide coverage is a well-known and often performed measurement that quantifies the number of reacting gold particles by measuring the charge required to fully reduce the gold oxide layer. With the quantity and nature of the gold oxide layer varying with respect to potential limits and time spent in the gold oxide formation region of the CV, this method of quantification is only comparable when comparing similar experiments.

The unstable nature of the nanoparticle will also have an effect on the electrochemical behaviour of a nanoparticle catalyst. By performing measurements or reactions on the nanoparticle, degradation will occur through dissolution, desorption and sintering. When studying aspects such as the catalytic activity of a nanoparticle based catalyst, this degradation should be considered and the reported catalyst properties should be as similar to the reacted catalyst as possible. Stability of gold nanoparticles from four different synthesis methods is discussed in Chapter 3, along with how the potential for degradation has been minimised prior to experimental measurements.

Chapter 3 ELECTROCHEMICAL STABILITY OF CARBON-SUPPORTED GOLD NANOPARTICLES IN ACIDIC ELECTROLYTE DURING CYCLIC VOLTAMMETRY

3.1 Introduction

Gold nanoparticles have been proven as useful materials in a range of applications including, heterogeneous catalysis, electrocatalysis and sensing [56, 57, 164-167]. In heterogeneous catalysis, many authors have shown that gold nanoparticles are active catalysts for reactions such as CO oxidation [3, 168], alcohol [169] and alkene oxidation [170-172]. Similarly, in electrocatalysis, gold-based nanoparticles have been shown to be active for glycerol oxidation [173] and the electrochemical reduction of CO_2 to CO [50, 72]. Furthermore, the addition of gold to platinum nanoparticles improves the stability of these nanoparticles during the oxygen reduction reaction in polymer electrolyte membrane fuel cells [51, 174].

As gold is expensive, it is generally beneficial to utilise the gold in the form of nanoparticles to maximise the specific surface area for catalytic reactions. An additional advantage of this is that gold nanoparticles have unique size-dependent electronic properties as they lose their metallic nature [37, 175-178]. Also, the high fraction of atoms occupying corners and edges of nanoparticles can provide vacant sites for binding reactants and have strained Au-Au bonds, changing the behaviour of gold in catalytic reactions [179, 180].

While gold nanoparticles have many advantages in catalytic processes, like all nanoparticles their small size can also lead to stability issues wherein a loss of specific surface area and their unique size-dependent properties can arise from dissolution and/or nanoparticle growth [181-185]. Of particular relevance is the Gibbs-Thomson effect, which predicts that nanoparticles should be less stable than the bulk material due to the changes in chemical potential brought about by the high curvature of the nanoparticle surface. This has been shown to strongly influence the dissolution of platinum nanoparticles with diameters of 2 nm or less [183]. Others have also shown that the anodic dissolution of platinum nanoparticles is strongly size dependent and follows a different mechanism to bulk platinum [184].

Surprisingly, despite the widespread interest in gold nanoparticle-based electrodes, to the best of our knowledge, there is only one prior study concerned with the electrochemical stability of gold nanoparticles [186]. In this previous paper, it was revealed that the stability of 12 nm gold nanoparticles was similar to bulk gold and that the citrate ligands used in the preparation of the nanoparticles did not prevent the oxidation of the gold. At anodic potentials of 1.37 V vs. SCE or above (in 0.01 M $HClO_4$) gold dissolution took place, and these dissolved gold species could be re-deposited once the potential was reduced, leading to the formation of larger nanoparticles. This anodic dissolution is consistent with previous work on bulk gold which is shown to occur in parallel with gold oxide formation at potentials above ~1.3 V vs. RHE [51, 125, 158, 159, 187]. In addition, this anodic gold dissolution is pH dependent and differs in potentiodynamic versus potentiostatic measurements due to kinetic hindrances caused by the oxide layer that forms [125]. It has also been shown that gold dissolution occurs during the reduction of anodically formed gold oxide [51, 125, 158, 187, 188] and that this can dominate the dissolution process when the anodic potential used to form the oxide is limited to less than 1.6 V vs. RHE [51]. Given the importance of gold oxide formation in the dissolution of gold, the finding that gold nanoparticles may be easier to oxidise than bulk gold [146] will have implications for the electrochemical stability of gold nanoparticles.

The gold dissolution (and redeposition of the dissolved gold species at reducing potentials) which can occur during cyclic voltammetry is frequently used to clean or pre-treat gold electrodes prior to other electrochemical measurements. Gold oxide reduction charge measurements from cyclic voltammetry are also often used to determine the electrochemically active surface area (EASA) [130, 189], with this EASA enabling specific electrocatalytic activity (i.e. activity measurements independent of surface area) to be made. For bulk gold electrodes this pre-treatment approach is well established, however, this pre-treatment is often applied to gold nanoparticle electrodes prior to examining their electrocatalytic activity [56, 57, 127, 146, 190-192]. Given that some gold dissolution will occur during this pre-treatment, it should be expected that changes in the particle size distribution will occur, thus making it difficult to establish structure- or size-based activity relationships based on initial nanoparticle morphology. Furthermore, if cyclic voltammetry is used to determine the EASA of nanoparticle electrodes, it must also be expected that the act of measurement will also alter the EASA itself.

Here, we evaluate the electrochemical stability of gold nanoparticles of various sizes during repetitive potential cycling by analysing changes in EASA together with TEM, XPS and EXAFS analysis to support the conclusions.

3.2 Experimental

Chemicals used include: gold(III) chloride trihydrate (99.9%, Sigma-Aldrich), isopropanol (100%, ASCC), sulfuric acid (ACS grade, Ajax Finechem), Vulcan XC-72R (>99%, Cabot), dichloromethane (ACS grade, Merck), sodium borohydride (95%, BDH Chemicals Ltd.), hydrochloric acid (34-37%, Fisher Scientific), nitric acid (ACS grade,

Merck), hexane (99+%, Sigma-Aldrich), 18.2 MΩ · cm deionized (DI) water (Sartorius Arium 611UV), and dissolved Nafion (LIQUion EW1100, Ion Power, Inc.)

Gold nanoparticle suspensions were produced following methods described by Martin et al. [94] Duff et al. [49] and Weare et al. [91] and atomically precise 0.8 nm Au_9 clusters were prepared by the method described by Wen et al. [193]. According to the methods used, the suspensions should contain gold nanoparticles with average diameters of 3.2 nm, 1.5 nm, 1.4 nm, and 0.8 nm respectively. The as-prepared gold nanoparticles were then adsorbed onto carbon black supports (Vulcan XC-72R) to a loading of 8-15 wt%. The loading (determined by AAS, see Section A1.3.1) was very similar to the targeted loading and all results have been analysed using the actual loading. The particles prepared by the Martin et al. [94] and Duff et al. [49] methods were adsorbed from aqueous suspensions whereas the Weare et al. [91] particles were adsorbed via evaporating a dichloromethane solution, and the Wen et al. [193] particles were deposited by adding hexane to a suspension of carbon support in solution of Au_9 in dichloromethane as outlined by Ovoshchnikov et al. [171]. Electrodes were prepared by ultrasonication of a 4:1 mixture of isopropanol and DI water containing 1.0 mg · mL^{-1} of Au/C electrocatalyst and 0.5 mg · mL^{-1} Nafion followed by spraying this suspension onto graphite foil at 80 °C. This procedure allows controlled formation of electrocatalytic layers with a catalyst loading of 1.2 ± 0.25 mg · cm^{-2} and a Nafion content of 33 wt%. The sprayed electrodes were uniform across their surface when viewed under an optical microscope at 600x magnification.

The electrodes were fitted to an electrochemical cell consisting of a Pt/Ir wire (area ca. 1.1 cm^2) counter electrode and a Ag/AgCl, saturated KCl reference electrode. All potentials have been converted to the RHE scale according to Equation 3-1 unless otherwise stated. The 0.5 M H_2SO_4 electrolyte was deaerated with argon (99.999% purity) for at least 10 minutes prior to the measurements. The cyclic voltammetry scanning sequence scanning between 0.21 and 1.56 V vs. RHE (0.0 and 1.35 V vs. Ag/AgCl) at 50 mV · s^{-1} commenced after the electrode was exposed to the electrolyte for 10 minutes while being maintained at the open circuit potential. A Gamry Reference 600 potentiostat was used throughout this study. To rule out the possibility that traces of Cl^- from the reference electrode influenced the electrochemical behaviour of the gold nanoparticles, cyclic voltammograms were also conducted using a reversible hydrogen reference electrode (Hydroflex, Gaskatel GmbH) and no significant differences were observed.

$$E_{RHE} = E_{Ag/AgCl} + E° + 0.0591pH \qquad 3\text{-}1$$

Particle size analysis was conducted using transmission electron microscopy (TEM) utilising a Philips CM200, operating at 200 kV. Samples were prepared by depositing and drying a drop of a dilute suspension of the electrocatalyst onto lacey carbon grids. Particle size distributions were measured by counting particles on multiple images obtained at the same magnification using the ImageJ software package (See Section A2.2 for the full analysis method).

X-ray absorption spectroscopy (XAS) was used to determine coordination number and bond lengths of fresh and aged catalysts. XAS measurements were performed on the XAS beamline (12-ID) at the Australian Synchrotron in fluorescence mode at the Au L_3 (11.919 keV) edge. All spectra were recorded at ambient temperature using a solid state 100-element Ge detector. A gold reference foil was measured simultaneously with the samples of interest. XAS data processing and analysis were performed following standard methods [194] utilising the IFEFFIT software package for the analysis [153, 195].

X-ray photoelectron spectroscopy (XPS) was performed using a Kratos Axis UltraDLD at a pressure of 1×10^{-9} torr with monochromatic Al Ka X-rays (1486.69 eV). A survey scan was performed on both fresh and electrochemically cycled samples with a pass energy of 160 eV, along with scans at the C 1s, P 2p, and Au 4f energy ranges with a pass energy of 20 eV. Survey, C 1s and P 2p scans had an acquisition time of 30 min each while Au 4f scans had an acquisition time of 40 min each. The binding energy in all data was referenced to the C 1s peak (284.6 eV), although there was little evidence of charging effects.

3.3 Results and discussion

3.3.1 Initial Particle Size of Gold Nanoparticles

The gold nanoparticle size in the as-prepared electrocatalysts was determined by TEM (Figure 3-1, Figure 3-2 and Table 3-1). As expected for the electrocatalysts prepared from the Au_9 clusters, very few nanoparticles could be observed, suggesting that the majority of the gold nanoparticles within this sample were too small to be imaged by TEM (i.e. less than ~1 nm). This is consistent with the theoretical size of the Au_9 clusters (~0.8 nm) [193] and our earlier TEM studies of support-immobilized Au_9 [169-171] and is supported by XPS analysis (shown later). The average gold nanoparticle diameters in the electrocatalysts prepared using other gold nanoparticles were larger than expected based on literature values given for the unsupported gold nanoparticles, indicating that some gold nanoparticle sintering occurs during deposition of gold nanoparticles onto the carbon support. For the purpose of clarity in this paper, the electrocatalysts samples will be referred to by the number-weighted average diameter of the as-prepared supported gold nanoparticles determined by TEM; i.e. 4.5 nm Au, 3.1 nm Au, and 2.9 nm Au respectively. Since we were unable to image the Au_9 nanoparticles, these will be referred to by their size as determined by Wen et al. [193]; i.e. 0.8 nm Au.

While we will refer to the samples by their initial number weighted average diameters, it should be noted that all samples have a distribution of particle sizes (Figure 3-2), and in particular the 4.5 nm Au sample has a very broad particle size distribution (PSD). To highlight this, in Table 3-1, we also report the specific surface area-weighted average particle size as well as the specific surface area calculated from the complete PSD.

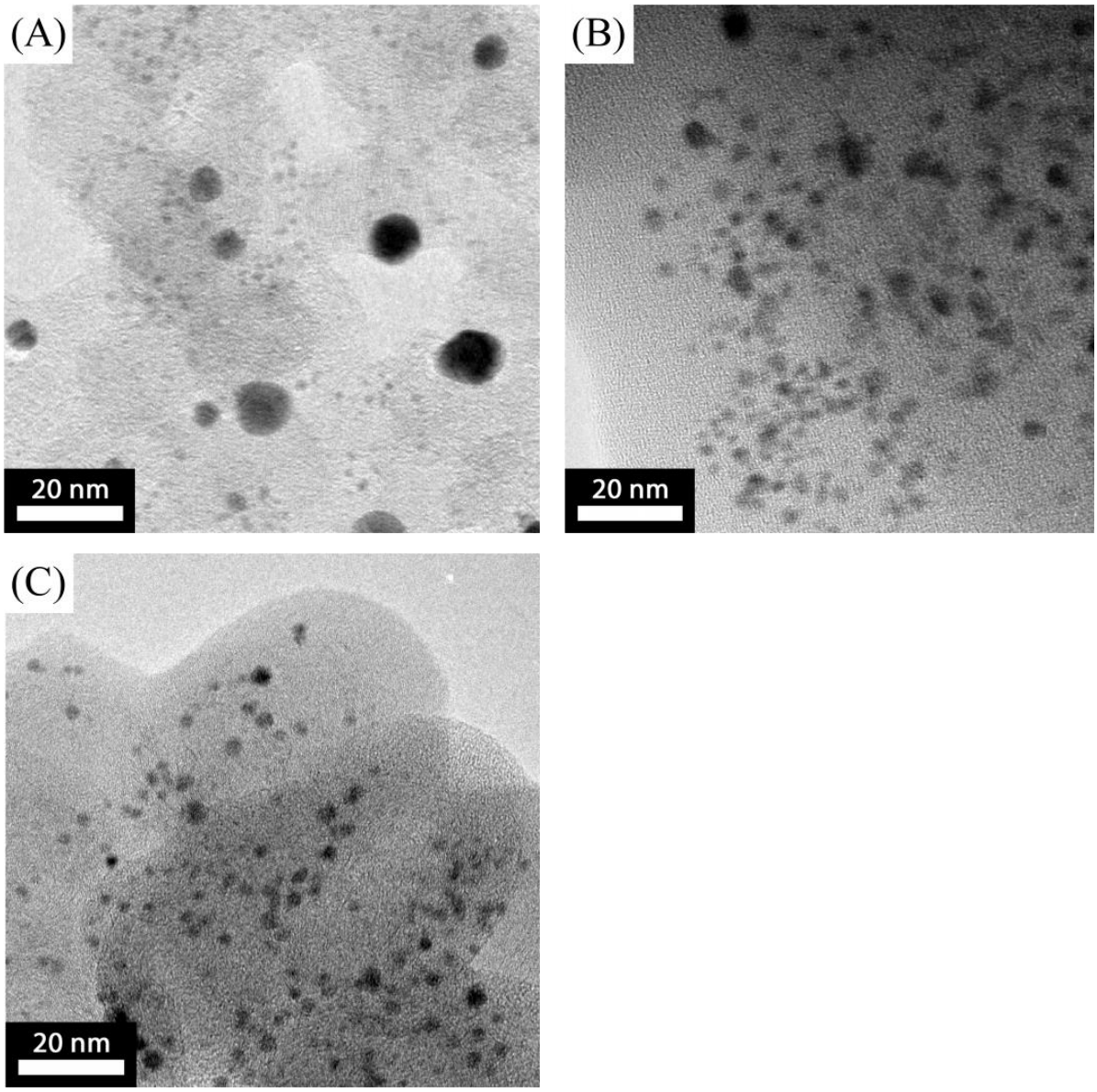

Figure 3-1. Representative TEM images of as-prepared Au/C electrocatalysts: 4.5 nm Au (A), 3.1 nm Au (B) and 2.9 nm Au (C).

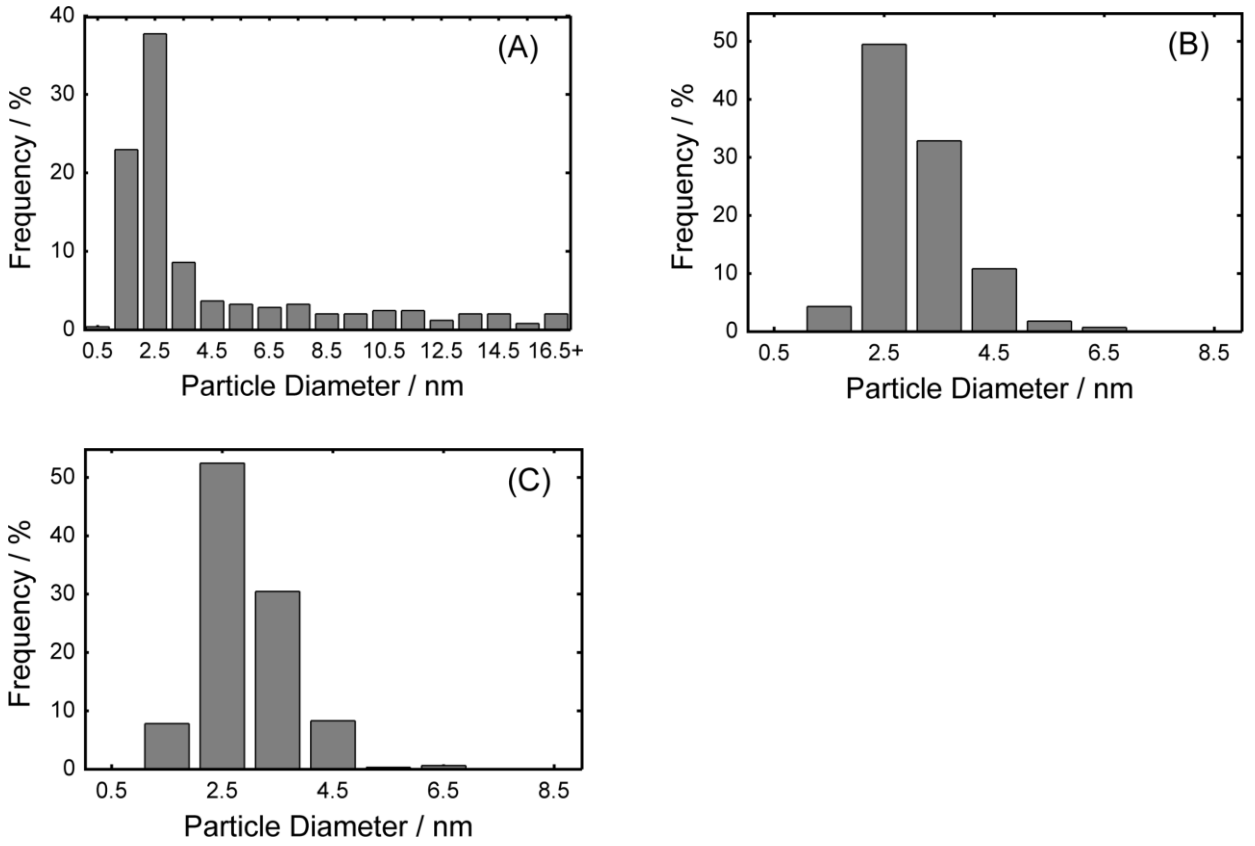

Figure 3-2. Particle size distribution of the as-prepared Au/C electrocatalysts based on analysis of TEM images (at least 240 particles had been measured per sample): 4.5 nm Au (A), 3.1 nm Au (B) and 2.9 nm Au (C).

Table 3-1. TEM-based particle size and specific surface area.

Sample	4.5 nm Au	3.1 nm Au	2.9 nm Au
Number weighted average diameter / nm	4.5	3.1	2.9
Std. Dev. of particle diameter / nm	3.9	0.8	0.8
S.S.A. weighted average diameter / nm	11.3	3.6	3.4
Specific surface area† / $m^2 \cdot g^{-1}$	27.5	86.6	91.4
Number of particles counted	244	277	614
Number of images used	8	7	14
Ligand in synthesis method	BH_4^-	$[P(CH_2OH)_4]^+$	$P(C_6H_5)_3$
Gold NP synthesis method	[94]	[49]	[91]

†The specific surface area (S.S.A.) calculated from the entire PSD using following equation: $.S.A. = \frac{\sum_{i=1}^{n} \pi D_i^2}{\sum_{i=1}^{n} \rho \frac{1}{6} \pi D_i^3}$, where D is the particle diameter, n is the number of particles with this specific diameter, and ρ is the particle density.

Importantly, TEM analysis of the supported nanoparticles after the preparation of the electrocatalytic layer (the electrocatalytic layer was removed from the graphite foil by ultrasonication in IPA) showed very similar particle size distributions to the as-made electrocatalysts, indicating that the electrode layer preparation technique used here does not significantly alter the size of the gold nanoparticles.

3.3.2 Redox Behaviour of Carbon-Supported Gold Nanoparticles

Cyclic voltammetry of the electrocatalytic layers reveals that the 4.5 nm Au, 3.1 nm Au, and 2.9 nm Au electrocatalysts exhibited behaviour typical for gold (Figure 3-3). For these materials, a cathodic peak between 1.0-1.2 V vs. RHE, corresponding to gold oxide reduction, is seen on all voltammograms and in some cases, the anodic formation of the gold oxide is observed at potentials above 1.4 V vs. RHE. We also observe a set of redox peaks around 0.4 – 0.6 V vs. RHE which we attribute to the redox active species on the surface of the carbon support material [163]. The potentials of the gold oxide formation and reduction are consistent with the redox behaviour of bulk gold in acidic electrolytes [130, 196]. Generally, we find that the characteristic shape of the gold voltammograms become more defined with time during repetitive cyclic voltammetry which might be related to either surface cleaning or reconstruction of the nanoparticles to more stable geometries. Given the importance of gold oxide in the anodic dissolution of gold and reductive dissolution via gold oxide, it is unfortunate that clear differences in the voltammograms are not observed which could help in understanding the differences in electrochemical stability of these nanoparticles (Section 2.3). Of particular interest is the gold particle size-dependence of the gold oxide formation, especially considering that others have shown that nanoparticles differ from bulk gold in this respect [146]. It is known that OH^- adsorption must compete with strongly adsorbed anions during the initial stages of anodic oxide formation on bulk gold and that this process depends on the type of the exposed crystal face [128, 196], which is a significant factor considering the size-dependence of crystal face stability [197]. In all cases, we find no evidence of the anodic process related to the adsorption of OH^- and O species to anion free surfaces [128] which were recently identified on 40 nm Au nanoparticles [146].

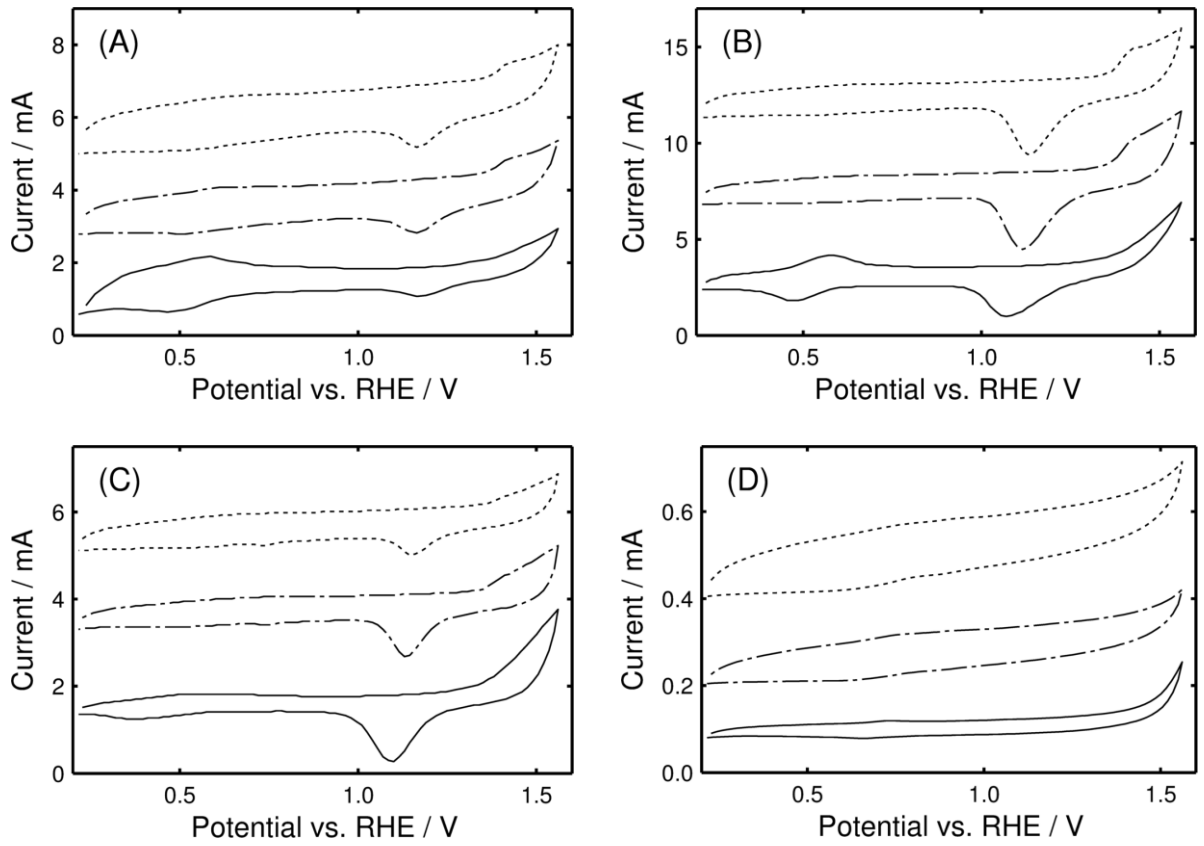

Figure 3-3. Cyclic voltammograms of the Au/C electrocatalysts CV scanned in 0.5 M H_2SO_4 between 0.21 V vs. RHE and 1.56 V vs. RHE at a scan rate of 50 $mV \cdot s^{-1}$: 4.5 nm Au (A), 3.1 nm Au (B), 2.9 nm Au (C), and 0.8 nm Au (D). Solid line - 2nd cycle, dashed line - 50th cycle, and dotted line - 100th cycle. Note that cycles are offset for clarity purposes and that the current has not been normalised due to the lack of TEM-based surface area measurements for the 0.8 nm Au sample.

Surprisingly, given the expected large fraction of exposed gold surface atoms on the 0.8 nm Au electrocatalyst (prepared from the atomically precise Au_9 clusters), no evidence of gold-like voltammetric behaviour is observed. Indeed, based on the crystal structure of Au_9 [176] one could, in principle, expect 100% of the gold atoms to be available for the gold/gold oxide redox reaction. The absence of such a pronounced gold oxide reduction peak may indicate that the 0.8 nm Au particles are either not easily electrochemically oxidised or, once oxidised, are very difficult to reduce. In either way, they behave quite differently to metallic, bulk-like gold species which is not surprising given previous work that revealed that Au_9 clusters have "a molecule-like HOMO-LUMO band gap" [193]. Given that the properties of small gold clusters are known to differ considerably from bulk gold [164], it seems likely that the smallest gold particles could have a much-reduced propensity to exhibit the normal gold/gold oxide redox behaviour. Others have suggested that the oxidation behaviour of gold nanoparticles differs from bulk gold [146, 198] and that the gold/gold oxide redox process becomes less reversible as the nanoparticle size decreases [105]. It has also been noted that the EASA and surface area calculated based on TEM data differ considerably as the nanoparticle size decreases [56]. Possibly related to these observations, the underpotential deposition of metals (commonly used to probe the surface

of gold electrodes) can be completely inhibited on small gold nanoparticles [82, 199, 200], and others have also suggested that underpotential deposition of hydrogen on very small Pt nanoparticles (<1.5 nm) can significantly underestimate the active surface area [149]. An alternative explanation for the apparent lack of gold redox behaviour could be that these small clusters are located within the pores of the Vulcan XC-72R carbon support [201] which are inaccessible to the electrolyte. While it is likely that some portion of the nanoparticles within the electrocatalytic layer are inaccessible to the electrolyte, we note that the ligand shell protecting the 0.8 nm Au clusters is on the order of 2 nm in diameter which should limit the adsorption of these clusters to pores of >2 nm and thus most of 0.8 nm Au species should be easily accessible to protons and water molecules.

It is possible that the phosphine ligands bound to 0.8 nm Au may inhibit gold oxide formation, although the 2.9 nm Au nanoparticles were also synthesised with the same ligands and these do exhibit the gold/gold oxide redox behaviour. However, the binding strength of the phosphine ligands to the smaller 0.8 nm Au clusters could be quite different to the 2.9 nm Au particles and thus it is still possible that these ligands inhibit the gold/gold oxide redox at the 0.8 nm Au clusters. XPS did show the presence of phosphorus for the 0.8 nm Au clusters but not in the 2.9 nm Au data, although EXAFS analysis suggested evidence of Au-P bonds in the as-prepared 2.9 nm Au samples, and that these are lost after 5 voltammetry cycles. Thus we conclude that it is likely that any inhibiting effect of the phosphine ligands is only applicable when considering the behaviour of the 0.8 nm Au sample or in the first few cycles for the 2.9 nm Au samples.

While it is clear that the apparent discrepancy between the high fraction of surface atoms and exceptionally low gold redox activity warrants further investigation, for the purposes of this work, investigation of the stability of the 0.8 nm Au material is shown via TEM and XPS analysis.

Interestingly, the 2.9 nm Au and 3.1 nm Au electrocatalysts, which have very similar particle size distributions, exhibit almost the same gold/gold oxide redox behaviour, despite the differences in the ligands used to stabilise the gold nanoparticles during the synthesis procedure (i.e. tetrakis(hydroxymethyl) phosphonium for 3.1 nm Au and triphenylphosphine for 2.9 nm Au). This further suggests the ligands from the surface of the 2.9 nm Au and 3.1 nm Au are lost during the deposition of the gold nanoparticles to the carbon support, lost within the first few potential cycles, or have minimal effect of the gold/gold oxide redox behaviour if present.

3.3.3 Repetitive Cyclic Voltammetry of Carbon-Supported Gold Nanoparticles

To assess the stability of the carbon supported 4.5 nm Au, 3.1 nm Au, and 2.9 nm Au nanoparticles, the charge associated with the cathodic reduction of gold oxide was determined as the electrodes were continuously cycled between 0.21 and 1.56 V vs. RHE at a scan rate of 50 $mV \cdot s^{-1}$ (Figure 3-4). Here the upper potential limit has been selected to minimise the anodic dissolution of the gold nanoparticles while permitting the gold/gold oxide redox behaviour to occur in order to facilitate gold oxide reduction charge

measurements. While 12 nm gold nanoparticles have been shown to dissolve at 1.51 V vs. RHE or above (measurements at 1.46 V vs. RHE showed no dissolution) [186], bulk gold dissolution is reported to occur above approximately 1.3-1.4 V vs. RHE [51, 125, 158, 159, 187] and thus some gold dissolution during cyclic voltammetry scans between 0.21 and 1.56 V vs. RHE should be expected. Furthermore, it is likely that the potential at which the dissolution of gold nanoparticles commences will be size-dependant as per the Gibbs-Thomson effect. In most cases, when using the gold oxide reduction charge for EASA determination, the anodic limit is selected to be the Burshtein minimum just prior to oxygen evolution potential (~1.65 V vs. RHE) [202] where complete oxide coverage is expected. While this is acceptable for bulk gold electrodes which have been pre-treated at these high anodic potentials, such a high anodic potential should be expected to dramatically alter gold nanoparticle morphologies and particle size distributions. Thus, a compromise between minimal gold dissolution and sufficient gold oxide formation for EASA measurements was used as a basis for selecting the anodic limit to investigate the stability of these nanoparticles during repetitive cyclic voltammetry.

Overall, the oxide reduction charge of the 4.5 nm Au, 3.1 nm Au, and 2.9 nm Au nanoparticles show qualitatively similar behaviour, with an initial period of increase, then either a constant plateau (Figure 3-4A) or a slow decrease (Figure 3-4B and Figure 3-4C). The uncertainties presented in the charge analysis reflect those introduced by the uncertainties in the loading of the electrocatalyst on the electrode and are consistent with literature reports where multiple electrodes have been examined [104, 105, 203, 204]. It should be noted that the potential of the gold oxide reduction during the repetitive cycling sequence does not show the same trend as the reduction charge, with the peak potential either staying constant or slowly increasing over the entire cycling sequence (Figure 3-5). Again it was found that the 3.1 nm Au and 2.9 nm Au electrocatalysts have very similar behaviour despite the differences in the ligands used to stabilise the initial gold nanoparticles used to prepare these electrocatalysts.

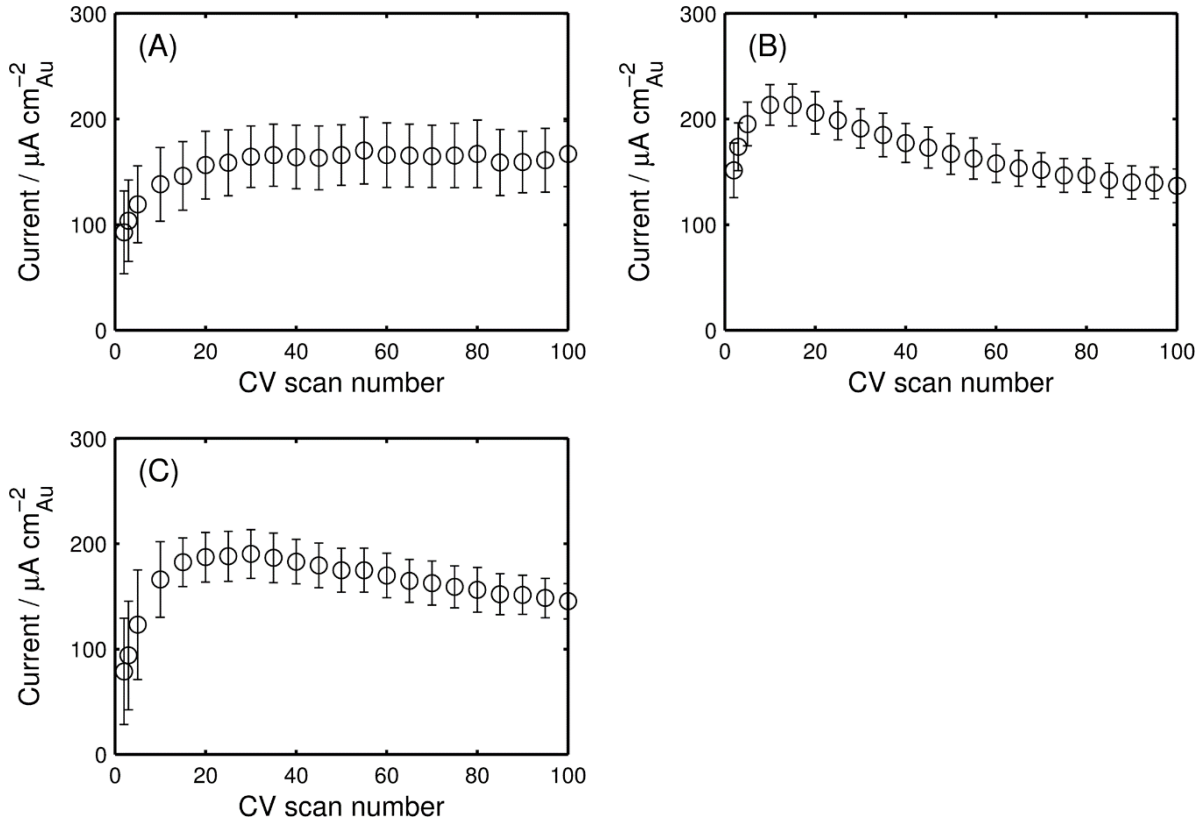

Figure 3-4. Gold oxide reduction peak charge measurements for 4.5 nm Au (A), 3.1 nm Au (B) and 2.9 nm Au (C). Each figure represents averaged data obtained using six different electrodes. Uncertainty bars represent a 95% confidence interval.

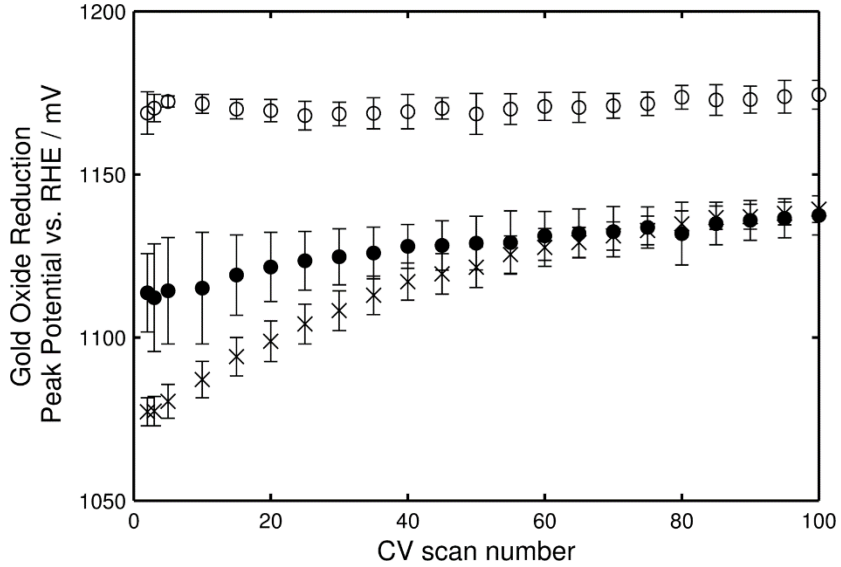

Figure 3-5. Gold oxide reduction peak potential measurements during electrochemical cycling. 4.5 nm Au (○), 3.1 nm Au (×) and 2.9 nm Au (●). Uncertainty bars represent 95% confidence interval.

The initial increase in the oxide reduction charge over the first 10-25 cycles suggests that an increase in the EASA occurs. We can rule out that this increase is due to the formation of smaller particles based on our EXAFS results (discussed in Section 3.3.4) and based on the gold oxide reduction peak not shifting to lower potentials [160]. Instead, we attribute the increase in EASA to the removal of ligands stabilising the gold nanoparticles, organic containments from the surface of gold particles within electrocatalytic layer [191], or improved accessibility of the gold surface due to either improvement in electrolyte contact and/or the restructuring of the gold nanoparticle surface. Unlike the electrochemical desorption of thiols from gold [205], no evidence for electron transfer mediated ligand removal is observed by cyclic voltammetry, although any anodic current associated with ligand removal could be masked by the capacitive current from the carbon support or the gold/gold oxide redox current. As the EXAFS data (discussed in Section 3.3.4) for 2.9 nm Au shows that Au-P bonds initially present in the sample are lost within the first 5 voltammetry cycles, ligand loss is a reasonable explanation for at least some of the increase in the observed gold oxide reduction charge over the first 10-25 cycles.

To assess whether the initial charge increase can be explained by an increase in gold-electrolyte contact, an electrocatalytic layer was maintained at open circuit potential for 6 hours to ensure complete wetting of the layer prior to the repetitive potential cycling sequence. In this case, almost no increase in charge was observed over the first few cycles (Figure 3-6) and thus we conclude that the majority of the initial increase (during cycle 1-20 in Figure 3-4) is due to improved electrolyte penetration within the electrocatalytic layer. As improved layer wettability should not influence the gold oxide reduction potential, the observation that the reduction peak potential is not correlated with the oxide reduction charge over the initial cycles is consistent with improved contact between gold surface and electrolyte.

While it appears that the increase in EASA over the initial cycles is largely due to improved wettability of the electrocatalytic layer, it is also possible that the surface restructuring of gold nanoparticles could increase the measured oxide reduction charge. As small gold nanoparticles are often dominated by Au(110) facets [56, 206], the rearrangement to more stable icosahedrons [207], terminated by Au(111) facets, would result in a small increase in the gold oxide reduction charge as the theoretical charge for the Au (110) and Au(111) surfaces are reported to be 272 and 444 mC cm^{-2} respectively [128].

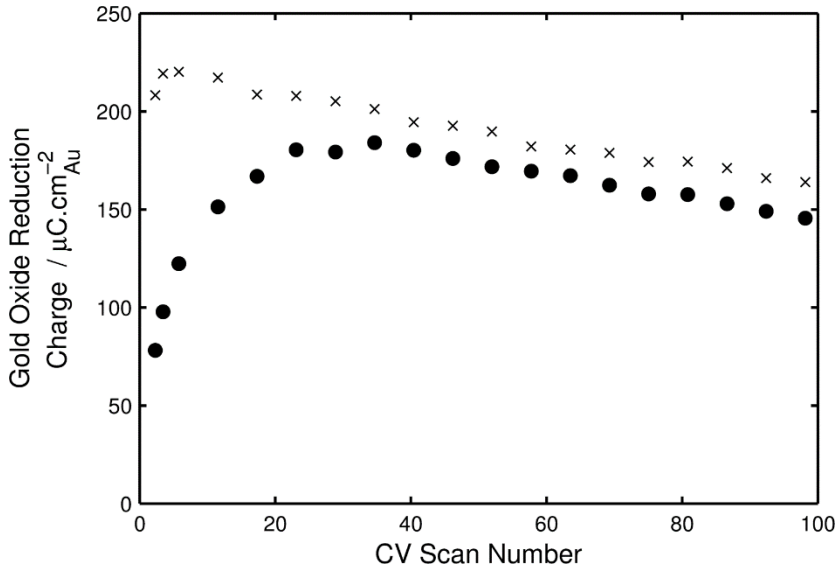

Figure 3-6. Gold oxide reduction charge measured during cyclic voltammetry for 3.1 nm Au. A typical data set measured after 10 minutes at OCP (•), the gold oxide reduction charge measurements after the electrode was maintained at OCP for 6 hours prior to the cyclic voltammetry (×).

After the initial increase in gold oxide reduction charge, the 2.9 nm Au and 3.1 nm Au electrocatalysts reach a similar maximum charge of around 190-210 $mC \cdot cm^{-2}_{Au}$, as expected from their similar surface areas calculated using the particle size distributions determined using TEM (Table 3-1). While the 4.5 nm Au electrocatalyst has only 30-32% of the theoretically available surface area compared to the 2.9 nm Au and 3.1 nm Au electrocatalysts (27.5 $m^2 \cdot g^{-1}$ c.f. 91.4 $m^2 \cdot g^{-1}$ and 86.6 $m^2 \cdot g^{-1}$, respectively), the 4.5 nm Au has a maximum charge of 170 $mC \cdot cm^{-2}_{Au}$, (Figure 3-4) suggesting that for these gold nanoparticles the measured charge is indeed proportional to EASA rather than edge/facial ratios as described in Section 2.4.

For both the 2.9 nm Au and 3.1 nm Au electrocatalysts, after 10 – 25 cycles, the measured gold oxide reduction charge decreases at an almost constant rate over the first 100 cycles, and this decrease continues to occur at a slower rate for at least 750 cycles (Figure 3-7). Generally, the loss of activity or specific surface area of electrocatalytic nanoparticles is associated with either the dissolution of metal from smaller particles and deposition back onto larger particles (i.e. Ostwald ripening), the sintering of neighbouring particles due to their mobility on the support [183, 185] or dissolution of the metal into the electrolyte without the subsequent deposition [183]. It is also possible that oxidation of the carbon support could lead to loss of the EASA via changes to the gold nanoparticle contact with the support, loss of electrically conductive pathways through the electrocatalytic layer [185], or even poisoning of the gold surface by oxidation products of the carbonaceous support.

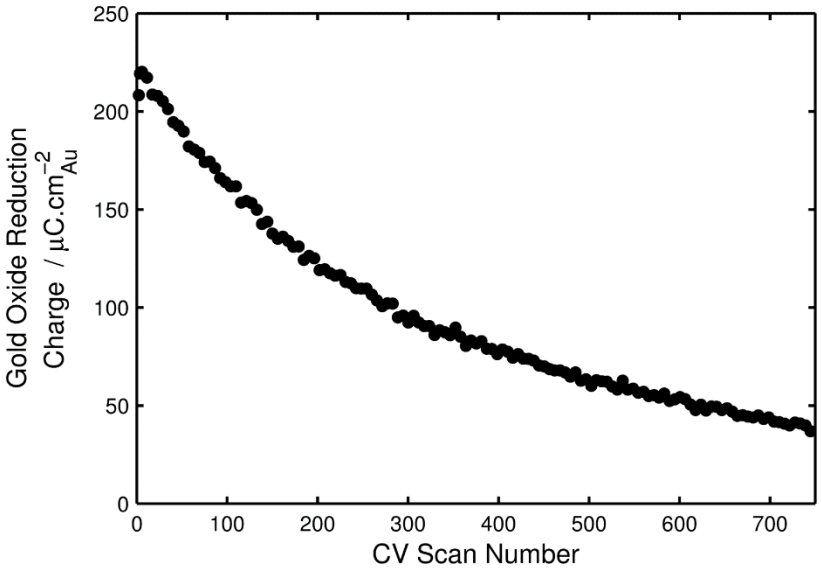

Figure 3-7. Long-term stability of the gold oxide reduction peak charge for 3.1 nm Au

As the gold oxide reduction charge reflects the EASA, the very clear decrease in the measured reduction charge suggests that either significant growth of gold nanoparticles occurs in these samples or that a fraction of the gold is lost from the electrocatalytic layer via dissolution or nanoparticle detachment. Atomic absorption spectroscopy confirmed that a small fraction of gold is indeed lost to the electrolyte via dissolution or detachment (approx. 3 % for 0.8 nm Au and 6 % for 3.1 nm Au after 100 cycles), and as the anodic limit of the cyclic voltammetry was less than 1.6 V vs. RHE, it is likely that the majority of this dissolved gold has been lost from the gold nanoparticles during the reduction of gold oxide [51]. As this dissolved gold would need to diffuse from the porous electrocatalytic layer, it is likely that much more gold was dissolved from the nanoparticles but was redeposited on remaining gold nanoparticles or the carbon support while the electrode was at more cathodic potentials than the gold oxide reduction potential, leading to changes in the particle size distribution (Section 3.3.4). While some gold is lost from the electrocatalytic layer, the decrease in the EASA is much greater than that predicted based on only a dissolution mechanism, suggesting that particle growth (via sintering or Ostwald ripening) is the largest contributor to the loss in EASA. A particle growth mechanism is also consistent with the finding that the loss in EASA for the 2.9 nm Au and 3.1 nm Au samples is accompanied by an increase in the potential of the oxide reduction peak [56].

Importantly the changes in EASA and gold reduction potential differ for the 4.5 nm Au electrocatalyst, where the gold oxide reduction charge and potential are constant after the initial 25 cycles, implying that these larger gold nanoparticles resist growth, or more correctly, that the EASA of this sample is largely unaffected by the repetitive potential cycling.

To confirm that the decrease in the EASA largely occurs in the potential range associated with the gold/gold oxide redox process, further experiments were performed

wherein the upper potential of the cyclic voltammetry scan range was limited to avoid gold oxide formation. In these measurements, the 3.1 nm Au sample was initially subjected to cyclic voltammetry scans between 0.21 and 1.56 V vs. RHE for 25 cycles to ensure ligand removal and complete electrolyte penetration of the electrocatalytic layer. Following this, a sequence of 20 cycles betweem 0.21-1.31 V vs. RHE and 5 cycles between 0.21-1.56 V vs. RHE was repeated 5 times. The block of 5 cycles up to the anodic limit of 1.56 V vs. RHE was used to enable gold oxide reduction measurements. The results reveal that the oxide reduction charge over these cycles (i.e. cycles 25-145) is almost completely stable which confirms the proposal that the nanoparticle instability is largely caused by dissolution and particle growth at the gold/gold oxide redox potentials (Figure 3-8). Once repetitive potential cycling between 0.21 and 1.56 V vs. RHE recommenced (i.e. cycles 146-200), the characteristic decrease in the gold oxide reduction charge is again observed, with the rate of decrease almost identical to the standard case.

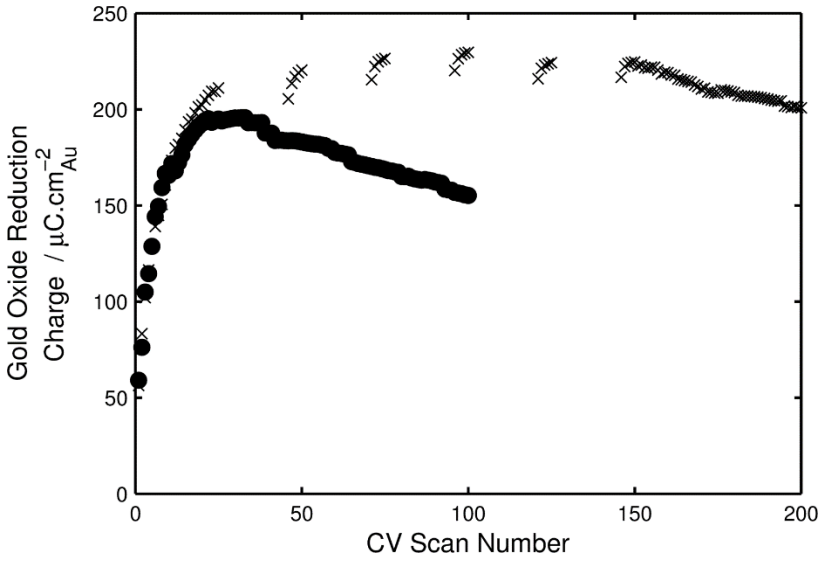

Figure 3-8. Gold oxide reduction charge measured during cyclic voltammetry. A typical data set for 3.1 nm Au where all voltammograms used the upper anodic limit of 1.56 V vs. RHE (•), 3.1 nm Au where voltammetry cycles 26-45, 51-70, 76-95, 101-120, and 126-145 had an upper anodic limit of 1.31 V vs. RHE to avoid the gold oxide formation potentials (×). The charge data in (×) is reported on for cycles 1-25, 46-50, 71-75, 96-100, 121-125 and 146-200 where the upper anodic limit of 1.56 V vs. RHE was used in order to enable gold oxide reduction charge measurement.

The results described above clearly indicate that during repetitive cyclic voltammetry, small gold nanoparticles are not stable in acidic electrolytes if the upper potential limit is above the gold oxide formation potential. This has several implications. First, it is clear that in applications where small gold nanoparticles experience anodic potentials high enough for gold oxide formation, instability could significantly hamper the long-term use of these nanoparticles. In many applications (e.g. electrochemical CO_2 reduction, electrochemical glycerol oxidation) the potentials should be low enough to avoid this instability, but in others (e.g. PEM fuel cell cathodes during start-up or shut-down [208]) it is very likely that loss of the electrochemically active surface area will occur. However, in cases where gold is used in alloy nanoparticles, the stability could well be different as

discussed elsewhere [51]. Second, the use of cyclic voltammetry to pre-treat and determine the EASA of gold nanoparticles must be used with caution due to the possibility of nanoparticle dissolution and growth. Recently others have also questioned the use of voltammetry to pre-treat gold nanoparticles, especially if the pre-treatment procedure is based on bulk gold behaviour [146]. As this pre-treatment and EASA is normally conducted prior to other electrochemical measurements, if the nanoparticle morphology and specific surface area are used to elucidate structure or size based activity measurement, it is suggested that some consideration of the nanoparticle stability should be made.

To confirm and support these conclusions regarding particle growth made on the basis of cyclic voltammetry, TEM, XAS and XPS analysis was performed on the electrocatalysts after electrochemical cycling.

3.3.4 Structure and Size of Carbon-Supported Gold Nanoparticles after Potential Cycling

TEM analysis strongly supports the hypothesis that repetitive potential cycling of the 2.9 nm Au and 3.1 nm Au electrocatalysts leads to nanoparticle growth (Figure 3-10 and Figure 3-9). In addition to the growth of the 2.9 nm Au and 3.1 nm Au electrocatalysts, the 0.8 nm Au electrocatalyst also showed evidence of growth as gold particles could be successfully imaged after 100 CV cycles.

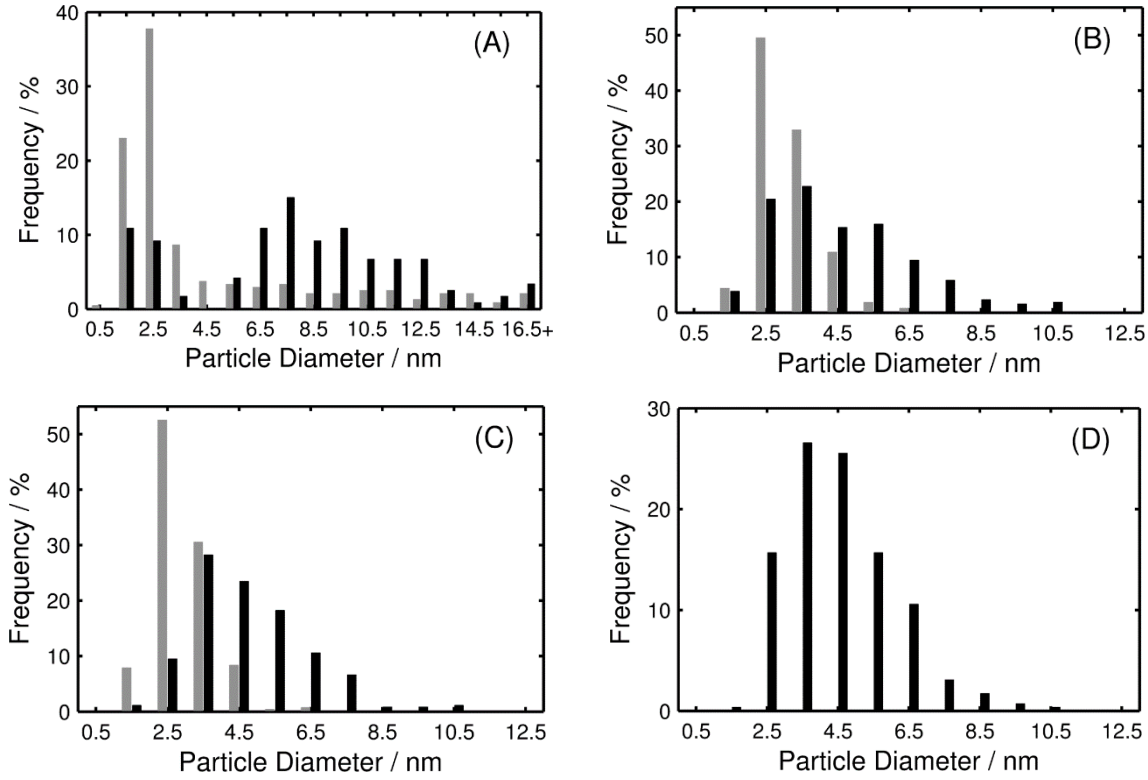

Figure 3-9. Particle size distribution of 4.5 nm Au (A), 3.1 nm Au (B), 2.9 nm Au (C), and 0.8 nm Au (D). As prepared sample particle size distributions are shown in grey and particle size distributions of samples after 100 cycles are shown in black.

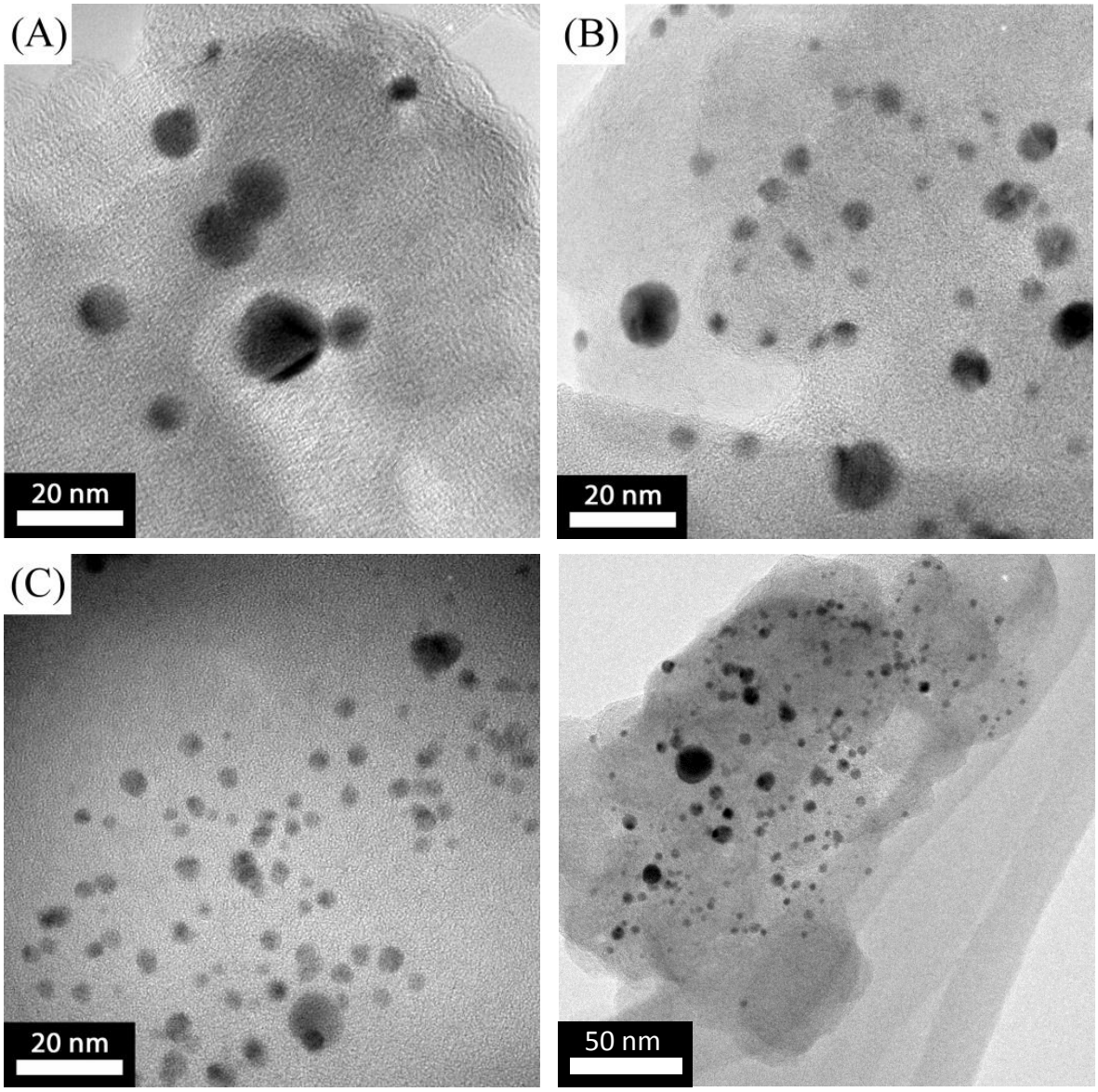

Figure 3-10. Representative TEM images of Au/C electrocatalysts after 100 cycles between 0.21 and 1.56 V vs. RHE at 50 mV· s^{-1} in 0.5 M H_2SO_4. 4.5 nm Au (A), 3.1 nm Au (B), 2.9 nm Au (C) and 0.8 nm Au (D).

Table 3-2. TEM-based particle size and specific surface area of Au/C electrocatalysts after 100 cycles between 0.21 and 1.56 V vs. RHE at 50 mV· s^{-1}.

Sample	4.5 nm Au	3.1 nm Au	2.9 nm Au	0.8 nm Au
Number weighted average diameter (nm)	8.2	4.6	4.7	4.5
Std. Dev. of particle diameter / nm	4.7	2.2	1.8	1.8
S.S.A. weighted average diameter / nm	11.3	6.8	5.9	5.6
Specific surface area / $m^2 \cdot g^{-1}$	27.5	45.8	53.1	55.9
Number of particles counted	116	661	380	294
Number of images used	17	24	13	2

In support of the overall stability of the 4.5 nm Au electrocatalysts EASA, while the TEM analysis post cycling certainly indicates that particle growth occurs, no change in specific surface area is observed in this material (Table 3-2) due to the fact that the specific surface area is heavily weighted by particles with larger diameter within the distribution. This observation highlights the importance of using the entire particle size distribution to calculate the surface area of the electrocatalysts rather than only the average particle size (equation for S.S.A. determination based on TEM data is shown in the notes of Table 3-1).

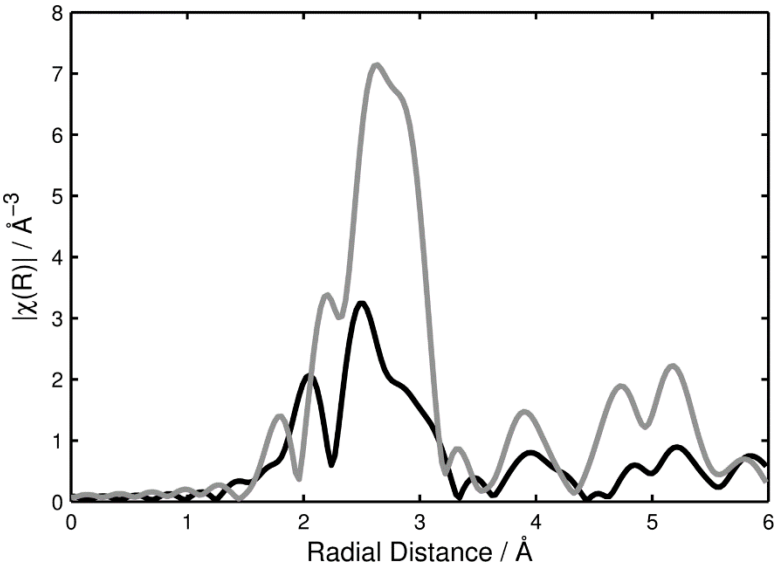

Figure 3-11. EXAFS R-space spectra for as-prepared (black line) and aged (grey line) 2.9 nm Au electrocatalyst.

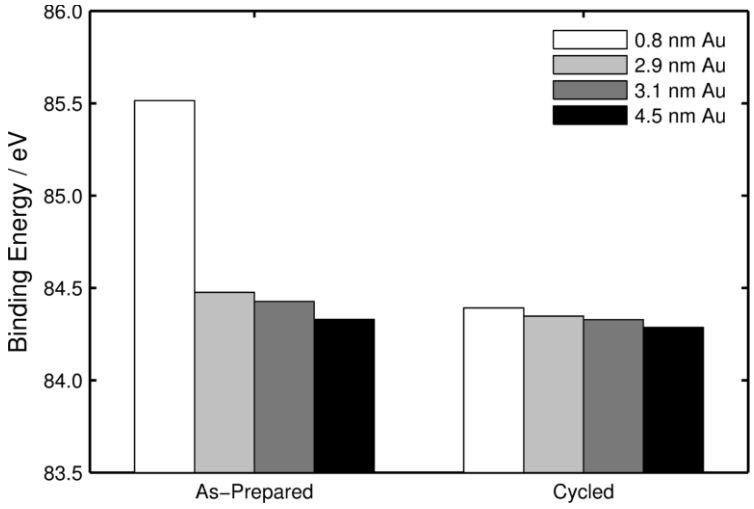

Figure 3-12. Au $4f_{7/2}$ peak binding energies for as-prepared electrodes and those after 100 cycles.

EXAFS was performed on the fresh and cycled 2.9 nm Au, 3.1 nm Au and 4.5 nm Au samples. All measurements were made in fluorescence mode at the Au L_3 edge (11.919 keV) at ambient temperature. The first three shell single scattering path approximations were fitted in the R-space, calculated with a k-weighting of 3 using the IFEFFIT software package [153, 195]. An amplitude reduction factor (S_0^2) of 0.799, calculated from a gold reference foil, was used for all subsequent fits. Across the scattering paths within each data set, the S_0^2 and threshold energy (E_0) were kept constant, while the variation in atomic bond length and the Debye-Waller factor were allowed to vary for each path. The results of this analysis show that all samples have a Au-Au bond length smaller than that of the gold reference foil (Table 3-3) as expected for gold nanoparticles of this size and consistent with the particle size–bond length trend described elsewhere (reference [30] and Figure 2-5).

It is worth noting that the freshly prepared 2.9 nm Au had an additional peak in the R-space transformed data at a radius of approximately 2.1 nm (Figure 3-11, black line). This is similar to the expected Au-P bond length (i.e. from the surface bound phosphine ligands) and may be the cause of an unexpectedly low gold coordination number calculated for the sample. However, XPS analysis (discussed later) of this sample did not detect any phosphorus in the as-prepared electrocatalyst. The apparent inconsistency between these two measurements could be related to the fact that the EXAFS data comes from the entire thickness of the electrocatalytic layer whereas the XPS data is only from the outermost surface of the layer or that the phosphine ligands can be lost from the sample under the UHV conditions of the XPS. In previous work, no phosphorus was observed in the XPS of Au nanoparticles using the same synthesis method as used for the 2.9 nm Au sample, which could confirm that the phosphine ligands can be lost under UHV conditions [176, 209]. Regardless of this, after the 5th voltammetry cycle, this EXAFS peak was no longer found, suggesting that the phosphine ligands are removed during cycling, which would contribute to the increase in the gold oxide reduction charge over the first few voltammetry cycles. For the 2.9 nm Au nanoparticle sample, the coordination number significantly increased with increasing CV cycles (Table 3-3) which again is consistent with particle growth during the electrochemical ageing. The other two nanoparticle samples, 3.1 nm Au and 4.5 nm Au, show a small increase in coordination number although these changes fall within the measurement uncertainties.

In-situ XANES was attempted to investigate the growth of the particles during the electrochemical cycling–with particular emphasis on the role gold oxide has on the ageing process. While the gold oxide white line was identifiable in the spectra for potentials >1.2 V vs. RHE, the signal to noise ratio was insufficient to quantify how much gold oxide was formed or whether part of this signal came from soluble gold associated with gold dissolution.

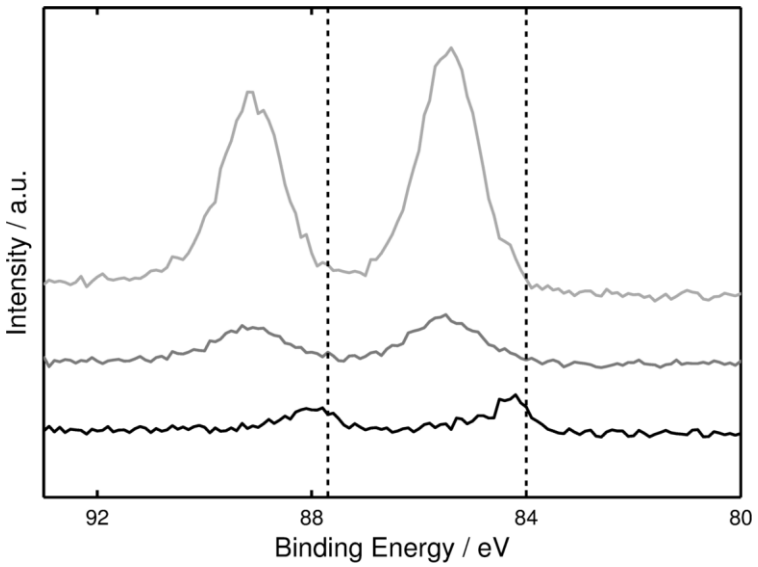

Figure 3-13. XP Au $4f_{7/2}$ spectra of the 0.8 nm Au electrodes. An as-prepared electrode (light grey line), an electrode exposed to 0.5 M H_2SO_4 for 10 minutes (dark grey line), and an electrode after 100 cyclic voltammetry cycles (black line). Vertical lines represent bulk gold binding energy for Au $4f_{7/2}$ (84.0 eV) and Au $4f_{5/2}$ (87.7 eV).

Table 3-3. EXAFS calculated coordination number, bond length and contraction of fresh and cycled particles.

Sample	# of CV cycles	Average coordination number	Bond length / nm	Bond length contraction / %
Gold Foil	-	12.5 ± 1.1	2.86 ± 0.09	0.0
2.9 nm Au	0	5.2 ± 1.1	2.82 ± 0.10	1.3
2.9 nm Au	5	7.5 ± 1.7	2.83 ± 0.11	1.1
2.9 nm Au	10	8.5 ± 1.0	2.83 ± 0.10	0.9
2.9 nm Au	30	11.8 ± 1.2	2.85 ± 0.10	0.3
2.9 nm Au	100	12.1 ± 1.2	2.85 ± 0.10	0.3
3.1 nm Au	0	8.4 ± 0.8	2.83 ± 0.10	1.0
3.1 nm Au	50	8.8 ± 0.9	2.84 ± 0.10	0.6
4.5 nm Au	0	10.4 ± 1.1	2.85 ± 0.09	0.2
4.5 nm Au	50	10.7 ± 1.0	2.86 ± 0.09	0.1

XPS was also performed to investigate the gold particle size before and after repetitive cyclic voltammetry. Typically, gold nanoparticles with diameters of 1.4 nm and larger will show XP spectra similar to bulk gold whereas smaller gold particles will show spectra with higher Au $4f_{7/2}$ binding energies [176]. Here, all four electrocatalysts were measured in two states: an as prepared electrocatalytic layer, and an electrocatalytic layer which had undergone 100 CV cycles. The XP spectra for a 0.8 nm Au electrocatalytic layer was also measured after it had been exposed to 0.5 M H_2SO_4 at OCP for 10 minutes.

The binding energies of the Au $4f_{7/2}$ electrons in the 2.9 nm Au, 3.1 nm Au and 4.5 nm Au samples were close to that for bulk gold (84.3-84.5 eV vs. 84.0 eV), and the 4.5 nm Au sample did not change after CV cycles which was as we expected for nanoparticles of these sizes [176]. However, the as-prepared electrode containing 0.8 nm Au had a considerably higher binding energy (85.5 eV) which confirms that the vast majority of gold in this sample is present as small gold clusters (Figure 3-12), which is in line with our earlier XPS investigations of Au_9 deposited on titania [176, 177].

Exposure of 0.8 nm Au clusters supported on carbon to H_2SO_4 caused a pronounced reduction in the Au $4f_{7/2}$ peak area (Figure 3-13). This would indicate that either the gold has been removed from the surface, or has been partially shielded during the XPS measurements. While atomic adsorption spectroscopy suggested that some gold dissolves into the solution (approx. 3 wt% of the gold from the 0.8 nm Au samples is dissolved over 100 cycles), the reduction of the XPS peak area is much larger than expected for such loss and indicates another factor is in play. This leads us to one of two conclusions: either the Nafion within the electrocatalytic layer becomes mobile while exposed to H_2SO_4 and then collapses to cover the gold nanoparticles during drying, or alternatively, the gold dissolved into the solution is only the gold on the outermost surface of the electrocatalytic layer. In either case, since the binding energy of the detectable gold species is not changing we can conclude that exposure to 0.5 M H_2SO_4 is not altering the particle size.

Comparison of the XPS P 2p spectra (to investigate the phosphorus-containing ligands used in the synthesis of the 0.8 nm Au, 2.9 nm Au and 3.1 nm Au samples), only showed the presence of phosphine (132 eV) and R3P-O compounds (135 eV) in the as-prepared catalytic layers of 0.8 nm Au and 3.1 nm Au respectively (Figure 3-14). The absence of phosphorus in the 2.9 nm Au sample may be due to the loss of ligands during the particle sintering which occurred during the adsorption of the gold nanoparticles to the carbon support or loss under the UHV conditions as discussed above. Loss of the phosphorus signal in the 0.8 nm Au layer that had been exposed to 0.5 M H_2SO_4 without cycling leads to the same conclusions as for the change in the gold spectra – either the Nafion in the top layer has shielded the nanoparticles or that the phosphine ligands desorbed into the H_2SO_4 electrolyte solution.

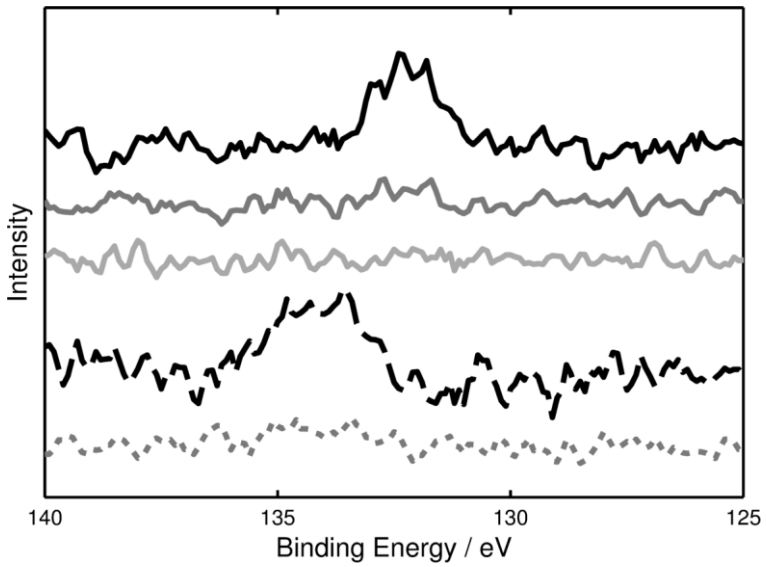

Figure 3-14. P 2p spectra for 0.8 nm Au and 3.1 nm Au. The spectra shown are: as-made 0.8 nm Au (black, solid line), 0.8 nm Au exposed to H_2SO_4 (dark grey, solid line), electrochemically cycled 0.8 nm Au (light grey, solid line), as-made 3.1 nm (black, dashed line), and electrochemically cycled 3.1 nm Au (light grey, dashed line).

3.4 Summary

Gold nanoparticles with initial average diameters in the range of 0.8 nm–4.5 nm grow during repetitive cyclic voltammetry. TEM analysis shows that the mean particle size shifts toward larger values and that the particle size distribution broadens to encompass a larger range of particle sizes, which was confirmed by EXAFS and XPS analysis. The particle growth is not influenced by the type of ligand used in the synthesis of the initial particles indicating that the stabilising ligands are likely to have been lost during the initial cyclic voltammograms.

Analysis of the gold oxide reduction peak charge reveals that the EASA is stable for electrodes containing larger (ca. > 4.5 nm) gold nanoparticles, whereas in the case of the materials containing smaller (ca. 3 nm) gold particles, both the oxide reduction charge and potential decrease slowly over the 100 CV cycles. For electrodes containing even smaller gold nanoparticles (0.8 nm, based on Au_9 clusters), gold/gold oxide redox behaviour typical for the bulk gold is not observed.

The results obtained have important implications for the fundamental analysis and practical use of gold nanoparticle-based electrocatalysts. Specifically, due to the significant growth which can occur during electrochemical potential cycling, nanoparticle stability should be evaluated as part of investigations into size-based electrochemical behaviour of gold nanoparticles. In addition, the observed instability of small gold nanoparticles may preclude these from long-term practical applications where high anodic potentials are experienced unless such materials can be stabilised to prevent particle growth.

Chapter 4 IN-SITU UV-VIS SPECTRO-ELECTROCHEMICAL INVESTIGATION OF THE REVERSIBLE FORMATION OF GOLD OXIDE LAYERS ON GOLD NANOPARTICLES

4.1 Introduction

4.1.1 Surface Plasmon Resonance

Surface plasmon resonance (SPR) is a phenomena occurring on metallic nanoparticles where their electrons become excited by incident light. If the light waves are of the correct wavelength, electronic oscillations will constructively interfere with the neighbouring atom's oscillations (Figure 4-1). These interactions form a resonating wave along the surface of the nanoparticle and cause a change in the absorption of different wavelengths of light. In spherical gold nanoparticles up to 100 nm in diameter, the wavelength of this absorption occurs around 520 – 600 nm [94, 210-213] and causes a colloidal solution to appear red/pink in colour.

The Mie theory is often used to predict the absorbance of a specific wavelength of light with respect to the particle diameter, dielectric function of the medium, the wavelength of the incident light, the refractive index of the particle, the refractive index of the medium, the concentration of the particles and the mean free path length. The derivation and calculations of these values and the absorbance is the topic of much research (e.g. refs [214-216]) however, to make the calculations more accessible to the average researcher, programmes such as MiePlot are available [217]. Such programmes, along with online calculators allow the peak absorbance wavelength to be calculated for a gold-gold oxide-electrolyte system.

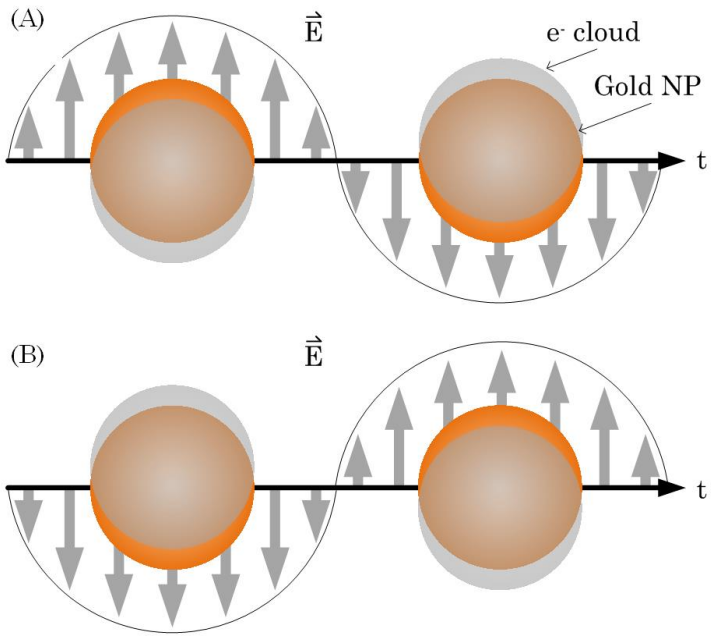

Figure 4-1. Fluctuations of the electron cloud around individual gold atoms achieve resonance causing absorption of particular wavelengths of incident photons.

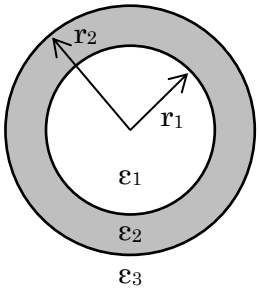

Figure 4-2. Representation of a gold-gold oxide-electrolyte core-shell system.

Due to the sensitive nature of the electron oscillations of SPR, many other factors can alter the shape and peak wavelength of the nanoparticle SPR feature. These factors include: nanoparticle size and shape [218-220], type of nanoparticle support [169], neighbouring nanoparticles [221], presence of stabilizing ligands [222], presence and type of electrolyte [220, 223], adsorbed ions [224] and the applied electronic environment [218, 225].

4.1.2 Surface Plasmon Resonance of Gold Nanoparticles

The SPR behaviour of gold is a well-known phenomenon where localized electron oscillations are measured on bulk gold as a characteristic SPR reflectivity wavelength (~660 nm [226-229]), or in the case of nanoparticles, as a characteristic absorption maxima (~520-600 nm [94, 210-213]). The study of the SPR behaviour of gold is of great importance to developing gold-based sensing [222, 226, 230-235], monitoring absorption of ions during electrocatalysis [236-239] and bioanalytical measurements [240, 241]. The SPR of gold

nanoparticles is of particular interest as the electronic effects inherent in the SPR feature are magnified due to the small (<50 nm) size of the particles [220].

Using the Mie theory, the peak wavelength and absorption was calculated via an online calculator provided by NanoComposix [242] for 23.9 nm gold particles without any gold oxide, with one monolayer of gold oxide and with two monolayers of gold oxide. It was found that the nanoparticle must gain volume, first by a factor of 1.122 to account for the increase in mass of due to the conversion of $Au \rightarrow Au_2O_3$ and second by a factor of 1.689 to account for the change in density between gold and gold oxide. As such, it was found that a single monolayer of gold oxide would increase a 23.9 nm gold particle to 24.4 nm in size, and similarly, two monolayers of gold oxide would increase the same particle to 24.8 nm (Table 4-1).

Table 4-1. Gold-gold oxide core-shell calculations based on an increase in mass and reduction in density when converting gold to gold oxide.

Number of monolayers of gold oxide	Diameter of gold core / nm	Thickness of gold oxide shell / nm	Total gold-gold oxide particle diameter / nm
0	23.9	0.00	23.9
1	23.3	0.54	24.4
2	22.7	1.05	24.8

Using the calculated core and shell dimensions, and the refractive indices of gold, gold oxide, 0.5 M H_2SO_4 and 1.0 M KOH, the peak absorption and intensity was calculated for a gold nanoparticle, a gold nanoparticle with one monolayer of gold oxide and a gold nanoparticle with two monolayers of gold oxide (Table 4-2). Care must be taken for these calculations as the refractive index of gold is wavelength-dependent [243], however this dependency was built into the online calculator [242]. The refractive index of gold oxide has been reported as 2.7 across the wavelength range that was calculated [244], and the refractive indices of 0.5 M H_2SO_4 (1.339 [245]) and 1.0 M KOH (1.338 [245]) are constant with respect to the wavelength.

Table 4-2. SPR peak wavelength and intensity for 0, 1, 2 monolayers of gold oxide on a 23.9 nm gold nanoparticle in air, 0.5 M H_2SO_4 and 1.0 M KOH.

Number of monolayers of gold oxide	Medium	SPR peak wavelength / nm	SPR peak intensity (cross sectional area) / nm^2
0	Air	505.6	251.1
0	0.5 M H_2SO_4	526.4	759.2
1	0.5 M H_2SO_4	536.0	856.9
2	0.5 M H_2SO_4	545.6	937.4
0	1.0 M KOH	525.8	757.1
1	1.0 M KOH	536.0	854.7
2	1.0 M KOH	545.6	935.2

These factors are all connected to the SPR feature as they alter the electron density of the gold nanoparticles. The effect of the alterations in electron density on the SPR feature have been highlighted by Mulvaney's experiments where changes in the SPR band of a single gold nanoparticle are measured as electrons are injected into the nanoparticle by cathodic polarisation in an electrochemical cell [225].

Given that the SPR feature is influenced by nearby chemicals such as gold oxide or the surrounding medium, an investigation into the SPR response during electrocatalytic reactions was considered. The electrocatalytic oxidation of glycerol was chosen as, in order to occur, it requires a partial layer of gold oxide to be present.

4.1.3 Electrocatalytic Glycerol Oxidation and Gold Oxide

The electrochemical formation of the gold oxide layer on gold nanoparticles is an important factor in several electrocatalytic applications [50, 133, 246, 247]. For example, the onset of glycerol oxidation is believed to coincide with the initial stages of gold oxide formation and ceases once complete gold oxide coverage is reached [84, 247]. Suggestions have also been made that the presence of alcohols will shift the potential at which gold oxide is formed/reduced [56, 133], however, this shift is undetectable in a simple CV scan due to the glycerol oxidation masking any gold oxide formation/reduction currents. This masking could be caused by either a large glycerol oxidation current overwhelming the gold oxide related currents, or by glycerol blocking the gold surface and thereby preventing gold oxide formation [247].

4.1.4 Surface Plasmon Resonance Response to Electrode Potential Changes

Several authors have investigated how the SPR of nanoparticles changes with respect to potential shifts. Jory et al. [235] cycled a 50 nm thick gold film in 0.01 M $HClO_4$ between 0.30 V and 0.35 V vs. SHE at a scan rate of 1 $mV \cdot s^{-1}$ and found the SPR peak position shifted by 0.04 nm, with a very close correlation between the relative charge of the electrode and the change in the SPR position. Iwasaki et al. [228] measured the differential of the SPR angle of a <50 nm thick gold film in 0.1 M $HClO_4$ and found it to be very similar to the corresponding CV scan. They also saw sulfate adsorption/desorption between 0.5 V and 1.0 V vs. RHE and suggest that this method of analysis could be used for further investigation of ionic adsorption processes.

More recently, the investigation of the SPR response has shifted to a layer of nanoparticles deposited on a conductive surface such as FTO or ITO. Toyota and Sagara [248] found that a step-change in potential from 0.6 V to 1.4 V vs. RHE in a 0.1 M phosphate buffer solution resulted in both a red-shift of the SPR peak and a reduction in the SPR intensity. They conclude that the SPR response is as a result of either surface processes or charge transfer processes between the ITO support and the nanoparticle. Novo et al. [225] cathodically shifted the potential of single gold nanorods and found that the SPR peak wavelength shifted by up to 7.8 $V \cdot nm^{-1}$. Byers et al. [221] recorded CV scans concurrently with SPR spectra in 0.1 M $NaSO_4$ and found the SPR response of single gold nanoparticles to be very sensitive to sulfate adsorption.

4.1.5 Sulfate Adsorption on Gold Electrodes

Given the importance of gold oxide coverage in electrocatalysis, it is worth noting that in H_2SO_4 electrolytes sulfate/bisulfate adsorption competes with water adsorption and hence gold oxide formation [249]. Ataka and Osawa [250] showed via IR spectroscopy that the anodic adsorption of sulfate/bisulfate anions begins at 0.5 V vs. RHE on a thin gold (111) film in H_2SO_4. The coverage of adsorbed sulfate/bisulfate increased as the potential was increased from 0.5 V to 0.75 V vs. RHE, where H_2O started to hydrogen bond to the adsorbed sulfate ions, forming bridges between adjacent sulfate ions and stabilising their adsorption. Complete coverage the surface by this H_2O-sulfate bridge structure is evidenced by the absence of additional spectral changes above 1.0 V vs. RHE. Horányi, Rizmayer & Joó [251] show via radiotracer studies that sulfate absorption begins at 0.4 V vs. RHE and achieves maximum coverage at 1.2 V vs. RHE before decreasing to almost zero coverage by 1.4 V vs. RHE as gold oxide formation occurs. This process is reversed during the cathodic scan where approximately 95% of the maximum sulfate coverage is re-adsorbed as gold oxide reduction begins at 1.2 V vs. RHE. Tian, Pell & Conway [202] show via electrochemical quartz crystal microbalance (E-QCM) that very little mass change occurs between 1.0 V and 1.4 V vs. RHE, due to sulfate ions being lost at the same rate as water is binding. During the cathodic scan, a large decrease in mass (approximately one-third of the previous increase) is seen as gold oxide is being reduced, followed very closely by a small increase in mass as the sulfate ions are re-adsorbed. Edens, Gao & Weaver [252] show via radiotracer and IR measurements that sulfate is only bound between ~0.0 V and 0.9 V vs. RHE, although these studies were performed with HSO_4^-/SO_4^{2-} concentrations of 5 mM, approximately 100 times lower than in the previous studies. Additionally, they also found via STM a maximum sulfate coverage of 0.2 monolayers, in contrast to a coverage of 0.4 monolayers put forward by Magnussen et al. [253]. Jory, Cann & Sambles [227] have correlated the sulfate adsorption/desorption peaks at 0.672 V vs. RHE in a gold CV scan with a corresponding red shift of the SPR band by approximately 0.6 nm.

4.1.6 Electrochemical Gold Oxide Formation

Gold oxide formation has been shown to follow two possible pathways in H_2SO_4 and $HClO_4$ respectively [202]. Path 1 is a series of three fast, sequential reactions put forward by Bruckenstein [145]:

$$\text{Au-Au-}(H_2O)_{surf} \rightarrow \text{Au-Au-}OH_{ads} + H^+ + e^- \quad 4\text{-}1$$

$$\text{Au-Au-}OH_{ads} \rightarrow \text{Au-Au=}O + H^+ + e^- \quad 4\text{-}2$$

$$\text{Au-Au=}O + H_2O \rightarrow \text{Au-}O\text{-Au-}(H_2O) \quad 4\text{-}3$$

Whereas path 2 is a set of reactions put forward by Xia and Birss [254]:

$$Au + H_2O \rightarrow \text{Au-}H_2O_{ads} \quad 4\text{-}4$$

$$\text{Au-}H_2O_{ads} \rightarrow \text{Au-}O + 2H^+ + 2e^- \quad 4\text{-}5$$

Both reaction pathways require adsorption of a H_2O molecule prior to oxidation. They also involve the transfer of two electrons, and the reaction from adsorbed oxygen to gold oxide; both of which alter the electron density of the surface gold atom. This electron density change has been observed via changes in the SPR spectrum [218, 225, 255, 256]. In contrast, gold oxide formation in NaOH or KOH takes place directly via an adsorbed OH^- ion (Equations 4-6 and 4-7) [257].

$$Au + OH^- \rightarrow AuOH + e^- \quad 4\text{-}6$$

$$AuOH + OH^- \rightarrow AuO + H_2O + e^- \quad 4\text{-}7$$

Although the gold oxide formation and reduction, and possibly sulfate/bisulfate adsorption, have a considerable impact on the electrocatalytic oxidation of alcohols, cyclic voltammetry during alcohol oxidation cannot be used to study the gold oxide formation at the gold surface as the alcohol oxidation currents dominate the voltammetric response. However, given the sensitivity of the SPR behaviour of gold nanoparticles, here we attempt to study these electrochemically-induced processes independently from the measured voltammetric response by performing UV-Vis spectroscopy simultaneously with cyclic voltammetry. This enables the spectroscopic identification of the reversible formation of the gold oxide layer in a range of electrolytes and, importantly, during the electrocatalytic oxidation of glycerol.

4.2 Experimental

Gold nanoparticles were synthesised by citrate reduction based on the Turkevich method [95]. Briefly, 0.5 L of a 1 mM aqueous solution of $HAuCl_4 \cdot 3H_2O$ (99.9%, Sigma-Aldrich) was brought to the boil with vigorous stirring. 0.290 g $Na_3C_6H_5O_7 \cdot 2H_2O$ (99.0%, Sigma-Aldrich) was dissolved in 10 mL of DI water and added to the stirred gold solution. Boiling was continued for 10 minutes whereupon heating was stopped. After an additional 10 minutes of stirring the solution was cooled to room temperature in an ice bath, made up to 1 L and stored in the dark.

Clean FTO slides (7 $\Omega \cdot sq^{-1}$, Cytodiagnostics) were functionalized by immersion in a 1% v/v methionic solution of (3-aminopropyl)triethoxysilane (APTES) (99%, Sigma-Aldrich) for 10 minutes. The slides were then rinsed with methanol and DI water then immersed in the gold colloidal solution for 24 hours. The slides were then dried in air and glued to a UV-Vis cuvette containing a pre-drilled 8 mm hole. The average particle diameter was measured via SEM to be 23.9 nm with a standard deviation of 4.1 nm. FTO surface coverage was determined as 28 ± 3%, respectively (Figure 4-5 and Figure 4-4 for an as-prepared gold/FTO slide).

Cyclic voltammetry was performed with a Gamry Reference 3000 potentiostat with a Pt/Ir counter electrode. A Ag/AgCl reference electrode was used for measurements in 0.5 M H_2SO_4 and a Hg/HgO reference electrode was used for measurements in 1 M KOH.

For ease of comparison, all potentials are presented versus the RHE (See Section A1.4.4 for reference electrode conversion factors).

UV-Vis spectroscopic measurements were performed using a Shimadzu Multispec-1501 photodiode array spectrophotometer. Absorption spectra were measured between 300 and 700 nm with a wavelength resolution of 1 nm and a time resolution of 1 s. The use of the photodiode array spectrophotometer enabled simultaneous measurement of the CV scan and absorbance spectra while the electrode potential was cycled between 0.21 V and 1.56 V. All CV scans were performed at 50 $mV \cdot s^{-1}$.

Several data processing calculations were made in order to analyse the data. Due to the different dielectric currents of the electrolytes [220], the absorbance calculations used a wavelength close to the maximum SPR absorbance at OCP for each electrolyte solution, namely, 535 nm for 0.5 M H_2SO_4, 525 nm for 1.0 M KOH and 540 nm for 1.0 M KOH/0.1 M glycerol. These wavelengths were measured when the particles were initially exposed to the electrolyte, prior to any cyclic voltammetry. The background was corrected to remove the overall decrease in absorbance with respect to time, a feature seen in all electrochemical-UV-Vis measurements. The normalisation was then achieved by fitting a polynomial curve through the absorbance measured at the cathodic limit of each CV scan. This curve was then subtracted from the absorbance data to set the cathodic limit to an absorbance value of 0. The same approach was then used to fit a curve to the absorbance measured at the anodic limit of the CV scan. This curve was used to normalise the data and set the absorbance at the anodic limit to a value of -1 (Figure 4-3). The first four CV scans were chosen as a subset of the entire dataset as they were very similar to each other and few changes in the surface coverage or PSD had occurred at by the end of the fourth CV scan. The normalised data was averaged over these first four CV scans to produce the absorbance-potential plot (e.g. Figure 4-12). The three-point differential absorbance was calculated for each data point according to Equation 4-8 where *Abs* is the absorbance and *i-1* and *i+1* denote the data point immediately before and after data point *i*. The differential data was averaged over the first four CV scans to produce the differential absorbance-potential plot (e.g. Figure 4-13). Differential plots similar to those described here have been used to analyse UV-Vis data in recent years [221, 228, 241] and are discussed in a recent paper regarding 'emerging tools for studying single entity electrochemistry' [258].

$$\Delta Abs_i = \frac{(Abs_{i-1} - Abs_i) + (Abs_i - Abs_{i+1})}{2} \qquad 4\text{-}8$$

The maximum wavelength data was also investigated by first calculating the maximum wavelength at each time step by fitting a Lorentz curve (Equation 4-9, where A is the total peak area, w is the peak width and λ_{max} is the peak wavelength) to the raw UV-Vis absorbance spectrum. This maximum wavelength data was averaged over the first four CV scans to produce the wavelength-potential plot (e.g. Figure 4-14). Finally, a three-point differential wavelength was calculated for each data point and averaged over the first four CV scans to produce the differential wavelength-potential plot (e.g. Figure 4-15).

$$\mathrm{Abs_i} = \frac{A \cdot w}{\pi}\left(1 + \frac{\lambda_i - \lambda_{max}}{w^2}\right) \qquad 4\text{-}9$$

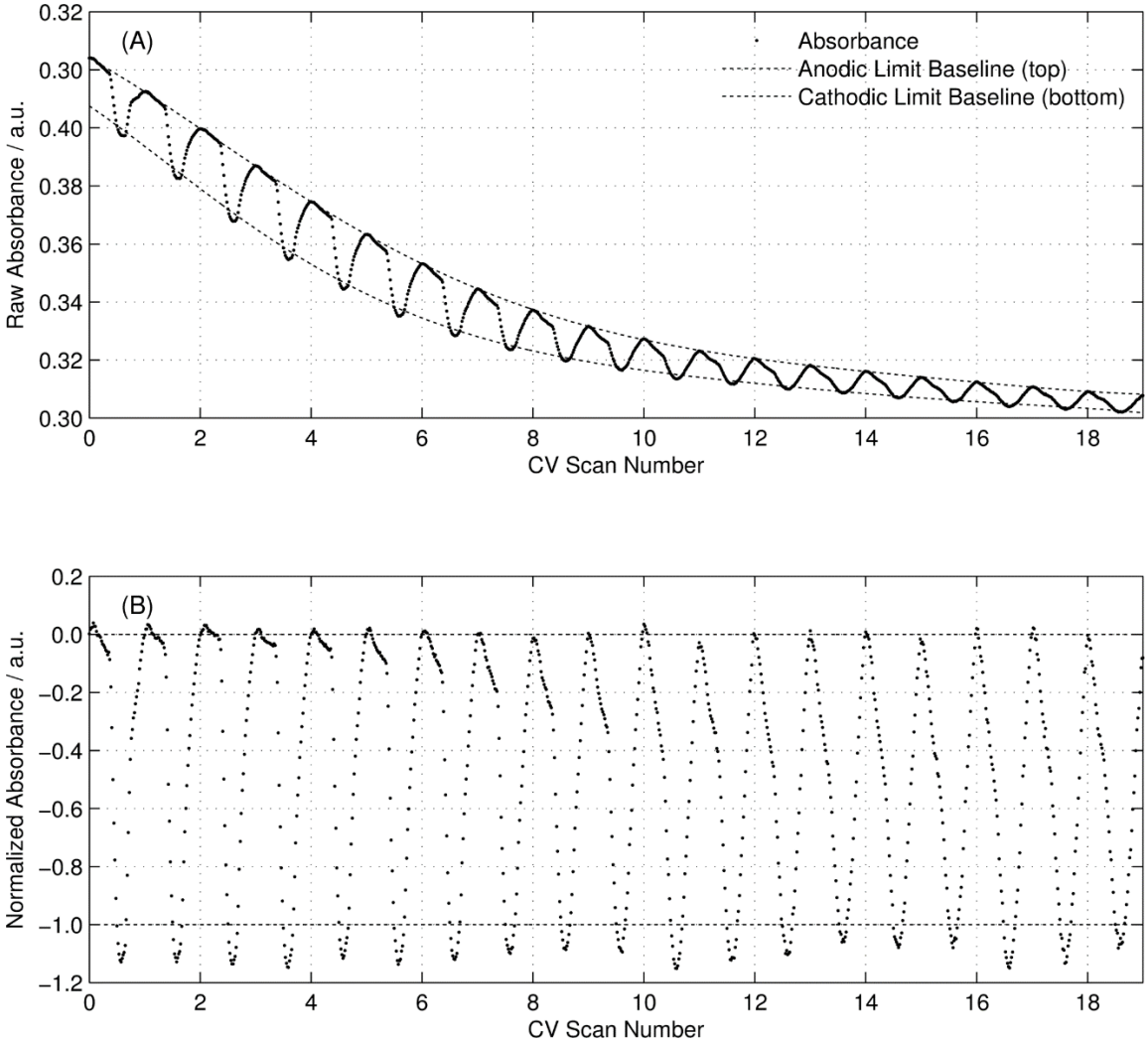

Figure 4-3. Raw absorbance (A) and normalised absorbance (B) data for gold/FTO in 0.5 M H_2SO_4 at 535 nm across 19 CV scans. The dashed line is the baseline correction to be applied to the data.

4.3 Results and Discussion

4.3.1 Particle Size Measurements

The average, as-prepared gold nanoparticle size was measured to be 23.9 nm, with a standard deviation of 4.1 nm (Figure 4-5 and Table 4-3). Due to the overall decrease seen in the absorbance data, and the knowledge of particle ageing discussed previously (Chapter 3), images of the slides after electrochemical cycling were analysed to investigate changes to particle size or surface coverage. These images showed the average nanoparticle size after electrochemical cycling in 0.5 M H_2SO_4 was 21.9 nm, with a standard deviation of 4.4 nm (Figure 4-4 and Table 4-3). This 2 nm reduction in average particle size is attributed to both the dissolution of gold from the nanoparticle surface, combined with the desorption of whole

nanoparticles into the electrolyte. It is considered that during this work that gold lost from the FTO surface diffuses away from the electrode and is not redeposited or readsorbed. The reduction in the frequency of large particles indicates that particle fusion is not occurring, which is reinforced by the presence of 'clumped' nanoparticles in both the as-prepared SEM images and the electrochemically cycled SEM images (Figure 4-5 and Figure 4-6). The geometric surface area coverage of 28 ± 3% for the as-prepared sample was reduced to 14 ± 1% for the electrochemically cycled sample, indicating that approximately half of the particles were lost from the FTO surface through desorption or complete dissolution.

Table 4-3. Particle distribution analysis for as-prepared and electrochemically cycled gold nanoparticles on an FTO slide.

	As-Prepared	**Electrochemically Cycled**
Number of particles counted	1058	472
Number weighted diameter / nm	23.9	21.9
Standard deviation / nm	4.1	4.4
Specific surface area / $m^2_{Au} \cdot g^{-1}_{Au}$	13.4	14.7
Geometric coverage	28 ± 3%	14 ± 1%
Surface density / nanoparticles $\cdot \mu m^{-2}$	628	347
FTO gold coverage / $cm^2_{Au} \cdot cm^{-2}_{FTO}$	1.13	0.52

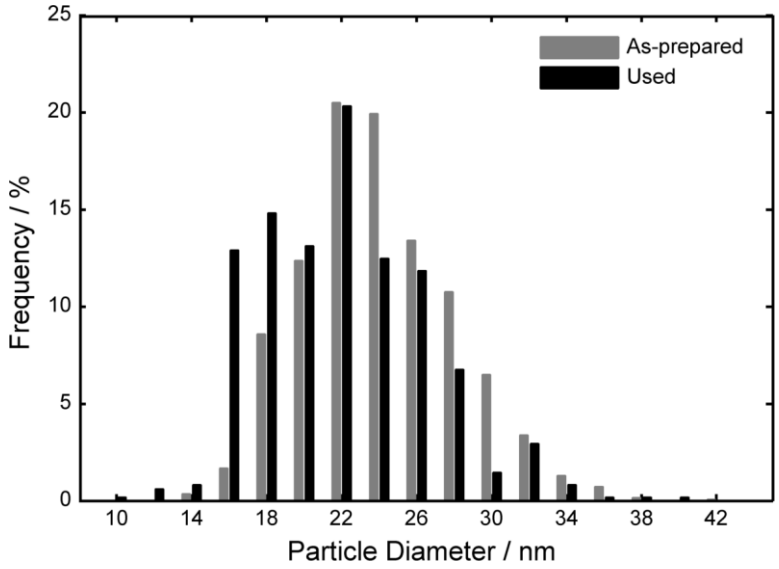

Figure 4-4. Particle size distribution of as-prepared and electrochemically cycled gold nanoparticles as measured from SEM images. The average particle statistics are provided in Table 4-3.

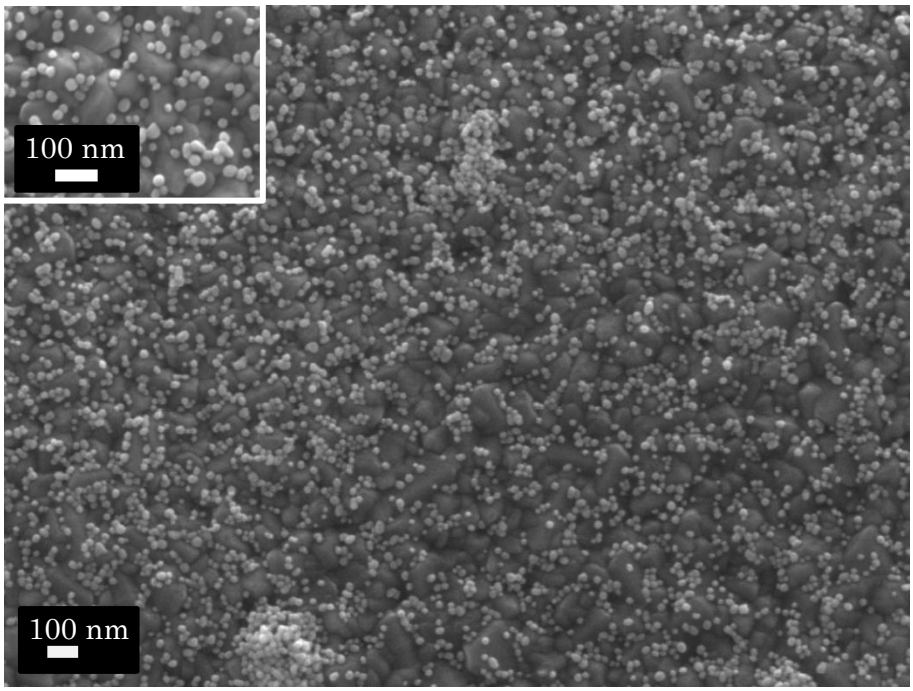

Figure 4-5. SEM images of as-prepared gold nanoparticles adsorbed on an FTO slide. Geometric gold coverage was measured as 28 ± 3% of the FTO slide.

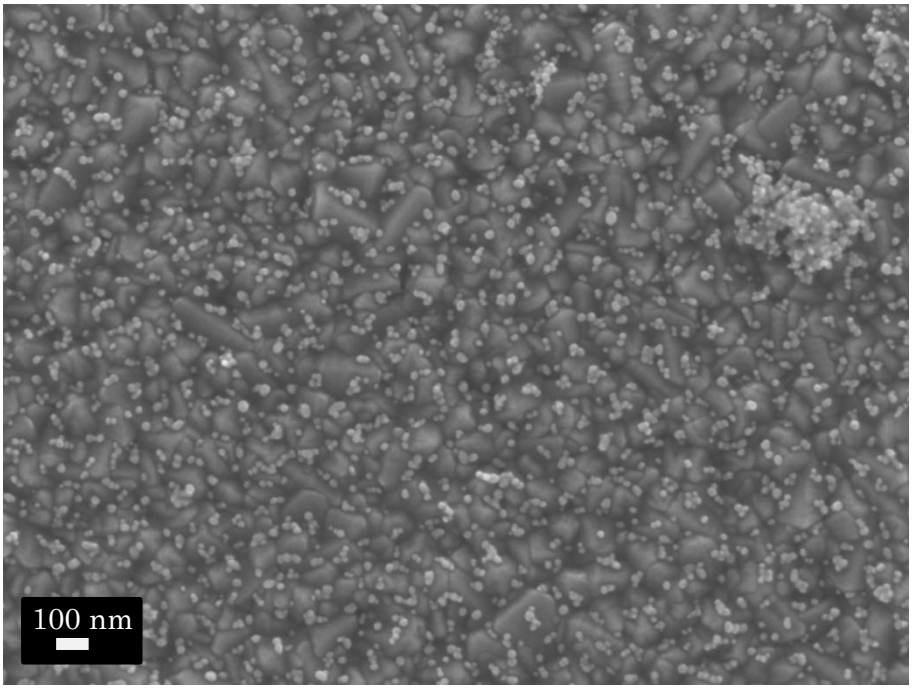

Figure 4-6. SEM image of a gold nanoparticle/FTO slide after electrochemical cycling in 0.5 M H_2SO_4. Geometric gold coverage was measured as 14 ±1% of the FTO slide.

4.3.2 Electrochemistry

The CV scans of the gold nanoparticle coated FTO slides (Figure 4-7) are consistent with previous publications [57, 140]. In 0.5 M H_2SO_4 the formation of gold oxide is observed during the sweep in the anodic direction to occur starting from around 1.15 V vs. RHE, whereas, in KOH, the onset of gold oxide occurs at slightly less anodic potentials of around 0.95 V vs. RHE. It is interesting to note that the gold oxide reduction charge differs in these electrolytes despite the fact that the anodic limit is similar on the RHE scale. We also observe a large cathodic feature around 0.7 V vs. RHE in KOH which is similar to that seen elsewhere [63] and likely to be due to oxygen reduction.

The stability of the gold nanoparticles was as expected; the electrochemically active surface area of gold on the electrode (proportional to the charge associated with the gold oxide reduction peak at 1.0-1.1 V vs. RHE) is found to decrease due to dissolution and desorption of the nanoparticles during the repetitive potential cycling [1, 51, 186]. This decrease in gold surface area is reflected in the difference between the anodic baseline and cathodic baseline in Figure 4-3A, where, between the start of CV#0 and the end of CV#19, the cyclic amplitude reduces by 61%. This response is expected as the 45% decrease in the number of particles, and the 2.0 nm decrease in the average particle size resulted in a total gold surface area reduction of 54% (Table 4-3).

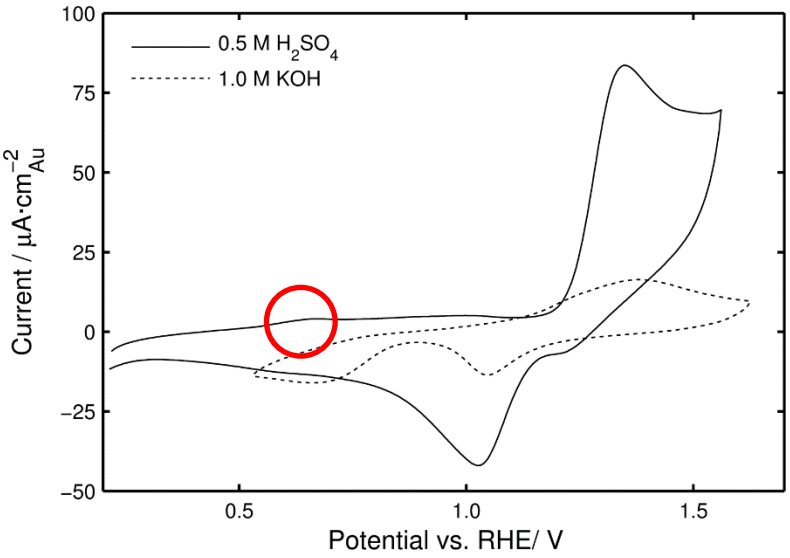

Figure 4-7. Initial gold nanoparticle CV scan in 0.5 M H_2SO_4 (solid line) and 1.0 M KOH (dashed line). The small node indicated in the red circle is attributed to sulfate adsorption [221].

4.3.3 Behaviour of the Surface Plasmon Resonance features in the UV-Vis Spectra

The as-prepared gold nanoparticles in solution prior to adsorption to the FTO slide exhibited a SPR band around 525 nm while the deposited gold/FTO nanoparticles in air exhibited a red-shift to 531 nm (Figure 4-8A). According to the Mie theory calculations carried out in Section 4.1.2 (Table 4-2), the expected peak wavelength of 23.9 nm particles is 505.6 nm, over 25 nm less than the measured wavelength. It would be expected that the addition of either 0.5 M H_2SO_4 or 1.0 M KOH would induce a red-shift of approximately 20 nm, however, the addition of 0.5 M H_2SO_4 (at OCP) induced only a small red-shift to 534 nm, whereas, the addition of 1.0 M KOH induced a blueshift to 526 nm (Figure 4-8B). These effects are attributed to the electron donating/withdrawing effect of the support/electrolyte rather than an aggregation of the nanoparticles [169] or changes in the refractive index of the medium.

As has already been mentioned, the overall decrease in the raw absorbance and a decrease in the amplitude of the potential-induced UV-Vis absorbance oscillations (Figure 4-3A) is attributed to loss of gold surface due to nanoparticle desorption and anodic dissolution during CV scanning in the potential range corresponding to the gold oxide region [1]. This leads to a change in the shape of the UV-Vis absorbance oscillations and in order to retain this initial information, the UV-Vis data has been averaged across only the first four CV scans.

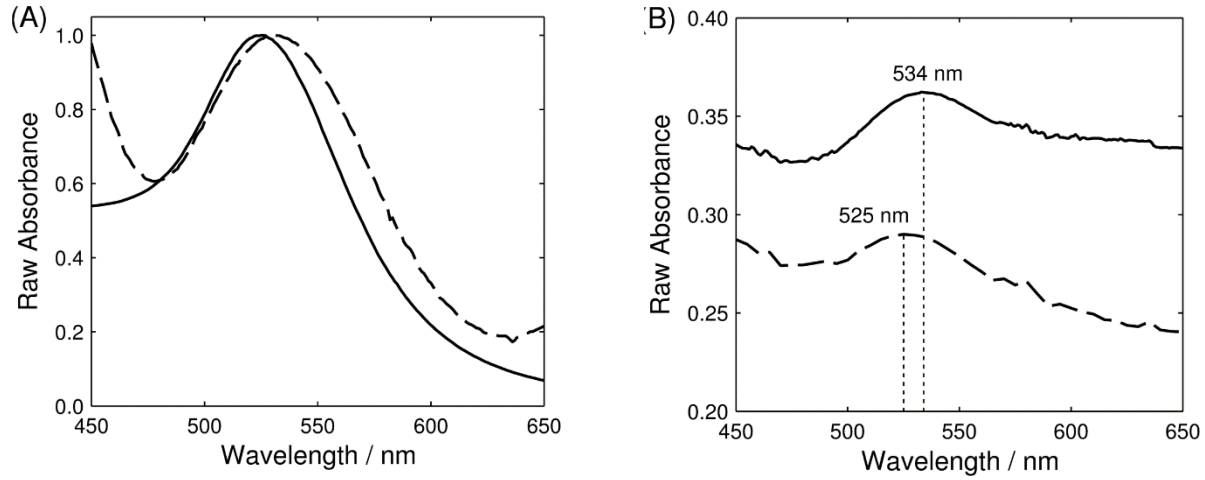

Figure 4-8. UV-Vis of as-prepared gold nanoparticles; in a colloidal solution (A-solid line), adsorbed to FTO in air (A-dashed line), adsorbed to FTO in a 0.5 M H_2SO_4 solution (B-solid line) and adsorbed to FTO in a 1.0 M KOH solution (B-dashed line). UV-Vis spectra of nanoparticles in solution are at OCP. No background removal was performed on these samples due to variabilities in the cuvettes and FTO slides.

As the potential is swept from the lower potential limit to around 1 V (the region where no Faradaic processes occur), the SPR feature decreases very slightly (Figure 4-9). As the potential is swept beyond 1 V vs. RHE, the measured absorbance decreases significantly due to the formation of gold oxide on the surface of the nanoparticles. This response is, according to the Mie theory calculations (Table 4-2), the opposite of what is expected. The

expected increase in absorbance is primarily based on the increase in particle size, and hence cross-sectional area, however, as the recorded absorption decreases, the gold-oxide shell must be contributing to changes in the SPR peak beyond its influence due to increase in particle size or changing the refractive index of the surface.

The isosbestic point around 545 nm in H_2SO_4 and 540 nm in KOH occurs due to this decrease in absorbance, coupled with the red-shift in the SPR peak wavelength (Figure 4-9). As expected [256], electron density changes within the particles as the potential is swept in the anodic direction induce the SPR peak wavelength to be red-shifted by about 5-10 nm over the potential window examined. While this red-shift is largely reversed when the potential is swept back in the cathodic direction, over a number of CV cycles the growth of particles is suggested via a SPR band shift at a reference potential. That is, at 0.51 V, the wavelength at the maximum SPR intensity was 536 nm during the third CV while it had increased to 541 nm, at the same potential, by the 19th CV. However, the suggestion of particle growth from these results is in disagreement with the SEM images of the electrochemically cycled sample. The measured decrease in average particle size means the observed wavelength increase must be due to a secondary factor such as an increased proportion of aggregated nanoparticles causing a redshift of the spectrum [259].

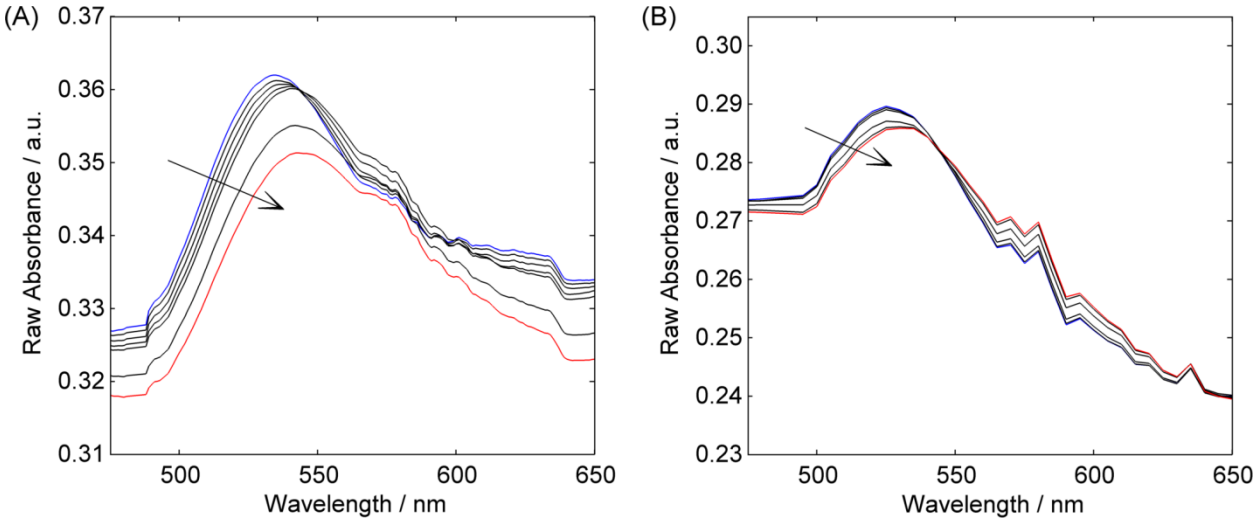

Figure 4-9. UV-Vis spectra with respect to potential for nanoparticles in 0.5 M H_2SO_4 (A) from 0.21 V (blue line) to 1.51 V (red line) in 0.2 V steps, and nanoparticles in 1.0 M KOH (B) from 0.58 V (blue line) to 1.58 V (red line) in 0.2 V steps.

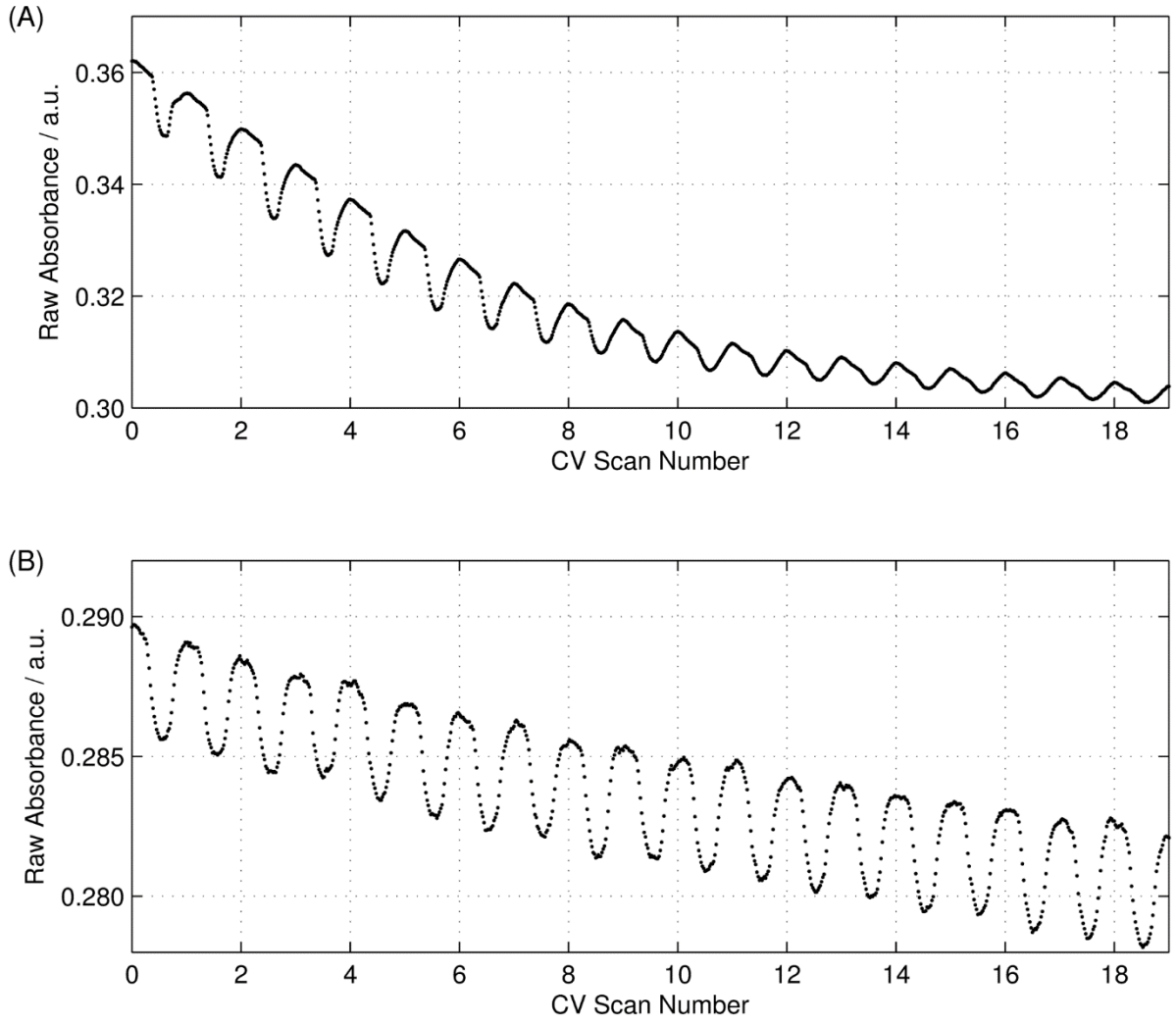

Figure 4-10. Raw UV-Vis absorbance data across 19 CV scans (A) at 535 nm for nanoparticles in 0.5 M H_2SO_4 and at 525 nm (B) for nanoparticles in 1.0 M KOH. The wavelengths for the absorbance intensity monitoring were selected to be close to the SPR peak wavelengths at open circuit potential for each sample.

4.3.4 Shift of the SPR Absorbance with Respect to Potential

To compare the absorbance as a function of potential, the normalised absorbance at 535 nm in H_2SO_4 and 525 nm in KOH was extracted from the raw absorbance data (Figure 4-10). These wavelength values were chosen as they were close to the SPR peak maximum wavelength for each electrolyte (534 nm and 526 nm, respectively) while the electrode was held at open circuit potential. For ease of comparison, the absorption values are normalised such that the data is 0 at the cathodic limit and is -1 at the anodic limit. The data decreases below -1 (Figure 4-12) as gold oxide formation continues during the initial stages of the sweep from the upper potential limit down toward the cathodic limit. This continues red-shifting the SPR band and hence, further lowers the absorbance at the monitored wavelength.

A plot showing changes in the SPR absorbance as a function of potential provides information regarding the localised electron density of the gold surface via the relative changes as secondary species are adsorbed onto or reacted with the electrode surface. For example, adsorption and desorption of sulfate ions have been shown to occur as a function of potential with almost no discernible hysteresis of the surface coverage when comparing ionic adsorption during the anodic scan and desorption during the cathodic scan (Figure 4-11) [202]. As such, changes in the SPR caused by the adsorption and desorption of these ions should be reversible without hysteresis between the anodic and cathodic scans.

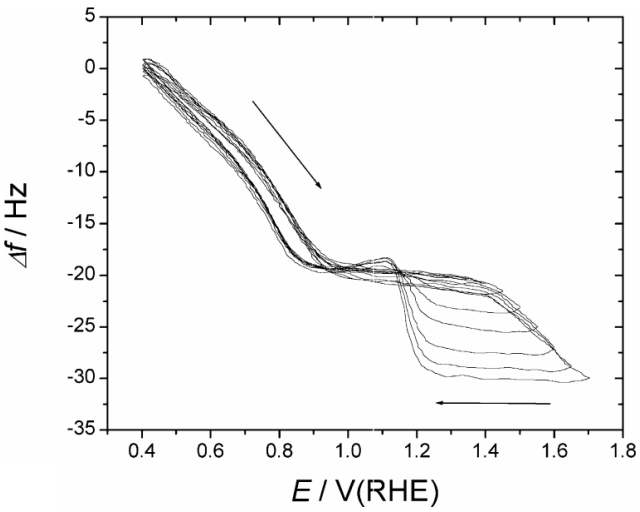

Figure 4-11. E-QCN frequency responses of a Au-coated electrode in 0.5 M H_2SO_4 for a range of different upper potential limits between 1.35 and 1.70 V vs. RHE at a sweep rate of 50 mV·s^{-1}. Sulfate adsorption/desorption, occurring between 0.4-0.8 V vs. RHE is responsible for the measured change in frequency over this range. Figure reprinted with permission from [202].

Importantly, in our study, the normalised absorbance intensity is not perfectly reversible between the anodic and cathodic sweep directions in both H_2SO_4 and KOH, but rather has considerable hysteresis at potentials corresponding to formation and reduction of gold oxide (Figure 4-12). In the anodic direction, a rapid drop in absorbance is observed at ~1.2 V, and ~1.1 V vs. RHE in H_2SO_4 and KOH electrolytes respectively (Figure 4-12) and is closely correlated with the onset of gold oxidation as observed on the cyclic voltammograms (Figure 4-7). The low absorbance remains until the reduction of the gold oxide begins at ~1.2 and ~1.3 V vs. RHE in H_2SO_4 and KOH electrolytes respectively (Figure 4-12) during the cathodic sweep direction. Continued gold oxide formation during initial stages of the downward scan, from 1.6 V to 1.2 V in the H_2SO_4 data, caused additional red-shifting of the SPR band, hence reducing the absorption intensity at the monitored wavelength.

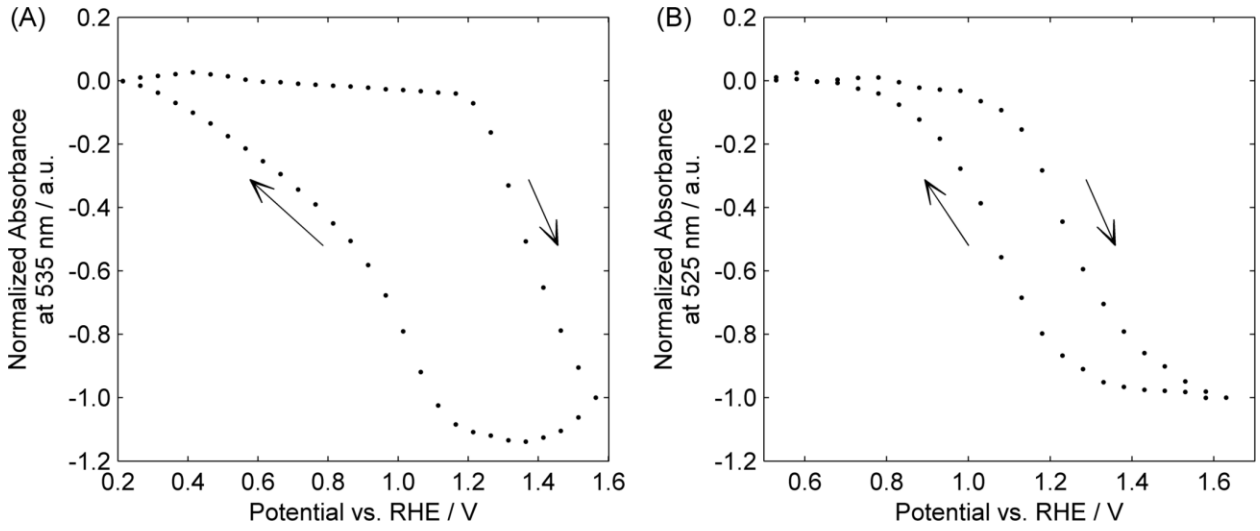

Figure 4-12. Normalised absorbance intensity data for nanoparticles in 0.5 M H_2SO_4 (A) at a wavelength of 535 nm, and nanoparticles in 1.0 M KOH (B) at a wavelength of 525 nm. The wavelength was chosen to be the peak wavelength when the particles were initially exposed to the electrolyte. Data has been averaged over four CV scans to reduce background noise within the data.

Despite the hysteresis, information can also be gathered when considering the symmetry of the normalised absorption plot. The asymmetry of the 0.5 M H_2SO_4 absorption plot (Figure 4-12A) indicates that after the gold oxide is reduced, a slow H_2O/sulfate adsorption exchange reaction is occurring during the remainder of the reverse scan. In contrast, the symmetrical absorption plot of the gold nanoparticles in 1.0 M KOH (Figure 4-12B) shows the SPR response to gold oxide formation via a decrease in absorption and a similar increase in absorption as the gold oxide is reduced. When considering the potential gap (i.e. the horizontal separation of the data points in the anodic vs. cathodic sweep directions) at a specific absorbance intensity, the hysteresis across these two regions is approximately 0.45 ± 0.05 V in the 0.5 M H_2SO_4 absorption plot during the gold oxide reduction region. The hysteresis is consistently measured to be 0.2 ± 0.04 V in the 1.0 M KOH absorption plot across the entirety of the plot. This indicates that the process causing the SPR absorption intensity decrease at the monitored wavelength is reversible with gold oxide reduction and ionic species desorption occurs in 1.0 M KOH at a similar rate to the gold oxide formation/adsorption that occurred during the anodic scan. It must be noted that the hysteresis separation of 0.2 V is also observed in the peak separation of the differential absorbance plot (Figure 4-13B) yet the separation of the gold oxide formation/reduction peaks in the CV (Figure 4-7) is approximately 0.33 V. It would be expected that if the SPR decrease is caused solely by gold oxide formation, the point of greatest rate of gold oxide formation (the CV peak at 1.38 V) would correlate to the point of greatest decrease (differential absorbance peak at 1.22 ± 0.02 V). As the differential absorption is greatest at a lower potential, this would indicate that the pre-oxide adsorption of H_2O/OH^- could be an important factor in the SPR decrease. The similarity of the oxide reduction peak on the CV scan (1.07 V vs. RHE) to the differential absorption peak on the cathodic scan (1.06 ± 0.02 V vs. RHE) indicates that either the gold oxide reduction, or the H_2O/OH^- desorption (which

occurs immediately after gold oxide reduction) could cause the SPR signal to return to its original state.

Comparing the above observations to the plot of normalised SPR absorption intensity as a function of potential in H_2SO_4 (Figure 4-12A), the asymmetric curve indicates that the process is not simply a reversal of the water adsorption/gold oxidation reaction that occurs during the anodic scan. The decrease in SPR absorption intensity at the monitored wavelength of 535 nm occurs at the same potential as the start of gold oxide formation according to the CV scan and, similarly, the increase in SPR absorption intensity occurs during the cathodic sweep at the same potential as gold oxide reduction begins according to the CV scan. However, there is an additional slow return of the SPR absorption intensity to the origin after the end of the gold oxide reduction peak at ~0.8 V, as shown in the CV scan. This reinforces the theory that adsorption of H_2O on the gold surface is causing the SPR decrease. While H_2O does adsorb to the gold surface in most electrolytes at potentials below the initiation of gold oxide formation, the competitive binding of the sulfate ions prevent H_2O adsorption, and hence, any SPR intensity decrease within the 0.2 V to 1.2 V region of the anodic scan. The rapid intensity decrease at 1.2 V occurs as the sulfate ions desorb and H_2O adsorbs followed immediately by gold oxide formation [251]. Immediately after gold oxide reduction in the cathodic scan, 95% of the maximum sulfate coverage is re-adsorbed yet the SPR absorption intensity plot does not go through a sharp intensity change, indicating that the sulfate ions do not influence the SPR absorption intensity.

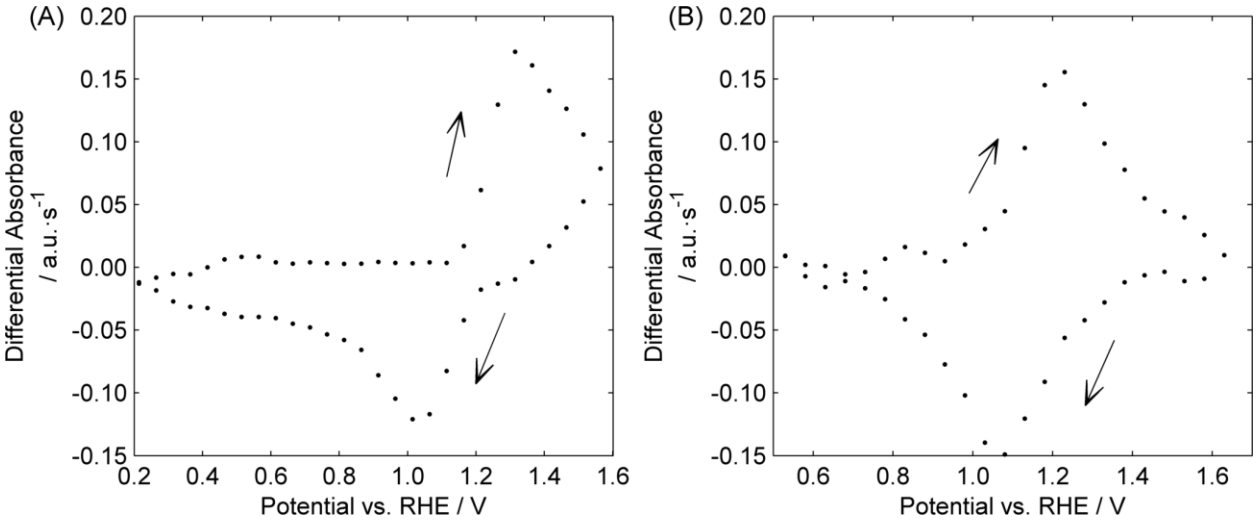

Figure 4-13. Differential of the normalised absorbance data for nanoparticles in 0.5 M H_2SO_4 (A) at a wavelength of 535 nm, and nanoparticles in 1.0 M KOH (B) at a wavelength of 525 nm. The wavelength was chosen to be the peak wavelength when the particles were initially exposed to the electrolyte. Data has been averaged over four CV scans to reduce background noise within the data.

Differentiating the absorption data (Figure 4-13A) shows that in the case of the H_2SO_4 data set, a remarkable similarity to its corresponding CV scan can be observed. The similarity arises, as already mentioned, due to the inhibition effects of the sulfate ions. As the anodic scan reaches 1.2 V, any bound H_2O can begin to oxidise the gold surface. Competition for adsorption sites between sulfate ions and H_2O shifts in favour of the H_2O as each time a H_2O molecule adsorbs, it oxidises the binding site at the surface of the gold. This leads to a rapid adsorption/oxidation reaction pathway and thus, causes the peak corresponding to the oxide formation at the gold surface in the differential of the SPR absorption intensity data. The gold oxide reduction/H_2O desorption occurs in reverse during the cathodic scan, with the sulfate ions preferentially adsorbing to the gold surface below ~1.2 V [251], once again inhibiting H_2O adsorption throughout the metallic region of the CV.

The resemblance to the CV is not apparent in the KOH data as there is no competitive adsorption to the gold surface. This means the H_2O/OH^- molecules/ions are available to oxidise the gold surface at a lower potential. The differential of the absorption data in KOH shows an increase in the rate of change of the SPR intensity prior to gold oxidation and a comparable rate change after the reduction of gold oxide. By observing these peaks at lower potentials for both processes we can confirm that the intensity changes are caused by oxygen species adsorbed to the surface rather than the direct oxidation or reduction of the gold surface.

4.3.5 Potential Dependence of the SPR Peak Maximum Wavelength

A single Lorentz curve was fitted to all SPR spectra to determine the SPR peak maximum wavelength for each data set at each time step. This was then plotted versus the electrode potential (Figure 4-14) to establish the amount of red-shift of the SPR band during anodic scanning, and blue-shift during cathodic scanning. As has already been described when considering the raw spectra (Figure 4-9), the SPR wavelength red-shift in H_2SO_4 appears to be a relatively constant 6.7 $nm \cdot V^{-1}$. This is comparable with the 8.6 $nm \cdot V^{-1}$ red-shift that Sagara et al. [260] measured on 11 nm citrate-capped gold nanoparticles over a potential range of 0.1 to 1.1 V vs. RHE. Additionally, we must also consider if the formation/reduction of gold oxide or adsorption/desorption of molecules is causing a red- or blue-shift of the SPR feature.

In the same way that the SPR absorption intensity will continue to decrease at the start of the cathodic scan in the H_2SO_4 data set, a small amount of hysteresis develops during the initial stages of the cathodic scan in the SPR peak wavelength data set. This is caused by additional gold oxidation continuing to produce red-shifting of the SPR band, counteracting the potential-based blue-shift. While the same effect is seen with the KOH data, the magnitude of the hysteresis is increased, perhaps due to a larger relative proportion of OH^- ions from the alkaline solution adsorbed (relative to H_2O molecules in the acidic solution) prior to gold oxide formation, thus delaying electron density changes in the gold surface until the formation has begun. Comparatively, in H_2SO_4, sulfate adsorption may be causing an electron density change in the gold surface meaning once gold oxide

formation begins, the substitution of sulfate ions for H_2O/OH^- is not represented in the red-shift of the SPR peak. It must be noted at this point that while the formation/reduction of gold oxide in H_2SO_4 is very closely aligned with the SPR intensity changes, it did not *appear* to affect the SPR wavelength in the SPR peak wavelength plot.

The alignment of the SPR peak wavelength to the gold oxide formation/reduction regions of the CV scan is seen most apparently in the KOH data when considering the differential of the wavelength versus potential data (Figure 4-15B). In a similar fashion to the differential of the SPR intensity of the H_2SO_4 data (Figure 4-13A), this differential of the wavelength bears a striking resemblance to the gold oxide formation/reduction region of the electrochemical CV scan. The alignment of the differential of the wavelength and the CV scan (Figure 4-20A) shows that the SPR wavelength is unaffected by the adsorption of H_2O/OH^- prior to surface oxidation, instead, any red- or blue-shift occurs simultaneously with during the oxidation or reduction of the gold surface. The cathodic currents measured on the CV below 0.9 V do not appear in the differential of the wavelength data. This leads to the conclusion that the reaction occurring at the lower potentials (presumably oxygen reduction) is not affecting the electronic density of the gold surface, and hence, not affecting the SPR feature.

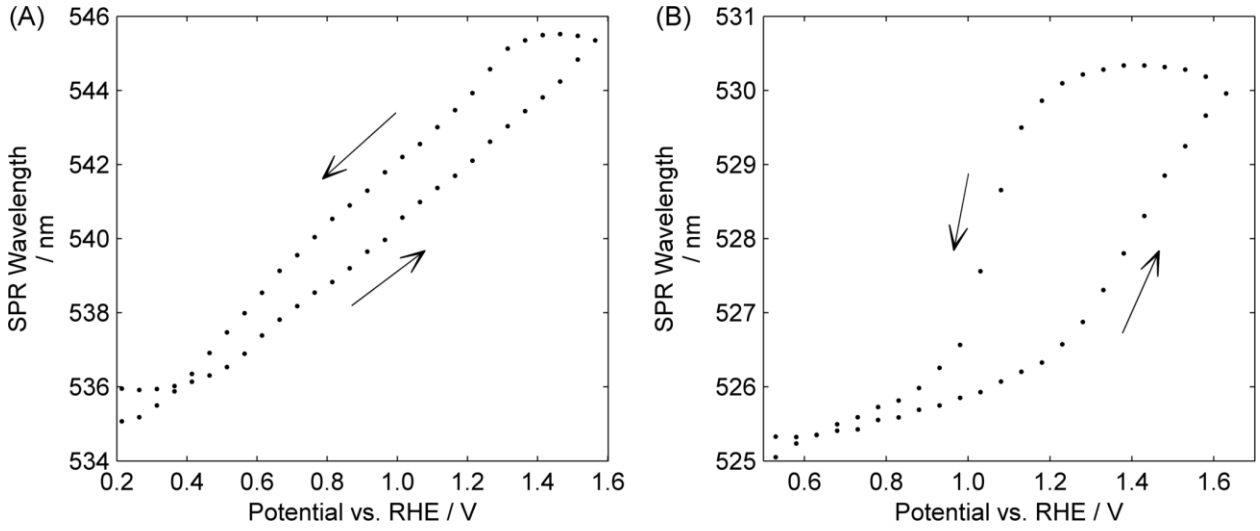

Figure 4-14. SPR peak maximum calculated by a single Lorentz peak fit to the raw UV-Vis spectra for nanoparticles in 0.5 M H_2SO_4 (A), and nanoparticles in 1.0 M KOH (B). Data has been averaged over four CV scans to reduce background noise within the data.

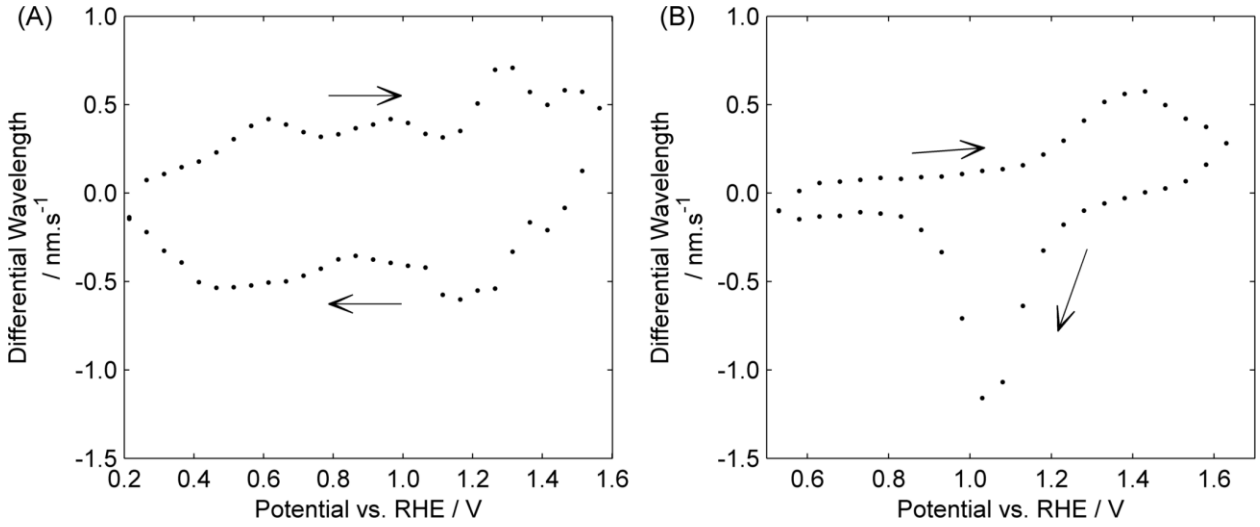

Figure 4-15. Differential of the SPR peak maximum calculated by a single Lorentz peak fit to the raw UV-Vis spectra for nanoparticles in 0.5 M H_2SO_4 (A) and nanoparticles in 1.0 M KOH (B). Data has been averaged over four CV scans to reduce background noise within the data.

Analysing the differential of the wavelength data in H_2SO_4 (Figure 4-15A) proves to be more problematic due to sulfate adsorption. Interestingly, while the sulfate adsorption is not apparent in the SPR absorption intensity or differential absorption intensity data (Figure 4-12A and Figure 4-13A), the differential of the SPR wavelength (Figure 4-15A) suggests that the sulfate adsorption does induce a peak wavelength change of the SPR band.

As previously discussed, sulfate begins to adsorb to gold surfaces around 0.5 V in a binding configuration that has been theorised to be either bidentate or tridentate [238]. At 0.75 V, H_2O begins to adsorb to the sulfate ions. At approximately 1.1 V, the sulfate-H_2O complex goes through a disorder-order transition [250]. These processes do not directly involve the transfer of electrons, and hence are difficult to identify on a typical electrochemical CV scan. Despite not being able to use the CV scan to identify the adsorption and transition potentials, it may be possible to investigate them further using the differential of the wavelength data. Two peaks on the differential data are apparent between 0.5 V and 1.15 V, which corresponds very closely to the potential associated with sulfate adsorption. As these peaks are of a similar magnitude to the gold oxide-induced SPR red-shift, any prospective resemblance to the electrochemical CV scan is lost. However, the information these peaks provide has the ability to open new avenues of investigation for surface reactions such as sulfate adsorption on electrode surfaces as described here.

4.3.6 Observations of the Glycerol Oxidation on Gold Nanoparticles

The anodic currents associated with the oxidation of glycerol on a gold surface are often larger than the gold oxide formation/reduction features and hence, mask the associated anodic/cathodic currents (Figure 4-16 cf. Figure 4-7). This leads to a loss of information of how the presence of glycerol alters the formation or reduction of gold oxide. Despite the loss of direct electrochemical information about gold oxide, several groups have

shown an inhibition of gold oxide formation in the presence of adsorbates such as alkoxides and aldehydes [247] or ethylene glycol [261] using secondary methods such as E-QCM. In contrast, Pt-Au nanoparticles have been used to show the presence of adsorbed methanol will promote the formation of gold oxide [262]. Our team has previously suggested that the presence of glycerol oxidation products such as glycerate will inhibit gold oxide formation by up to 0.1 V [57].

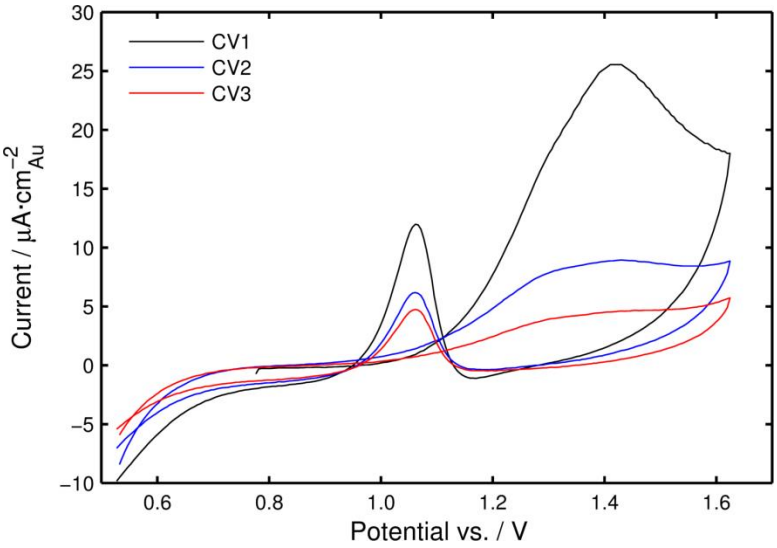

Figure 4-16. The first three CV scans of gold nanoparticles, adsorbed to FTO in a solution of 1.0 M KOH and 0.1 M glycerol.

The techniques used to produce the SPR absorption intensity and peak wavelength plots discussed in the H_2SO_4 and KOH results were applied to time-resolved UV-Vis spectra measured using solutions of 1.0 M KOH and a range of concentrations of glycerol. It was found that with a 0.5 M glycerol solution, changes in the UV-Vis spectra were only seen during the first CV scan while using higher concentrations showed the response did not produce a regular cycle and had no apparent relationship with the CV scan or electrode potential. A solution of 1.0 M KOH and 0.1 M glycerol showed a clear, cyclic UV-Vis response during the first two CV scans only (Figure 4-17), that is, the SPR absorption intensity was expected to decrease during the gold oxide region of the CV, followed by an increase in intensity during gold oxide reduction. The overall downward trend of the SPR absorption peak was not seen in the case of the KOH/glycerol data, however, variations larger than that associated with the underlying signal noise were seen throughout the experiments. This, along with the loss of cyclic information, and the diminishing glycerol oxidation currents in the CV scans implies that the gold nanoparticles are being deactivated rather than desorbed from the FTO surface or dissolved into the solution. This could be due to the layer not being fully reduced through oxide reduction inhibition [57], or through poisoning of the gold surface by glycerol oxidation products [56].

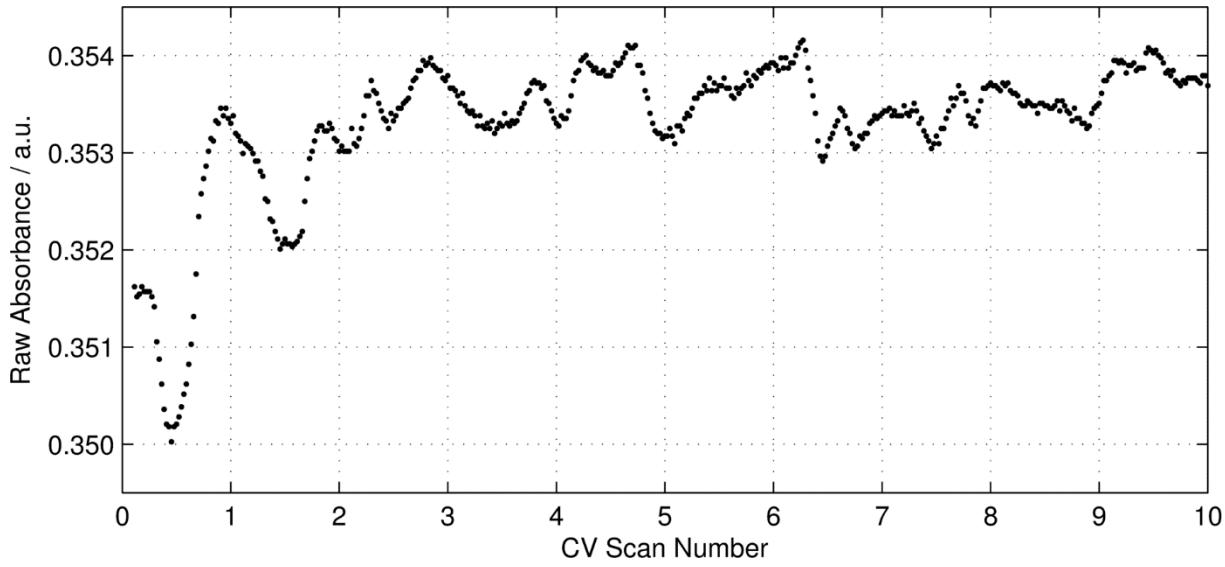

Figure 4-17. The UV-Vis absorbance at 540 nm during the first 10 CV scans of gold nanoparticles, adsorbed to FTO, in a solution of 1.0 M KOH and 0.1 M glycerol.

As the raw absorbance data (Figure 4-17) had no cathodic or anodic 'baseline', the data could not be normalised or averaged over the first four CV scans. The raw absorbance intensity at 540 nm, when plotted versus the electrode potential (Figure 4-18A), showed a decrease in intensity around potentials at which gold oxide is expected to form, and a corresponding increase in absorbance during the reverse cathodic scan. While additional information is difficult to identify in this plot, the differential absorbance for the first CV scan (Figure 4-18B, black line) shows an 'anodic' peak around 1.25-1.30 V and a 'cathodic' peak at 1.15 V. Subsequent CV scans demonstrate the reduction in data quality, although the 'cathodic' peak at 1.15 V is still identifiable in the second CV scan (Figure 4-18B, blue line).

Similarly, the maximum wavelength of the SPR feature was fitted to a Lorentz curve for each spectrum (Figure 4-19A). These results are similar to the glycerol-free H_2SO_4 and KOH results, with a red-shift during the anodic scan and a blue-shift during the cathodic. As with the differential absorbance data, during the first CV scan, the differential SPR wavelength shows both an 'anodic' and a 'cathodic' peak corresponding to gold oxide formation and reduction, respectively. Additionally, similar to the KOH differential wavelength plot (Figure 4-15B), other reactions on the surface of the gold do not appear in the differential absorbance or differential wavelength plots. This suggests that the glycerol oxidation reaction (including adsorption or desorption) is not affecting the electron density of the gold nanoparticles or refractive index of the surrounding medium.

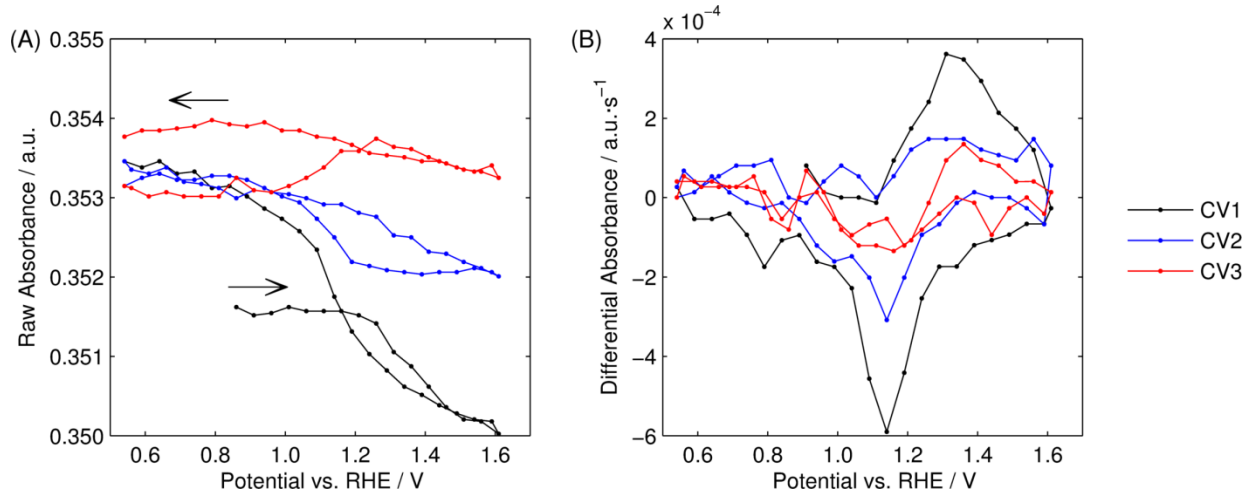

Figure 4-18. The absorbance intensity (A) and differential absorbance intensity (B) in relation to the potential of gold nanoparticles in a solution of 1.0 M KOH and 0.1 M glycerol. Due to the lack of cyclic regularity, the data has not been normalised or averaged over successive CV scans.

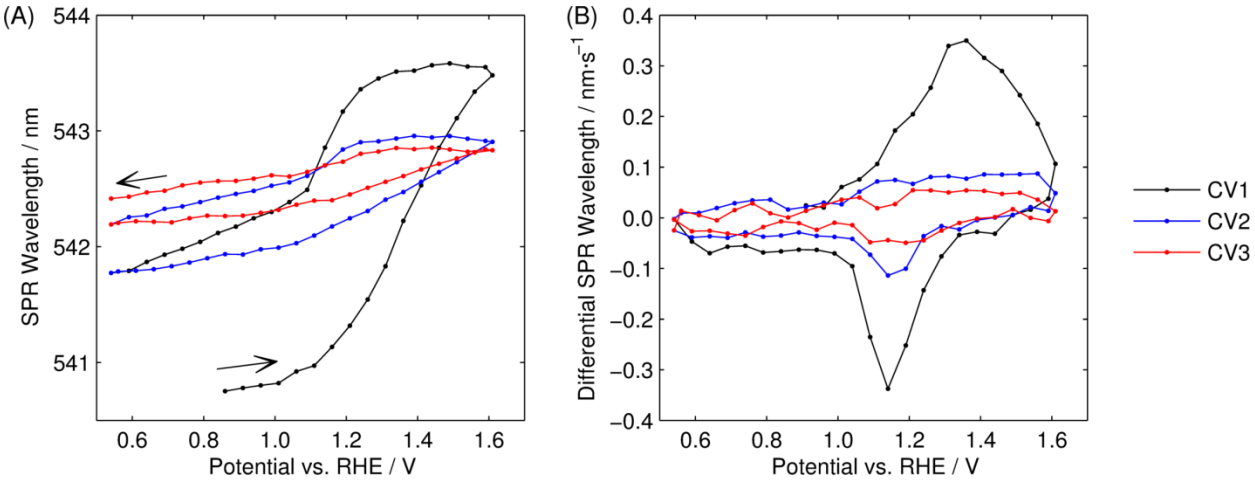

Figure 4-19. The SPR wavelength (A) and differential SPR wavelength (B) in relation to the potential of gold nanoparticles in a solution of 1.0 M KOH and 0.1 M glycerol. Due to the lack of cyclic regularity, the data has not been averaged over successive CV scans.

By overlaying plot of the differential wavelength of the SPR feature as a function of potential with the CV scan in KOH both with and without glycerol, the changes to the gold oxide formation/reduction behaviour due to the addition of glycerol can be seen (Figure 4-20). By observing the differential wavelength data (Figure 4-20A), it can be seen that in the absence of glycerol, the gold oxide formation peak appears at 1.38 V and the gold oxide reduction peak appears at 1.05 V, a potential gap of 0.33 V. In the presence of 0.1 M glycerol, gold oxide formation peak appears at a lower potential of 1.36 V while the reduction peak feature shifts to 1.14 V, a potential gap of 0.22 V.

These results show that the presence of glycerol in this system will increase the reversibility of the gold oxide formation/reduction reaction by reducing the potential of the forward reaction by 0.02 ± 0.01 V and increasing the potential of the reverse reaction by

0.09 ± 0.01 V (Figure 4-21). This promotion of the gold oxide reduction reaction is contradictory to the hypothetical 0.1 V inhibition previously postulated by our group [57]. The apparent inhibition is seen in the overlay of the CV scans of the two solutions (Figure 4-21A) where the glycerol oxidation peak on the forward scan occurs after the gold oxide formation peak, however, according to the data in the differential wavelength plot (Figure 4-21B), the gold oxide formation reaction is occurring at lower potentials. While the mechanism for the promotion is unknown to us, the spectroscopic observation of the previously unobserved gold oxide behaviour provides a new technique for researchers to view the underlying gold oxide formation and reduction peaks while conventional electrochemistry monitors catalytic reactions.

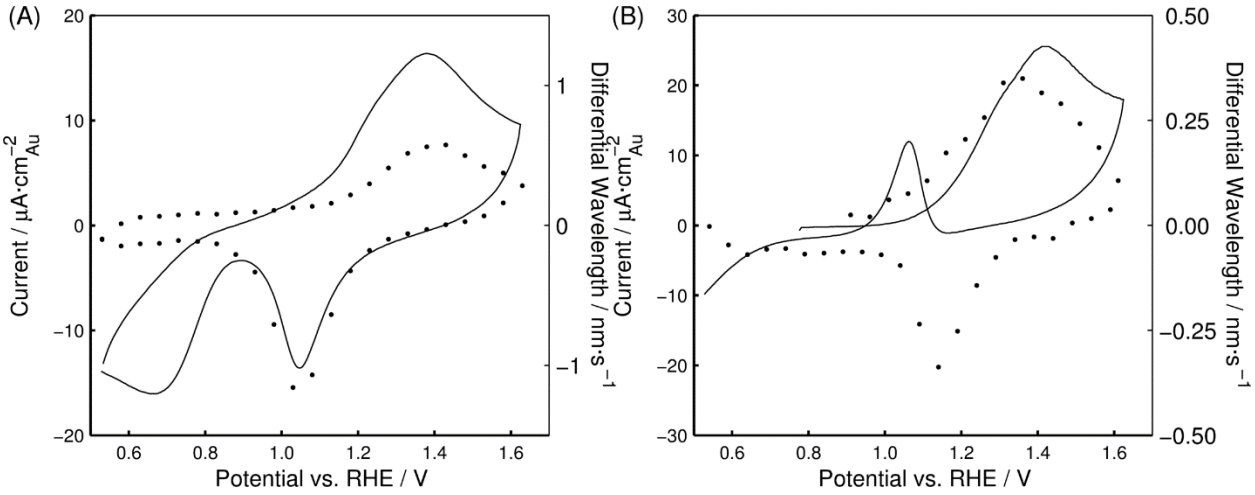

Figure 4-20. A comparison of the CV scan (solid line) and differential SPR wavelength (·) for gold nanoparticles in (A) 1.0 M KOH and (B) 1.0 M KOH and 0.1 M glycerol.

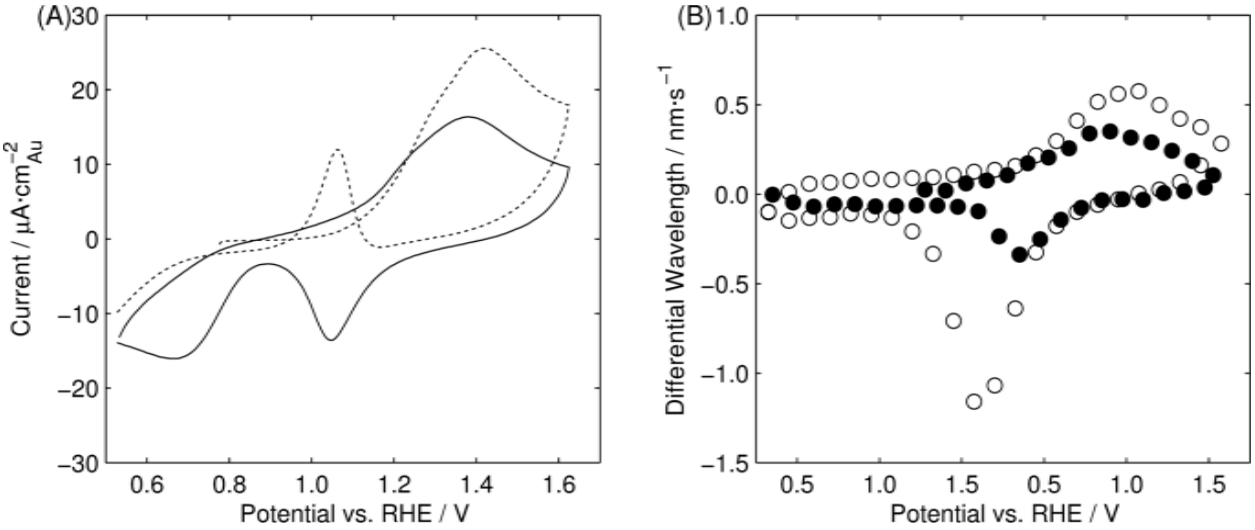

Figure 4-21. (A) Overlay of the 1.0 M KOH CV (solid line) and 1.0 M KOH + 0.1 M glycerol CV (dotted line). (B) Overlay of the differential wavelength for 1.0 M KOH (○) and 1.0 M KOH + 0.1 M glycerol (●).

4.4 Summary

By utilising the SPR absorption intensity or band maximum wavelength properties, a spectroscopic CV such as the differential of the SPR intensity and the differential of the SPR wavelength has been found to be very useful when probing surface reactions. The inhibition of, and the SPR intensity reduction effects of the adsorption of H_2O on the gold nanoparticle surface can be seen in the SPR intensity and differential of the SPR intensity data of gold in 0.5 M H_2SO_4. The adsorption of sulfate ions and subsequent surface transitions are apparent in the differential of the wavelength data providing another avenue for future research in the surface binding of molecules on nanoparticles.

Gold oxide formation and reduction, and the corresponding electron density changes are visible in the red-shift/blue-shift of the SPR wavelength of gold in 1.0 M KOH via the differential of the wavelength. This SPR wavelength correlation is not as apparent in 0.5 M H_2SO_4 due to the comparative electronic effects of the sulfate ion adsorption to the gold oxide formation. Comparisons of the experimental results with the expected SPR changes described by the Mie theory indicate that changes in the SPR wavelength and peak intensity are not adequately explained by changes in the refractive index of the gold oxide or electrolyte medium.

The techniques used to produce the spectroscopic CV scans in the pure electrolyte solutions were applied to a solution of 1.0 M KOH and 0.1 M glycerol. It was found that the presence of glycerol is not directly seen on any of the UV-Vis potential-absorbance intensity or potential-wavelength plots, indicating that the catalytic oxidation of glycerol does not directly affect the gold surface electron density. The gold oxide formation reaction is seen to be promoted by 0.02 ± 0.01 V while the corresponding reduction reaction is promoted by 0.09 ± 0.01 V. This leads to narrowing of the peak separation of the gold oxide formation/reduction reactions from 0.33 V in the KOH electrolyte to 0.22 V in the KOH/glycerol electrolyte.

Results reported here have opened a new pathway for the investigation of electrode surface chemistry, whether it is investigating surface binding as shown with the H_2SO_4 data, or investigating the promotion or inhibition of the gold oxide formation reaction as shown with the KOH/glycerol data.

Chapter 5 REDUCTION OF CO_2 ON ELECTRODES CONTAINING GOLD NANOPARTICLES

5.1 Introduction

5.1.1 Carbon Dioxide and the Atmosphere

Greenhouse gases are continuing to be problematic to the future of Earth. In the past century, the CO_2 concentration in the atmosphere has increased from 285 ppm in the early 1900's to over 400 ppm today, where it is still growing [67]. The atmospheric CO_2 growth rate has increased from 0.75 ppm per year in 1959 to 1.86 ppm per year in 2000 where it has remained through to recent recordings in 2014 [263]. This flattening of the growth curve is the beginning to reducing the impact of climate change on Earth; however, in order to lower the atmospheric CO_2 concentration, we must decrease the emission of greenhouse gases either by reducing their production or by removing them from the waste gases.

A summary of the recent history of CO_2 emissions in the "Global Carbon Budget 2016" [264] shows that 470-590 gigatonnes of carbon have been released into the Earth's atmosphere since the beginning of the industrial revolution. Approximately 27% of these emissions have been removed by plant and soil based absorption and a further 30% through ocean-based uptake, however, the remaining 42% has accumulated in the atmosphere. While plant-based CO_2 removal may be relatively benign, ocean acidification is putting shell- and coral-based lifeforms at risk while climate change is producing a feedback loop through mechanisms such as melting ice releasing additional greenhouse gases.

These CO_2 releases, along with the increasing levels of other greenhouse gases such as methane, nitrous oxide and chlorofluorocarbons are of major concern to the environment of Earth. These gases, by virtue of their chemical structure, are a major cause of the climate change crisis that is currently sweeping the planet. Annually, over 44.8 Gt-CO_2e[3] of greenhouse gases are released due to human-based activities. If this was converted into solid carbon, it could cover Christchurch in a 2.5 m thick layer of diamond in a year, or fill five average New Zealand houses with charcoal every second. As a comparison, if the CO_2

[3] Greenhouse gases have different "global warming potentials" and are thus normalized to an equivalent volume of CO_2, expressed as "CO_2e".

remains as a gas at ambient temperature and pressure, it would cover New Zealand to a depth of 65 m every year.

CO_2 emissions from the electricity/heat and industrial sectors are typically generated at a fixed location via the combustion of hydrocarbons. These two sectors make up almost half of the total CO_2 emissions worldwide (Figure 5-1) and are a prime target for emission reduction strategies. By capturing greenhouse gases at their source, their release into the atmosphere is prevented; this is typically achieved by sequestration methods such as underground injection into porous rock formations. There are potential risk factors in these storage methods as the CO_2 still has potential to be released into the environment; however, this is minimised by specific selection of the sequestration rock where there is a non-porous, capping layer of a secondary rock creating a physical barrier to prevent release to the atmosphere.

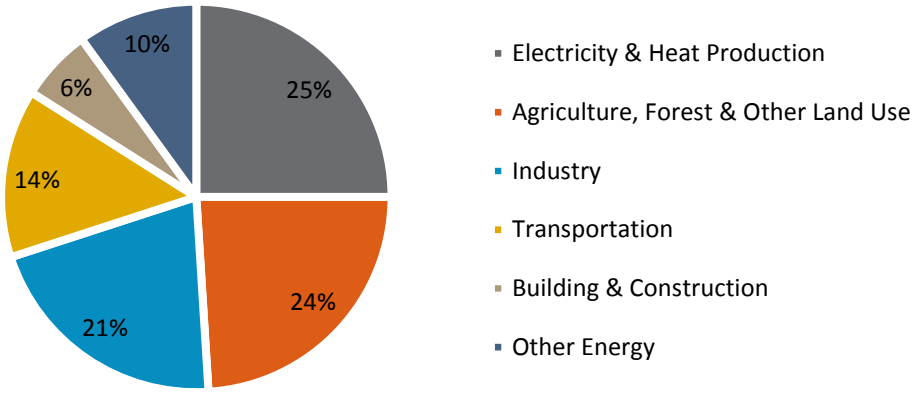

Figure 5-1. Global CO_2 emissions from 2010 separated by sector [265].

As of the end of 2015, there were 15 industrial-scale carbon capture and storage (CCS) facilities operating globally, with an additional 17 projects in their advanced planning or construction phases. The operational facilities have a total capacity of 0.028 Gt-CO_2 storage per year, with significant investment required to reach the 0.54 Gt-CO_2 storage by 2025 required by the IEA to meet their "2°C Scenario" [266]. While these CCS facilities are reducing the global CO_2 release, other methods such as electrochemical CO_2 reduction have been investigated to return the carbon component to a more useable state.

Carbon capture can take the form of physical or chemical absorption, physical separation, and cryogenic separation. Gas storage can then take the form of terrestrial sequestration, ocean sequestration, depleted oil/gas reservoir sequestration, or as solid CO_2. Alternatively, the captured gas can be chemically converted into useable products or used as a feedstock for bacterial or algae growth which can then be used as a biofuel [267]. These processes all have an inherent economical cost associated with them, discouraging their implementation by the producers. For this reason, as a part of the Kyoto Protocol,

governments have created a limited supply of 'carbon credits' to establish an economic cost to greenhouse gas emission. The increased cost of emitting greenhouse gases generates an interest in emission reduction, hopefully producing a "*stabilisation of greenhouse gas concentrations in the atmosphere at a level that would prevent dangerous anthropogenic interference with the climate system*" [268].

While the reduction of CO_2 and other greenhouse gases could be achieved through technological advancement effectively rendering fossil fuels obsolete, the infrastructure of the modern world relies heavily on fossil fuels and will take time to change without significant disturbance to society. Major producers of CO_2 emissions include electricity/heat production (25%), industry (21%), agriculture (24%) and transportation (14%) [265], of which the first two produce concentrated greenhouse gases at a centralised location. If these producers are able to capture and store waste gases via CCS, thereby preventing their release into the atmosphere, there is the potential for the elimination of just under 50% of the annual greenhouse gas emissions worldwide.

5.1.2 Utility of Carbon Dioxide

The oxidation or combustion of organic molecules will inevitably lead toward the formation of CO_2 whereupon it can no longer be oxidised under normal conditions (Figure 5-2A). The final CO_2 product implies that without a way to remove it from the system (in this case, the Earth and its atmosphere), the concentration will continue to increase continuously. This causes concern when considering CCS as a means of carbon storage; the CO_2 is only being prevented from entering the atmosphere, not being removed from the entire system. While carbon sequestration methods currently provide the largest capacity for CO_2 storage, they are inherently flawed as they are prone to gradual release through seepage and diffusion, or sudden release due to geological events such as earthquakes [269].

In all of the CCS processes, energy is required in order to capture and recycle or store CO_2. Rather than burning fossil fuels to produce this energy, renewable power sources such as tidal, solar or wind generators can be used. These renewable energy sources are fundamentally variable, often with an element of unpredictability; however, the energy recovered from these sources can be stored either in a battery or as a chemical energy carrier. By reducing CO_2 using a renewable energy source, it can be chemically converted in an environmentally friendly approach back into a useable fuel source, e.g. CO, CH_4, CH_3OH or HCOOH (Figure 5-2B).

5.1.3 Carbon-Based Catalysis

The reduction of CO_2 into a useable fuel has garnered a lot of attention over the past decade [4, 21, 45, 74, 110]. While the final oxidation product of organics is CO_2, the reduction products of CO_2 can conceivably consist of any carbon-based molecule (Figure 5-2). The mechanism and final products of CO_2 reduction depend on the reactant availability, the reaction conditions, and the presence and type of catalyst. For example, Christophe, Doneux and Buess-Herman [270] studied the reaction products of CO_2 reduction on copper/gold catalysts and showed that a copper electrocatalyst produced CO

and CH_4 as its main products, while the copper-gold alloy catalysts produced more CO and less CH_4 as a function of the gold content. A gold catalyst in the same study produced only CO.

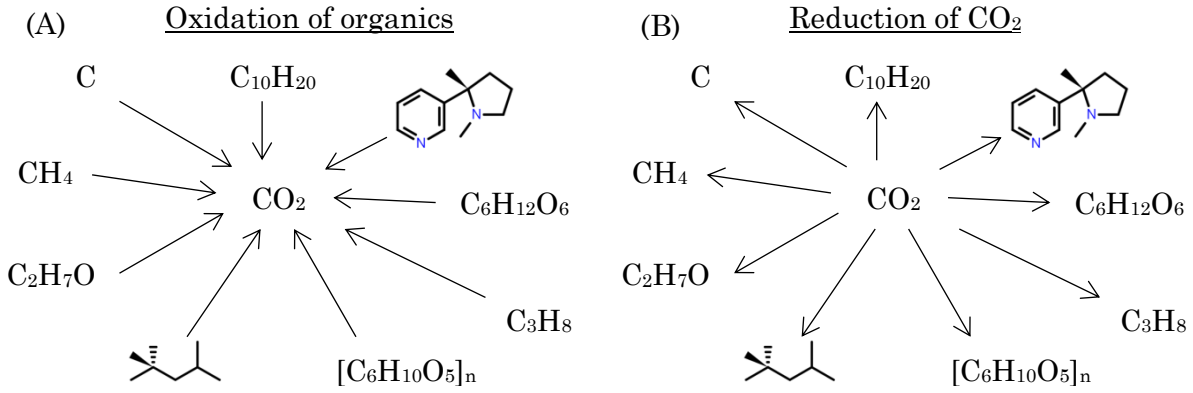

Figure 5-2. A brief depiction of how all organics will oxidise towards the stable CO_2 molecule (A), however, reduction of CO_2 can conceivably produce any organic molecule (B).

By adjusting the reaction conditions to produce the desired organic product, the usefulness of the chemical reduction of CO_2 can begin to be realised. For example, using a gold-based catalyst will essentially produce CO as the main product of the CO_2 reduction reaction (Equation 5-1). A chemical storage process can then be developed around the use of CO either as energy storage or by using CO as a precursor in additional chemical reactions (Figure 5-3). Effective use of a catalyst will minimise the energy demand of the conversion processes, resulting in a more efficient energy storage system.

$$CO_2 + 2H^+ + 2e^- \rightleftharpoons CO + H_2O \qquad 5\text{-}1$$

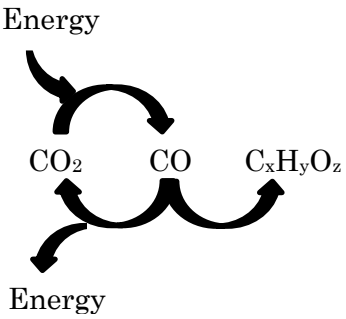

Figure 5-3. The energy storage/use cycle from CO_2 capture and chemical conversion.

5.1.4 Carbon Dioxide Reduction

The reduction of CO_2 can have two distinct targets; either conversion into a fuel to reduce global dependencies on oil reserves, or conversion into industrially useful chemicals, such as methanol (total annual production > 70 million tonnes). The best way to attain the CO_2 for reduction is by capturing the gas on-site, at high concentrations and while CO_2 capture from the atmosphere does have some interesting upcoming research [271-273], the

low CO_2 concentration compared to an industrial setting has been shown to be a significant disadvantage to this method of carbon capture.

Table 5-1. Energy density of various CO_2 reduction products.

Name	Formula	LHV / MJ · kg^{-1}
Carbon Dioxide	CO_2	0
Formic Acid	HCOOH	5.55
Carbon Monoxide	CO	10.11
Formaldehyde	HCHO	19.02
Methanol	CH_3OH	19.93
Carbon	C	32.80
Methane	CH_4	50.01

Reduction of CO_2 into a fuel source is focused on increasing the energy density of the fuel (Table 5-1) and can go through many intermediates, and different pathways. For example, the production of methane has been shown to occur on different catalysts, through different pathways where each step in the pathway involves the transfer of two electrons, e.g.;

$$CO_2 \rightarrow HCOOH \rightarrow HCHO \rightarrow CH_3OH \rightarrow CH_4 \qquad 5\text{-}2$$

$$CO_2 \rightarrow CO \rightarrow C \rightarrow CH_2 \rightarrow CH_4 \qquad 5\text{-}3$$

For these specific reaction pathways, pathway (Equation 5-2) occurs when the reaction proceeds in a condensed media [274] and pathway (Equation 5-3) occurs when reacting CO_2 via photocatalysis on TiO_2 [275]. The specific pathway and final reaction products will depend on both the reaction conditions and the catalyst involved as the choice of the catalyst have a major effect on the carbon chemistry. For example, electrochemical CO_2 reduction on gold and silver will, in most cases, terminate in a CO product whereas copper and chromium based catalysts can have methane as the major product (Table 5-2).

Table 5-2. The two principal carbon-based products from CO_2 reduction in 0.05 M $KHCO_3$ at 0 °C and -1.3 V vs. RHE [69].

Catalyst Metal (bulk)	Primary Carbon Product (Current Efficiency / %)		Secondary Carbon Product (Current Efficiency / %)	
Cr	CH_4	(0.74)	CO	(0.49)
Cu	CH_4	(24.7)	CO	(16.5)
Ag	CO	(40.7)	HCOOH	(20.5)
Sn	HCOOH	(28.5)	C_2H_4	(0.95)
Ir	HCOOH	(1.0)	CO	(0.53)
Au	CO	(16.9)	HCOOH	(10.3)
Pt	HCOOH	(5.5)	CO	(1.2)
Pb	HCOOH	(16.5)	CH_4	(0.39)

Two main metal catalysts used for catalytic carbon chemistry are gold and platinum. This is a result of their high affinity for carbon due to their electronic structure and interatomic bond lengths. However, a major disadvantage to platinum chemistry is that if it is used industrially, it can be poisoned by CO as well as sulfur-based compounds. This poisoning reduces the availability of reaction sites and the catalyst must be regenerated before it is used again. While gold can be poisoned by sulfur-based compounds, it does not have this disadvantage with regards to CO, making it a desirable catalyst for CO_2 reduction.

5.1.5 Carbon Dioxide Reduction Reactors

CO_2 reduction is catalysed via three main types of catalysis; photocatalysis, gas-phase heterogeneous catalysis and electrocatalysis. Photocatalysis can be performed in a fluidised bed reactor, slurry reactor, honeycomb monolith/annular reactor, concentrated solar reactor etc. [276]. Two main design criteria are essential to a photocatalytic CO_2 reduction reactor; (1) whether to have a fluidised catalyst or fixed bed and (2) whether to have concentrated solar irradiation, ambient solar irradiation or an artificial light source. As the CO_2 conversion rate and final product distribution are heavily dependent on the quantity and quality of the incident light, reactor designers tailor their reactor around these criteria, along with the final criteria: the nature of the catalyst to be used.

The most well-known reactor for CO_2 reduction using a heterogeneous catalyst is the "Sabatier reactor" where CO_2 is reduced in the presence of H_2 to form CH_4 and water [277]. This is performed on a nickel catalyst at temperatures of 250-400 °C. NASA installed a Sabatier reactor on the ISS in October 2010 as a means to scrub the astronaut's atmosphere of CO_2 and to produce a fresh supply of water (Equation 5-6). The hydrogen required for the reaction is provided from the water electrolysis (Equation 5-4) used for oxygen generation. Furthermore, by adding a pyrolysis reactor (Equation 5-7), astronauts will be able to reduce the methane to carbon + hydrogen, forming an almost completely closed cycle [278].

$$2H_2O \xrightarrow{\text{electrolysis}} 2H_2 + O_2 \qquad 5\text{-}4$$

$$O_2 + C \xrightarrow{\text{respiration}} CO_2 \qquad 5\text{-}5$$

$$CO_2 + \overbrace{2H_2}^{\text{from (5-4)}} + 2H_2 \xrightarrow{\text{Sabatier}} 2H_2O + CH_4 \qquad 5\text{-}6$$

$$CH_4 \xrightarrow{\text{pyrolysis}} C + 2H_2 \qquad 5\text{-}7$$

5.1.5.1 Electrocatalytic Carbon Dioxide Reduction

Electrocatalytic reactors are also used to achieve higher yields than photocatalytic reactors [279] and are able to be run at lower temperatures than heterogeneous reactors [280]. These electrocatalytic reactors use a fixed catalytic layer and apply an electric potential to drive the reduction reaction. As with the photocatalytic reactor, the CO_2 can be delivered to the catalyst surface either dissolved in an electrolyte, or in its gaseous form in

an electrochemical cell that has been based on solid electrolytes. The choice of catalyst, catalytic layer formation, reaction conditions and the potential of the applied current will all affect the catalyst activity, selectivity and end-products of the reaction, leading to many possible types of reactors and catalytic conditions [69].

In this chapter, the reduction of CO_2 on gold nanoparticles in an electrocatalytic reactor is investigated via two distinct sets of experiments performed on the Au/C catalyst. In the first set of experiments the Au:C ratio was varied by diluting the Au/C catalytic ink with a carbon black ink. In the second set of experiments the catalytic layer thickness was varied while keeping the Au:C ratio constant at 15.1 wt% Au. Comparisons were made to a bulk gold plate, as well as a carbon black electrode layer and the bare titanium substrate disc.

5.2 Experimental

5.2.1 Catalyst Preparation

Gold nanoparticles were prepared according to the Weare method [91], outlined in Chapter 3 and Appendix 1. Au/C ink was prepared by adding an appropriate volume of the 0.5 $mg \cdot mL^{-1}$ Nafion in a 4:1 IPA:DI water solution to a 15.1 wt% 3.2 nm Au/carbon catalyst, prepared as described in Appendix 1.1.4. The catalyst was suspended in the ink by ultrasonication for 30 minutes. A fresh surface on a titanium disc was produced by sanding with 320 grit sandpaper, ultrasonication and baking at 120 °C for 30 minutes. The disc was then heated to 80 °C and the catalytic ink was spray coated onto the fresh surface. The disc was then baked at 120 °C for 15 minutes to ensure any remaining IPA and water was evaporated out of the catalytic layer. The cooled disc was weighed before and after the application of the catalytic layer to determine the layer mass and by extension, the layer thickness.

5.2.2 Cell preparation

0.2 M $KHCO_3$ (99.7% ACS reagent, Sigma-Aldrich) was saturated with CO_2 by bubbling 50 $mL \cdot min^{-1}$ CO_2 through 150 mL of the solution until a stable pH of approximately 6.98 was recorded. The reaction cell was set up as previously seen [281] using a two-chamber, three electrode H-type cell (Figure 5-4) filled with the CO_2 saturated $KHCO_3$ solution. The two chambers were separated by a Nafion 115 cation exchange membrane, allowing for the transfer of K^+ ions while minimising the migration of CO_2 reduction products from the catholyte chamber to the anolyte chamber. A Ag/AgCl reference electrode and platinum foil counter electrode (A = 18 cm^2) were used for all experiments. During the electrochemical measurements, the catholyte was continuously bubbled with CO_2 at a rate of 10 mL min^{-1} to ensure that the electrolyte remained saturated with CO_2 and to transfer the gaseous products to the GC for analysis.

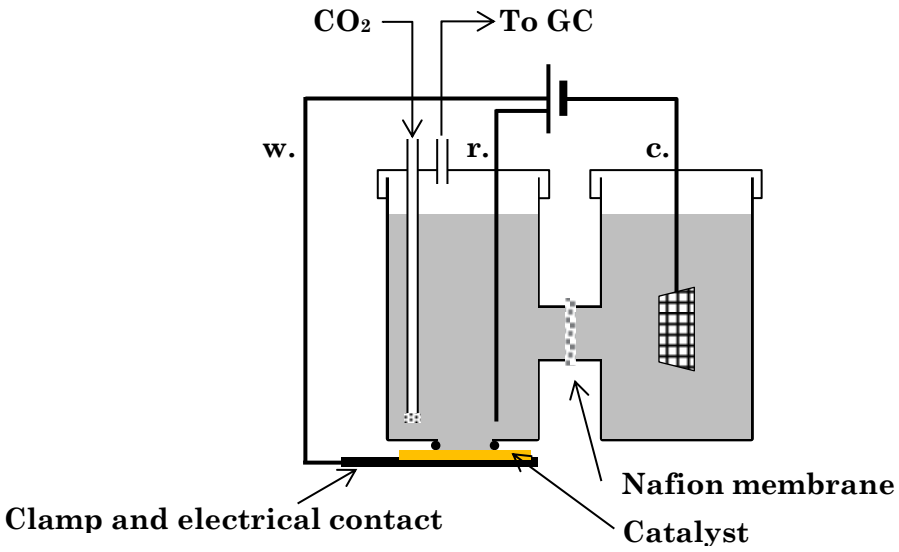

Figure 5-4. Cell layout for the CO_2 reduction experiments. A Nafion membrane separates the working and counter electrodes to prevent oxidation of any CO_2 reduction products on the counter electrode. CO_2 was flowed through a bubbler at 10 mL· min^{-1}.

5.2.3 Electrochemistry

A Gamry Reference 3000 potentiostat was used to perform CO_2 reduction via galvanostatic measurements by applying a constant current of -15.71 mA (-5 mA · cm^{-2}_{geo}) to the cathode for four hours. The solution resistance increased over time due to the movement of K^+ ions through the membrane. As such, the solution resistance was measured via P-EIS every 15 minutes at -5 mA · cm^{-2} with a potential amplitude of 5 mV rms and a frequency range of 100 kHz to 10 Hz to allow for post-run IR correction. Gas products were measured every 15 minutes via an in-line GC (SRI Instruments, methanizer FID and TCD detectors, Haysep-D column) equipped with an auto-sampler and products in the liquid phase were measured via a single HPLC measurement (using a SUPELCOGEL C-610H column) at the conclusion of the experiment.

5.3 Results

5.3.1 Cyclic Voltammetry in 0.2 M $KHCO_3$

For comparison to the behaviour of the bulk gold electrode, and to ensure that appropriate potential limits were used during CV experiments, cyclic voltammetry testing was first performed on a bulk gold plate (A = 3.14 cm^2) in CO_2 saturated 0.2 M $KHCO_3$. The CV scans of the bare gold plate, run at 50 mV · s^{-1} with a maximum potential of 1.4 V vs. RHE, showed the gold oxide reduction peak at 0.69 V vs. RHE (Figure 5-5). CV scans were also performed before and after all CO_2 reduction experiments to monitor any changes of the EASA or identify differences between electrodes.

Despite being able to measure the area of the oxide reduction peak of the gold plate, the same calculation was only feasible for the thickest gold nanoparticle-containing layers when using the highest gold loading as no other electrodes exhibited measurable oxide reduction peaks on their respective CV scans (Figure 5-6).

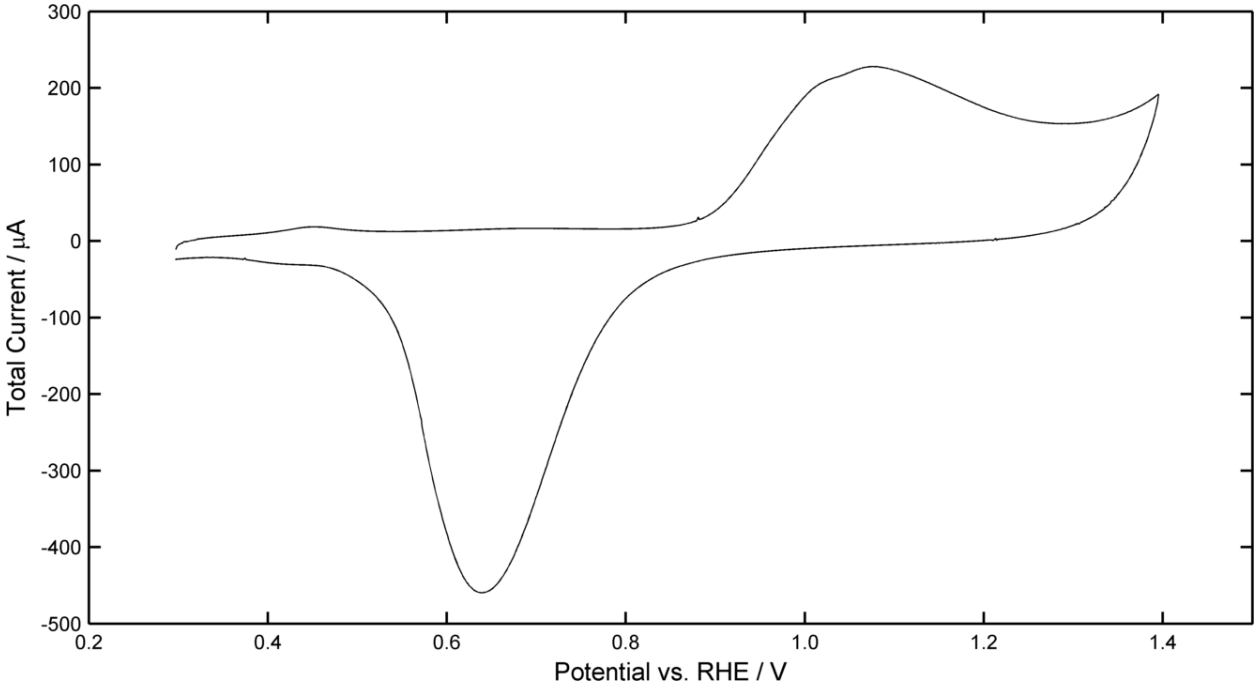

Figure 5-5. Typical CV of the bare gold plate in 0.2 M $KHCO_3$ with a sweep rate of 50 mV· s^{-1}.

The electrochemically active gold surface area measurements on the catalytic layers were inconsistent with estimated TEM-based surface area and as such, the TEM-based surface area was unable to be used for current density calculations. For example, the oxide reduction peak for a catalyst with 15.1 wt% gold loading (Figure 5-6) measured 425 μC, equivalent of 1.10 cm^2 gold surface area, assuming a specific charge density of 386 $\mu C \cdot cm^{-2}$. The total mass of gold in the catalytic layer was 0.249 mg and, with a specific surface area of 707 $cm^2 \cdot mg^{-1}$ (based on the particle size determined by TEM), the estimated surface area was 176 cm^2. The disparity between the EASA of 1.1 cm^2 and the TEM-based surface area of 176 cm^2 is caused either by the carbon in the electrode masking the oxide reduction peak, by changes to the oxide formation potential due to nano-effects or by a reduction in the *effective* number of the gold nanoparticles due to poor wetting out, or electrical conductivity throughout the catalytic layer. In the case of the carbon support causing masking or nano-effects of the particles, the results in Chapter 3 show that the EASA is >50% of the TEM-based surface area for similar sized particles measured in 0.5 M H_2SO_4. This suggests that the entire layer has not been fully utilized as a result of poor wetting of the layer, or poor electrical conductivity through the layer.

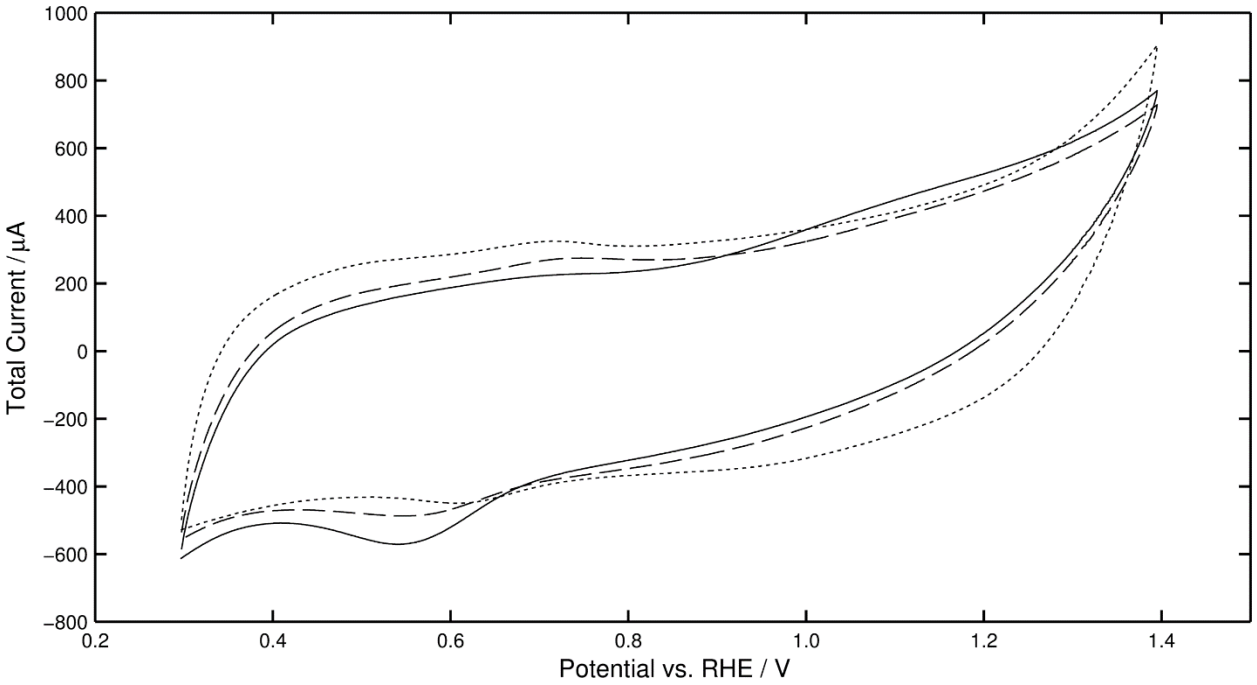

Figure 5-6. CV of Au/C electrode in 0.2 M $KHCO_3$ with a sweep rate of 50 $mV \cdot s^{-1}$. The catalyst loading is 15.1 wt% (solid line), 7.5 wt% (dashed line) and 1.5 wt% (dotted line). The redox peak seen most clearly on the dotted line at 0.6-0.7 V is associated with the fresh carbon used to dilute the sample rather than gold oxide reduction.

5.3.2 Carbon Dioxide Reduction – Bulk versus Nanoparticle-Based Electrodes

The initial CO_2 reduction experiments involved a galvanostatic charge of -5 $mA \cdot cm^{-2}_{geo}$ applied for four hours to a gold plate immersed into 0.2 M $KHCO_3$. This bulk gold electrode produced H_2, CO and a small amount of $HCOO^-$, however, the performance of this electrode was not stable with a constant increase of H_2 production and a constant decay in CO production (Figure 5-7). The greatest level of CO production was 2.45 $\mu mol \cdot min^{-1}$, which was achieved in the first 15 minutes. The rate of CO production at the end of the experiment was 0.59 $\mu mol \cdot min^{-1}$. The four-hour experiment on the gold plate produced a total of 0.28 mmol CO, 0.82 mmol H_2, and 0.053 mmol $HCOO^-$ leading to a faradaic efficiency of 98.4%.

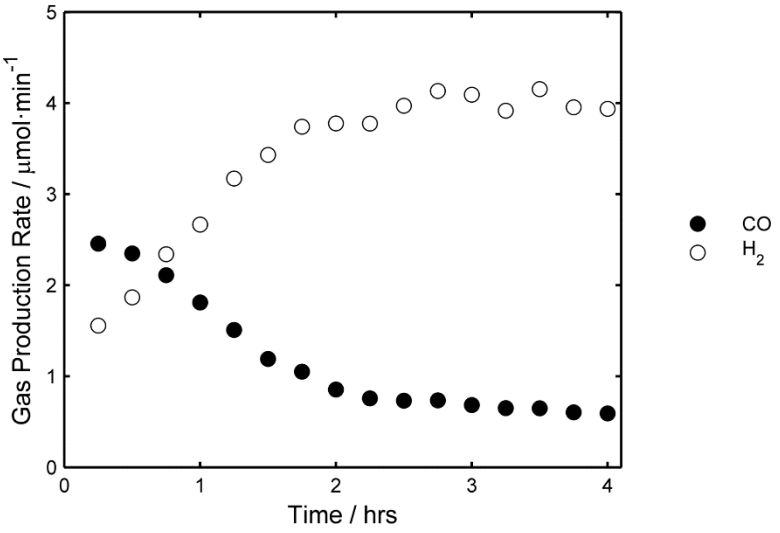

Figure 5-7. CO and H_2 production rates on a Au plate in 0.2 M $KHCO_3$.

The CO_2 reduction behaviour of the bulk gold electrode was compared with that of a typical gold nanoparticle-containing catalytic layer (with 15.1 wt% Au/C) produced by spray coating on a titanium disc. The mass of the exposed catalytic layer was measured to be 1.07 mg, consisting of 0.11 mg gold, 0.61 mg carbon black, and 0.36 mg Nafion. This cathode achieved a stable CO production rate of 1.10 $\mu mol \cdot min^{-1}$, a rate of just under one-half the maximum rate of the gold plate. The significant difference in the case of nanoparticle-based catalytic layers was that CO production remained stable throughout all galvanostatic experiments (Figure 5-8). This catalytic layer produced a total of 0.25 mmol CO, 0.88 mmol of H_2 and 0.011 mmol $HCOO^-$ leading to a faradaic efficiency of 97.3% during the four-hour long experiment.

When considering the stability of the two cathodes, the gold plate produced 71% of the total CO during the first half of the experiment and had a consistent diminishing production rate whereas the nanoparticles produced only 47% of the total CO during the same two hours period. The stability of the nanoparticles was apparent in all experiments, the longest of which was 6.5 hours and had a stable production rate of 1.06 $\mu mol \cdot min^{-1}$ with a total amount of 0.41 mmol of CO produced overall.

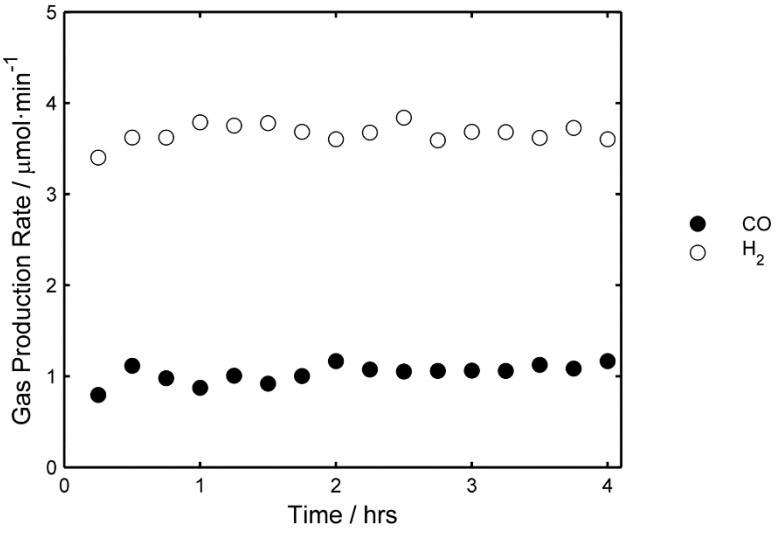

Figure 5-8. CO and H_2 production rates on a Au/C catalytic layer in 0.2 M $KHCO_3$.

One of the main reasons nanoparticles are chosen for catalysis is their larger specific surface area compared to bulk gold. For example, the EASA measured from the gold oxide reduction peak of the bulk gold electrode recorded a surface area of 3.75 cm^2 while the EASA for the same peak on the nanoparticles measured 1.10 cm^2. Comparing these surface areas to the total CO production, the surface-specific CO production is 74.6 $\mu mol \cdot cm^{-2}$ for the gold plate and 229 $\mu mol \cdot cm^{-2}$ for the nanoparticles. Assuming the long-term trend of the nanoparticle stability continues and the gold plate remains less active than the nanoparticles (further discussed in Section 5.3.6), the differences in the specific rate of production between gold plate and nanoparticles will only favour the nanoparticles to a greater and greater degree.

The average formic acid production for all 15.1 wt% catalytic layers was 14.0 μmol over the entire four-hour duration. Comparatively, the formic acid production for the blank carbon sample was 12.2 μmol, and for the gold plate, it was 52.9 μmol. As such, while it appears that the bulk gold surface is active for formic acid production, very little additional formic acid activity is seen when comparing the Au/C catalyst to the carbon black catalyst.

5.3.3 Carbon Dioxide Reduction – Gold Loading Effects

The effect of gold loading in a catalytic layer has been investigated by our group previously when Marshall et al. [57] measured the activity of glycerol oxidation on 4.6 nm gold particles. Their conclusions showed that the specific activity of the gold nanoparticles is affected by catalytic layer properties such as the layer thickness. As such, they state that while higher nanoparticle loaded layers (15 wt% – 20 wt% Au) does have a higher glycerol oxidation rate, the lower nanoparticle loadings (5 wt% – 10 wt%) have a higher oxidation rate *per Au site*.

This relationship between catalytic layer properties and the nanoparticle specific activity suggested a comparable study to an investigation on the effects on CO_2 reduction when altering the gold loading within a catalytic layer. The layer composition was altered

by mixing the Au/C catalytic ink with a pure carbon black-based ink prior to spray coating the Ti electrode. A catalytic layer produced by this dilution method was previously found to be essentially identical to a catalyst produced from a low nanoparticle loading of gold on carbon [57]. This improves the reliability of the study as all nanoparticles are produced from the same synthesis and can be assumed identical to the initial TEM measurements.

Four different catalytic layer gold loadings were measured; 15.1 wt%, 7.5 wt%, 1.5 wt% and 0.15 wt%. It was found that the greatest rate of CO production came from the 15.1 wt% layer (Figure 5-9A), however, there was no significant difference in the rate of CO production in some of the 1.5 wt% gold loading catalysts (Table 5-3). This suggests that the gold within the layers containing a lot of gold is not being fully utilised, whether through poorer layer conductivity, or mass transport blocking caused by denser electrocatalytic layers.

Table 5-3. CO production experiments with varying gold loadings within the catalytic layers. Experiments were performed in 0.2 M $KHCO_3$ with a geometric current density of -5 mA· cm^{-2}. The explanation of how to calculate the layer thickness is discussed in Section 5.3.4.

Gold Loading / wt%	Mass of catalytic layer / mg	Layer thickness / μm	Stable CO production rate* / μmol · min^{-1}	Normalized CO production*/ μmol · min^{-1} · mg_{Au}^{-1}	Total CO production / mmol
Bulk	-	-	2.5 ± 0.1	-	0.28 ± 0.02
15.1	2.47 ± 0.01	8.2 ± 0.2	0.988 ± 0.01	6.2 ± 0.5	0.11 ± 0.01
7.5	2.85 ± 0.01	10.1 ± 0.3	0.719 ± 0.02	7.8 ± 0.6	0.16 ± 0.01
1.5	3.01 ± 0.01	11.3 ± 0.3	0.556 ± 0.01	29 ± 2	0.08 ± 0.006
1.5	2.54 ± 0.01	9.5 ± 0.3	0.974 ± 0.03	60 ± 5	0.22 ± 0.02
0.15	2.68 ± 0.01	10.2 ± 0.3	0.279 ± 0.02	162 ± 15	0.069 ± 0.006
0.15	2.50 ± 0.01	9.5 ± 0.3	0.042 ± 0.004	26 ± 3	0.009 ± 0.001
0.00	2.19 ± 0.01	8.3 ± 0.3	0.000 ± 0.001	-	0.006 ± 0.001

*The electrode with 0% Au loading produced CO at a rate of 0.0025 μmol · min^{-1}. This CO is produced by the supporting Ti disc and has been subtracted from all reported Au/C values.

By considering only the direct CO production of the catalytic layers (Figure 5-9A), it appears that there is little variation between 15.1 wt%, 7.5 wt% and 1.5 wt% gold loading. This effect is seen more profoundly when considering the mass-normalized rate of CO production (Figure 5-9B). Here it is obvious that lower gold loadings (0.15 wt% – 1.5 wt%) produce more CO per gold site, however, both the overall production rate and normalised production rate must be considered before an optimum industrial solution is found. As such, an intermediate gold loading of 1.5 wt% to 5 wt% will continue to produce sufficient quantities of CO without an excess of gold within the catalytic layer.

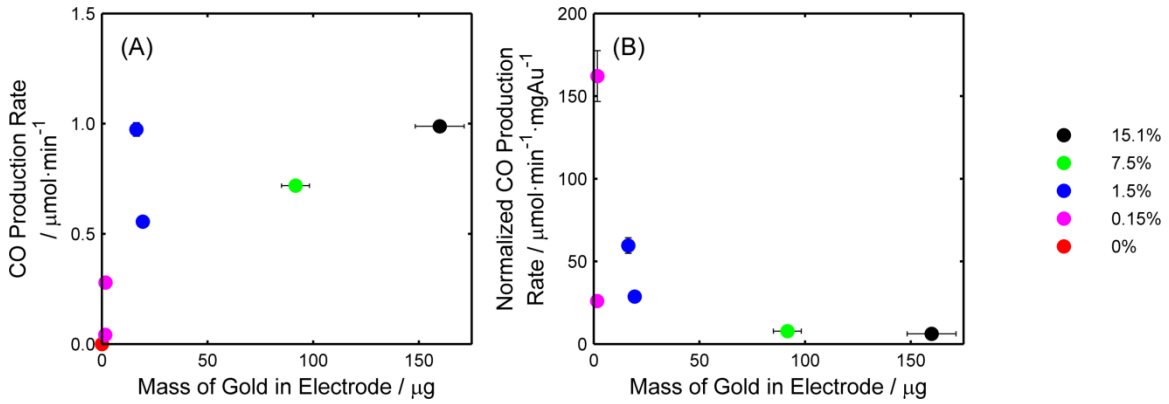

Figure 5-9. CO production (A) and mass-normalized CO production (B) with respect to catalyst gold loading of 3.2 nm Au nanoparticles with 0.15 wt% to 15.1 wt% loading on carbon. Experiments were performed in a solution of 0.2 M $KHCO_3$ at a current density of -5 mA· cm^{-2}, at ambient temperature and pressure.

5.3.4 Carbon Dioxide Reduction – Layer Thickness Effects

In order to complement the gold loading results, a set of experiments were devised where the mass of gold present in the electrode layer was altered by adjusting the layer thickness rather than dilution of the catalyst; essentially, more or less of the Au/C ink was sprayed to the substrate when forming the electrode. It was hypothesised that if the two layers had an equal mass of gold available for reaction yet different layer thicknesses, the CO production rate may be similar. This hypothesis required the assumption that the carbon support is inert with respect to any reaction, and a decrease in the Au:C ratio does not interfere with mass transport of products or reactants.

The thickness of each layer was calculated using the reported densities of gold (19.3 $g \cdot cm^{-3}$), carbon black (pellet density of 0.4 $g \cdot cm^{-3}$ [282]) and Nafion (1.7 $g \cdot cm^{-3}$ [283]). The layer density remained constant for the layer thickness experiments as the ratio of all three components was controlled to be 10.1 wt% gold, 56.6 wt% carbon and 33 wt% Nafion. The layer density was calculated to be 0.617 $g \cdot cm^{-3}$, which lead to layer thicknesses of 2 to 9 μm (Table 5-4).

It was found that as the mass of gold in the catalytic layer decreased, the total CO production rate increased (Figure 5-10A). This trend is counter-intuitive as it was assumed that decreasing the number of gold sites within the catalytic layer would decrease the CO production rate. These experiments have shown that as the number of gold surface sites decreases, each surface site is correspondingly responsible for more CO_2 reduction (Figure 5-10B). As experiments in 0.5 M H_2SO_4 on catalytic layers that were 30 μm thick (Chapter 2) showed that electrolyte penetration was sufficient to ensure that all of the gold was in contact with the electrolyte, it is believed that the results here cannot be due to poor electrolyte penetration.

Table 5-4. CO production for the four-hour experiments comparing varying layer thicknesses of 15.1 wt% gold loaded catalysts. Experiments were performed in 0.2 M $KHCO_3$ with a geometric current density of -5 mA· cm^{-2}.

Gold Loading / wt%	Mass of catalytic layer / mg	Layer thickness / μm	Stable CO production rate* / μmol · min^{-1}	Normalized CO production rate* / μmol · min^{-1} · mg_{Au}^{-1}	Total CO production / mmol
Bulk	-	-	2.5 ± 0.1	-	0.28 ± 0.02
15.1	2.47 ± 0.01	8.2 ± 0.3	0.99 ± 0.03	6.2 ± 0.5	0.11 ± 0.01
15.1	2.02 ± 0.01	6.7 ± 0.2	1.86 ± 0.02	14.2 ± 1	0.38 ± 0.03
15.1	1.78 ± 0.01	5.9 ± 0.2	1.04 ± 0.01	9.0 ± 0.7	0.25 ± 0.02
15.1	1.67 ± 0.01	5.5 ± 0.2	1.04 ± 0.02	9.6 ± 0.7	0.24 ± 0.02
15.1	1.42 ± 0.01	4.7 ± 0.1	1.45 ± 0.02	15.8 ± 1	0.30 ± 0.02
15.1	0.63 ± 0.01	2.1 ± 0.1	2.29 ± 0.004	56.1 ± 4	0.55 ± 0.04

*The electrode with 0 wt% Au loading produced CO at a rate of 0.0025 μmol · min^{-1}. This CO is produced by the supporting Ti disc and has been subtracted from all reported Au/C values.

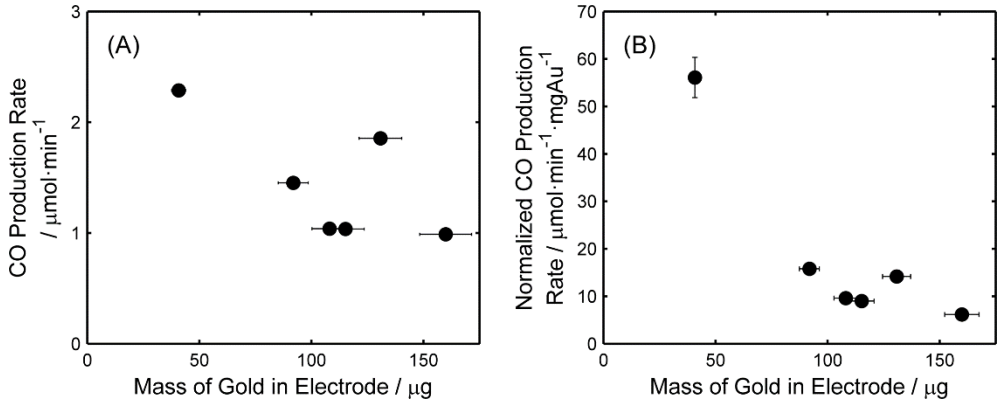

Figure 5-10. CO production (A) and mass-normalized CO production (B) with respect to the mass of 3.2 nm gold nanoparticles with 15.1 wt% gold loading on carbon. Experiments were performed in a solution of 0.2 M $KHCO_3$ at a current density of -5 mA· cm^{-2}, at ambient temperature and pressure.

As the electrolyte availability to the gold sites was concluded to not be an influential factor, the remaining variable was the amount of carbon present in the sample. As the carbon black support is only active for the hydrogen evolution reaction, it is possible here that this carbon uses the applied current for the HER at the expense of CO_2 reduction products on the gold. As such, the mass of carbon in the catalytic layer was compared to the rate of CO and H_2 production (Figure 5-11). The CO production is, as previously discussed, higher for the electrodes containing more gold however the trend of increased CO production as the layer thickness decreases is still apparent in the 15.1 wt% gold loading data.

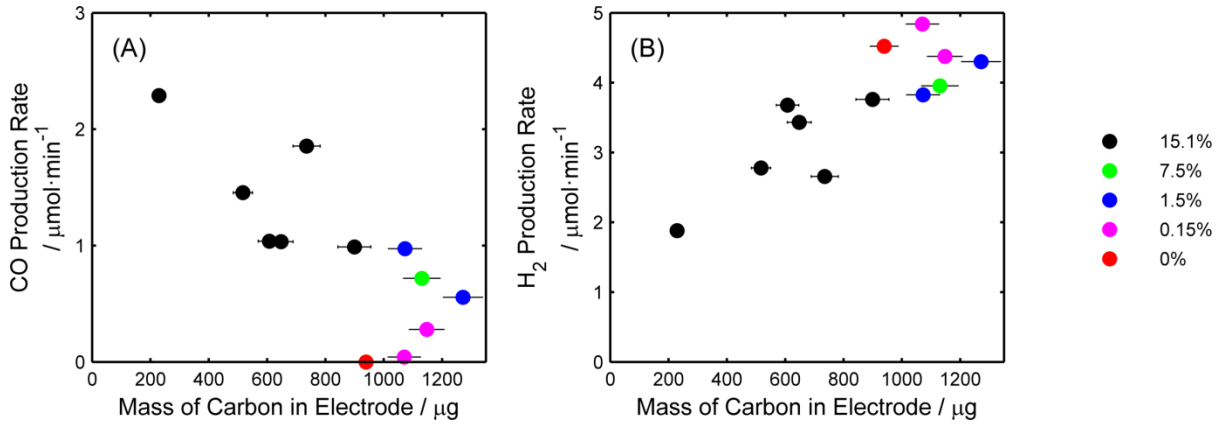

Figure 5-11. CO production (A) and H_2 production (B) as a function of the mass of carbon on the electrode. Gold loading on the catalytic layers is denoted in the legend.

The H_2 production rate appears to be very well correlated to the mass of carbon in the catalytic layer, with a *Pearson product-moment correlation coefficient* (PCC) of 0.83, where a value of 1 is perfect positive correlation, a value of 0 is no measurable correlation, and a value of -1 is perfect negative correlation. As a comparison, the PCC for the relationship between the gold loading on the catalyst and CO production, across all data points, is 0.57. These correlations suggest that the amount of carbon in the layer has a very influential role in the final product distribution produced by the catalytic layer. As has been seen earlier (Figure 5-7), some hydrogen will evolve from the gold surface which prevents the complete correlation of the carbon/hydrogen relationship.

The apparent consequence of this carbon/hydrogen relationship is that thinner catalyst layers have a greater *specific* CO production rate. The proposed reason for this is due one of two reasons: either the carbon in the catalytic layer is contributing to the hydrogen production, or the dissolved CO_2 is prevented from penetrating through the entire catalytic layer.

In the first case, if the carbon sites within the thin catalytic layers become saturated with hydrogen, i.e. the HER is kinetically limited, the overpotential for additional hydrogen evolution will increase and as a result, the CO_2 reduction will occur on gold catalytic sites at a greater rate. Comparatively, as the catalytic layers become thicker and the current remains unchanged, the current density proportionally decreases, the overpotential decreases, and the hydrogen production rate increases. This increase in hydrogen production will cause an equivalent reduction in CO_2 production in catalytic layers with a higher mass.

Alternatively, if the dissolved CO_2 is not penetrating the catalytic layer, the gold sites further from the catalyst surface will only be performing the HER. This decrease in the CO_2 concentration within the catalytic layer will result in greater quantities of hydrogen being produced. For example, if a gold site is exposed to a CO_2 saturated solution and it is assumed that it will produce CO and H_2 in a 2:3 ratio (i.e. 40 % CO faradaic efficiency, 60 % H2 faradaic efficiency) then it would be expected to have a 2:3 ratio of the products.

However, if only the first 25% of the catalytic layer is exposed to CO_2 and the remaining catalyst is only exposed to the electrolyte then 75% of the active sites are only catalysing the HER. This would lead to a 1:6 ratio of the products.

5.3.5 Lower Limits of Gold Loading

Two limits exist when considering the lower bounds of the gold loading; a theoretical limit of an infinitely reduced layer thickness, and a physical limit of sufficient catalyst to produce a coherent catalytic layer. The theoretical limit can simply be ascribed identical behaviour to the blank titanium disc, and as such will have negligible CO production. However, the physical limit is less rigidly defined. For the purposes of providing a suitable definition around this limit, a coherent layer must include the ability for lateral electrical conduction and must be internally bonded within its own structure. The long-term behaviour and stability of the entire layer, or of the gold, carbon and Nafion components are not constrained within this definition as they may be altered as experiments are carried out.

The reaction vessel was constructed by clamping the catalyst-coated titanium disc to the glass cell, using a flexible o-ring to provide the liquid seal (Figure 5-12A). For calculations within the previous sections, it is assumed that the entirety of the catalytic layer is available for reaction. Despite the fact that the layer is entirely penetrated with electrolyte during the initial CV scans, there are several potential situations that could result in the complete layer not remaining electrochemically active during CO_2 reduction.

Situation 1. The deeper sections of the layer are dried-out, or electrical conductivity is hampered by gas formation. This will leave only the surface of the electrode and the areas near the clamped o-ring as electrochemically active (Figure 5-12B).

Situation 2. Only an annular ring of the catalyst is in direct contact with the titanium disc due to gas formation within or below the catalytic layer (Figure 5-12C).

Situation 3. The gold nanoparticles themselves are not as electrochemically active as would be expected in $KHCO_3$. This is supported by the fact that there is only $1/80^{th}$ of the expected oxide reduction charge seen in the pre-galvanostatic CV scans. Even if only $1/80^{th}$ of the surface is active, the specific activity of the nanoparticles is still significantly larger than the specific activity for the bulk gold, i.e. 229 $\mu mol \cdot cm^{-2}$ and 74.6 $\mu mol \cdot cm^{-2}$ for the nanoparticles and bulk gold respectively (See Section 5.3.2).

With the current information available, it is unclear if the electrocatalytic layer is only partially electrochemically available to the solution or if the EASA is, for some reason, significantly lower than expected (i.e. we can not separate between situation 1, 2, or 3). For example, if the deeper particles of the catalytic layer were was unavailable due to poor electrical conductivity as gas was formed (Situation 1), the expected response from decreasing the thickness of the catalyst layer would be constant CO production until the

thickness of the 'wet' section of the catalytic layer was equal to the entire layer thickness, i.e. the thickness of the 'wet' layer doesn't change, however the overall layer thickness will eventually be equal to, or less than, the maximum 'wet' thickness. At this point, the 'fully wet' layer has been reached and any further reduction in layer thickness would result in a reduction in CO production. As this is not the case, the drying out, or reduction in electrical conductivity is unlikely to be the cause for any lower-than-expected gold activity.

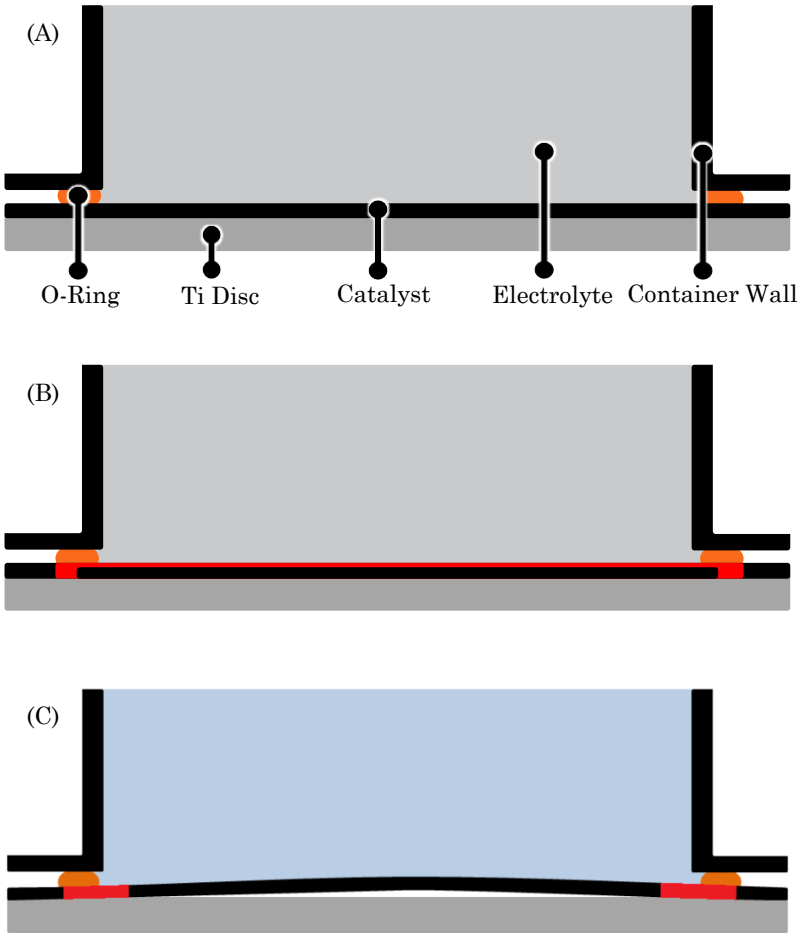

Figure 5-12. Basic schematic of the cathodic chamber and relative positioning of the catalytic layer (A). Schematic of electrical conduction (shown in red) through the catalytic layer assuming Ti-catalyst contact only occurs near the clamped o-ring and only through the top surface of the catalytic layer (B). Schematic of electrical conduction of the catalytic layer assuming Ti-catalyst contact only occurs near the Ti-catalyst connection points (shown in red) (C). The catalyst is lifted off the surface of the titanium due to gas formation within or below the catalytic layer.

With a catalytic layer mass of 2.0 mg to 3.0 mg, the overall layer was observed to be cohesive in terms of its self-supporting structure, i.e. the layer will form a catalytic sheet that withstands expected external forces such as bubble formation or electrolyte convection. However, these layers do not adhere to the titanium disc and, upon rinsing under a flow if DI water after a CO_2 reduction experiment, will detach as Au/C/Nafion sheets (Figure 5-13). This clean separation from the titanium disc is attributed to gas production either deep within, or below the catalytic layer, at such a rate that it is unable to move through the

layer to the bulk electrolyte. As such, through the action of hundreds of very small bubbles, sufficient vertical pressure is placed on the layer to detach it from the metallic surface. A coarse, sandpaper finish was attempted to provide additional roughness to the titanium surface, however, no appreciable difference was ascertained.

Figure 5-13. A digital microscope image showing the used catalytic layer tearing, and subsequently detached from the titanium disc.

5.3.6 Carbon Dioxide Reduction – Long Term Experiments

Three significant long-term experiments were performed on 15.1 wt% Au/C catalytic layers; a nine-hour experiment with 46 wt% Nafion content within the layer, a 6.5 hour experiment with 33 wt% Nafion content, and a 10 hour experiment with; (a) 33 wt% Nafion content and (b) 10 CV scans every two hours to artificially age the catalyst. From previous measurements of the gold oxide reduction peak charge (Chapter 3) it was determined that the available surface area of gold would quickly diminish when larger quantities of Nafion were present in the layer and in a similar set of experiment as those in Section 2.8.5, the CO production for these higher content layers was also measured. It was found that the CO production rate of 1.10 $\mu mol \cdot min^{-1}$ or 6.01 $\mu mol \cdot min^{-1} \cdot mg_{Au}^{-1}$ was stable over the entire nine-hour duration of the 46 wt% Nafion content experiment (Figure 5-14). A similar experiment with a 6.5-hour duration and 33 wt% Nafion content showed a stable CO production rate of 1.06 $\mu mol \cdot min^{-1}$, or 8.89 $\mu mol \cdot min^{-1} \cdot mg_{Au}^{-1}$ (Figure 5-15).

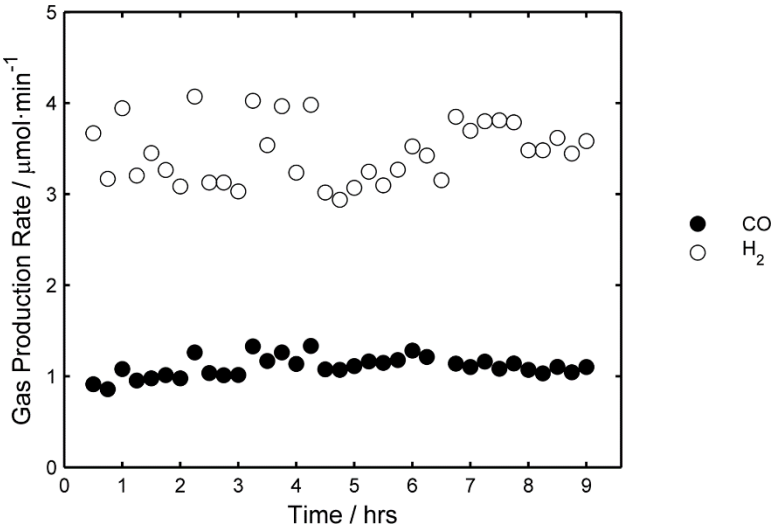

Figure 5-14. CO and H_2 production rates on a Au/C catalytic layer, with a Nafion content of 46 wt%, in 0.2 M $KHCO_3$.

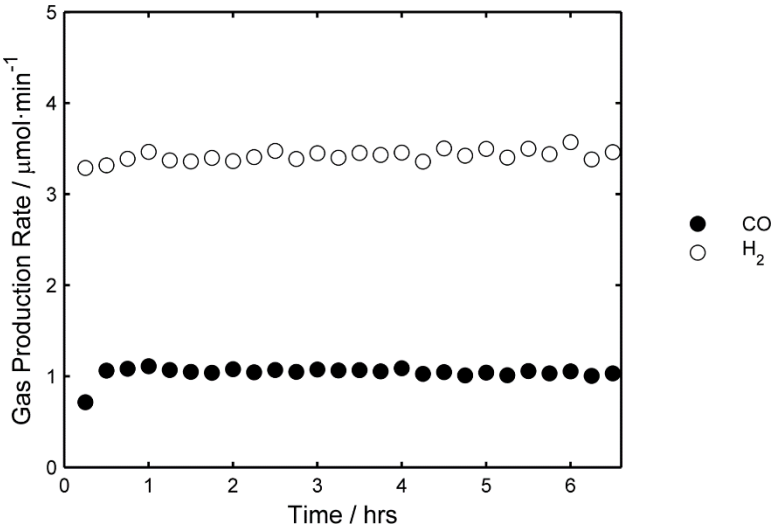

Figure 5-15. CO and H_2 production rates on a Au/C catalytic layer, with a Nafion content of 33 wt%, in 0.2 M $KHCO_3$.

The final stability experiment consisted of the standard 10 CV scans to ensure wetting out of the layer, followed by two hours of galvanostatic CO_2 reduction. This sequence of 10 CV scans followed by two hours of CO_2 reduction was repeated another four times for a total of 50 CV scans and 10 hours of galvanostatic measurements. It was found that instead of degradation of the catalyst during each set of CV scans, the activity towards CO production increased from the initial average of 0.940 µmol min^{-1} after the first set of 10 CV scans, to 1.27 µmol · min^{-1} after the fifth set of CV scans (Figure 5-16). This apparent increase in CO production may suggest that the CV scans, instead of degrading the gold nanoparticles via ageing effects (Chapter 4), actually activate the gold by cleaning the surface of any impurities, in a similar way that others have shown how bulk gold electrodes [284] and copper electrodes [281] were reactivated for CO_2 reduction.

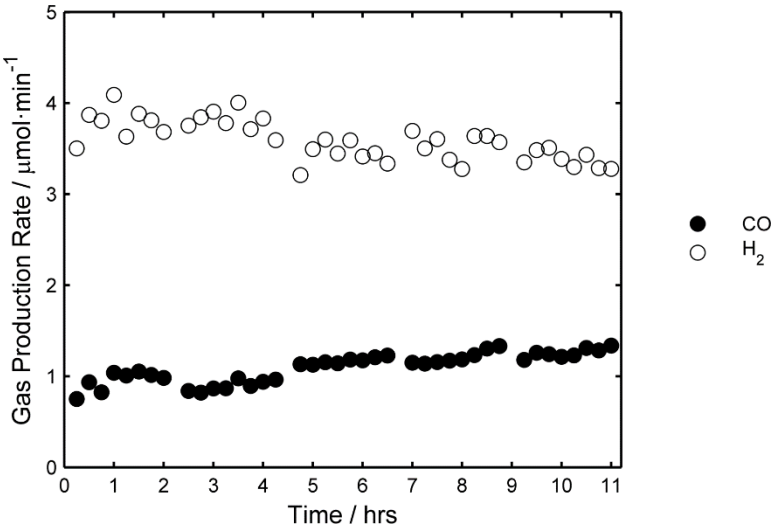

Figure 5-16. CO and H_2 production rates on a Au/C catalytic layer in 0.2 M $KHCO_3$. 10 CV scans were performed prior to each two hour period of galvanostatic measurements. A Nafion content of 33 wt% was used for this experiments

5.4 Summary

Here we have shown how 3.2 nm gold nanoparticles, stabilised with phosphine ligands and supported on carbon black, reduce CO_2 that has been dissolved in a 0.2 M $KHCO_3$ solution. While a bulk gold plate will produce 0.28 mmol CO during a four-hour experiment, the rate of production decays throughout the experiment duration, ending with a rate of 0.59 $\mu mol \cdot min^{-1}$. Comparatively, the catalytic layer containing gold nanoparticles produce up to 0.25 mmol CO during an identical four-hour experiment yet retained a constant rate of CO production of 1.10 $\mu mol \cdot min^{-1}$. When compared on a surface area basis, the nanoparticles were found to produce CO three times faster than the bulk gold plate. These results indicate that performing long-term CO_2 reduction on nanoparticles will produce more CO, at a more consistent production rate, than using a bulk gold electrode.

A gold loading ranging between 1.5 wt% and 15.1 wt% Au/C was found to have little effect on the CO production rate, with an average production rate of 0.81 $\mu mol \cdot min^{-1}$. Gold loadings of 0.15 wt% Au/C produced significantly less CO, with an average CO production rate of 0.16 $\mu mol \cdot min^{-1}$. When considering these electrodes on a gold mass-basis, the low loading (1.5 wt%) gold catalysts showed a clear superiority over the high loading (7.5 wt% – 15.1 wt%) catalysts due to their significantly smaller gold mass, yet equivalent CO production rate. These low loadings would be an ideal target for commercially produced CO_2 reduction electrodes by keeping the cost of the gold to a minimum without jeopardising the CO production rate.

The thickness of the catalytic layers was found to have an inverse relationship with the CO production rate. While the thickest catalytic layer used in this chapter was 11.4 µm thick is still well below the 26.6 µm upper limit suggested in Chapter 2, the thinner layers were still able to produce more CO than thicker layers, both as an absolute production

volume, and as a gold mass normalised production rate. These findings suggest that the carbon support plays an influential role in the CO_2 reduction reaction, either by contributing to a portion of the evolved hydrogen or by preventing CO_2 transfer through the catalytic layer.

Long-term experiments (up to nine hours) showed a remarkable stability of the gold nanoparticle, especially considering the ageing seen described in Chapter 3. When performing the CO_2 reduction reactions, the gold nanoparticles are below the gold dissolution potential and do not form gold oxide. As the dissolution of gold and the formation and reduction of gold oxide are the two main contributors to gold nanoparticle degradation, significant changes to the gold nanoparticles within this chapter may not be occurring. Interestingly, when exposed to CV scans intermittently during the galvanostatic measurements, the CO_2 reduction activity appears to increase, most likely due to surface cleaning occurring at the higher potentials.

Chapter 6 CONCLUSIONS & RECOMMENDATIONS

The following chapter will reiterate the key findings of this work. This section will provide an overview of gold nanoparticles with respect to their surface area measurements and electrochemical driven degradation. It will also summarise the UV-Vis response of potential cycling as well as electrocatalytic reduction of CO_2.

6.1 Surface Area Measurements and Calculations

The measurement and calculation of the physical and electrochemical characteristics of nanoparticles is an essential step in the quantification of nano-sized catalysts. Physical measurement techniques consist of electron imaging, where images are taken of the nanoparticles and are directly measured. These measurements are then converted into an appropriate particle size distribution and specific surface area. Difficulties arise from deciding what to consider as 'appropriate' when the particle diameter will vary depending on how the distribution has been weighted. The four standard weighting methods will produce particle sizes in the order: S.S.A. weighted < number weighted < area weighted < volume weighted.

It is well known that as nanoparticles sizes fall below ~8 nm, the inter-atomic distance begins to decrease. Nanoparticle shapes have been modelled with the smallest particles favouring a less dense octahedral structure and larger particles favouring FCC-based shapes. Despite this, synchrotron techniques such as EXAFS have been used to identify inter-atomic distances decreasing as the particle size decreases, with some authors measuring a bond length approximately 6% shorter than that of bulk gold.

In addition to the physical measurements, the surface area of particles can be measured via electrochemical measurements such as measuring the gold oxide reduction charge or underpotential deposition of copper. For example, by measuring the gold oxide reduction charge, the electrochemically active surface area can be calculated via a predetermined specific surface area. These measurements can be more appropriate when considering the activity of the catalyst as it will disregard any inactive surface area. The major complication experienced with this method of surface area measurement is due to how the specific surface area has been found. By using a range of assumption including deciding exactly what form, and at what stage of the electrochemical measurement a single monolayer of gold oxide is formed, the specific surface area has been reported to be

anywhere from 192 $\mu C \cdot cm^{-2}$ to 723 $\mu C \cdot cm^{-2}$. Measurements comparing the gold oxide reduction surface charge density of nanoparticles compared with bulk gold show that a unique specific charge density should be determined for each nanoparticle type prior to any additional experimentation.

6.2 Nanoparticle Stability during Electrochemical Cycling

While measuring the gold oxide reduction charge is useful to determine or monitor the electrochemically active surface area of a catalyst, applying oxidative potentials to the gold will alter the gold's surface. Electro-polishing or electro-roughening are techniques that use the dissolution of gold and rearrangement of the surface atoms to produce an altered electrochemical surface. While the dissolution of the surface layer of gold atoms does not affect the general form of a bulk gold electrode, losing the surface layer can have a comprehensive effect on the behaviour and morphology of a nanoparticle with only a few shells.

By performing CV scans on small gold nanoparticles (0.8 nm – 4.5 nm), produced through different synthesis methods, we were able to study the effect of enhanced electrochemical degradation of the nanoparticle surface. A small amount of dissolution was measured (up to 6% over 100 CV scans) as well as a global shift in the particle size distributions towards larger particles. This occurred due to the removal of stabilising ligands from the particles, and the particles only being quasi-attached to the carbon support. This meant that as the nanoparticles interacted with each other, they were able to sinter together. These measurements were confirmed via EXAFS measurements showing an increasing particle size for all measured samples as the extent of electrochemical degradation was increased. Long term degradation experiments showed that the 3.1 nm Au catalyst began with a surface charge density of 220 $\mu C \cdot cm^{-2}_{Au}$ and after 750 CV scans, this value had decreased to 28 $\mu C \cdot cm^{-2}_{Au}$.

6.3 UV-Vis Spectroscopic Measurements during Electrochemical Cycling

The electronic manipulation of the surface plasmon resonance of gold is a technique whose full usefulness is still being discovered. The SPR feature is heavily dependent on the local environment of the gold surface and as such, can be blue- or red-shifted by increasing or decreasing the electronic density of the gold surface. This technique was first investigated in 0.5 M H_2SO_4 and 1.0 M KOH by recording full UV-Vis spectra while simultaneously performing CV scans on the gold samples. It was found that as the gold surface was oxidised, the SPR peak wavelength was red-shifted up to 10 nm, while the SPR absorption experienced a significant decrease in intensity during the gold oxide portion of the CV. The red-shift and intensity decrease were reversed during the cathodic scans, although hysteresis was present for measurements in both electrolytes.

By performing a differentiation on the SPR absorption intensity measurements, we were able to produce an intensity-based spectroscopic CV for the 0.5 M H_2SO_4 sample, with

clear features near the gold oxide formation/reduction features on the electrochemical CV scan. The equivalent intensity-based spectroscopic CV for the 1.0 M KOH sample was less similar to its corresponding electrochemical CV however it did still show gold oxide-based features. As an alternative method of analysis, a differential of the SPR peak wavelength was produced. In a converse manner, the wavelength-based spectroscopic CV in 0.5 M H_2SO_4 did not appear to be similar to its corresponding electrochemical CV as it also displayed sulfate adsorption peaks of similar magnitude to gold oxide related peaks. While a direct replica of the electrochemical information wasn't attainable, the ability to identify adsorption peaks by this method may prove useful for future adsorption based experiments. The wavelength-based spectroscopic CV in 1.0 M KOH showed an almost identical plot when compared to the electrochemical CV, proving that while the intensity-based spectroscopic CV may be superior in some methods (i.e. in H_2SO_4 solutions), other spectroscopic methods should not be ignored.

These UV-Vis measurement operations were used to produce intensity-based and wavelength-based spectroscopic CV scans were for gold nanoparticles in an aqueous solution of 1.0 M KOH and 0.1 M glycerol. While the nanoparticles became less active for glycerol oxidation, the first three electrochemical CV scans were able to be used to create the spectroscopic CV scans. The gold oxide reduction feature on both spectroscopic CV scans suggested that the presence of glycerol promoted the reduction of gold oxide formation by 0.09 ± 0.01 V, whereas previously we had expected glycerol to inhibit gold oxide reduction by up to 0.1 V.

6.4 Electrocatalytic Reduction of Carbon Dioxide

CO_2 was reduced on a bulk gold electrode and gold nanoparticle based electrodes in a solution of 0.2 M $KHCO_3$. In these experiments, we found that while the bulk gold electrode began with a high rate of CO_2 reduction, over the space of four hours of galvanostatic charging, this rate decreased by over 75%. A gold nanoparticle based electrode, during the same four-hour period of galvanostatic charging, began at a lower rate of CO_2 reduction and concluded with a rate almost double that of the bulk gold electrode. If these rates were considered on a gold EASA basis, the gold nanoparticle based electrode was over three times more productive than the bulk gold electrode.

The effect of gold loading on the carbon support was investigated and found that lower gold loadings of 1.5 wt% Au reduced equal amounts of CO_2 as the 15.1 wt% Au electrodes. When this is considered in terms of EASA, the 1.5 wt% Au electrodes are shown to be drastically more efficient. Similar experiments were performed on the effect of the catalytic layer thickness. Previous experiments had shown that an upper electrode thickness limit of 26.6 μm was required to ensure rapid availability of the entirety of the layer and all layers in these experiments remained well below this limit. Despite the assurance that the thickness of the layer should not have had an effect on the electrochemical availability of the catalyst, it was found that as the layer thickness decreased the rate of CO_2 reduction increased. It was found that this is likely to be caused by the carbon support playing an

active role in the cell. By participating in the hydrogen evolution reaction, the carbon surface may be able to influence the electrode potential to the extent that it doesn't reach a great enough overpotential for the gold surface to be fully utilised for CO_2 reduction. In this way, by reducing the thickness of the catalytic layer, the amount of carbon is reduced and the extent of the hydrogen evolution reaction is decreased. The potential of the electrode can then increase and drive the CO_2 reduction reaction forward at a greater rate, despite the equivalent reduction in gold surface area.

Long-term CO_2 reduction experiments of up to 11 hours were performed on the gold nanoparticle electrodes, which were found to be stable throughout the duration of the experiments. Intermittent CV scanning during the long-term experiments was shown to increase the rate of CO_2 reduction, possibly due to the CV scans cleaning impurities from the electrodes.

6.5 Suggestions for Further Work

6.5.1 Surface Area and Degradation

While there are commonly used methods for estimating the surface area of nanoparticles, using a single gold oxide reduction charge for all measurements is problematic. I believe a full review of the literature on this topic will demonstrate the large range of techniques and justifications that are used by authors and an attempt should be made to find a surface area comparison that will unify both nanoparticle/gold surface area calculations and physical/electrochemical surface area measurements. In addition to this, researchers who intend to use nanoparticles in an electrochemical environment must be aware of the long-term stability of the nanoparticles and be careful when preparing and cleaning the samples prior to testing that they are not unknowingly ageing the sample.

6.5.2 Spectroscopic Measurements

The in-situ measurement of the UV-Vis spectrum during cyclic voltammetry has provided a new method for monitoring gold nanoparticle stability as well as the electrochemical promotion or inhibition of the gold/gold oxide reaction. By being able to extract a spectroscopic CV, there is potential to be able to identify surface reactions or adsorption of molecules when they would not be observable during typical electrochemical methods. From this work, new areas of investigation include:

- Establishing an adsorption mechanism that will tightly bind the glass nanoparticles to the conductive surface. This will remove the underlying loss of SPR absorption intensity that occurs with nanoparticle loss from the surface.
- Investigation of the adsorption of ions to the gold surface. This could be found by performing ligand exchange reactions, underpotential deposition of copper or lead, or pH- or electrochemical-based adsorption.
- Investigation of other organic reactions to identify which chemicals cause promotion or inhibition of the gold surface oxidation and reduction.

- Once these aspects are understood, comparison of the activity of different nanoparticles and other, non-organic reactions can be investigated.
- It would also be interesting to see if other electrochemical processes could be investigated using this type of synchronised UV-Vis/electrochemical measurements. For example, could the SPR absorption intensity or peak wavelength be monitored during CO_2 reduction? If this is able to be performed, the build-up of impurities on the gold surface, and their subsequent removal via CV scanning may be able to be established using this method of inquiry.
- The spectroscopic CV scans examined in this thesis were only performed on gold nanoparticles however other metal catalysts, particularly silver, exhibit SPR behaviour. The principals behind how the gold SPR feature is affected by its electrochemical are equally applicable to these other metals and as such; studies into the synchronised spectroscopic/electrochemical measurements could be undertaken.

6.5.3 Carbon Dioxide Reduction

The nanoparticle catalysts used in the study of CO_2 reduction were remarkably stable across 9-11 hours of galvanostatic charging. This stability should be studied further, in order to find the limits on the catalytic reaction. These studies should address questions such as:

- How large can the catalytic electrode be made? As the electrode layer thickness is most active as a thin layer, the answer to this question could quantify how large a commercial CO_2 reduction reactor could be.
- How much charge can be applied to the catalyst? With the application of additional charge to the surface, the potential will invariably increase and drive both the CO_2 reduction reaction and the hydrogen evolution reaction forward. The answer to this question will determine the faradaic efficiency of the process as well as how much charge is required to reduce the desired quantity of CO_2.
- How much catalyst is required? As there was very little increase in CO_2 reduction with respect to the increases in the amount of gold present in the catalyst, the cost of catalytic layers can be minimised by producing a catalytic layer with less gold, while still reducing sufficient quantities of CO_2.

Commercial catalysts and catalytic layers have many design variables; however, determining an active catalyst that will perform consistently without degradation is essential. This thesis and the research contained within it are another step on the ladder to producing such a catalyst, and hopefully, lessening the impact of CO_2 and other greenhouse gases on our environment.

Chapter 7 REFERENCES

1. Steven, J.T., et al., *Electrochemical stability of carbon-supported gold nanoparticles in acidic electrolyte during cyclic voltammetry.* Electrochimica Acta, 2016. **187**: p. 593-604.
2. Hutchings, G.J., *Vapor phase hydrochlorination of acetylene: Correlation of catalytic activity of supported metal chloride catalysts.* Journal of Catalysis, 1985. **96**(1): p. 292-295.
3. Haruta, M., et al., *Novel Gold Catalysts for the Oxidation of Carbon Monoxide at a Temperature far Below 0°C.* Chemistry Letters, 1987. **16**(2): p. 405-408.
4. Hashmi, A.S.K. and G.J. Hutchings, *Gold Catalysis.* Angewandte Chemie International Edition, 2006. **45**(47): p. 7896-7936.
5. Teles, J.H., S. Brode, and M. Chabanas, *Cationic Gold(I) Complexes: Highly Efficient Catalysts for the Addition of Alcohols to Alkynes.* Angewandte Chemie International Edition, 1998. **37**(10): p. 1415-1418.
6. Hashmi, A.S.K., et al., *A New Gold-Catalyzed C–C Bond Formation.* Angewandte Chemie International Edition, 2000. **39**(13): p. 2285-2288.
7. Hashmi, A.S.K. and M. Rudolph, *Gold catalysis in total synthesis.* Chemical Society Reviews, 2008. **37**(9): p. 1766-1775.
8. Rudolph, M. and A.S.K. Hashmi, *Gold catalysis in total synthesis-an update.* Chemical Society Reviews, 2012. **41**(6): p. 2448-2462.
9. Hashmi, A.S.K. and G.J. Hutchings, *Gold Catalysis - the journey continues.* Catalysis Science & Technology, 2013. **3**(11): p. 2861-2861.
10. Yang, W. and A.S.K. Hashmi, *Mechanistic insights into the gold chemistry of allenes.* Chemical Society Reviews, 2014. **43**(9): p. 2941-2955.
11. Pflasterer, D. and A.S.K. Hashmi, *Gold catalysis in total synthesis - recent achievements.* Chemical Society Reviews, 2016. **45**(5): p. 1331-1367.
12. Hashmi, A.S.K., *Dual Gold Catalysis.* Accounts of Chemical Research, 2014. **47**(3): p. 864-876.
13. Raubenheimer, H.G. and H. Schmidbaur, *The Late Start and Amazing Upswing in Gold Chemistry.* Journal of Chemical Education, 2014. **91**(12): p. 2024-2036.
14. Rosca, D.-A., J.A. Wright, and M. Bochmann, *An element through the looking glass: exploring the Au-C, Au-H and Au-O energy landscape.* Dalton Transactions, 2015. **44**(48): p. 20785-20807.
15. Dorel, R. and A.M. Echavarren, *Gold(I)-Catalyzed Activation of Alkynes for the Construction of Molecular Complexity.* Chemical Reviews, 2015. **115**(17): p. 9028-9072.

16. Obradors, C. and A.M. Echavarren, *Intriguing mechanistic labyrinths in gold(i) catalysis.* Chemical Communications, 2014. **50**(1): p. 16-28.
17. Xiao, J. and X. Li, *Gold α-Oxo Carbenoids in Catalysis: Catalytic Oxygen-Atom Transfer to Alkynes.* Angewandte Chemie International Edition, 2011. **50**(32): p. 7226-7236.
18. Corma, A., A. Leyva-Pérez, and M.J. Sabater, *Gold-Catalyzed Carbon−Heteroatom Bond-Forming Reactions.* Chemical Reviews, 2011. **111**(3): p. 1657-1712.
19. Nevado, C., *Gold catalysis: recent developments and future trends.* Chimia (Aarau), 2010. **64**(4): p. 247-51.
20. Sengupta, S. and X. Shi, *Recent Advances in Asymmetric Gold Catalysis.* ChemCatChem, 2010. **2**(6): p. 609-619.
21. Sardar, R., et al., *Gold Nanoparticles: Past, Present, and Future†.* Langmuir, 2009. **25**(24): p. 13840-13851.
22. Haruta, M., *Catalysis of gold nanoparticles deposited on metal oxides.* CATTECH, 2002. **6**(3): p. 102-115.
23. Meyer, R., et al., *Surface chemistry of catalysis by gold.* Gold Bulletin, 2004. **37**(1-2): p. 72-124.
24. Okazaki, K., et al., *Electronic structures of Au supported on TiO.* Applied Catalysis A: General, 2005. **291**(1–2): p. 45-54.
25. Taylor, K.J., et al., *Ultraviolet photoelectron spectra of coinage metal clusters.* The Journal of Chemical Physics, 1992. **96**(4): p. 3319-3329.
26. Henglein, A., *Physicochemical properties of small metal particles in solution: "microelectrode" reactions, chemisorption, composite metal particles, and the atom-to-metal transition.* The Journal of Physical Chemistry, 1993. **97**(21): p. 5457-5471.
27. Henry, C., *Size Effects on Structure and Morphology of Free or Supported Nanoparticles*, in *Nanomaterials and Nanochemistry*, C. Bréchignac, P. Houdy, and M. Lahmani, Editors. 2007, Springer Berlin Heidelberg: Berlin, Heidelberg. p. 3-34.
28. Glockler, G., *The Structure of Crystals. By Ralph W. G. Wyckoff.* The Journal of Physical Chemistry, 1935. **40**(3): p. 422-422.
29. Szczerba, W., H. Riesemeier, and A.F. Thünemann, *Bond length contraction in gold nanoparticles.* Analytical & Bioanalytical Chemistry, 2010. **398**(5): p. 1967-1972.
30. Miller, J.T., et al., *The effect of gold particle size on AuAu bond length and reactivity toward oxygen in supported catalysts.* Journal of Catalysis, 2006. **240**(2): p. 222-234.
31. Fairbanks, M.C., et al., *An EXAFS study of the cluster molecule $Au_{55}(PPh_3)_{12}Cl_6$.* Solid State Communications, 1990. **73**(6): p. 431-436.
32. Apai, G., et al., *Extended X-Ray — Absorption Fine Structure of Small Cu and Ni Clusters: Binding-Energy and Bond-Length Changes with Cluster Size.* Physical Review Letters, 1979. **43**(2): p. 165-169.
33. De Crescenzi, M., et al., *Surface electron-energy-loss fine-structure investigation on the local structure of copper clusters on graphite.* Physical Review B, 1987. **35**(12): p. 5997-6003.
34. Cleveland, C.L., et al., *Structural evolution of larger gold clusters.* Zeitschrift für Physik D Atoms, Molecules and Clusters, 2014. **40**(1): p. 503-508.
35. Uppenbrink, J. and D.J. Wales, *Packing schemes for Lennard-Jones clusters of 13 to 150 atoms: minima, transition states and rearrangement mechanisms.* Journal of the Chemical Society, Faraday Transactions, 1991. **87**(2): p. 215-222.
36. Heath, S.T.L., *The works of Archimedes.* 1897, London: C. J. Clay and Sons.

37. Valden, M., X. Lai, and D.W. Goodman, *Onset of catalytic activity of gold clusters on titania with the appearance of nonmetallic properties.* Science, 1998. **281**(5383): p. 1647-1650.
38. Janz, A., et al., *Fundamental Calculations on the Surface Area Determination of Supported Gold Nanoparticles by Alkanethiol Adsorption.* Langmuir, 2010. **26**(9): p. 6783-6789.
39. Xiang, Y., et al., *Tuning the morphology of gold nanocrystals by switching the growth of {110} facets from restriction to preference.* Journal of Physical Chemistry C, 2008. **112**(9): p. 3203-3208.
40. Chowdhury, A.-N., et al., *Fabrication of Au(1 1 1) facet enriched electrode on glassy carbon.* Journal of Electroanalytical Chemistry, 2009. **634**(1): p. 35-41.
41. Wang, Z.L., *Transmission Electron Microscopy of Shape-Controlled Nanocrystals and Their Assemblies.* The Journal of Physical Chemistry B, 2000. **104**(6): p. 1153-1175.
42. Gong, J., *Structure and Surface Chemistry of Gold-Based Model Catalysts.* Chemical Reviews, 2012. **112**(5): p. 2987-3054.
43. Chen, Y., S. Milenkovic, and A.W. Hassel, *Reactivity of Gold Nanobelts with Unique {110} Facets.* ChemPhysChem, 2010. **11**(13): p. 2838-2843.
44. Jana, N.R., et al., *Anisotropic Chemical Reactivity of Gold Spheroids and Nanorods.* Langmuir, 2002. **18**(3): p. 922-927.
45. Rodriguez, P. and M.T.M. Koper, *Electrocatalysis on gold.* Physical Chemistry Chemical Physics, 2014. **16**(27): p. 13583-13594.
46. BełTowska-Brzezinska, M., T. ŁUczak, and R. Holze, *Electrocatalytic oxidation of mono- and polyhydric alcohols on gold and platinum.* Journal of Applied Electrochemistry, 1997. **27**(9): p. 999-1011.
47. Beden, B., et al., *Electrocatalytic oxidation of saturated oxygenated compounds on gold electrodes.* Journal of Catalysis, 1987. **104**(1): p. 37-46.
48. Kitco.com. *Price History*. [cited 2016 7th December]; Available from: www.kitco.com.
49. Duff, D.G., A. Baiker, and P.P. Edwards, *A new hydrosol of gold clusters. 1. Formation and particle size variation.* Langmuir, 1993. **9**(9): p. 2301-2309.
50. Chen, Y., C.W. Li, and M.W. Kanan, *Aqueous CO_2 Reduction at Very Low Overpotential on Oxide-Derived Au Nanoparticles.* Journal of the American Chemical Society, 2012. **134**(49): p. 19969-19972.
51. Cherevko, S., et al., *Electrochemical dissolution of gold in acidic medium.* Electrochemistry Communications, 2013. **28**: p. 44-46.
52. Bond, G.C. and D.T. Thompson, *Catalysis by gold.* Catalysis Reviews-Science and Engineering, 1999. **41**(3-4): p. 319-388.
53. Lahr, D.L. and S.T. Ceyer, *Catalyzed CO Oxidation at 70 K on an Extended Au/Ni Surface Alloy.* Journal of the American Chemical Society, 2006. **128**(6): p. 1800-1801.
54. Andreeva, D., et al., *Low-Temperature Water–Gas Shift Reaction over Au/α-Fe_2O_3.* Journal of Catalysis, 1996. **158**(1): p. 354-355.
55. Kwon, Y., et al., *Electrocatalytic Oxidation of Alcohols on Gold in Alkaline Media: Base or Gold Catalysis?* Journal of the American Chemical Society, 2011. **133**(18): p. 6914-6917.
56. Padayachee, D., et al., *Influence of particle size on the electrocatalytic oxidation of glycerol over carbon-supported gold nanoparticles.* Electrochimica Acta, 2014. **120**(0): p. 398-407.

57. Marshall, A.T., V. Golovko, and D. Padayachee, *Influence of gold nanoparticle loading in Au/C on the activity towards electrocatalytic glycerol oxidation.* Electrochimica Acta, 2015. **153**(0): p. 370-378.
58. Prati, L. and M. Rossi, *Gold on Carbon as a New Catalyst for Selective Liquid Phase Oxidation of Diols.* Journal of Catalysis, 1998. **176**(2): p. 552-560.
59. Carrettin, S., et al., *Oxidation of Glycerol Using Supported Gold Catalysts.* Topics in Catalysis, 2004. **27**(1): p. 131-136.
60. Haruta, M., *Size- and support-dependency in the catalysis of gold.* Catalysis Today, 1997. **36**(1): p. 153-166.
61. Bamwenda, G.R., et al., *The influence of the preparation methods on the catalytic activity of platinum and gold supported on TiO_2 for CO oxidation.* Catalysis Letters, 1997. **44**(1): p. 83-87.
62. Molina, L.M. and B. Hammer. *Some recent theoretical advances in the understanding of the catalytic activity of Au*. in *Catalysis by Gold*. 2005. Elsevier.
63. Chen, W. and S. Chen, *Oxygen Electroreduction Catalyzed by Gold Nanoclusters: Strong Core Size Effects.* Angewandte Chemie International Edition, 2009. **48**(24): p. 4386-4389.
64. Anand, P. and R.K. Saxena, *A comparative study of solvent-assisted pretreatment of biodiesel derived crude glycerol on growth and 1,3-propanediol production from Citrobacter freundii.* New Biotechnology, 2012. **29**(2): p. 199-205.
65. Kerr, B.J., W.A. Dozier, and K. Bregendahl. *Nutritional Value of Crude Glycerin for Nonruminants*. 2007.
66. Demirel-Gülen, S., M. Lucas, and P. Claus, *Liquid phase oxidation of glycerol over carbon supported gold catalysts.* Catalysis Today, 2005. **102–103**(0): p. 166-172.
67. N.A.S.A. *Global Mean CO_2 Mixing Ratios*. Available from: http://data.giss.nasa.gov/modelforce/ghgases/.
68. Jones, H.P. and O.J. Schmitz, *Rapid Recovery of Damaged Ecosystems.* PLoS ONE, 2009. **4**(5): p. e5653.
69. Azuma, M., et al., *Electrochemical reduction of carbon dioxide on various metal electrodes in low-temperature aqueous potassium hydrogen carbonate media.* J. Electrochem. Soc., 1990. **137**: p. 1772-8.
70. Tripkovic, V., et al., *Electrochemical CO_2 and CO Reduction on Metal-Functionalized Porphyrin-like Graphene.* The Journal of Physical Chemistry C, 2013.
71. Shaw, S.K., et al., *Role of axially coordinated surface sites for electrochemically controlled carbon monoxide adsorption on single crystal copper electrodes.* Physical Chemistry Chemical Physics, 2011. **13**(12): p. 5242-5251.
72. Kauffman, D.R., et al., *Experimental and Computational Investigation of Au_{25} Clusters and CO_2: A Unique Interaction and Enhanced Electrocatalytic Activity*. J. Am. Chem. Soc., 2012. **134**: p. 10237-10243.
73. Delley, B., *From molecules to solids with the DMol3 approach.* Journal of Chemical Physics, 2000. **113**(18): p. 7756-7764.
74. Kuhl, K.P., et al., *New Insights into the Electrochemical Reduction of Carbon Dioxide on Metallic Copper Surfaces.* Energy & Environmental Science, 2012. **5**(5): p. 7050-7059.
75. Martínez, A., *Size Matters, but Is Being Planar of Any Relevance? Electron Donor−Acceptor Properties of Neutral Gold Clusters up to 20 Atoms.* The Journal of Physical Chemistry C, 2010. **114**(49): p. 21240-21246.

76. Green, I.X., et al., *Spectroscopic observation of dual catalytic sites during oxidation of CO on a Au/TiO₂ catalyst.* Science, 2011. **333**(6043): p. 736-739.
77. Wang, L., et al., *Superior catalytic properties in aerobic oxidation of olefins over Au nanoparticles on pyrrolidone-modified SBA-15.* Journal of Catalysis, 2011. **281**(1): p. 30-39.
78. Hohenberg, P. and W. Kohn, *Inhomogeneous Electron Gas.* Physical Review, 1964. **136**(3B): p. B864-B871.
79. Burgess, R.W. and V.J. Keast, *TDDFT Study of the Optical Absorption Spectra of Bare Gold Clusters.* The Journal of Physical Chemistry C, 2014. **118**(6): p. 3194-3201.
80. Newville, M., *IFEFFIT: interactive XAFS analysis and FEFF fitting.* J Synchrotron Radiat, 2001. **8**(Pt 2): p. 322-324.
81. Webb, S.M., *SIXpack: a graphical user interface for XAS analysis using IFEFFIT.* Physica Scripta, 2005. **2005**(T115): p. 1011.
82. Plowman, B.J. and R.G. Compton, *Inhibition of Cu Underpotential Deposition on Au Nanoparticles: The Role of the Citrate Capping Agent and Nanoparticle Size.* ChemElectroChem, 2014. **1**(6): p. 1009-1012.
83. Burke, L.D. and M. McRann, *Thick oxide growth on gold in base.* Journal of Electroanalytical Chemistry and Interfacial Electrochemistry, 1981. **125**(2): p. 387-399.
84. Hutchings, G.J., *Catalysis by gold.* Catalysis Today, 2005. **100**(1–2): p. 55-61.
85. Willets, K.A. and R.P.V. Duyne, *Localized Surface Plasmon Resonance Spectroscopy and Sensing.* Annual Review of Physical Chemistry, 2007. **58**(1): p. 267-297.
86. Freestone, I., et al., *The Lycurgus Cup — A Roman nanotechnology.* Gold Bulletin, 2007. **40**(4): p. 270-277.
87. British Museum Collection Database, *1958,1202.1.* British Museum.
88. Saha, K., et al., *Gold Nanoparticles in Chemical and Biological Sensing.* Chemical Reviews, 2012. **112**(5): p. 2739-2779.
89. Faraday, M., *The Bakerian Lecture: Experimental Relations of Gold (and Other Metals) to Light.* Philosophical Transactions of the Royal Society of London, 1857. **147**: p. 145-181.
90. Cariati, F. and L. Naldini, *Preparation and properties of gold atom cluster compounds: octakis-(triarylphosphine)enneagold trianion.* Journal of the Chemical Society, Dalton Transactions, 1972(20): p. 2286-2287.
91. Weare, W.W., et al., *Improved Synthesis of Small (dCORE ≈ 1.5 nm) Phosphine-Stabilized Gold Nanoparticles.* Journal of the American Chemical Society, 2000. **122**(51): p. 12890-12891.
92. Brust, M., et al., *Synthesis of thiol-derivatised gold nanoparticles in a two-phase Liquid-Liquid system.* Journal of the Chemical Society, Chemical Communications, 1994. **0**(7): p. 801-802.
93. Hussain, I., et al., *Size-Controlled Synthesis of Near-Monodisperse Gold Nanoparticles in the 1−4 nm Range Using Polymeric Stabilizers.* Journal of the American Chemical Society, 2005. **127**(47): p. 16398-16399.
94. Martin, M.N., et al., *Charged Gold Nanoparticles in Non-Polar Solvents: 10-min Synthesis and 2D Self-Assembly.* Langmuir, 2010. **26**(10): p. 7410-7417.
95. Turkevich, J., P.C. Stevenson, and J. Hillier, *A study of the nucleation and growth processes in the synthesis of colloidal gold.* Discussions of the Faraday Society, 1951. **11**(0): p. 55-75.

96. Davies, A.E., *The Kinetics of the Coagulation of Gold Sols. An Investigation of the "Thermo-Senescence Effect" exhibited at Elevated Temperatures.* The Journal of Physical Chemistry, 1928. **33**(2): p. 274-284.
97. Granqvist, C.G. and R.A. Buhrman, *Ultrafine metal particles.* Journal of Applied Physics, 1976. **47**(5): p. 2200-2219.
98. Bredig, G. and F. Haber, *Ueber Zerstäubung von Metallkathoden bei der Elektrolyse mit Gleichstrom.* Berichte der deutschen chemischen Gesellschaft, 1898. **31**(3): p. 2741-2752.
99. Seitz, O., et al., *Preparation and characterisation of gold nanoparticle assemblies on silanised glass plates.* Colloids and Surfaces A: Physicochemical and Engineering Aspects, 2003. **218**(1–3): p. 225-239.
100. Tian, F. and K. J. Klabunde, *Nonaqueous gold colloids. Investigations of deposition and film growth on organically modified substrates and trapping of molecular gold clusters with an alkyl amine.* New Journal of Chemistry, 1998. **22**(11): p. 1275-1283.
101. Kissinger, P.T. and W.R. Heineman, *Cyclic Voltammetry.* Journal of Chemical Education, 1983. **60**(9): p. 702.
102. Fernández, P.S., et al., *Platinum nanoparticles produced by EG/PVP method: The effect of cleaning on the electro-oxidation of glycerol.* Electrochimica Acta, 2013. **98**(0): p. 25-31.
103. Hoare, J.P., *A Cyclic Voltammetric Study of the Gold-Oxygen System.* Journal of the Electrochemical Society, 1984. **131**(8): p. 1808-1815.
104. Pozio, A., et al., *Comparison of high surface Pt/C catalysts by cyclic voltammetry.* Journal of Power Sources, 2002. **105**(1): p. 13-19.
105. Hayden, B.E., et al., *CO Oxidation on Gold in Acidic Environments: Particle Size and Substrate Effects.* The Journal of Physical Chemistry C, 2007. **111**(45): p. 17044-17051.
106. Hamelin, A., *Cyclic voltammetry at gold single-crystal surfaces. Part 1. Behaviour at low-index faces.* Journal of Electroanalytical Chemistry, 1996. **407**(1–2): p. 1-11.
107. Andrews, E.M., J. Flake, and Y. Fang, *CO_2 Electrocatalytic Reduction at Gold and Copper Electrodes: Role of Particle Size and Surface Chemistry.* Meeting Abstracts, 2015. **MA2015-01**(25): p. 1523.
108. Delacourt, C. and J. Newman, *Mathematical Modeling of CO_2 Reduction to CO in Aqueous Electrolytes.* J. Electrochem. Soc., 2010. **157**(Copyright (C) 2013 American Chemical Society (ACS). All Rights Reserved.): p. B1911-B1926.
109. Gao, D., et al., *Size-Dependent Electrocatalytic Reduction of CO_2 over Pd Nanoparticles.* Journal of the American Chemical Society, 2015. **137**(13): p. 4288-4291.
110. Hori, Y., *Electrochemical CO_2 Reduction on Metal Electrodes*, in *Modern Aspects of Electrochemistry*, C.G. Vayenas, R.E. White, and M.E. Gamboa-Aldeco, Editors. 2008, Springer New York: New York, NY. p. 89-189.
111. Hori, Y., et al., *Electrocatalytic process of CO selectivity in electrochemical reduction of CO_2 at metal electrodes in aqueous media.* Electrochimica Acta, 1994. **39**(11): p. 1833-1839.
112. Stone, F.S. and D. Waller, *Cu–ZnO and Cu–ZnO/Al_2O_3 Catalysts for the Reverse Water-Gas Shift Reaction. The Effect of the Cu/Zn Ratio on Precursor Characteristics and on the Activity of the Derived Catalysts.* Topics in Catalysis, 2003. **22**(3): p. 305-318.

113. Hansen, H.A., et al., *Understanding Trends in the Electrocatalytic Activity of Metals and Enzymes for CO_2 Reduction to CO.* The Journal of Physical Chemistry Letters, 2013. **4**(3): p. 388-392.
114. Zhu, W., et al., *Active and Selective Conversion of CO_2 to CO on Ultrathin Au Nanowires.* Journal of the American Chemical Society, 2014. **136**(46): p. 16132-16135.
115. Mistry, H., et al., *Exceptional Size-Dependent Activity Enhancement in the Electroreduction of CO_2 over Au Nanoparticles.* Journal of the American Chemical Society, 2014. **136**(47): p. 16473-16476.
116. Kauffman, D.R., et al., *Efficient Electrochemical CO_2 Conversion Powered by Renewable Energy.* ACS Applied Materials & Interfaces, 2015. **7**(28): p. 15626-15632.
117. Hall, A.S., et al., *Mesostructure-Induced Selectivity in CO_2 Reduction Catalysis.* Journal of the American Chemical Society, 2015. **137**(47): p. 14834-14837.
118. Zhu, W., et al., *Monodisperse Au Nanoparticles for Selective Electrocatalytic Reduction of CO_2 to CO.* Journal of the American Chemical Society, 2013.
119. Oesch, U. and J. Janata, *Electrochemical study of gold electrodes with anodic oxide films—I. Formation and reduction behaviour of anodic oxides on gold.* Electrochimica Acta, 1983. **28**(9): p. 1237-1246.
120. Laitinen, H.A. and M.S. Chao, *The Anodic Surface Oxidation of Gold.* Journal of The Electrochemical Society, 1961. **108**(8): p. 726-731.
121. Burke, L.D., M.E. Lyons, and D.P. Whelan, *Influence of ph on the reduction of thick anodic oxide films on gold.* Journal of Electroanalytical Chemistry and Interfacial Electrochemistry, 1982. **139**(1): p. 131-142.
122. Oesch, U. and J. Janata, *Electrochemical study of gold electrodes with anodic oxide films—II. Inhibition of electrochemical redox reactions by monolayers of surface oxides.* Electrochimica Acta, 1983. **28**(9): p. 1247-1253.
123. Burke, L.D., M.M. McCarthy, and M.B.C. Roche, *Influence of solution pH on monolayer and multilayer oxide formation processes on gold and palladium.* Journal of Electroanalytical Chemistry and Interfacial Electrochemistry, 1984. **167**(1–2): p. 291-297.
124. Frelink, T., W. Visscher, and J.A.R. van Veen, *The third anodic hydrogen peak on platinum; Subsurface H_2 adsorption.* Electrochimica Acta, 1995. **40**(5): p. 545-549.
125. Cherevko, S., et al., *A Comparative Study on Gold and Platinum Dissolution in Acidic and Alkaline Media.* Journal of The Electrochemical Society, 2014. **161**(12): p. H822-H830.
126. Hamelin, A., *Underpotential deposition of lead on single crystal faces of gold: Part I. The influence of crystallographic orientation of the substrate.* Journal of Electroanalytical Chemistry and Interfacial Electrochemistry, 1984. **165**(1–2): p. 167-180.
127. Price, S.W.T., et al., *Exploring the First Steps in Core-Shell Electrocatalyst Preparation: In Situ Characterization of the Underpotential Deposition of Cu on Supported Au Nanoparticles.* Journal of the American Chemical Society, 2011. **133**(48): p. 19448-19458.
128. Angerstein-Kozlowska, H., et al., *Elementary steps of electrochemical oxidation of single-crystal planes of Au—I. Chemical basis of processes involving geometry of anions and the electrode surfaces.* Electrochimica Acta, 1986. **31**(8): p. 1051-1061.

129. Chen, Y.-S., et al., *Electrochemical impedimetric biosensor based on a nanostructured polycarbonate substrate.* International Journal of Nanomedicine, 2012. **7**: p. 133-140.
130. Burke, L.D. and P.F. Nugent, *The Electrochemistry of Gold: I. The Redox Behavior of the Metal in Aqueous Media.* Gold Bull. (London), 1997. **30**: p. 43-53.
131. Santos, M.C., L.H. Mascaro, and S.A.S. Machado, *Voltammetric and rotating ring-disk studies of underpotential deposition of Ag and Cu on polycrystalline Au electrodes in aqueous H_2SO_4.* Electrochimica Acta, 1998. **43**(16–17): p. 2263-2272.
132. Chen, Z., et al., *Electrochemical impedance spectroscopy detection of lysozyme based on electrodeposited gold nanoparticles.* Talanta, 2011. **83**(5): p. 1501-1506.
133. Bott-Neto, J.L., et al., *Au/C catalysts prepared by a green method towards C3 alcohol electrooxidation: A cyclic voltammetry and in situ FTIR spectroscopy study.* Journal of Electroanalytical Chemistry, 2014. **735**: p. 57-62.
134. Yancey, D.F., E.V. Carino, and R.M. Crooks, *Electrochemical Synthesis and Electrocatalytic Properties of Au@Pt Dendrimer-Encapsulated Nanoparticles.* Journal of the American Chemical Society, 2010. **132**(32): p. 10988-10989.
135. Trasatti, S. and O.A. Petrii, *Real surface area measurements in electrochemistry*, in *Pure and Applied Chemistry*. 1991. p. 711.
136. Nagaraju, D.H. and V. Lakshminarayanan, *Electrochemically Grown Mesoporous Gold Film as High Surface Area Material for Electro-Oxidation of Alcohol in Alkaline Medium.* The Journal of Physical Chemistry C, 2009. **113**(33): p. 14922-14926.
137. Carvalhal, R.F., R. Sanches Freire, and L.T. Kubota, *Polycrystalline Gold Electrodes: A Comparative Study of Pretreatment Procedures Used for Cleaning and Thiol Self-Assembly Monolayer Formation.* Electroanalysis, 2005. **17**(14): p. 1251-1259.
138. Hoogvliet, J.C., et al., *Electrochemical Pretreatment of Polycrystalline Gold Electrodes To Produce a Reproducible Surface Roughness for Self-Assembly: A Study in Phosphate Buffer pH 7.4.* Analytical Chemistry, 2000. **72**(9): p. 2016-2021.
139. Finot, M.O., G.D. Braybrook, and M.T. McDermott, *Characterization of electrochemically deposited gold nanocrystals on glassy carbon electrodes.* Journal of Electroanalytical Chemistry, 1999. **466**(2): p. 234-241.
140. Park, J.-E., T. Momma, and T. Osaka, *Spectroelectrochemical phenomena on surface plasmon resonance of Au nanoparticles immobilized on transparent electrode.* Electrochimica Acta, 2007. **52**(19): p. 5914-5923.
141. Ballarin, B., et al., *RF-sputtering preparation of gold-nanoparticle-modified ITO electrodes for electrocatalytic applications.* Nanotechnology, 2011. **22**(27).
142. Kesavan, S. and S. Abraham John, *Spontaneous grafting: A novel approach to graft diazonium cations on gold nanoparticles in aqueous medium and their self-assembly on electrodes.* Journal of Colloid and Interface Science, 2014. **428**: p. 84-94.
143. Kumar, S. and S. Zou, *Electrooxidation of Carbon Monoxide on Gold Nanoparticle Ensemble Electrodes: Effects of Particle Coverage.* The Journal of Physical Chemistry B, 2005. **109**(33): p. 15707-15713.
144. Tremiliosi-Filho, G., L.H. Dall'Antonia, and G. Jerkiewicz, *Limit to extent of formation of the quasi-two-dimensional oxide state on Au electrodes.* Journal of Electroanalytical Chemistry, 1997. **422**(1): p. 149-159.
145. Bruckenstein, S. and M. Shay, *An in-situ weighing study of the mechanism for the formation of the adsorbed oxygen monolayer at a gold electrode.* Journal of

Electroanalytical Chemistry and Interfacial Electrochemistry, 1985. **188**(1): p. 131-136.
146. Wang, Y., et al., *Surface oxidation of gold nanoparticles supported on a glassy carbon electrode in sulphuric acid medium: contrasts with the behaviour of 'macro' gold.* Physical Chemistry Chemical Physics, 2013. **15**(9): p. 3133-3136.
147. Van Hardeveld, R. and F. Hartog, *The statistics of surface atoms and surface sites on metal crystals.* Surface Science, 1969. **15**(2): p. 189-230.
148. Campbell, C.T., S.C. Parker, and D.E. Starr, *The Effect of Size-Dependent Nanoparticle Energetics on Catalyst Sintering.* Science, 2002. **298**(5594): p. 811-814.
149. Maillard, F., S. Pronkin, and E.R. Savinova, *Influence of size on the electrocatalytic activities of supported metal nanoparticles in fuel cells related reactions*, in *Handbook of Fuel Cells*. 2010, John Wiley & Sons, Ltd.
150. Balerna, A., et al., *Extended x-ray-absorption fine-structure and near-edge-structure studies on evaporated small clusters of Au.* Physical Review B, 1985. **31**(8): p. 5058-5065.
151. Balerna, A., et al., *A structural investigation on small gold clusters by EXAFS.* Surface Science, 1985. **156, Part 1**: p. 206-213.
152. Stahel, W., *The normal distribution is the log-normal distribution.* 2014, ETH Zürich.
153. Ravel, B. and M. Newville, *ATHENA, ARTEMIS, HEPHAESTUS: data analysis for X-ray absorption spectroscopy using IFEFFIT.* Journal of Synchrotron Radiation, 2005. **12**(4): p. 537-541.
154. Joly, Y., *X-ray absorption near edge structure calculations beyond the muffin-tin approximation.* Phys. Rev. B, 2001. **63**: p. 125120-125129.
155. Wong, J., *Extended x-ray absorption fine structure: A modern structural tool in materials science.* Materials Science and Engineering, 1986. **80**(2): p. 107-128.
156. Bearden, J.A. and A.F. Burr, *Reevaluation of X-Ray Atomic Energy Levels.* Reviews of Modern Physics, 1967. **39**(1): p. 125-142.
157. Ma, W., et al., *Investigating electron-transfer processes using a biomimetic hybrid bilayer membrane system.* Nat. Protocols, 2013. **8**(3): p. 439-450.
158. Cherevko, S., et al., *Gold dissolution: towards understanding of noble metal corrosion.* RSC Advances, 2013. **3**(37): p. 16516-16527.
159. Rand, D.A.J. and R. Woods, *A study of the dissolution of platinum, palladium, rhodium and gold electrodes in 1 m sulphuric acid by cyclic voltammetry.* Journal of Electroanalytical Chemistry and Interfacial Electrochemistry, 1972. **35**(1): p. 209-218.
160. Lakbub, J., et al., *Electrochemical Behaviors of Single Gold Nanoparticles.* Electroanalysis, 2011. **23**(10): p. 2270-2274.
161. Ngamchuea, K., et al., *In Situ Detection of Particle Aggregation on Electrode Surfaces.* ChemPhysChem, 2015. **16**(11): p. 2338-2347.
162. Okada, T., et al., *Ion and Water Transport Characteristics of Perfluorosulfonated Ionomer Membranes with H^+ and Alkali Metal Cations.* The Journal of Physical Chemistry B, 2002. **106**(6): p. 1267-1273.
163. Wang, J., et al., *Effect of carbon black support corrosion on the durability of Pt/C catalyst.* Journal of Power Sources, 2007. **171**(2): p. 331-339.
164. Bond, G.C., C. Louis, and D.T. Thompson, *Catalysis by Gold*. 2006: Imperial College Press.

165. Ahmad, M.Z., et al., *Optical characterisation of nanostructured Au/WO_3 thin films for sensing hydrogen at low concentrations.* Sensors and Actuators B: Chemical, 2013. **179**(0): p. 125-130.
166. Ahmad, M.Z., et al., *Hydrogen sensing using gold nanoclusters supported on tungsten trioxide thin films.* International Journal of Hydrogen Energy, 2013. **38**(29): p. 12865-12877.
167. Padayachee, D., V. Golovko, and A.T. Marshall, *The effect of MnO_2 loading on the glycerol electrooxidation activity of Au/MnO_2/C catalysts.* Electrochimica Acta, 2013. **98**: p. 208-217.
168. Herzing, A.A., et al., *Identification of Active Gold Nanoclusters on Iron Oxide Supports for CO Oxidation.* Science (Washington, DC, U. S.), 2008. **321**: p. 1331-1335.
169. Adnan, R.H., et al., *Factors influencing the catalytic oxidation of benzyl alcohol using supported phosphine-capped gold nanoparticles.* Catalysis Science & Technology, 2015. **5**(2): p. 1323-1333.
170. Donoeva, B.G., D.S. Ovoshchnikov, and V.B. Golovko, *Establishing a Au Nanoparticle Size Effect in the Oxidation of Cyclohexene Using Gradually Changing Au Catalysts.* ACS Catalysis, 2013: p. 2986-2991.
171. Ovoshchnikov, D.S., et al., *Tuning the selectivity of a supported gold catalyst in solvent- and radical initiator-free aerobic oxidation of cyclohexene.* Catalysis Science & Technology, 2014. **4**(3): p. 752-757.
172. Turner, M., et al., *Selective oxidation with dioxygen by gold nanoparticle catalysts derived from 55-atom clusters.* Nature, 2008. **454**(7207): p. 981-983.
173. Zhang, J., et al., *A remarkable activity of glycerol electrooxidation on gold in alkaline medium.* Electrochimica Acta, 2012. **59**(0): p. 156-159.
174. Selvaganesh, S.V., et al., *Durable electrocatalytic-activity of Pt-Au/C cathode in PEMFCs.* Physical Chemistry Chemical Physics, 2011. **13**(27): p. 12623-12634.
175. Kohyama, M., et al., *Theoretical Studies of the Atomic and Electronic Structure of Nano-Hetero Metal/Inorganic Material Interfaces in Collaboration with Electron Microscopy Observations.* Materials Transactions, 2007. **48**(4): p. 675-683.
176. Anderson, D.P., et al., *Chemically-synthesised, atomically-precise gold clusters deposited and activated on titania.* Physical Chemistry Chemical Physics, 2013. **15**(11): p. 3917-3929.
177. Anderson, D.P., et al., *Chemically synthesised atomically precise gold clusters deposited and activated on titania. Part II.* Physical Chemistry Chemical Physics, 2013. **15**(35): p. 14806-14813.
178. Andersson, G.G., et al., *Phosphine-stabilised Au_9 clusters interacting with titania and silica surfaces: The first evidence for the density of states signature of the support-immobilised cluster.* The Journal of Chemical Physics, 2014. **141**(1): p. 014702.
179. Bus, E., J.T. Miller, and J.A. van Bokhoven, *Hydrogen Chemisorption on Al_2O_3-Supported Gold Catalysts.* The Journal of Physical Chemistry B, 2005. **109**(30): p. 14581-14587.
180. Lee, Y., et al., *Enhancement of electrocatalytic activity of gold nanoparticles by sonochemical treatment.* Chemical Communications, 2010. **46**(31): p. 5656-5658.
181. Campbell, C.T., S.C. Parker, and D.E. Starr, *The effect of size-dependent nanoparticle energetics on catalyst sintering.* Science, 2002. **298**(5594): p. 811-4.

182. Shao-Horn, Y., et al., *Instability of Supported Platinum Nanoparticles in Low-Temperature Fuel Cells.* Topics in Catalysis, 2007. **46**(3): p. 285-305.
183. Holby, E.F., et al., *Pt nanoparticle stability in PEM fuel cells: influence of particle size distribution and crossover hydrogen.* Energy & Environmental Science, 2009. **2**(8): p. 865-871.
184. Tang, L., et al., *Electrochemical Stability of Nanometer-Scale Pt Particles in Acidic Environments.* Journal of the American Chemical Society, 2010. **132**(2): p. 596-600.
185. Mayrhofer, K.J.J., et al., *Non-destructive transmission electron microscopy study of catalyst degradation under electrochemical treatment.* Journal of Power Sources, 2008. **185**(2): p. 734-739.
186. Cruickshank, A.C. and A.J. Downard, *Electrochemical stability of citrate-capped gold nanoparticles electrostatically assembled on amine-modified glassy carbon.* Electrochimica Acta, 2009. **54**(23): p. 5566-5570.
187. Cadle, S.H. and S. Bruckenstein, *Ring-disk electrode study of the anodic behavior of gold in 0.2M sulfuric acid.* Analytical Chemistry, 1974. **46**(1): p. 16-20.
188. Vesztergom, S., M. Ujvári, and G.G. Láng, *RRDE experiments with potential scans at the ring and disk electrodes.* Electrochemistry Communications, 2011. **13**(4): p. 378-381.
189. Woods, R., *Chemisorption at electrodes*, in *Electroanalytical Chemistry: a Series of Advances*, A.J. Bard, Editor. 1976, Marcel Dekker: New York. p. 1-162.
190. Park, I., et al., *Electrocatalytic activity of carbon-supported Pt–Au nanoparticles for methanol electro-oxidation.* Electrochimica Acta, 2007. **52**(18): p. 5599-5605.
191. Schmidt, T.J., et al., *Characterization of High-Surface-Area Electrocatalysts Using a Rotating Disk Electrode Configuration.* Journal of The Electrochemical Society, 1998. **145**(7): p. 2354-2358.
192. Garsany, Y., et al., *Experimental Methods for Quantifying the Activity of Platinum Electrocatalysts for the Oxygen Reduction Reaction.* Analytical Chemistry, 2010. **82**(15): p. 6321-6328.
193. Wen, F., et al., *Crystal Structure, Electrochemical and Optical Properties of $[Au_9(PPh_3)_8](NO_3)_3$.* European Journal of Inorganic Chemistry, 2008. **2008**(1): p. 106-111.
194. Sayers, D.E. and B.A. Bunker, *X-ray absorption: principles, applications, techniques of EXAFS, SEXAFS, and XANES*. 1988. p. 211-253.
195. Ravel, B., *ATOMS: crystallography for the X-ray absorption spectroscopist.* Journal of Synchrotron Radiation, 2001. **8**(2): p. 314-316.
196. Conway, B.E., *Electrochemical oxide film formation at noble metals as a surface-chemical process.* Progress in Surface Science, 1995. **49**(4): p. 331-452.
197. Barnard, A.S., et al., *Nanogold: A Quantitative Phase Map.* ACS Nano, 2009. **3**(6): p. 1431-1436.
198. Boyen, H.G., et al., *Oxidation-resistant gold-55 clusters.* Science, 2002. **297**(5586): p. 1533-6.
199. Oviedo, O.A., L. Reinaudi, and E.P.M. Leiva, *The limits of underpotential deposition in the nanoscale.* Electrochemistry Communications, 2012. **21**: p. 14-17.
200. Batchelor-McAuley, C., et al., *Correction factors for the analysis of voltammetric peak currents measured using staircase voltammetry.* Journal of Electroanalytical Chemistry, 2015. **758**: p. 1-6.

201. Raghuveer, V. and A. Manthiram, *Mesoporous Carbon with Larger Pore Diameter as an Electrocatalyst Support for Methanol Oxidation.* Electrochemical and Solid-State Letters, 2004. **7**(10): p. A336-A339.
202. Tian, M., W.G. Pell, and B.E. Conway, *Nanogravimetry study of the initial stages of anodic surface oxide film growth at Au in aqueous $HClO_4$ and H_2SO_4 by means of EQCN.* Electrochimica Acta, 2003. **48**(18): p. 2675-2689.
203. Guerin, S., et al., *Combinatorial Electrochemical Screening of Fuel Cell Electrocatalysts.* Journal of Combinatorial Chemistry, 2004. **6**(1): p. 149-158.
204. Hayden, B.E., D. Pletcher, and J.-P. Suchsland, *Enhanced Activity for Electrocatalytic Oxidation of Carbon Monoxide on Titania-Supported Gold Nanoparticles.* Angewandte Chemie International Edition, 2007. **46**(19): p. 3530-3532.
205. Sumi, T. and K. Uosaki, *Electrochemical Oxidative Formation and Reductive Desorption of a Self-Assembled Monolayer of Decanethiol on a Au(111) Surface in KOH Ethanol Solution.* The Journal of Physical Chemistry B, 2004. **108**(20): p. 6422-6428.
206. Wain, A.J., *Imaging size effects on the electrocatalytic activity of gold nanoparticles using scanning electrochemical microscopy.* Electrochimica Acta, 2013. **92**: p. 383-391.
207. Barnard, A.S. and Y. Chen, *Kinetic modelling of the shape-dependent evolution of faceted gold nanoparticles.* Journal of Materials Chemistry, 2011. **21**(33): p. 12239-12245.
208. Rabis, A., P. Rodriguez, and T.J. Schmidt, *Electrocatalysis for Polymer Electrolyte Fuel Cells: Recent Achievements and Future Challenges.* ACS Catalysis, 2012. **2**(5): p. 864-890.
209. Ruzicka, J.-Y., et al., *Toward Control of Gold Cluster Aggregation on TiO2 via Surface Treatments.* The Journal of Physical Chemistry C, 2015. **119**(43): p. 24465-24474.
210. Heider, E.C., et al., *An indium tin oxide electrode modified with gold nanorods for use in potential-controlled surface plasmon resonance studies.* Microchimica Acta, 2013. **180**(11): p. 1013-1020.
211. Ruiz, V., et al., *UV/Vis Spectroelectrochemical Evidence of Rectification of Quantized Charging in Monolayer-Protected Gold Cluster Films.* Small, 2006. **2**(1): p. 56-58.
212. Doyen, M., K. Bartik, and G. Bruylants, *UV-Vis and NMR study of the formation of gold nanoparticles by citrate reduction: observation of gold-citrate aggregates.* J Colloid Interface Sci, 2013. **399**: p. 1-5.
213. Toyota, A., N. Nakashima, and T. Sagara, *UV-visible transmission-absorption spectral study of Au nanoparticles on a modified ITO electrode at constant potentials and under potential modulation.* Journal of Electroanalytical Chemistry, 2004. **565**(2): p. 335-342.
214. Haiss, W., et al., *Determination of Size and Concentration of Gold Nanoparticles from UV−Vis Spectra.* Analytical Chemistry, 2007. **79**(11): p. 4215-4221.
215. Amendola, V. and M. Meneghetti, *Size Evaluation of Gold Nanoparticles by UV−vis Spectroscopy.* The Journal of Physical Chemistry C, 2009. **113**(11): p. 4277-4285.
216. Bhui, D.K., et al., *Synthesis and UV–vis spectroscopic study of silver nanoparticles in aqueous SDS solution.* Journal of Molecular Liquids, 2009. **145**(1): p. 33-37.
217. Laven, P.; Available from: http://www.philiplaven.com/.

218. Mulvaney, P., et al., *Drastic Surface Plasmon Mode Shifts in Gold Nanorods Due to Electron Charging.* Plasmonics, 2006. **1**(1): p. 61-66.
219. Khlebtsov, N.G., *Determination of Size and Concentration of Gold Nanoparticles from Extinction Spectra.* Analytical Chemistry, 2008. **80**(17): p. 6620-6625.
220. Eustis, S. and M.A. El-Sayed, *Why gold nanoparticles are more precious than pretty gold: Noble metal surface plasmon resonance and its enhancement of the radiative and nonradiative properties of nanocrystals of different shapes.* Chemical Society Reviews, 2006. **35**(3): p. 209-217.
221. Byers, C.P., et al., *Single-particle plasmon voltammetry (spPV) for detecting anion adsorption.* Nano Letters, 2016.
222. Sheridan, A.K., et al., *Waveguide surface plasmon resonance sensing: Electrochemical desorption of alkane thiol monolayers.* Sensors and Actuators B: Chemical, 2006. **117**(1): p. 253-260.
223. Yamada, M., et al., *Electroreductive Deposition of Anthraquinone Derivative Attached Au Clusters: Optical Properties and Scanning Tunneling Microscopy Observation of the Electrodeposited Cluster Film.* Langmuir, 2001. **17**(8): p. 2363-2370.
224. Weber, M. and F.C. Nart, *New Results on the Adsorption of Sulfate Species at Polycrystalline Gold Electrodes. An in Situ FTIR Study.* Langmuir, 1996. **12**(7): p. 1895-1900.
225. Novo, C., et al., *Electrochemical Charging of Single Gold Nanorods.* Journal of the American Chemical Society, 2009. **131**(41): p. 14664-14666.
226. Iwasaki, Y., et al., *Analysis of electrochemical processes using surface plasmon resonance.* Sensors and Actuators B: Chemical, 1998. **50**(2): p. 145-148.
227. Jory, M.J., P.S. Cann, and J.R. Sambles, *Surface-plasmon voltammetry using a gold grating.* Journal of Physics D: Applied Physics, 2010. **43**(38): p. 385301.
228. Iwasaki, Y., et al., *Time differential surface plasmon resonance measurements applied for electrochemical analysis.* Electroanalysis, 1997. **9**(16): p. 1239-1241.
229. Jory, M.J., et al., *A surface-plasmon-based optical sensor using acousto-optics.* Measurement Science and Technology, 1995. **6**(8): p. 1193.
230. Iwasaki, Y., T. Horiuchi, and O. Niwa, *Detection of Electrochemical Enzymatic Reactions by Surface Plasmon Resonance Measurement.* Analytical Chemistry, 2001. **73**(7): p. 1595-1598.
231. Fu, E., et al., *Resonance wavelength-dependent signal of absorptive particles in surface plasmon resonance-based detection.* Sensors and Actuators, B: Chemical, 2007. **123**(1): p. 606-613.
232. Kurihara, K. and K. Suzuki, *Theoretical Understanding of an Absorption-Based Surface Plasmon Resonance Sensor Based on Kretchmann's Theory.* Analytical Chemistry, 2002. **74**(3): p. 696-701.
233. Dallaire, A.M., et al., *Electrochemical plasmonic sensing system for highly selective multiplexed detection of biomolecules based on redox nanoswitches.* Biosensors and Bioelectronics, 2015. **71**: p. 75-81.
234. Patskovsky, S., A.-M. Dallaire, and M. Meunier, *Electrochemical surface plasmon resonance sensing with absorptive redox mediator film.* Sensors and Actuators B: Chemical, 2016. **222**: p. 71-77.
235. Jory, M.J., et al., *Surface-plasmon opto-electrochemistry.* Sensors and Actuators B: Chemical, 1996. **35**(1–3): p. 197-201.

236. Iwasaki, Y., et al., *Electrochemical reaction of $Fe(CN)_6^{3-/4-}$ on gold electrodes analyzed by surface plasmon resonance.* Surface Science, 1999. **427–428**: p. 195-198.
237. Alpatova, N.M., et al., *Polybithiophene Heterogeneity: A Differential Cyclic Voltabsorptometry Study.* Russian Journal of Electrochemistry. **40**(3): p. 229-234.
238. Cumberland, S.L. and G.F. Strouse, *Analysis of the Nature of Oxyanion Adsorption on Gold Nanomaterial Surfaces.* Langmuir, 2002. **18**(1): p. 269-276.
239. Chang, S.C., A. Hamelin, and M.J. Weaver, *Dependence of the electrooxidation rates of carbon monoxide at gold on the surface crystallographic orientation: a combined kinetic-surface infrared spectroscopic study.* The Journal of Physical Chemistry, 1991. **95**(14): p. 5560-5567.
240. Boecker, D., et al., *Differential Surface Plasmon Resonance Imaging for High-Throughput Bioanalyses.* Analytical Chemistry, 2007. **79**(2): p. 702-709.
241. Berger, C.E.H. and J. Greve, *Differential SPR immunosensing.* Sensors and Actuators B: Chemical, 2000. **63**(1–2): p. 103-108.
242. NanoComposix. Available from: https://nanocomposix.com/pages/plasmonics.
243. Johnson, P.B. and R.W. Christy, *Optical Constants of the Noble Metals.* Physical Review B, 1972. **6**(12): p. 4370-4379.
244. Cook, K.M. and G.S. Ferguson, *Determination of the Wavelength-Dependent Refractive Index of a Gold-Oxide Thin Film.* The Journal of Physical Chemistry C, 2011. **115**(46): p. 22976-22980.
245. Wolf, A.V., *Aqueous solutions and body fluids: their concentrative properties and conversion tables.* 1966: Hoeber Medical Division, Harper & Row.
246. Burke, L.D. and P.F. Nugent, *The electrochemistry of gold: II the electrocatalytic behaviour of the metal in aqueous media.* Gold Bulletin, 1998. **31**(2): p. 39-50.
247. Zhang, Z., L. Xin, and W. Li, *Supported gold nanoparticles as anode catalyst for anion-exchange membrane-direct glycerol fuel cell (AEM-DGFC).* International Journal of Hydrogen Energy, 2012. **37**(11): p. 9393-9401.
248. Toyota, A. and T. Sagara, *Time dependent spectral change upon potential step perturbation for Au nanoparticles immobilized on an organic monolayer-modified ITO electrode.* Colloids and Surfaces a-Physicochemical and Engineering Aspects, 2006. **286**(1-3): p. 62-69.
249. Adžić, R.R., S. Strbac, and N. Anastasijević, *Electrocatalysis of oxygen on single crystal gold electrodes.* Materials Chemistry and Physics, 1989. **22**(3): p. 349-375.
250. Ataka, K.-i. and M. Osawa, *In Situ Infrared Study of Water−Sulfate Coadsorption on Gold(111) in Sulfuric Acid Solutions.* Langmuir, 1998. **14**(4): p. 951-959.
251. Horányi, G., E.M. Rizmayer, and P. Joó, *Radiotracer study of the adsorption of Cl^- and HSO_4^- ions on a porous gold electrode and on underpotential deposited metals on gold.* Journal of Electroanalytical Chemistry and Interfacial Electrochemistry, 1983. **152**(1): p. 211-222.
252. Edens, G.J., X. Gao, and M.J. Weaver, *The adsorption of sulfate on gold(111) in acidic aqueous media: adlayer structural inferences from infrared spectroscopy and scanning tunneling microscope.* Journal of Electroanalytical Chemistry, 1994. **375**(1): p. 357-366.
253. Magnussen, O.M., et al., *In situ scanning tunnelling microscopy observations of a disorder-order phase transition in hydrogensulfate adlayers on Au(111).* Faraday Discussions, 1992. **94**(0): p. 329-338.

254. Xia, S.J. and V.I. Birss, *A multi-technique study of compact and hydrous Au oxide growth in 0.1 M sulfuric acid solutions.* Journal of Electroanalytical Chemistry, 2001. **500**(1–2): p. 562-573.
255. Mulvaney, P., *Surface Plasmon Spectroscopy of Nanosized Metal Particles.* Langmuir, 1996. **12**(3): p. 788-800.
256. Chapman, R. and P. Mulvaney, *Electro-optical shifts in silver nanoparticle films.* Chemical Physics Letters, 2001. **349**(5–6): p. 358-362.
257. Chen, A. and J. Lipkowski, *Electrochemical and Spectroscopic Studies of Hydroxide Adsorption at the Au(111) Electrode.* The Journal of Physical Chemistry B, 1999. **103**(4): p. 682-691.
258. Wang, Y., X. Shan, and N. Tao, *Emerging tools for studying single entity electrochemistry.* Faraday Discussions, 2016. **193**(0): p. 9-39.
259. Poonthiyil, V., et al., *Gold Nanoparticles Decorated with Sialic Acid Terminated Bi-antennary N-Glycans for the Detection of Influenza Virus at Nanomolar Concentrations.* ChemistryOpen, 2015. **4**(6): p. 708-716.
260. Sagara, T., N. Kato, and N. Nakashima, *Electroreflectance Study of Gold Nanoparticles Immobilized on an Aminoalkanethiol Monolayer Coated on a Polycrystalline Gold Electrode Surface.* The Journal of Physical Chemistry B, 2002. **106**(6): p. 1205-1212.
261. Ureta-Zañartu, M.S., et al., *Electrooxidation of methanol and ethylene glycol on gold and on gold modified with an electrodeposited polyNiTSPc film.* Electrochimica Acta, 2007. **52**(28): p. 7857-7864.
262. Luo, J., et al., *An EQCN assessment of electrocatalytic oxidation of methanol at nanostructured Au–Pt alloy nanoparticles.* Electrochemistry Communications, 2001. **3**(4): p. 172-176.
263. Keenan, T.F., et al., *Recent pause in the growth rate of atmospheric CO_2 due to enhanced terrestrial carbon uptake.* Nature Communications, 2016. **7**: p. 13428.
264. Le Quéré, C., et al., *Global Carbon Budget 2016.* Earth Syst. Sci. Data, 2016. **8**(2): p. 605-649.
265. CAIT Climate Data Explorer. 2015 12/08/2016]; Available from: http://cait.wri.org.
266. International Energy Agency, *Tracking Clean Energy Progress 2016*. 2016.
267. Riemer, P., *Greenhouse gas mitigation technologies, an overview of the CO_2 capture, storage and future activities of the IEA Greenhouse Gas R&D programme.* Energy Conversion and Management, 1996. **37**(6–8): p. 665-670.
268. United Nations General Assembly, *United Nations Framework Convention on Climate Change.* 1992.
269. Olah, G.A., G.K.S. Prakash, and A. Goeppert, *Anthropogenic Chemical Carbon Cycle for a Sustainable Future.* Journal of the American Chemical Society, 2011. **133**(33): p. 12881-12898.
270. Christophe, J., T. Doneux, and C. Buess-Herman, *Electroreduction of carbon dioxide on copper-based electrodes: Activity of copper single crystals and copper-gold alloys.* Electrocatalysis, 2012. **3**: p. 139-146.
271. Kothandaraman, J., et al., *Conversion of CO_2 from Air into Methanol Using a Polyamine and a Homogeneous Ruthenium Catalyst.* Journal of the American Chemical Society, 2016. **138**(3): p. 778-781.
272. Holmes, G. and D.W. Keith, *An air–liquid contactor for large-scale capture of CO_2 from air.* Philosophical Transactions of the Royal Society of London A: Mathematical, Physical and Engineering Sciences, 2012. **370**(1974): p. 4380-4403.

273. Dixon, T., et al., *Outdoor Prototype Results for Direct Atmospheric Capture of Carbon Dioxide.* Energy Procedia, 2013. **37**: p. 6079-6095.
274. Tennakone, K., A.H. Jayatissa, and S. Punchihewa, *Selective photoreduction of carbon dioxide to methanol with hydrous cuprous oxide.* Journal of Photochemistry and Photobiology A: Chemistry, 1989. **49**(3): p. 369-375.
275. Dey, G.R., *Chemical Reduction of CO_2 to Different Products during Photo Catalytic Reaction on TiO_2 under Diverse Conditions: an Overview.* Journal of Natural Gas Chemistry, 2007. **16**(3): p. 217-226.
276. Liu, G., et al., *Engineering TiO_2 nanomaterials for CO_2 conversion/solar fuels.* Solar Energy Materials and Solar Cells, 2012. **105**: p. 53-68.
277. Harding, P., *Soyuz TMA-01M docks with ISS as crews conduct hardware installation*. 2010.
278. Christian, J., et al., *Compact and Lightweight Sabatier Reactor for Carbon Dioxide Reduction*, in *41st International Conference on Environmental Systems*. 2011, American Institute of Aeronautics and Astronautics.
279. Kondratenko, E.V., et al., *Status and perspectives of CO2 conversion into fuels and chemicals by catalytic, photocatalytic and electrocatalytic processes.* Energy & Environmental Science, 2013. **6**(11): p. 3112-3135.
280. Tsiplakides, D. and S. Balomenou, *Milestones and perspectives in electrochemically promoted catalysis.* Catalysis Today, 2009. **146**(3–4): p. 312-318.
281. Lim, C.F.C., D.A. Harrington, and A.T. Marshall, *Altering the selectivity of galvanostatic CO_2 reduction on Cu cathodes by periodic cyclic voltammetry and potentiostatic steps.* Electrochimica Acta, 2016. **222**: p. 133-140.
282. Cabot Corporation, *Vulcan XC-72*. Billerica, MA.
283. Zook, L.A. and J. Leddy, *Density and Solubility of Nafion: Recast, Annealed, and Commercial Films.* Analytical Chemistry, 1996. **68**(21): p. 3793-3796.
284. Kedzierzawski, P. and J. Augustynski, *Poisoning and Activation of the Gold Cathode during Electroreduction of CO_2.* Journal of The Electrochemical Society, 1994. **141**(5): p. L58-L60.

Appendix A1. EXPERIMENTAL PROCEDURES

A1.1 Colloidal Preparation and Diameter Measurement

A1.1.1 23.9 nm Au

23.9 nm Au nanoparticles were produced using the Turkevich method [95]. Synthesis began by dissolving 0.1973 g $HAuCl_4 \cdot 3H_2O$ in 500 mL DI water in a 1.0 L volumetric flask. With stirring, the solution was brought to the boil and 0.2897 g $Na_3C_6H_5O_7 \cdot 2H_2O$ (sodium citrate) was added with boiling continued for 10 minutes after the colour change occurred. The solution was stirred without heating for an additional 10 minutes followed by rapid cooling to room temperature in an ice bath. The solution was made up to 1.0 L and stored out of direct light.

A1.1.2 4.5 nm Au

4.5 nm Au nanoparticles were produced following a modification of the method laid out by Martin et al. [94]. Three solutions were produced prior to synthesis;

Solution 1: 0.49 g $HAuCl_4 \cdot 3H_2O$ was mixed with 20 mL DI water and 210 µL 37% HCl then made up to 25 mL. This produced a solution of 50 mM Au and 100 mM HCl.

Solution 2: 0.050 g NaOH was dissolved in 15 mL DI water followed by 0.0474 g $NaBH_4$ then the solution was made up to 25 mL. This produced a solution of 50 mM NaOH and 50 mM $NaBH_4$.

Solution 3: 533.5 mg carbon was weighed into a conical flask and stirred with 50 mL DI water for three hours.

For the synthesis, 6.9 mL of solution 1 was added to 280.2 mL DI water in a stirred conical flask. 18.3 mL of solution 2 was added rapidly and the solution instantly turned a dark red/brown colour. Solution 3 was added 1 minute later and left to stir for 20 hours. The solution was then filtered, well washed with DI water and dried in an oven at 70 °C for 5 hours. The powder was ground and placed in a jar for future use.

A1.1.3 3.1 nm Au

3.1 nm Au nanoparticles were produced following the method laid out by Duff, et al. [49]. Four solutions were produced prior to synthesis;

Solution 1: 2.0114 g NaOH was dissolved in 250 mL DI water to produce a 0.2 M NaOH solution.

Solution 2: 0.25 mL 80% THPC was mixed with 19.75 mL DI water to produce a 1% v/v THPC solution.

Solution 3: 10 mL 50 mM Au solution was mixed with 10 mL DI water to produce a 25 mM Au solution.

Solution 4: 408.5 mg carbon was suspended in 10 mL DI water

For the synthesis, 11.4 mL solution 1 was added to 231 mL DI water followed by 7.5 mL solution 2. After 2 minutes of mixing, 10.2 mL solution 3 was added. After the colour change was seen, solution 4 was added and stirring continued for 20 hours to ensure complete deposition. The solution was then filtered, well washed with DI water and dried overnight in an oven at 60 °C. The powder was ground and placed in a jar for future use.

A1.1.4 2.9 nm Au and 3.2 nm Au

2.9 nm Au and 3.2 nm Au nanoparticles were produced following the method laid out by Weare, et al. [91] as follows: 1.0062 g $HAuCl_4 \cdot 3H_2O$ was dissolved in 60 mL DI water in a round bottom flask. 60 mL toluene was stirred into the gold solution. 1.4012g TOAB was added to the flask and stirred for 5 minutes, during which the solution turned to a dark red colour. A fresh solution of 2.0207 g $NaBH_4$ in 10 mL DI water was stirring into the solution for 10 minutes. Approximately 1.5 – 2 minutes into the stirring the toluene phase turned a milky white colour.

The water was decanted from the solution then 100 mL of a NaCl saturated water solution was added to the toluene and shaken vigorously. The water phase was then decanted again and the rinsing procedure was repeated three more times for a total of four NaCl/water washes. The gold/toluene was filtered into a round bottom flask through celite in approximately four filtrates. The toluene was dried after each 20 mL filtrate with the final filtrate drying until it was a viscous paste.

Deuterated chloroform was used to transfer the gold into another flask. 300 mL n-pentane was dribbled down the side of the flask to crash the gold nanoparticles out of solution. The gold/chloroform/pentane solution was filtered to remove the gold from the solution. The filtered gold was then washed with five successive hexane then methanol/water washes, followed by a final hexane wash. The dried powder was then washed six times with a mixture of chloroform and pentane. The gold was then dissolved off the filter using 20 mL DCM, in eight aquilots. The gold/DCM suspension was then dried under a vacuum and the final crystal was placed into a jar for future use.

Deposition of the nanoparticles involved dissolving 30.5 mg of the gold nanoparticle in DCM and adding it to 204.4 mg carbon black suspended in 20 mL DCM. As the DCM dried, the nanoparticles deposited onto the carbon surface. This method of nanoparticles production was used for both particle syntheses, with the final PSD of the nanoparticles

only measured after deposition to the carbon support. The deposition of the nanoparticles to the support induces particle sintering, thus small variations in the deposition method can lead to variations in the final PSD.

A1.2 Electrode Preparation

A1.2.1 Spray Coating

The preparation technique of spray coating was decided primarily due to the advantages for EXAFS study. By having catalytic layers with approximately 10 wt% loading on the carbon support, the layer had a molecular gold fraction of just 0.67%. An acceptable EXAFS signal required a sufficiently thick layer to provide fluorescence data, however not so thick that mass transfer effects started blocking the deeper portions of the layer.

A1.2.2 Ink Preparation

For the first stage of ink preparation, the expected mass of ink sprayed was calculated. For example, when preparing four electrodes, each of which required 1.17 mg of the catalyst, a total of at least 1.1 times the minimum mass was required. In this example, at least 5.2 mg of the catalyst was measured into a centrifuge tube. An equivalent volume of the 0.5 $mg \cdot mL^{-1}$ Nafion solution (0.5 $mg \cdot mL^{-1}$ Nafion in a 4:1 IPA:DI water solution) was added to make a final solution with 1 $mg \cdot mL^{-1}$ of the Au/C catalyst. The ink was then ultrasonicated at 53 kHz for 10 minutes then 35 kHz for 20 minutes. The ink was always used as a fresh preparation to limit any catalyst settling or flocculation.

A1.2.3 Catalytic Layer Preparation

A three- or four-hole aluminium mask was used for spray coating. The mask was placed over graphite sheet and heated to 80 °C while the ink was being ultrasonicated. Three aquilots of the fresh ink were placed into an airbrush to ensure uniformity of the ink transfer. The ink was then sprayed as an even layer over the aluminium mask until all the ink was sprayed. The compressed air was provided to the airbrush at approximately 0.5 bar. After the three aquilots were sprayed, the graphite sheet was cooled then glue (via an epoxy glue) to a pre-drilled cuvette and dried overnight.

A1.3 Additional Sample Preparation

A1.3.1 Atomic Absorption Spectroscopy

The gold content of all Au/C catalysts was measured via atomic absorption spectroscopy on a Varian SpectrAA 220FS spectrometer. Sample preparation involved accurately weighing 4-6 mg of the Au/C catalyst into a beaker. In a fume hood, 15 mL concentrated HCl and 5 mL concentrated HNO_3 were added to the beaker which was then covered to prevent contamination and to minimize NO_2 release. The solution was stirred for 4 hours then filtered into a 50 mL volumetric flask. The beaker and filter paper were rinsed with DI water and the flask was made up to 50 mL. The gold concentration of the Au/C

solution was estimated using the targeted gold loading value. A standard solution was produced following the same method with approximately 1 mg $HAuCl_4 \cdot 3H_2O$. The Au/C solution was diluted to four different concentrations ranging from 0.5 ppm to 3 ppm and the standard solution was diluted to 6 different concentrations ranging from 0.0 ppm to 5 ppm.

A1.3.1.1 **Atomic Absorption Spectroscopy Example Calculation**

5.89 mg of a Au_{101}/C catalyst with an estimated loading of 10 wt% was dissolved and filtered into a 50 mL volumetric flask. In addition, 0.905 mg $HAuCl_4 \cdot 3H_2O$ was dissolved and filtered into a 50 mL volumetric flask. The gold content of the ligand-stabilized nanoparticle ($Au_{101}[P(C_6H_5)_3]_{21}Cl_5$) is 77.77 wt% and the gold content of the $HAuCl_4 \cdot 3H_2O$ is 56.96 %. Considering these factors, the two filtered solution are calculated to be 9.16 ppm and 10.3 ppm for the Au/C filtrate and Au filtrate, respectively. The solutions were diluted according to Table A1-1.

Table A1-1. Example of the dilution of the dissolved gold filtrate for AAS measurement.

Sample Name	Solution	Dissolved Solution / mL	DI Water / mL	Total Volume / mL	Estimated Concentration / ppm
S1	Standard	0.00 mL	10.0 mL	10.0 mL	0.00
S2	Standard	1.00 mL	9.00 mL	10.0 mL	1.03
S3	Standard	2.00 mL	8.00 mL	10.0 mL	2.06
S4	Standard	3.00 mL	7.00 mL	10.0 mL	3.09
S5	Standard	4.00 mL	6.00 mL	10.0 mL	4.12
S6	Standard	5.00 mL	5.00 mL	10.0 mL	5.15
Au_{101}-A	Au/C	0.60 mL	9.40 mL	10.0 mL	0.550
Au_{101}-B	Au/C	1.00 mL	9.00 mL	10.0 mL	0.916
Au_{101}-C	Au/C	2.00 mL	8.00 mL	10.0 mL	1.83
Au_{101}-D	Au/C	3.00 mL	7.00 mL	10.0 mL	2.75

Following AAS measurements, the data shown in Table A1-2 was received. A scatter plot was produced to ensure the concentration vs. absorbance correlation was linear and a linear fit was found for the data. In this example, the equation that describes the known sample is given by Equation A1-1, where Abs_s is the measured absorbance and C_s is the known sample concentration. The accurate concentration of each of the Au/C samples can then be calculated by Equation A1-2 with results provided in Table A1-3.

$$Abs = 0.01186 * C + 0.00020 \quad \text{A1-1}$$

$$C_s = \frac{\text{Abs}_S - 0.00020}{0.01186} \quad \text{A1-2}$$

Table A1-2. Absorption results from atomic absorption spectroscopy.

Sample Name	Estimated Concentration / ppm	Absorbance
S1	0.00	0.0003
S2	1.03	0.0123
S3	2.06	0.0247
S4	3.09	0.0368
S5	4.12	0.0491
S6	5.15	0.0614
Au_{101}-A	0.550	0.0061
Au_{101}-B	0.916	0.0100
Au_{101}-C	1.83	0.0202
Au_{101}-D	2.75	0.0297

Table A1-3. Calculated concentrations of the Au/C samples.

Sample Name	Estimated Concentration / ppm	Calculated Concentration / ppm
Au_{101}-A	0.550	0.500
Au_{101}-B	0.916	0.826
Au_{101}-C	1.83	1.69
Au_{101}-D	2.75	2.49

The calculated Au/C concentrations were then converted into the original filtrate concentration via Equation A1-3 and finally, into a Au/C mass loading via Equation A1-4 where C_f is the filtrate concentration, V_t is the total sample volume, V_s is the filtrate volume used to make the sample, V_f is the filtrate volume, $Au_{wt\%}$ is the mass loading of gold on the Au/C catalyst, $m_{Au/C}$ is the mass of Au/C weighed into the beaker to be dissolved and *AuContent* is the gold content of the nanoparticle. The final result shows the true Au/C loading was 9.09 wt% (Table A1-4)

$$C_f = \frac{C_s * V_t}{V_s} \quad \text{A1-3}$$

$$Au_{wt\%} = \frac{C_f * V_f}{m_{Au/C} * AuContent} \quad \text{A1-4}$$

Table A1-4. Results from the calculation of the Au/C gold loading.

Sample Name	Calculated Concentration / ppm	Calculated Filtrate Concentration / ppm	Calculated Gold Loading / wt%
Au_{101}-A	0.500	8.33	9.09
Au_{101}-B	0.826	8.26	9.02
Au_{101}-C	1.69	8.43	9.20
Au_{101}-D	2.49	8.29	9.05
Average		8.33	9.09

A1.3.1.2 **Atomic Absorption Spectroscopy Results**

Five different catalysts were deposited to carbon black with the final gold loading on the carbon black tested via AAS. The final carbon loading was lower than the targeted loading due to losses in the filtrate during washing or due to insufficient dissolution of the gold during the AAS preparation. The 3.2 nm nanoparticles showed a higher than expected loading due to incomplete carbon transfer or incorrectly characterized NP-ligand structure. The expected loading (Table A1-5) is the calculated value assuming all of the nanoparticles in the colloidal solution deposited to the carbon black.

Table A1-5. Concentration results from atomic absorption spectroscopy.

Particle Diameter / nm	Preparation Method	Expected Loading / wt% Au	AAS Reported Loading / wt% Au
0.8	[193]	9.42	8.19
2.9	[91]	10.07	7.96
3.1	[49]	*	15.3
3.2	[91]	12.97	15.1
4.5	[94]	12.62	9.01

*This sample was prepared by a previous student.

A1.3.2 Electron Microscopy

A1.3.2.1 **Scanning Electron Microscopy**

SEM samples were prepared for the 23.9 nm nanoparticle by washing the fresh or used Au/FTO slide with DI water and subsequently drying the slide in ambient conditions. The slide was then mounted to the SEM sample holder with conductive carbon tape and an additional portion of the conductive carbon tape was adhered to the upper, conductive FTO surface of the slide, as well as being adhered to the sample holder to prevent charging under the electron beam. Images were then taken of the gold/FTO surface, ensuring sufficient images to provide a representative sample for particle size analysis.

A1.3.2.2 **Transmission Electron Microscopy**

TEM samples of the fresh Au/C catalyst were prepared by suspending 1-2 mg of the dried powder in IPA and providing ultrasonication at 53 kHz for 10 minutes. The solution was then diluted by adding several drops of the suspension to 5-10 mL fresh IPA. The approximate concentration was targeted by ensuring the final solution was slightly cloudy yet remained clear enough to be semi-translucent.

TEM samples of electrocatalytic layers were produced by cutting the graphite sheet from the cuvette and placing it in 1-1.5 mL IPA. The IPA/catalytic layer was then placed in the ultrasonic bath at a frequency of 53 kHz for 10 minutes or until the catalyst detached from the graphite, whichever process took longer. These solutions were typically at the 'slightly cloudy' translucency and needed no additional, or only minimal additional IPA.

Once the semi-translucent solutions were obtained, a lacey-carbon TEM grid was held with reverse (self-closing) tweezers and 2x10 μL aquilots of the solution were pipetted onto the grid, ensuring the first aquilot was dry before the second was added. The TEM grid was then dried by vacuum pump and stored for TEM imaging. Images were then taken of the Au/C catalyst, ensuring sufficient images to provide a representative sample for particle size analysis.

A1.4 Potentiostatic Techniques

A1.4.1 The Cell

Electrochemical measurements were performed using a Gamry Reference 3000 potentiostat in a typical 3 cell set-up. A Pt/Ir wire was used as a counter electrode with a Ag/AgCl (Sat. KCl) reference electrode for acidic or neutral solutions and a Hg/HgO (1.0 M KOH) reference electrode for alkaline solutions.

A1.4.2 Electrochemical Measurements

Several different types of electrochemical measurements were made using the Gamry Reference 3000 potentiostat. Specific descriptions of these techniques are explained in their appropriate sections within this thesis. Techniques used included;

- Cyclic voltammetry (CV),
- Galvanostatic charging
- Open circuit potential (OCP),
- Potentiostatic electrochemical impedance spectroscopy (P-EIS).

A1.4.3 Cyclic Voltammetry Charge Analysis

The electrochemically active surface area (EASA) of the gold and gold nanoparticle electrodes was measured by integrating the gold oxide reduction peak and converting this value into the total charge passed through the electrode (Equation A1-5, where $I \bullet V$ is the integrated peak area and *S.R.* is the sweep rate). This total charge can then be converted into the number of gold surface sites converted into Au_2O_3 via Equation A1-6, where *S.S.A.*

is the specific surface area of the crystal structure (a value of 386.4 $\mu C \cdot cm^{-2}$ is used in this thesis).

$$Q = \frac{I*V}{S.R.} \quad \text{A1-5}$$

$$EASA = \frac{Q}{S.S.A.} \quad \text{A1-6}$$

For example, Figure A1-1 was recorded on a gold plate with a geometric surface area of 3.14 cm^2 in 0.5 M H_2SO_4 at a sweep rate of 100 $mV \cdot s^{-1}$ and the integrated value ($I \bullet V$) was measured as 3.3785×10^{-1} $mA \cdot V$. This is converted to a charge by dividing by 0.100 $V \cdot s^{-1}$, resulting in a total charge value of 3.38 mC. Using Equation A1-6, we find an EASA of 8.74 cm^2. This shows that the EASA is 2.78 times greater than the geometric surface area, indicating, in this example, that either the gold surface is not atomically flat, the gold oxide layer was thicker than a single monolayer, or a combination of both of these reasons.

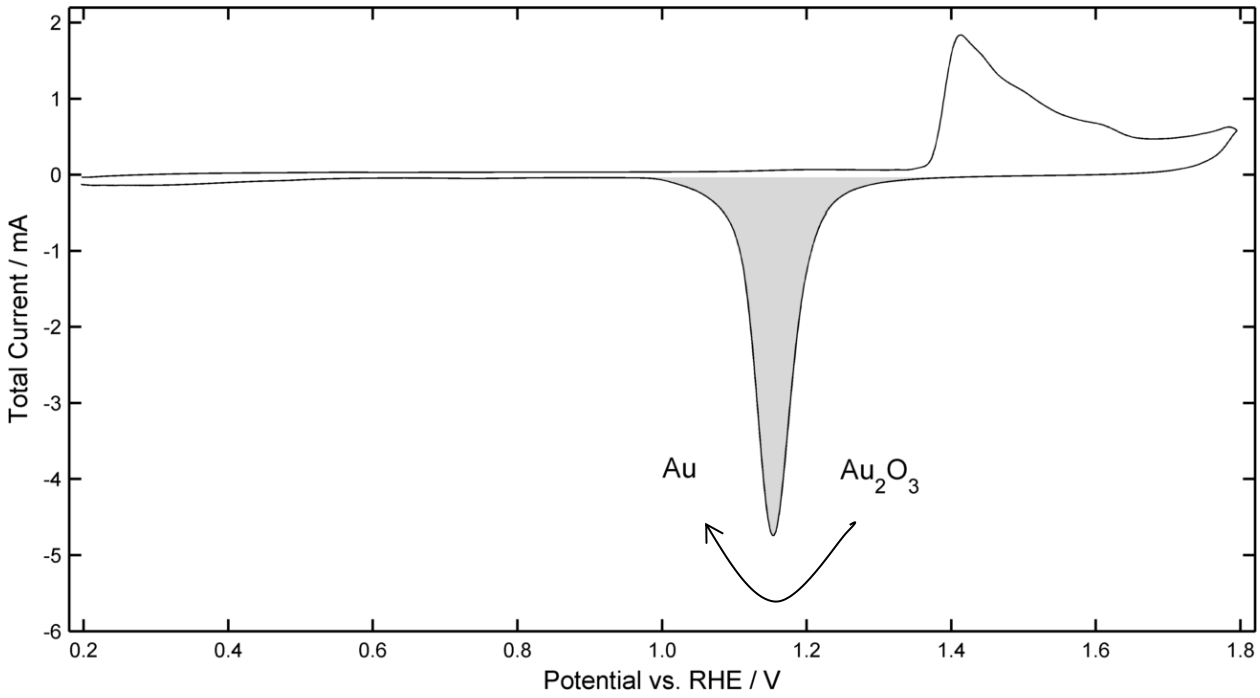

Figure A1-1. Gold plate CV scan recorded in 0.5 M H_2SO_4 with a sweep rate of 100 $mV \cdot s^{-1}$. The shaded area represents the charge corresponding to gold oxide reduction.

A1.4.4 Reference Electrodes

Three types of reference electrodes were used in this research; a reversible hydrogen electrode, a Ag/AgCl (Sat. KCl) electrode and a Hg/HgO (1.0 M KOH) electrode. For ease of comparability, reference potentials were converted to the RHE electrode scale for all measurements shown within this thesis (Table A1-6).

Table A1-6. Reference electrode conversions.

Reference Electrode	Solution	pH	RHE vs. Reference / V
Ag/AgCl (Sat. KCl)	0.5 M H_2SO_4	0.29	+0.214
	0.5 M K_2SO_4	7.00	+0.611
	1.0 M $HClO_4$	0.00	+0.197
	0.2 M $KHCO_3$	Variable	Variable
Hg/HgO (1.0 M KOH)	1.0 M KOH	14.00	+0.925

Appendix A2 PARTICLE SIZE ANALYSIS

A2.1 Overview

Nanoparticle sizes were measured directly via representative TEM or SEM images. Particle sizes were measured in ImageJ software; with measured data exported into Excel for manipulation. As discussed in Chapter 3, the average particle size must be considered as a part of a particle size distribution, not as a single size that represents the entire distribution. Table A2-1 shows the different sizes, dependent on the dimension averaged. Note; particles are referred to by their number weighted average for ease of communication and for conformities sake.

Table A2-1. Particle size distribution for all nanoparticles showing the difference in particle size depending on how the distribution is calculated. The standard deviation for each average particle diameter is shown in brackets.

Particle	Number weighted average / nm		Area Weighted Average / nm		Volume Weighted Average / nm		Specific Surface Area Weighted Average / nm	Specific Surface Area / $m^2 \cdot g^{-1}$
23.9 nm Au	23.9	(4.1)	24.3	(4.1)	25.2	(4.1)	25.2	12.3
4.5 nm Au	4.5	(4.0)	6.0	(4.3)	7.4	(4.9)	11.3	27.5
4.5 nm Au*	8.2	(4.0)	9.0	(4.2)	9.7	(4.4)	11.3	27.5
3.1 nm Au	3.1	(0.9)	3.2	(0.9)	3.3	(0.9)	3.6	86.6
3.1 nm Au*	4.6	(2.2)	5.1	(2.2)	5.6	(2.4)	6.8	45.8
2.9 nm Au	2.9	(0.8)	3.0	(0.8)	3.2	(0.8)	3.4	91.4
2.9 nm Au*	4.7	(1.6)	5.0	(1.6)	5.3	(1.7)	5.9	53.1
0.8 nm Au*	4.5	(1.5)	4.7	(1.6)	5.0	(1.6)	5.6	55.9

* refers to particles that have been electrochemically aged via 100 CV scans between 0.21 and 1.56 V vs. RHE in 0.5 M H_2SO_4.

Table A2-2. Number of particles counted and images used for each PSD

Particle	Number of particles counted	Number of representative images
23.9 nm Au	1058	1
4.5 nm Au	244	8
4.5 nm Au*	116	17
3.1 nm Au	277	7
3.1 nm Au*	661	24
2.9 nm Au	614	14
2.9 nm Au*	380	13
0.8 nm Au*	294	2

* refers to particles that have been electrochemically aged via 100 CV scans between 0.21 and 1.56 V vs. RHE in 0.5 M H_2SO_4.

2.2 ImageJ Analysis Method

The particle size distributions were measured by using ImageJ, a free image analysis programme released by the US NIH. The technique used followed a tutorial produced by Dr. Jan-Yves Ruzicka (http://mesa.ac.nz/2013/03/particle-sizing-using-imagej), however, in the interest of ensuring the techniques used within this thesis are retained, this section outlines the methods used for this analysis. At the time of the publication of this thesis, ImageJ could be downloaded from the NIH website (https://imagej.nih.gov). Due to the range of contrast of the gold, carbon support, lacey carbon, FTO slide and the blank background, measurements were unable to be automated, therefore individual particles were sized.

For the analysis, a single image magnification was selected such that 1) there were sufficient particles to ensure a statistically representative sample of particles could be measured and 2) the largest range of particles sizes could be measured *without* requiring the image capturing process to focus on a specific particle size. Each image was opened in the ImageJ software and the "Oval" tool was selected. The image was then scaled appropriately to allow sufficient accuracy when selecting individual nanoparticles. An oval or sphere (obtained by holding the 'shift' key while drawing an oval) was drawn around an individual particle and the 'Ctrl+m' was pressed to record the particle. The oval/sphere that was drawn for the particle remained overlaid on the image to ensure the same particle wasn't measured twice. This option was toggled by following the menu options: Analyze-Set Measurements-Add to Overlay.

Once all particles in each image had been measured, the image was closed without closing the results window and the next image opened. Once all images in a single data set had been measured, the results were imported into Excel by selecting the data in the 'Results' window and copy-pasting into a new worksheet. This data included; a count of all particles, the image each measurement was taken from, the cross sectional surface area of each particle (measured in pixels^2) and any additional information selected in the 'Set Measurements' window. One of the images was then opened in Paint and length of the scale bar was measured to find the exact number of pixels per nanometer. This value was then used to scale the measurements and the PSD could be obtained.

2.3 Representative Images

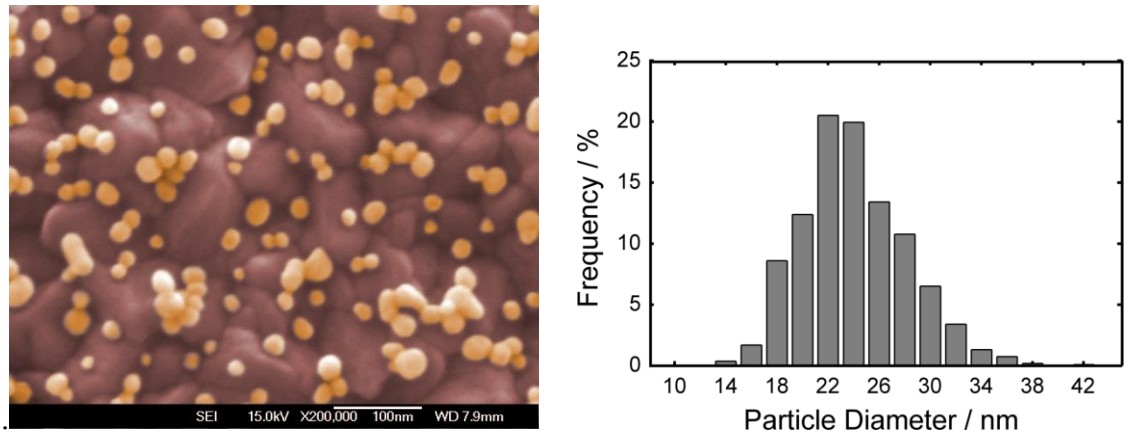

Figure A2-1. Representative image and PSD of 23.9 nm Au nanoparticles.

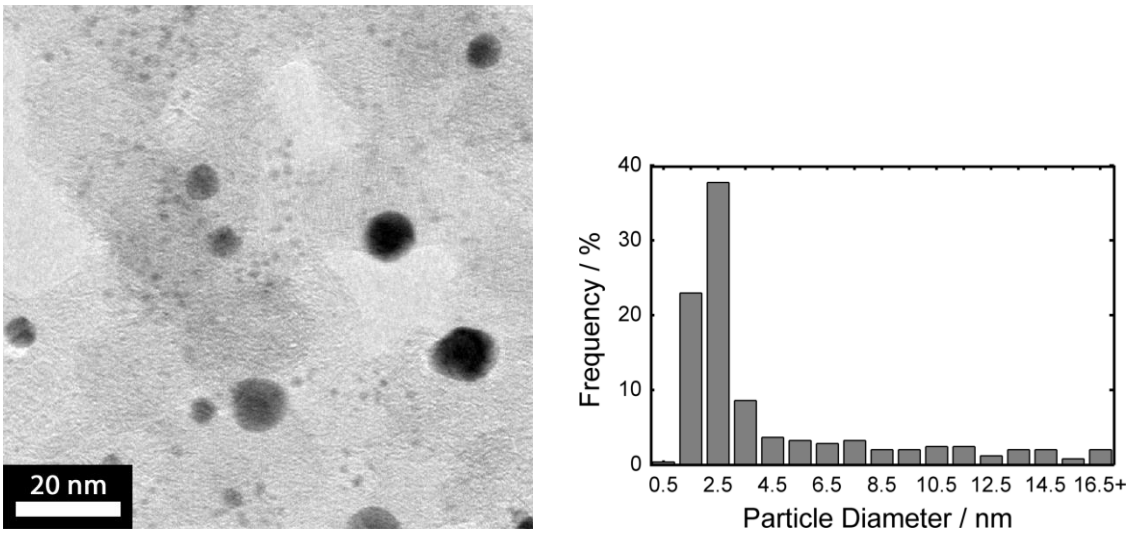

Figure A2-2. Representative image and PSD of 4.5 nm Au nanoparticles.

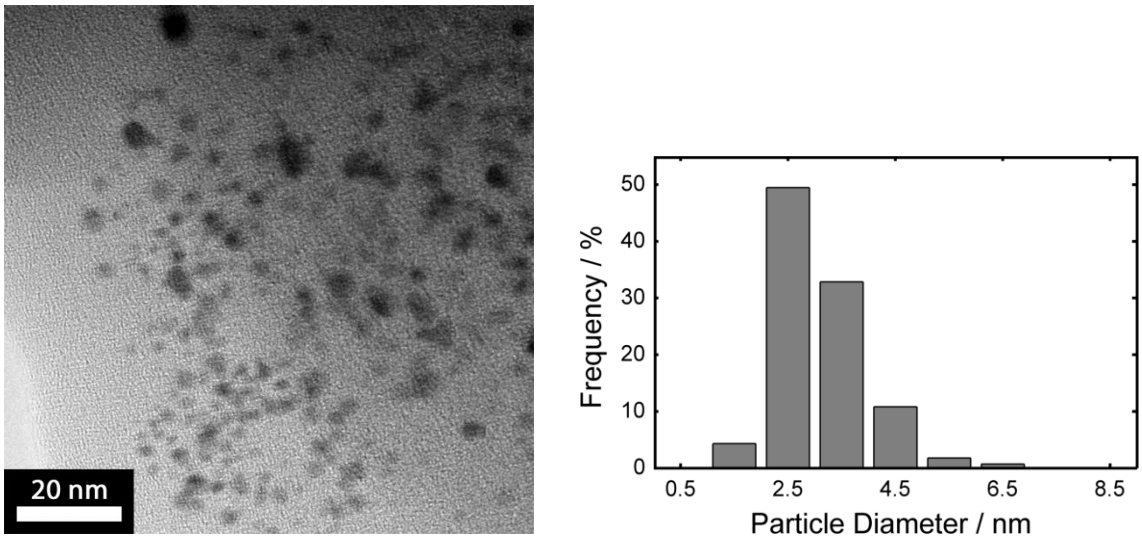

Figure A2-3. Representative image and PSD of 3.1 nm Au nanoparticles.

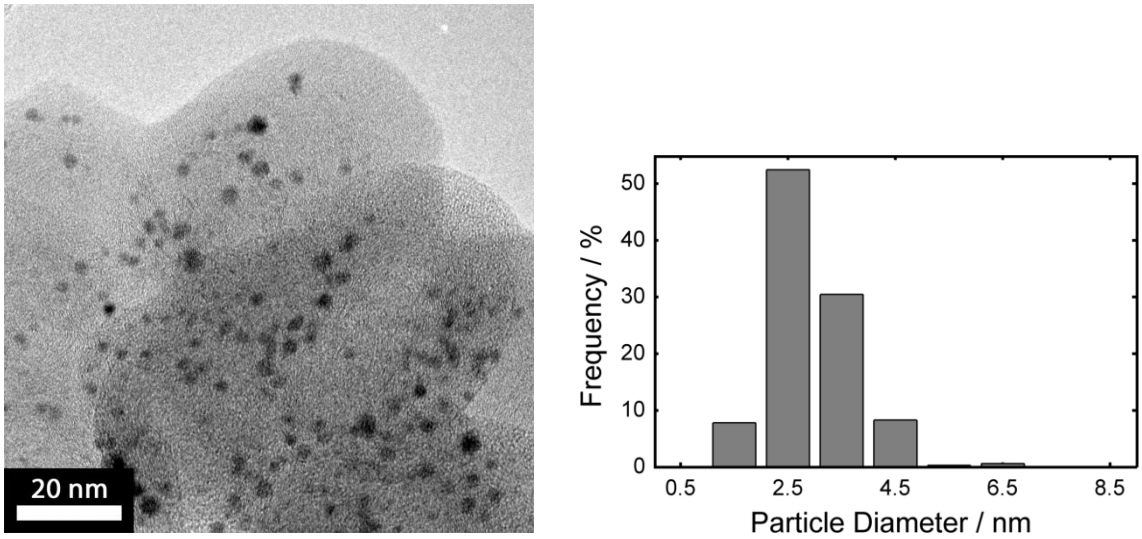

Figure A2-4. Representative image and PSD of 2.9 nm Au nanoparticles.

Appendix A3 X-RAY PHOTOELECTRON SPECTROSCOPY

A3.1 Experimental

A3.1.1 Catalytic Layer

Catalytic layers as described in Section A1.2 were prepared for all samples. In brief, the Au/C catalyst was suspended with Nafion in a 4:1 IPA solution via ultrasonication at a catalyst concentration of 1 $mg \cdot mL^{-1}$ and a Nafion concentration of 0.5 $mg \cdot mL^{-1}$. Catalytic layers were either stored for XPS measurement or glued to a cuvette for ageing. After ageing the catalytic layer and graphite sheet were cut from the cuvette and dried in a desiccator at ambient conditions until ready for XPS measurements.

Several different aspects of electrode preparation and usage were investigated using XPS (Table A3-1). These included if the phosphine ligand would deposit to a pure carbon sample (sample referred to as "C+PPH_3") and if it did, whether it would appear in the XPS measurement (Sample 1). The effect of exposing the sample to H_2SO_4 was also examined (Sample 2 and Sample 3). The effect of 100 CV scans was also tested for all four nanoparticles that had been deposited to carbon (Sample 2 and all other remaining samples).

A3.1.2 XPS Measurements

XPS was performed at the University of Auckland on a Kratos Axis UlraDLD spectrophotometer at a pressure of 1×10^{-9} torr with monochromatic Al Ka X-rays (1486.69 eV). A survey scan was performed on both fresh and electrochemically cycled samples with a pass energy of 160 eV, along with scans at the C 1s, P 2p, and Au 4f energy ranges with a pass energy of 20 eV. Survey, C 1s and P 2p scans had an acquisition time of 30 min each while Au 4f scans had an acquisition time of 40 min each.

A3.1.3 XPS Analysis

XPS data was analysed using CasaXPS. Each spectrum was aligned, if necessary, by adjusting the recorded binding energy of the C 1s peak to 284.6 eV. This adjustment was performed equally across the survey scan and the element specific scans for each sample. All scans were loaded into CasaXPS and 'Regions' were applied across the F 1s, O 1s, C 1s, S 2s, P 2p and Au 4f peak regions. Gaussian peaks were then fitted within these regions, with two peaks being applied to both the C 1s region and Au 4f region to improve the accuracy of the fitting procedure. The same regions and curves were fitted to each spectrum separately and the spectra were scaled according to their corresponding C 1s peak area. The at% and wt% of each molecule was extracted (Table A3-1) and the ratio of gold:carbon was calculated.

Table A3-1. Sample information and XPS results for C+PPH_3, 0.8 nm Au, 2.9 nm Au, 3.1 nm Au and 4.5 nm Au samples.

Sample Number	1	2	3	4	5	6	7	8	9	10
Nanoparticle Size / nm	-	0.8	0.8	0.8	2.9	2.9	3.1	3.1	4.5	4.5
Number of CV Scans	0	0	0	100	0	100	0	100	0	100
Exposure to H_2SO_4	No	No	Yes	Yes	No	Yes	No	Yes	No	Yes
Was PPh_3 present in the fresh sample?	Yes	Yes	Yes	Yes	Yes	Yes	Yes	Yes	No	No
Atomic %										
Fluorine	71.1	24.5	44.6	75.3	72.6	64.3	72.7	39.4	70.3	35.4
Oxygen	3.4	24.1	15.0	5.4	4.1	7.9	4.6	18.6	3.5	22.3
Carbon	25.0	48.6	37.7	17.0	20.7	26.1	18.8	39.4	24.7	38.9
Sulfur	0.5	2.4	1.5	0.5	0.6	0.8	0.5	1.7	0.5	2.5
Phosphorus	0.0	0.0	0.0	0.1	0.0	0.0	0.2	0.0	0.0	0.0
Gold	0.0	0.4	1.2	1.6	2.0	1.0	3.2	0.8	1.0	1.0
Weight %										
Fluorine	65.6	53.9	32.5	19.8	49.1	49.7	42.2	30.5	54.3	26.6
Oxygen	2.8	3.4	9.7	17.3	2.5	5.4	2.4	12.8	2.4	14.9
Carbon	30.8	16.3	36.6	52.4	18.7	26.9	14.6	40.7	25.5	39.0
Sulfur	0.8	0.7	1.9	3.4	0.7	1.1	0.5	2.4	0.6	3.3
Phosphorus	0.0	0.1	0.0	0.0	0.0	0.0	0.2	0.0	0.0	0.0
Gold	0.0	25.6	19.3	7.1	29.1	16.9	40.1	13.4	17.2	16.2
Gold:Carbon Ratio	0.0	1.57	0.53	0.13	1.55	0.63	2.75	0.33	0.68	0.42

Most of the normalised, binding energy corrected Au 4f spectra can be seen to have peaks at slightly higher binding energies that the literature value of 84.0 eV and 87.7 eV. This could be due to the binding energy correction being inaccurate by ~0.2-0.3 eV. However, the Au 4f peaks for the fresh sample and the H_2SO_4 exposed sample of the 0.8 nm Au nanoparticle are beyond the possibility for any such inaccuracies to correct. The peak binding energy for the Au $4f_{5/2}$ peak was found to be 88.7 eV while the binding energy for the Au $4f_{7/2}$ peak was found to be 85.2 eV. The C+PPH_3 sample showed no evidence of gold (Figure A3-1). The phosphorus peak was only seen in the fresh samples of the 0.8 nm Au and 3.1 nm Au nanoparticles and was not seen in either the H_2SO_4 exposed sample nor the aged samples (Figure A3-2).

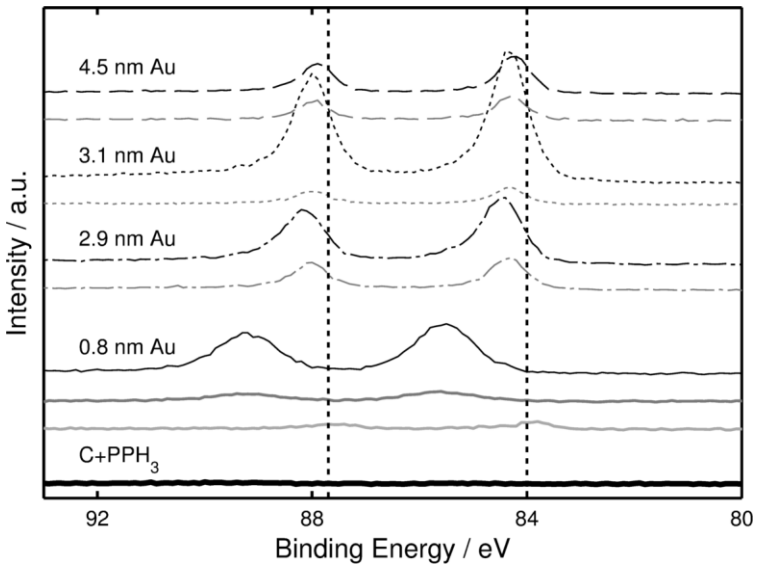

Figure A3-1. Au 4f XPS spectrum for 4.5 nm Au (dashed line), 3.1 nm Au (dotted line), 2.9 nm Au (dash-dot line), 0.8 nm Au (thin solid line) and C+PPH3 sample (thick solid line). Different preparation methods were used prior to XPS measurements including freshly created catalytic layers (black lines), catalytic layer exposed to H_2SO_4 for 10 minutes (dark grey line – only for 0.8 nm Au), and catalytic layer has been through 100 CV scans (light grey line).

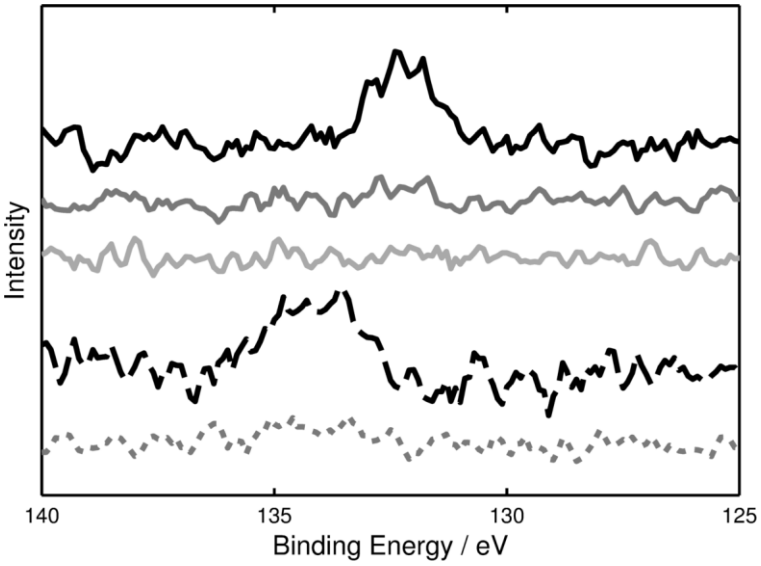

Figure A3-2. P 2p XPS spectrum for 2.9 nm Au (dashed line) and 0.8 nm Au (solid line). Different preparation methods were used prior to XPS measurements including freshly created catalytic layers (black lines), catalytic layer exposed to H_2SO_4 for 10 minutes (dark grey line – only for 0.8 nm Au), and catalytic layer has been through 100 CV scans (light grey line).

FROM IL PENTAMERONE; OR THE TALE OF TALES

TO WHOMSO HATH READ THESE WORDS CORRECTLY

BY M.R.S.D.

An in these pages ye did find
Aught error, as ye whilom read,
Then to these fauls be always blind,
For art must guile e'en Argus' head

And if ye have found good in these,
And will their petty slips defend,
Then shut your eyes, and trust, like Mars,
That what was wrong will rightly end.

Ride not cock-proud on pack-ass' loin,
Go simply with the beggar's coin,
And ye shall with true wisdom join.

But peace to barking, currish pen!
When ye have read – then read again:
Read backwards, sideways. So godden!